

**INVESTIGATIONS OF SCALING EFFECTS ON  
SUBMARINE PROPELLER AND STERN BOUNDARY LAYER FLOWS**

**Office of Naval Research  
Defense Experimental Program to Stimulate Competitive Research (DEPSCoR)  
ONR Grant No. N00014-99-1-0534**

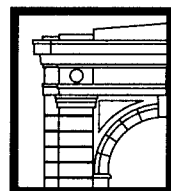
**FINAL REPORT**

**David H. Bridges,  
Allison Cruthird Cash and John L. Freudenthal  
Department of Aerospace Engineering  
James Worth Bagley College of Engineering  
Mississippi State University  
Mississippi State, MS 39762**

**August 2004**

**DISTRIBUTION STATEMENT A**

**Approved for Public Release  
Distribution Unlimited**



**JAMES WORTH  
BAGLEY  
COLLEGE OF ENGINEERING  
MISSISSIPPI STATE UNIVERSITY**

**BEST AVAILABLE COPY**

**MSSU-ASE-04-02**

**20041012 036**

## **DEPARTMENT OF AEROSPACE ENGINEERING**

**ANTHONY J. VIZZINI, PH. D.**

HEAD, DEPARTMENT OF AEROSPACE ENGINEERING

**DAVID L. LAWRENCE, P. E.**

DIRECTOR, RASPET FLIGHT RESEARCH LABORATORY

## **JAMES WORTH BAGLEY COLLEGE OF ENGINEERING**

**ROBERT P. TAYLOR, PH. D.**

INTERIM DEAN

For additional copies or information, address correspondence to:

Department of Aerospace Engineering

Mississippi State University

P.O. Box A

Mississippi State, MS 39762

Telephone (662) 325-3623

Fax (662) 325-7730

Mississippi State University does not discriminate on the basis of race, color,  
religion, national origin, sex, age, disability, or veteran status.



## **INVESTIGATIONS OF SCALING EFFECTS ON SUBMARINE PROPELLER AND STERN BOUNDARY LAYER FLOWS**

Office of Naval Research  
Defense Experimental Program to Stimulate Competitive Research (DEPSCoR)  
ONR Grant No. N00014-99-1-0534

### **FINAL REPORT**

David H. Bridges,  
Allison Cruthird Cash and John L. Freudenthal  
Department of Aerospace Engineering  
Bagley College of Engineering  
Mississippi State University  
Mississippi State, MS 39762

August 2004



MSSU-ASE-04-02

### Acknowledgments

Funds for this study were provided by the Office of Naval Research Defense Experimental Program to Stimulate Competitive Research (DEPSCoR), Grant No. N00014-99-1-0534. The program monitors were Drs. L. Patrick Purtell and Candace Wark (Dr. Wark has since returned to her faculty position at the Illinois Institute of Technology). These funds included the support for the two graduate students, Allison Cruthird Cash and John L. Freudenthal, who participated in this investigation.

Additional funds were supplied by the Mississippi State University Department of Aerospace Engineering, John C. McWhorter III, Head (now retired), in the form of matching funds. The financial assistance provided by Dr. McWhorter and the financial management assistance provided by Ms. Carol Martin and Ms. Stephanie Hall were much appreciated.

Drs. Lafayette K. Taylor and Kidambi Sreenivas, formerly of the SimCenter at the Mississippi State University Engineering Research Center and now at the University of Tennessee – Chattanooga SimCenter, provided the necessary direction to Mrs. Cash for the computational studies, and their significant contributions are greatly appreciated. Engineer Martin Donnelly of the Naval Surface Warfare Center – Carderock Division (NSWCCD) oversaw the model setup and testing in the Large Cavitation Channel. Drs. Joel Park and Michael Cutbirth, on-site engineers at the LCC, were responsible for the velocity data acquisition with the LCC's LDV system. The contributions of all of the staff of the NSWCCD and the LCC who assisted in these tests are greatly appreciated. Mr. Jim Shrock assisted with various repair and assembly jobs on the MSU water tunnel, and his help was much appreciated, as was the help of the staff of the Raspet Flight Research Laboratory, who also assisted in repairs to the water tunnel. Drs. Keith Koenig and Z. U. A. Warsi of the Department of Aerospace Engineering at Mississippi State University were very helpful in their reviews of the theses and this report. Finally, the first author would like to express his gratitude to his two graduate students, both of whom performed exceptionally well and did a very large amount of work.



### Abstract

The simulation of flows past ships poses a particular challenge because of the size of the ship and the resulting large values of dimensionless parameters such as Reynolds number. As a result, the only simulation method that can duplicate the required parameters is computational fluid dynamics (CFD). However, the drawback of CFD at these large scales is the lack of data available for validation of the CFD solutions. To provide some insight into this problem, experimental measurements were made on a small-scale model and a large-scale model. The small-scale model was 0.286 m (0.940 ft) long and was tested in a water tunnel facility located at Mississippi State University. A method of obtaining drag values from wake profile measurements was developed and the measurements were made using a laser Doppler velocimeter (LDV) system. The large-scale model was 7.03 m (23.0 ft) long and was tested in the U. S. Navy William B. Morgan Large Cavitation Channel (LCC). Computational simulations of the flows at both of these scales were obtained to see how well the solutions agreed with the experimental results over a very large change in length scale. This was of particular interest since the factor of the increase in length scale in going from the LCC model to the full-scale prototype is approximately the same as the factor of the increase in length scale between the small-scale and large-scale models. The drag coefficients of both models were measured. The thrust coefficients for a propeller on the large-scale model were measured over a range of advance ratio. The drag coefficients for both models and the propeller thrust coefficients for the large-scale model were obtained from the computational simulations. The experimental and CFD drag coefficients were in reasonable agreement for the small-scale model. For the large-scale model, the computational simulations showed a continuous decrease in the drag coefficient with Reynolds number, typical behavior for a flow in which the drag is dominated by skin friction. However, the large-scale model experiments showed that the drag coefficient leveled off at larger Reynolds number, indicating the likely presence of a separated region that would cause the drag to be dominated by pressure forces rather than by skin friction. LDV measurements of the flow at the stern of the large-scale model indicated a small separated region with reversed flow. Such a region was not obvious in the computational solutions. The computed and measured propeller thrust coefficients were in excellent agreement. It was concluded that a higher resolution grid and solution was probably necessary to capture fully the separated region behind the submarine and accurately predict the drag behavior. This is a not uncommon problem in CFD, where large scale geometries at large Reynolds number require large grids with high resolution to simulate the flow accurately.

## Table of Contents

Acknowledgments .....	ii
Abstract .....	iii
Table of Contents.....	iv
List of Symbols.....	vi
1. INTRODUCTION.....	1
1.1 Statement of the problem .....	1
1.2 Submarine and propeller geometries.....	2
1.3 Overview of report.....	3
2. RESULTS OF COMPUTATIONAL SIMULATIONS .....	4
2.1 Overview of chapter.....	4
2.2 Computational methods .....	4
2.3 Results .....	5
3. EXPERIMENTAL STUDIES ON SMALL-SCALE MODEL.....	7
3.1 Overview of chapter.....	7
3.2 Wake profile drag method.....	7
3.3 Experimental apparatus.....	8
3.4 Experimental results.....	9
4. EXPERIMENTAL STUDIES ON LARGE-SCALE MODEL.....	12
4.1 Overview of chapter.....	12
4.2 Experimental apparatus and procedure .....	12
4.2.1 Facility.....	12
4.2.2 Model.....	12
4.2.3 Instrumentation and data reduction.....	13
4.3 Results.....	15
4.3.1 Drag .....	15
4.3.2 Propeller thrust.....	16
4.3.3 Boundary layer measurements.....	17
5. COMPARISON OF COMPUTATIONAL AND EXPERIMENTAL RESULTS .....	23
5.1 Drag .....	23
5.2 Propeller thrust.....	24

6. CONCLUSIONS.....	25
References .....	26
Figures .....	beginning on p. 28
Appendices .....	after p. 53

### List of Symbols

$b$	Wake width scale
$C_D$	Coefficient of drag
$c_l$	Wake width parameter obtained from curve fits, used to compute drag coefficient
$c_u$	Wake velocity deficit parameter obtained from curve fits, used to compute drag coefficient
$D$	Propeller diameter
$D_h$	Model hull diameter
$d$	Model hull diameter (small-scale model)
$F_x$	Axial force as measured by body dynamometer
$f_x$	Axial force as measured by propeller dynamometer
$J$	Advance ratio
$K_T$	Propeller thrust coefficient
$l_0$	Wake width scale
$n$	Propeller rotational speed
$Re_L$	Reynolds number based on length
$U_0$	Velocity outside model wake
$u_0$	Centerline velocity deficit in wake
$V$	Forward speed, free stream velocity
$x$	Coordinate for axial or streamwise velocity component
$x_0$	Virtual origin for power-law variations of wake parameters
$z$	Transverse coordinate for wake measurements
$z_0$	Wake centerline location, obtained from curve fits
$\nu$	Kinematic viscosity
$\rho$	Density

## 1. INTRODUCTION

### 1.1 Statement of the problem

It is a well-established law of experimental fluid dynamics that in order to achieve dynamic similarity between prototypes and experimental models, the values of certain dimensionless parameters such as the Reynolds number have to be matched between the prototype and the model. It is also a well-established fact that because of the large length scales involved, experiments involving ship prototypes rarely achieve complete dynamic similarity. It is usually very difficult to match values of the Reynolds numbers, and almost always impossible to match Reynolds and Froude numbers simultaneously. The ship study problem is often quoted in elementary textbooks on fluid mechanics as an example of incomplete similarity (e.g. Fox and McDonald 1998).

The advent of computational fluid dynamics (CFD) solutions in recent years has meant that it is now possible to simulate flows at the required values of the dimensionless parameters, allowing ship designs to be "tested" before construction begins. However, the issue of validation of the computational results then arises. If the new ship designs are different enough from existing models and prototypes, there are no data available by which the computational simulations can be validated. While CFD has undergone significant development over the past few years, in many ways it is still in a developmental stage and so information that can attest to the validity of the solutions is welcomed.

This leads to the purpose of the current study. The goal was to study experimentally two submarine models, one that would fit inside a relatively small water tunnel located at Mississippi State University (MSU), and a second model that is used in the U. S. Navy's William B. Morgan Large Cavitation Channel (LCC) located in Memphis, TN. The length of the MSU model was to be approximately 1 ft, and the length of the LCC model was to be approximately 23 ft, so that there would be over an order of magnitude difference in size. The flows past these models were to be simulated computationally, in order to see how well the computational solutions tracked the measured flows over large changes in length scale and hence Reynolds number. In particular, the drag of the submarine's bare hull and the thrust provided by a propeller attached to an appended hull were to be measured and computed, and the results compared. The goal was to see if these results would provide some information as to how well the computational solutions would predict the actual flow over the change in length scale involved in going from the LCC model to a full-scale prototype.

## 1.2 Submarine and propeller geometries

As just mentioned, there were essentially three studies conducted in this investigation – an experimental study using a small scale model in the MSU water tunnel, an experimental study using a much larger scale model in the LCC, and a computational study of both model geometries and a full-scale geometry. The common threads in these three different studies were the submarine hull geometry and the propeller geometry. The submarine hull and propeller geometries were dictated by the models to be used in the LCC, so the LCC hull and propeller geometries will be discussed at some length here. The hull geometry was a standard axisymmetric hull (DTMB Model 5495-3). The hull outline is shown in Figure 1.1. For the drag studies, the hull geometry had no sail or appendages. The geometry included a “dummy hub” and afterbody geometry that corresponded to a configuration used in a previous test on this model (see Bridges 2004 and the discussion below). Fins with NACA 0012 airfoil cross-sections were added to the stern in a standard cruciform arrangement for the configuration used in the thrust studies. A photograph showing the arrangement of these appendages on the LCC model is shown in Figure 1.2.

The propeller geometry used in these studies corresponded to the David Taylor Model Basin Propeller No. 4381 (hereinafter referred to as P4381). This propeller was originally designed and built as part of a study of the effects of skew on marine propellers (Boswell 1971). P4381 was the unskewed propeller in this series. Interestingly, this study was funded by several commercial shipping companies, and so the propeller design itself and the results of the study were unclassified. The fact that P4381 has an unclassified geometry and that the actual model propeller still exists has resulted in a number of both experimental and computational studies being performed on it, including the current study.

The actual propeller used in the LCC experiments is shown in Figure 1.3, in both a photograph (from Hecker and Remmers 1971) and an Autocad IGS file (courtesy Martin Donnelly, NSWCCD). A plan drawing of one of the blades (from Boswell 1971) is also included in the figure. The actual P4381 is a five-bladed propeller with a diameter of 1 ft, an expanded area ratio of 0.725, an NACA  $a = 0.8$  section meanline, and an NACA 66 section thickness distribution with NSRDC modifications to the nose and tail thicknesses. The design advance coefficient  $J$  was 0.889, and the design thrust loading coefficient  $C_{Th}$  was 0.534 (Boswell 1971). Open-water data for the thrust coefficient  $K_T$  and ten times the torque coefficient  $10K_Q$  are shown in Figure 1.4 (data from Hecker and Remmers 1971).

P4381 was chosen for the LCC tests for both its existence, which saved the cost of manufacturing a new propeller, and for its status as an unclassified geometry. The drawback of using this propeller, however, was that it was not designed to be used on the hull model that was used. The overall propeller diameter  $D$  was smaller than that of propellers normally attached to the hull model used in the LCC experiments, and the propeller hub was not tapered. The hub diameter was smaller than that of propellers normally attached to the model hull. This obstacle was overcome by attaching a tapered hull extension to the shaft of the motor in the model, and then attaching the propeller to this hull extension. The hull extension and dummy hub are shown in the drawing in Figure 1.5 (the shaded portion of the figure is the hull extension and dummy hub), and the hull extension and P4381 are shown mounted on the model hull in the photograph in Figure 1.5. The hull extension was designed such that it rotated with the propeller. The hull extension continued the hull slope down to the diameter of the hub on P4381. The

“dummy hub,” shown in the drawing in Figure 1.5, was used initially for calibration purposes prior to the powered tests. An elliptic tip was attached behind the propeller, as shown in Figure 1.5. The powered tests were conducted using the hull extension, propeller, and elliptic tip. The drag studies were conducted using the hull extension, the dummy hub, and the elliptic tip. The configuration consisting of the tapered hull extension, P4381 and the elliptic tip was duplicated for the computational thrust studies. The configuration consisting of the tapered hull extension, the dummy hub and the elliptic tip was duplicated for the MSU model and the computational hull model for the drag studies.

### 1.3 Overview of report

The computational studies were performed by a graduate student, Allison Cruthird Cash, utilizing the resources of the SimCenter located in the Engineering Research Center at Mississippi State University. The experimental study conducted at MSU was performed by a graduate student, John Freudenthal, utilizing a small water tunnel at MSU. The theses that resulted from these investigations (Cash 2001; Freudenthal 2002) are included in this report as Appendices A and B, respectively. These theses form essentially self-contained reports of the work involved. Therefore, in the main body of this report, the significant results from these works will be summarized in individual chapters, and the reader will be referred to the appendices for the details of the studies. Chapter 2 will summarize the computational studies, and Chapter 3 will summarize the experimental studies conducted in the MSU water tunnel. The experiments involving the large-scale model in the LCC were conducted by the principal investigator. These results will be discussed in detail in Chapter 4, and then the results of the three different studies will be compared in Chapter 5. Conclusions will be given in Chapter 6.

A word concerning the experimental study conducted at MSU is in order. Initially, as stated above, the drag of a bare submarine hull and the thrust of a powered model were to be measured in both experimental facilities (MSU and LCC). A submarine model approximately 11 in long and 1 in in diameter and matching the LCC model geometry was constructed for the MSU tunnel. As discussed previously, the propeller that was to be used on the LCC model was P4381. When the propeller was actually acquired, it was discovered that the propeller diameter was 1 ft, yielding a propeller-to-body diameter ratio of approximately 0.5 for the LCC model. This would have implied a propeller diameter of 0.5 in for the MSU model. It was decided that it would be extremely difficult to manufacture an accurate model of the propeller at that scale, and so the decision was made to conduct only unpowered studies in the MSU water tunnel and measure only the drag on the MSU model without a propeller. These results will be compared to the computational simulations and the LCC experimental results. The powered tests were conducted in the LCC and the resulting thrust coefficient measurements will be compared with the computational results.

## 2. RESULTS OF COMPUTATIONAL SIMULATIONS

### 2.1 Overview of chapter

Because of the availability of personnel and computer time, the computational study (Appendix A) was fairly extensive and actually exceeded the scope of the studies described in Chapter 1. There were four phases to the computational investigation: (1) simulations of the flow past the bare hull geometry at the three different length scales discussed in Chapter 1 and the corresponding drag calculations; (2) simulations of an isolated Propeller 4381 (so-called "open water" studies); (3) simulations of powered motion with P4381 mounted on the hull with stern appendages; and (4) simulations of the submarine crashback maneuver (forward motion and reverse propeller rotation). The computational methods and other computational issues will be summarized here. The results of the first three phases will be discussed here briefly, and phases (1) and (3) will be discussed in more detail in Chapter 5, when the results of all three studies are brought together. The reader will be referred to Appendix A for the discussion of the crashback simulations.

### 2.2 Computational methods

The flow solver used in the computations was a Reynolds-averaged Navier-Stokes solver called " $U^2NCLE$ ," for "Unstructured Unsteady Computation of FieLd Equations." It is capable of obtaining solutions for viscous, incompressible, high Reynolds number flows on unstructured grids through the use of a pseudo-compressibility method. For more details on this solver, see Hyams (2000) and Hyams *et al.* (2000)\*. Two different eddy-viscosity turbulence models were used, a one-equation model by Spalart and Allmaras (see Spalart and Allmaras 1992) and a two-equation model referred to as the "q- $\omega$ " model (see Coakley and Hsieh 1985). A composite unstructured/structured surface grid was generated for the hull model and a multielement unstructured mesh was generated for the volume outside of the hull. See pp. 15-17 of Appendix A for more details concerning the grid generation.

The simulations were conducted on a super cluster of 256 dual gigahertz Pentium III computers. All of the bare hull simulations were conducted using local time stepping and were run until they converged to steady-state solutions. The average computation time for the bare hull simulations was approximately 10 hours. The bare hull simulations typically converged in 500 time steps, although the simulations were usually run to 1500 time steps to

---

\* Both Appendices A and B contain lists of references. Only those references in those lists which are referred to in the main body of the report are included in the list of references for the main body of the report.



ensure convergence. The isolated propeller simulations were run with local time stepping for approximately 400 time steps, and then the solver was switched to a minimum time step for an additional 600 to 700 time steps. Convergence was usually achieved in the vicinity of 700 total time steps, with a computational time of 23 hours. The convergence histories of these runs can be seen in Figures (A)3.4, (A)3.5, and (A)3.8\*. Figure (A)3.5 is of interest in that it compares the convergence histories among the different types of grids and turbulence models used in the bare hull studies. This figure shows that all of the different combinations converge to the same level within approximately 700 time steps.

The propelled hull simulations were a bit more problematic. The solution was first calculated for 400 time steps using local time stepping. Then, the stepping was switched to a minimum time step. The rotating propeller was handled by locally regenerating the grid in the vicinity of the propeller for each time step, thus simulating an actual rotating propeller on a fixed body. The flow was calculated for 800-1000 time steps until it reached a periodic state with a very small peak-to-peak amplitude, as shown in Figure (A)3.11. The periodic nature of the "converged" solution is appropriate for the thrust force produced by the rotating propeller. The total computational time for each of these solutions was typically 23 to 26 hours.

## 2.3 Results

The results of the computational studies for the drag coefficient of the bare hull are shown in Figures 2.1 and 2.2. Figure 2.1 shows the results for just the LCC model studies, comparing the two different turbulence models used. This figure shows that the "q- $\omega$ " model consistently predicted a higher drag coefficient over this range of Reynolds number. Figure 2.2 shows the results for all three ranges of Reynolds number examined. The MSU model was 0.940 ft long, the LCC model was 23.0 ft long, and a full-scale prototype was assumed to be 384 ft long, yielding an overall Reynolds number range for the simulations of  $7.7 \cdot 10^5 < Re_L < 1.6 \cdot 10^9$ . The computational simulations for the MSU model and the prototype were conducted using only the "q- $\omega$ " model and the results for all three length scales seem to fall consistently on a single curve (note the logarithmic scale for  $Re_L$ ). The continuous decrease in drag coefficient indicates a drag dominated by viscous shear or skin friction as opposed to pressure drag. The results for the drag coefficients will be discussed in more detail in Chapter 5.

The results of the computational studies of the isolated propeller (the simulations of the open-water studies) are shown in Figure 2.3. This figure shows the computational results using both turbulence models for the propeller thrust and torque coefficients as functions of advance ratio  $J$ . These results are compared with experimental data from Hecker and Remmers (1971) that are illustrated in Figure 1.4. The computational results are in very good agreement with the experimental results for the range of advance ratio studied. It should be noted that the design advance ratio for P4381 was 0.889 (Boswell 1971).

The results for the simulations of powered motion using P4381 and an appended hull are shown in Figures (A)4.5 through (A)4.8. The experimental data in these figures are from the LCC tests to be discussed in Chapter 4,

---

\* The figures and equations in Appendices A and B were not renumbered when these theses were incorporated into this report. In the main body of this report, figure and equation numbers in Appendices A and B will be preceded by an "(A)" or "(B)", e.g. Figure (A)3.4 is Figure 3.4 in Appendix A. A figure number not preceded by a letter will refer to a figure in the main body of the report.

so a full discussion of these results will be deferred until Chapter 5. It is sufficient at this time to note that the computational results were in very good agreement with the experimental data. It was discovered during these studies that the computations could not be conducted for the powered configuration using the “q- $\omega$ ” turbulence model. The turbulence model became unstable and diverged in a relatively few time steps. The suspected culprit was the surface grid on the propeller. The propeller tips were very fine and required a large number of points for adequate resolution. The grid generator occasionally created minute “divots” in the surface topology, especially near sharp edges. The “q- $\omega$ ” turbulence model was especially sensitive to such disturbances, hence the instability when these cases were attempted. Since there was very little difference between the results for the “q- $\omega$ ” and Spalart-Allmaras turbulence models, the computational studies were continued from this point using only the Spalart-Allmaras model.

Additional effects of Reynolds number are explored in Section 4.3 of Appendix A. Figure (A)4.20 illustrates the continuous reduction in the skin friction coefficient for the bare hull as Reynolds number increases, which is what one normally expects. Figure (A)4.21 compares the flow in the exit plane of the isolated propeller at two extremes of the Reynolds number range. This figure shows regions of higher velocity near the propeller blades at the lower Reynolds number. These regions disappear at the higher Reynolds number. Figure (A)4.22 compares the overall isolated propeller flow field at these two values of the Reynolds number and illustrates the fact that the propeller has a greater influence on the surrounding flow field at the lower Reynolds number. Figure (A)4.23 compares the flow in the region of the stern planes at the two values of the Reynolds number for the appended hull without propeller, this time showing a greater influence of the stern planes on the surface pressure distribution at the higher Reynolds number. The conclusion drawn from these studies was that for the hull and propeller flow fields, the Reynolds number had a localized effect on flow field characteristics.

Sections 4.4 and 4.5 of Appendix A deal with hull/propulsor interactions and the crashback maneuver, respectively. While these results are of interest, these studies were outside the immediate scope of the current study. The reader is referred to Appendix A for the details of these results.

### 3. EXPERIMENTAL STUDIES ON SMALL-SCALE MODEL

#### 3.1 Overview of chapter

The experimental studies on the small scale model (Appendix B) were conducted in a water tunnel located at Mississippi State University (MSU) using a laser Doppler velocimeter (LDV) system to obtain wake velocity profiles. A previously-developed method for extracting drag data from two-dimensional wake velocity profiles by Dimotakis (1977) was extended to axisymmetric flows. The implementation of this method allowed the determination of the drag of the model solely from LDV wake velocity measurements. The method will be summarized briefly, the water tunnel and model will be described briefly, and the results of the measurements will be summarized.

#### 3.2 Wake profile drag method

The method by Dimotakis began by integrating the momentum equation around a control volume surrounding a two-dimensional body. This procedure was repeated for an axisymmetric body, as shown in Figure (B)2.1. The resulting equation for the drag coefficient is given by Equation (B)(2.46). This equation is written in terms of radial integrals of mean and fluctuating streamwise velocity components and of the mean pressure coefficient. The turbulent wake flow was then assumed to be self-preserving, and the appropriate forms of the mean and fluctuating velocities and the mean pressure were assumed, as shown in Equations (B)(2.48) through (B)(2.50). The result for the drag coefficient in terms of the associated length and velocity scales and integrals of the dimensionless self-similar distributions of velocity and pressure is given by Equation (B)(2.60). The length and velocity scales were assumed to vary according to standard power law relations so that the length scale increased as  $x^{1/3}$  and the velocity scale decreased as  $x^{-2/3}$ , in the specific forms

$$\frac{u_o}{U_o} = c_u \left( \frac{x - x_o}{d} \right)^{-2/3} \quad \frac{l_o}{d} = c_l \left( \frac{x - x_o}{d} \right)^{1/3}$$

In these formulae,  $u_o$  and  $l_o$  are the velocity and length scales, respectively, for the self-preserving wake,  $U_o$  is the velocity outside the wake,  $x$  is the downstream distance measured from the trailing edge of the model,  $x_o$  is a virtual origin determined from fits to the experimental data,  $d$  is the model diameter, and  $c_u$  and  $c_l$  are constants of proportionality determined from fits to the experimental data. When these variations are included in Equation (B)(2.60), and the results are extrapolated to very large  $x$ , the terms involving the fluctuating velocity component and the mean pressure coefficient become negligible, and the result is given by Equation (B)(2.64). This equation is

further simplified if the body diameter  $d$  is very small compared to the radius  $R$  of the control volume. The result, given by Equation (B)(2.65), is

$$C_D = \frac{8c_u c_l^2}{\ln 2}$$

The method was implemented as follows. The streamwise velocity component profile in the radial direction was obtained at several locations downstream of the model. Each of these profiles were fit to the function

$$u(z) = U_0 - u_0 \exp \left[ -\ln 2 \left( \frac{z - z_0}{l_0} \right)^2 \right]$$

using the “genfit” routine in Mathcad. In this formula,  $u(z)$  is the measured streamwise velocity component, and  $z$  is the transverse position coordinate. The variable  $z_0$  is the nominal wake centerline, and  $l_0$  is the wake half-width defined as the point such that when  $z - z_0 = l_0$ , the wake velocity deficit is half its maximum value on the wake centerline. The parameters  $U_0$ ,  $u_0$ ,  $z_0$ , and  $l_0$  were obtained from the fits. The axial variations of the parameters  $u_0$  and  $l_0$  were then fit to the functions of  $x$  given above, again using the “genfit” routine in Mathcad, and the constants  $c_u$  and  $c_l$  were obtained from the fits and used to calculate  $C_D$ . The resulting value was adjusted to take into account the pressure gradient in the empty test section. The correction for the contribution to the apparent drag force caused by the nonzero pressure gradient was

$$D_p = \frac{dp}{dx} V_{body}$$

where  $V_{body}$  is the volume of the model. This is the so-called “buoyancy drag” correction, which is exact if the pressure gradient is constant. Data from the thesis by Lindsey (1998) were used to compute the test section pressure gradient and its associated uncertainty.

The advantage of the wake profile method is that a significant amount of information goes into the calculation of the drag coefficient. However, the drawback is that it takes a significant amount of time to acquire the information. This limited the number of cases that could be tested in the time available for the experiments.

### 3.3 Experimental apparatus

The MSU water tunnel has an axisymmetric test section that has a diameter of 11 in and a length of approximately 4 ft. The top test section speed is approximately 30 ft/s. Details of the design and construction of this facility may be found in the report by Wells (1964). This facility was extensively renovated in the late 1990s, and the results of this renovation and the initial tests in the renovated facility may be found in the thesis by Lindsey (1998; see also the Appendix to Bridges, 2001). Further work on the facility was done for the current study; see Section 3.1 of Appendix B for further discussion of the facility and the recent work done on the facility.

The velocity measurement system used was a Dantec two-component FiberFlow LDV system. Because the test section of the water tunnel is axisymmetric, the beams had to enter the test section perpendicular to the test section wall and traverse a diameter of the test section. This meant that only one pair of beams could be used and

hence only one velocity component, the streamwise component, could be measured. For more details of the LDV system and its calibration, see Sections 3.2 and 3.3 of Appendix B.

As stated earlier, the submarine model was 11.278 in (286.47 mm) long. The details of the model are discussed in Section 3.4 of Appendix B, and the model as mounted in the MSU water tunnel is shown in Figure (B)3.5.

### 3.4 Experimental results

Results for the velocity profiles in the empty test section are shown in Figures (B)4.1 through (B)4.5. These results, particularly Figure (B)4.5, show some repeatable variations in the streamwise velocity distributions that were believed to be due to irregularities in the Plexiglas wall of the test section, possibly caused by distortions of the wall when the tunnel was pressurized. Lindsey (1998) had noted such distortions in his work. These will be commented on again below. Figures (B)4.6 and (B)4.7 show the distribution of the RMS component of the streamwise velocity across the test section. These show a free stream turbulence level of slightly over 1%, which is higher than desired but deemed reasonable for the tests being conducted. Figures (B)4.9 through (B)4.12 show the total uncertainty levels estimated for the empty test section measurements. Figure (B)4.12, in particular, places the uncertainty levels in the proper perspective and shows that the total uncertainties in the empty test section measurements were relatively small.

Section 4.3 of Appendix B contains the wake profile results. It took essentially one day of effort to acquire each set of velocity profiles. The mean velocity profiles and turbulence intensity profiles are shown in Figures (B)4.14 through (B)4.23. The profiles seem to indicate a "drift" in the profile location. This apparent shift was caused by a slight misalignment between the test section centerline and the LDV axial traverse axis, which was determined from the measurements to be less than 0.7 deg. This misalignment was the reason for choosing the centerline position  $z_0$  as one of the fit parameters. Figures (B)4.24 through (B)4.26 show representative velocity profiles that have been corrected for the centerline "shift" and include the uncertainties in the individual velocity measurements. The typical uncertainty in a velocity measurement was 3% of  $U_0$  at a given profile and the typical uncertainty in the  $z$  location was 0.675 mm.

Figures (B)4.27 and (B)4.28 show the velocity profiles plotted in similarity variables. The positive values on the abscissa correspond to the side of the wake closest to the LDV system. As the LDV measurement volume moved across the test section, the data acquisition rate and the signal quality dropped to the point where it was just possible to measure the complete wake on both sides, but not to completely span the test section. This is why the profiles are asymmetric in  $z$  with respect to the number of data points obtained. There were also some apparent asymmetries in the wake measurements themselves which are apparent in the figures. The reasons for these asymmetries were not discovered. This issue will be discussed briefly below.

The results for the axial variations of velocity deficit and wake width are shown in Figures (B)4.30 and (B)4.31, respectively. It should be noted that there are no uncertainty bars on these figures. The uncertainty analyses were conducted for the individual velocity measurements, as discussed in Section 4.2 of Appendix B and shown in Figures (B)4.24 through (B)4.26, as just mentioned. As a result of time constraints on the completion of

Appendix B, the uncertainty analysis on the axial variation fits and the final calculation of  $C_D$  were not included in Appendix B. That uncertainty analysis will be discussed here.

The problem was to take the uncertainties in  $u$  and  $z$  and compute the uncertainties in the parameters  $u_0$ ,  $b$ ,  $c_u$  and  $c_l$  arising from the curve fits\*, and then use these uncertainties to compute the uncertainty in the drag coefficient  $C_D$ . This was accomplished using a Monte Carlo method, similar to the procedure outlined in Coleman and Steele (1999). The typical uncertainties in  $u$  and  $z$  were randomly distributed over the velocity profile data, using the normal-distribution random-number generator in Mathcad with a mean of 0 and a standard deviation of 0.368 ( $= 1/e$ ). The values of  $V_0$ ,  $u_0$ ,  $z_0$ , and  $b$  were then computed using the “genfit” function. This procedure was repeated 10,000 times. The resulting uncertainties in  $u_0$  and  $b$ , taken as twice the standard deviations of  $u_0$  and  $b$  from the 10,000 results, were on the order of 5% and 6% of the mean values of  $u_0$  and  $b$ , respectively. The distributions of  $u_0/U_0$  and  $b/D$  with  $x/D$  are shown in Figures 3.1 and 3.2, respectively. These are Figures (B)4.35 and (B)4.36 repeated with the uncertainty bars added (only the experimental values used in the fits to obtain  $c_u$  and  $c_l$  are shown in Figures 3.1 and 3.2). As can be seen in these figures, the uncertainty in  $b/D$  was somewhat larger than the uncertainty in  $u_0/U_0$ , and the uncertainty in  $b/D$  tended to grow in the streamwise direction, reaching a maximum of approximately 7% of the mean value of  $b$  at  $x/D = 28$ . The individual values of  $b/D$  tended to show more scatter than the corresponding values of  $u_0$  (see *e.g.* Figure 4.31 of Appendix B).

The uncertainties in  $u_0/U_0$  and  $b/D$  were then randomly distributed over the values of  $u_0/U_0$  and  $b/D$  using the same normal-distribution random-number generator as before and the values of  $c_u$  and  $c_l$  were computed using the “genfit” function. This procedure was also repeated 10,000 times. The resulting uncertainties in  $c_u$  and  $c_l$ , taken as twice the standard deviations of  $c_u$  and  $c_l$  from the 10,000 results, were 4% and 15% of the mean values of  $c_u$  and  $c_l$ . The larger uncertainties in  $b/D$  were reflected in the relatively large uncertainty in  $c_l$ . The relatively large uncertainty in  $c_l$  was a bit surprising, since the associated uncertainties in the width parameter  $b/D$  were typically of the order of 6%, reaching the peak value of 7% only at the most downstream location. It had been noted in performing the curvefits that the values of  $c_u$  and particularly  $c_l$  were sensitive to small changes in the data. This is probably due to the power-law nature of the function that was being used, and the fact that a fit to a power law in  $x$  was being attempted over a relatively small range of  $x$ . Using the values of the uncertainties in  $c_u$  and  $c_l$ , the corresponding uncertainty in the drag coefficient was found to be  $\Delta C_D \approx \pm 0.06$ , or 30% of the value  $C_D = 0.195$  computed using the procedure described above. The relatively large uncertainty in  $c_l$  was magnified even further because of the appearance of the square of  $c_l$  in the formula for the drag coefficient. It is believed that a refinement in LDV techniques would reduce the uncertainties in the results to acceptable levels. The contribution to the uncertainty from the uncertainty in the pressure gradient term was negligible, due to the small contribution of the pressure gradient term to the drag coefficient itself.

As discussed in Section 4.3.3 of Appendix B, the value of  $C_D = 0.195$  was obtained by averaging the values of  $u_0$  and  $b$  as functions of  $x/D$  found over three days of testing, during which the tunnel pressure was allowed to bleed down over time. Over two more days of testing, the tunnel pressure was maintained at a high value and a

---

\* Through an inadvertent switch in notation, the wake width parameter is denoted by “ $b$ ” instead of “ $l_0$ ” in Chapter 4 of Appendix B. In the discussion to follow, the notation change will be maintained, so that the current discussion is consistent with the usage in Appendix B.

value of  $C_D = 0.201$  was obtained by averaging the values of  $u_\theta/U_0$  and  $b/D$  found during these tests. The uncertainty analysis just presented was performed only for the first set of data, due to the computational effort involved. These results should be representative of the results as a whole.

As noted above, there were some unexplained anomalies in the data. Figure (B)4.5 shows the repeatable velocity variation across the empty test section which was believed to be due to distortion of the test section wall. This figure also shows an apparent overall shift in the velocity of approximately 0.1 m/s. This was believed to be due to some anomaly in the LDV electronics which only occurred sporadically, usually at relatively long time intervals, but occasionally during velocity surveys. Finally, (B)4.27 and (B)4.28 display an apparent asymmetry in the wake, which was also thought to be due to test section wall distortion or possibly a misalignment of the LDV traverse in the direction perpendicular to the flow. A series of experiments was to be conducted to try to identify the sources of these various anomalies. The first was the apparent shift in the velocity values. A long-duration test of the test section speed ahead of the model was started. The results are shown in Figure (B)4.34, which shows one such apparent shift at a time of approximately 12 minutes. While this test was being conducted, the water tunnel ruptured, and there was not enough time to repair and continue the tests before the project ended.

## 4. EXPERIMENTAL STUDIES ON LARGE-SCALE MODEL

### 4.1 Overview of chapter

The large-scale studies were conducted in the Large Cavitation Channel, as discussed earlier. Measurements of drag and LDV surveys of the velocity field at the stern were made on a bare hull model with the “dummy hub” geometry discussed in Chapter 1. Measurements of propeller thrust force were made over a range of advance ratios. Measurements of the boundary layer at four axial locations were also made. The experimental apparatus and procedure will be described and then the results discussed in detail.

### 4.2 Experimental apparatus and procedure

#### 4.2.1 Facility

The experiments to be described in this chapter were conducted in the William B. Morgan Large Cavitation Channel (LCC), located in Memphis, Tennessee. This facility is part of the Carderock Division of the Naval Surface Warfare Center (NSWCCD) and was first made operational in 1991. The LCC has a test section that is 3.05 m (10 ft) high, 3.05 m (10 ft) wide, and 12.2 m (40 ft) long. The maximum test section speed is approximately 18 m/s (35 kts), and the pressurization range for the test section extends from 3.5 kPa (0.05 psia) to 415 kPa (60 psia). The freestream turbulence level is less than 0.5%. Details of the design, construction, and operation of this facility may be found in Etter and Wilson (1992; 1993). More recently Park, Cutbirth and Brewer (2002) have done an extensive study of the performance characteristics of the LCC and have documented in detail the flow temporal and spatial uniformity and the turbulence levels in the facility, as well as the data acquisition equipment and procedures for velocity measurements in the LCC test section. According to Park *et al.* (2002), the temporal stability of the LCC test section flow speed is  $\pm 0.15\%$  for test section velocities between 0.5 and 18 m/s. The test section velocity is spatially uniform to within  $\pm 0.60\%$  for velocities between 3 and 16 m/s. The turbulence level in the facility is between 0.2% and 0.5% for test section velocities from 0.5 to 15 m/s, with no harmonics appearing in the power spectra of the velocity signals. For all of the tests conducted during this study, the tunnel pressure was set at 30 psig at the test section top.

#### 4.2.2 Model

As discussed in Chapter 1, the model used was a standard axisymmetric hull form (DTMB 5495-3). The hull contour is shown in Figure 1.1. For the drag studies, the configuration included the “dummy hub” that is



represented in the top portion of Figure 1.5 and did not include stern planes. For the powered studies, P4381 and the stern planes were added as shown in the lower portion of Figure 1.5.

#### 4.2.3 Instrumentation and data reduction

The forces on the hull model were measured using a AMTI 6-component dynamometer. This device is an internal force balance that was attached between the strut and the model. It was set up to measure forces in all three directions and moments about all three axes. The dynamometer was calibrated by a member of the NSWCCD staff who oversaw the setup and the initial use of the balance in the model at the LCC. The dynamometer voltages were converted to forces and moments using supplied calibration data. The systematic errors for this dynamometer are shown in Table 4.1 (the notation " $2\sigma$ " indicates the value of twice the standard deviation).

**Table 4.1** Estimates of systematic error for AMTI dynamometer

	$F_x$	$F_y$	$F_z$	$M_x$	$M_y$	$M_z$
% of full scale, max	0.18	0.17	0.6	0.59	0.19	0.65
% of full scale, min	-0.11	-0.28	-0.75	-0.49	-0.21	-0.67
$2\sigma$ (% of full scale)	0.08	0.12	0.33	0.34	0.12	0.43
full scale, eng. units	5000 lbs	5000 lbs	5000 lbs	2500 ft-lbs	25000 ft-lbs	5000 ft-lbs
$2\sigma$ , eng. units	4 lbs	6 lbs	16.5 lbs	8.5 ft-lbs	30 ft-lbs	21.5 ft-lbs

The forces on the propeller itself were measured with a MicroCraft 6-component propeller dynamometer. This dynamometer was a multi-component cylindrical assembly that attached to the propeller on its upstream face. The dynamometer is shown in the upper portion of Figure 1.5, just ahead of the hub extension. Strain gauges were glued to 12 flexures in order to measure three orthogonal forces and three moments. The gauges were arranged in Wheatstone bridge circuits with two to four arm circuits connected in parallel for each channel. The placement of multiple bridges was intended to cancel interactions from other forces and moments. This particular design had small interactions (<2%) except for bending moment interactions on the orthogonal side forces of about 41%. Care had to be taken to properly zero the balance so as to not artificially remove possible interactions.

A 6 x 12 calibration matrix was used to calculate the forces and moments from the six input voltages. This matrix provided first and second order interactions of the various forces and moments and yielded a dynamometer error of less than 1% of each channel's full scale value. The multi-component construction of this dynamometer caused hysteresis effects that were the chief source of error. The estimates of the systematic error for this dynamometer are shown in Table 4.2.

The strain gage signals passed through slip rings to Vishay Model 2310 Instrumentation Amplifiers outside the tunnel. These amplifiers provided excitation voltage, bridge zeroing, gain, and filtering of the signals. For these tests, all filters were turned off, resulting in a wideband setting during the tests. The conditioned signals were then passed to the computer A/D inputs. Due to a limited number of slip ring connections it was necessary to group some

of the bridge excitation lines to the dynamometer. Due to multiple bridges connected in parallel the current draw along these excitation lines could result in a voltage drop. As the dynamometer was calibrated with individual excitation for each force or moment channel, additional calibration checks were conducted to adjust individually the gain of each channel to account for the lower excitation voltage. The details of these corrections are not discussed here except to state that the corrections adequately reduced any error introduced to levels quoted from calibration data.

**Table 4.2** Estimates of systematic error for MicroCraft propeller dynamometer

Component	Load limit	Error as % of full scale ( $2\sigma$ )
$f_x$ (thrust)	2000 lbs	0.40
$f_y$ (side force)	500 lbs	0.55
$f_z$ (normal force)	500 lbs	0.68
$m_x$ (torque)	500 ft-lbs	0.17
$m_y$ (pitch)	500 ft-lbs	0.17
$m_z$ (yaw)	500 ft-lbs	0.02

The “ $2\sigma$ ” values in Tables 4.1 and 4.2 were used as the systematic uncertainties in computing the uncertainties in the forces measured by the body and propeller dynamometers. The propeller and body dynamometer channels were sampled at a rate of 100 Hz for a period of 10 sec, yielding 1000 samples per channel. Twice the standard deviation of the samples acquired during the tests was used as the measure of the random uncertainty.

Measurements of the velocity field at the model’s stern were obtained using the LCC’s Dantec laser Doppler velocimeter (LDV) system. This system is described in detail in the report by Park, Cutbirth and Brewer (2002). The system consists of 4 Dantec BSA 57N11 signal processors, 3 fiber optic probes, two Spectra Physics 6 W argon-ion lasers, a Dantec 3-D traverse, and Dantec Flow software. The LDV system was calibrated using a rotating disc. The resulting uncertainty in the calibration is reported by Park *et al.* (2002) to be less than 0.018 m/s at a disc speed corresponding to a tunnel speed of 15 m/s. Based on the results presented in Park *et al.*, the overall uncertainty in individual LDV measurements of the velocity was assumed to be 0.3%. This value was used in the calculation of the force coefficients, Reynolds numbers, and advance ratios.

The density and viscosity of the water were obtained by measuring the temperature of the water and using curve fits to compute the density and viscosity. Calibrations of the temperature transducers have shown an uncertainty of  $\pm 2.0$  deg C, caused by a drift in the calibrations of the transducers. Since the sensitivity coefficients at a normal operating temperature of 27 deg C are 0.028 %/deg C and 2.22 %/deg C for the density and viscosity, respectively, the uncertainty in the temperature leads to uncertainties in the density and viscosity of 0.056% and

4.44%, respectively\*. These values were used as the systematic uncertainties for the density and viscosity. Because the systematic uncertainty in the temperature was much larger than random uncertainties recorded in the measurements (typically 0.002 deg C), the total uncertainties in the density and viscosity were essentially equivalent to the systematic uncertainties.

The uncertainty in the propeller speed was 1 RPM or  $0.0167 \text{ s}^{-1}$ . The uncertainty in the propeller diameter was assumed to be 0.0625 in or 0.5% of the propeller diameter. The uncertainty in the hull model length was assumed to be 1.5 in or 0.54% of the overall model length. The uncertainty in the hull model diameter was assumed to be 0.125 in or 0.51% of the model diameter.

The Reynolds number based on length,  $Re_L$ , was computed from

$$Re_L = \frac{VL}{\nu}$$

where  $V$  is the free stream or tunnel speed,  $L$  is the body length, and  $\nu$  is the kinematic viscosity. The advance ratio  $J$  was computed from

$$J = \frac{V}{nD}$$

where  $V$  is the free stream or tunnel speed,  $n$  is the propeller speed in revolutions per second, and  $D$  is the propeller diameter. The drag coefficient  $C_D$  was computed from

$$C_D = \frac{F_x}{\frac{1}{2} \rho V^2 \frac{\pi}{4} D_h^2}$$

where  $F_x$  is the axial force from the body dynamometer,  $\rho$  is the fluid density,  $D_h$  is the hull diameter, and  $\pi D^2/4$  is the projected frontal area of the submarine hull. The thrust coefficient  $K_T$  was computed from

$$K_T = \frac{f_x}{\rho n^2 D^4}$$

where  $f_x$  is the axial force measured by the propeller dynamometer,  $\rho$  is the fluid density, and  $D$  is the propeller diameter. Typically the drag coefficient was plotted as a function of Reynolds number and the thrust coefficient was plotted as a function of advance ratio.

## 4.3 Results

### 4.3.1 Drag

The results for the drag coefficient as a function of Reynolds number are shown in Figure 4.1. Over most of the Reynolds number range tested, the drag coefficient demonstrated a decrease in value consistent with a drag dominated by skin friction. However, as the Reynolds number approached the upper end of the range tested, the drag coefficient appeared to level off. This would indicate that separation was taking place and that the drag coefficient had become “locked” at that value, behavior similar to that of the drag coefficient of a circular cylinder

---

\* Information from unpublished report provided to author by LCC personnel.

or sphere as the Reynolds number increases. With the results given above for the uncertainties in the various parameters, the resulting uncertainty in the Reynolds number was typically on the order of 5% (caused mostly by the systematic uncertainty in the temperature measurement). The average uncertainty in the drag coefficient was 3.6%.

The evidence for separation on the rear of the model is shown in Figures 4.2 through 4.8. These figures show the results of the LDV surveys in the vicinity of the model stern. The component denoted by  $U_x$  is the streamwise velocity component. The component denoted by  $U_z$  is the transverse velocity component, which is the component perpendicular to the LCC test section floor and positive up (*i.e.* this velocity component is measured in a reference frame attached to the LCC test section). Both mean and fluctuating value contours are shown for both velocity components. The contour that forms the upper boundary of each region is the outline of the submarine hull and dummy hub, plus the centerline of the water tunnel. The measurements were made on the lower surface of the model, to avoid any effects due possibly to the model support strut, hence the negative values of  $z/R$  reported ( $R$  is the model hull radius). Figures 4.2, 4.3, and 4.4 are summaries of the measurements at tunnel set speeds of 2 kts, 5 kts, and 10 kts, respectively. Figures 4.5 through 4.8 are expanded views of each component at a tunnel set speed of 20 kts. These figures do show a very small separated region just behind the elliptic tip at the trailing edge of the model. There are negative values of  $U_x$ , indicating reversed flow behind the elliptic tip. There are also large values of the fluctuating components along the edge of the presumably reversed flow region, indicating the presence of significant mean velocity gradients which typically bound separated and/or reversed flow regions. It should be noted that these are apparently the *only* separated flow regions to be found for this model. These figures show the presence of the separated flow over the entire range of tunnel speeds tested. It is conjectured that the drag of the submarine hull behaves similarly to other geometries. At lower Reynolds number, the drag is dominated by the skin friction, which decreases as the Reynolds number increases. Eventually the contribution to the drag from the skin friction drops below that from pressure drag caused by the separated flow at the stern of the model. Since this pressure drag is essentially independent of Reynolds number, the overall drag coefficient levels off.

#### 4.3.2 Propeller thrust

The propeller thrust studies were conducted at LCC tunnel set speeds of 5 kts, 10 kts, 15 kts, and 20 kts, and for propeller speeds ranging from 200 RPM to 1200 RPM. The results for the propeller thrust as a function of advance ratio are shown in Figure 4.9. The rather larger uncertainty bars in Figure 4.9a are the result of the systematic uncertainty in the propeller dynamometer. In Table 4.2, the systematic uncertainty is 8 lb<sub>f</sub>, which is close to the mean value of the propeller force at some propeller speeds for a tunnel set speed of 5 kts. As the free stream speed increased, the propeller force increased also, and the relative uncertainty decreased. Figure 4.9a shows all of the results, and Figure 4.9b shows the results for 10 kts, 15 kts, and 20 kts over a more limited range of advance ratio. A typical value of the uncertainty in the thrust coefficient, neglecting some of the more extreme cases, was approximately 8%. The uncertainty in the advance ratio was typically 1.8%. The data show that the results were not dependent on Reynolds number over the range tunnel and propeller speeds tested. The data tended to fall on a single curve when plotted versus advance ratio. This demonstrated the repeatability of the data, since similar values of advance ratio could be obtained for widely different values of tunnel and propeller speed.

### 4.3.3 Boundary layer measurements

In addition to the drag and thrust measurements that were the main reason for this study, the boundary layer velocity at several axial locations toward the rear of the model was measured in some detail. These results are discussed here. Although these measurements were not directly related to the main purpose of this study, it was believed that they might be of value to researchers attempting to validate methods related to boundary layers at very large values of the Reynolds number.

The locations of the boundary layer surveys are shown in Figure 4.10. Because the model strut was located on the upper surface of the model, the boundary layer surveys were conducted on the lower side, away from the strut. The surveys were conducted in the model center plane (the plane containing the model axis and perpendicular to the test section floor). In Figure 4.10, the flow is from right to left, as indicated by the arrow, and the abscissa is distance in mm measured from the stern of the model. Because of the difficulties involved in attempting to measure the boundary layer in a direction perpendicular to the model wall, the surveys were conducted in a direction perpendicular to the submarine model axis, as shown in Figure 4.10. The  $x/L$  location of each traverse is noted on the figure. Two velocity components were measured, the  $u$  component in the direction parallel to the model axis, and the  $v$  component perpendicular to the LCC test section floor (and hence perpendicular to the model axis). In Figure 4.10,  $u$  is positive to the left and  $v$  is positive up (in the positive  $z$  direction). Mean and fluctuating components were measured, as was the correlation  $(u'v')^{1/2}$ .

The free stream pressure distribution is shown in Figure 4.11. These pressures were obtained from taps mounted on the wall of the LCC test section. The  $x/L$  values in this figure are identical to the  $x/L$  values for the model. The first survey, at  $x/L = 0.615$ , was conducted in a region of essentially constant pressure. The other three surveys were conducted in a region of adverse pressure gradient.

The profiles of mean and fluctuating velocity components and of the Reynolds stresses are shown in Figures 4.12 through 4.15. The boundary layer thickness  $\delta$  was defined as the  $y$  coordinate where the  $u$  velocity component reached a value of  $0.99U$ , where  $U$  was the reference velocity at a particular location. The  $y$  coordinate was obtained by subtracting the local model radius  $R_{local}$  from the measured  $z$  coordinate and then changing the sign (the  $z$  values in Figure 4.10 are measured from the model centerline). Each caption in Figures 4.12 through 4.15 gives the local reference velocity  $U$ , the boundary layer thickness, and the ratio of the boundary layer thickness to the local model radius for each boundary layer survey.

Figure 4.12 shows the boundary layer at  $x/L = 0.615$ . At this location, the wall is parallel to the free stream direction and so the  $v$  velocity component is essentially zero, as one might expect. In this case the boundary layer thickness as just defined corresponds to the standard definition of the boundary layer thickness. The boundary layer appears to behave as a typical turbulent boundary layer. As  $x/L$  increases, however, the local slope of the model wall becomes significant and the vertical velocity component  $v$  becomes more pronounced, as can be seen most clearly in Figure 4.15. Note that the vertical velocity component in this figure is positive. As the flow curves around the stern of the model, it is directed upward, and thus yields a positive velocity relative to the fixed reference frame of the LCC test section. Note also at this location that the ratio  $\delta/R_{local}$  has reached a value of 0.89, using the

definition of  $\delta$  given above. In this region, it is not likely that the boundary layer would behave as a two-dimensional boundary layer.

Because of the lack of measurements normal to the model wall and the additional complications of having to deal with an axisymmetric turbulent boundary layer, no further analysis of the boundary layer data was attempted. The data are included here primarily for validation of computational methods, particularly in the instance in which a researcher might attempt to compute the flow past this geometry with the goal of capturing the boundary layer accurately. The data could then be used to judge the success of the method. The "raw data" for the velocity profiles and the pressure coefficient distributions are included in tables immediately following this section.

**Table 4.3** Boundary layer data:  $x/L = 0.615$ ,  $U = 5.42$  m/s,  $\delta = 53.0$  mm

$y/\delta$	$u/U$	$v/U$	$u'/U$	$v'/U$	$(u'v')^{1/2}/U$
0.0038	0.4884	-0.0001	0.0884	0.0395	0.0279
0.0057	0.544	0.003	0.089	0.039	0.0291
0.0094	0.558	0.0033	0.0808	0.0392	0.0228
0.0151	0.588	0.0021	0.0808	0.0402	0.0249
0.0264	0.644	0.0051	0.0813	0.0379	0.0206
0.0396	0.67	0.0066	0.0787	0.0383	0.0235
0.0584	0.697	0.0056	0.0767	0.0397	0.0235
0.0811	0.719	0.0032	0.0746	0.0404	0.0255
0.107	0.748	0.0058	0.0702	0.0373	0.0249
0.138	0.768	0.0043	0.0672	0.0414	0.0285
0.172	0.776	0.0058	0.0672	0.0391	0.0279
0.211	0.8	0.0086	0.0656	0.0394	0.0279
0.255	0.817	0.0113	0.0645	0.0376	0.0302
0.304	0.834	0.0108	0.0591	0.0395	0.0296
0.356	0.857	0.0128	0.0581	0.0362	0.0273
0.415	0.872	0.0096	0.0567	0.0371	0.0285
0.477	0.892	0.009	0.0539	0.034	0.0261
0.545	0.912	0.0142	0.0469	0.0323	0.0249
0.617	0.93	0.0144	0.0451	0.0295	0.0221
0.694	0.944	0.0132	0.0402	0.0295	0.0206
0.777	0.959	0.0147	0.0389	0.0273	0.0198
0.863	0.976	0.0158	0.0325	0.0231	0.014
0.956	0.986	0.0145	0.0258	0.0209	0.0114
1.054	0.995	0.0133	0.0223	0.0203	0.0114
1.158	0.998	0.0148	0.0165	0.0171	0.0057
1.267	0.999	0.0154	0.0158	0.0166	0.0057
1.38	1.003	0.0156	0.0155	0.0153	0
1.499	1.001	0.0166	0.0143	0.0147	0
1.623	1.001	0.014	0.0142	0.0151	0
1.753	1.002	0.015	0.0143	0.015	0
1.889	1.002	0.0166	0.014	0.0137	0.0057
2.172	1.001	0.0149	0.0136	0.0135	0.0057
2.455	0.999	0.0121	0.0139	0.0131	0

**Table 4.4** Boundary layer data:  $x/L = 0.706$ ,  $U = 5.41$  m/s,  $\delta = 58.6$  mm

$y/\delta$	$u/U$	$v/U$	$u'/U$	$v'/U$	$(u'v')^{1/2}/U$
0.0017	0.399	0.0004	0.119	0.0203	-0.0198
0.0034	0.443	0.0065	0.0975	0.0368	0.0353
0.0068	0.512	0.0094	0.0815	0.0398	0.0324
0.0119	0.569	0.0136	0.0835	0.0408	0.0357
0.0222	0.615	0.0088	0.0785	0.039	0.0329
0.0341	0.648	0.0104	0.0843	0.0396	0.0384
0.0512	0.684	0.0135	0.0789	0.0379	0.0334
0.0717	0.717	0.0112	0.0742	0.0362	0.0313
0.0956	0.733	0.0109	0.07	0.0408	0.0338
0.123	0.755	0.0147	0.0678	0.0382	0.0319
0.154	0.77	0.0138	0.0657	0.0401	0.0334
0.189	0.797	0.0142	0.0622	0.0375	0.0303
0.229	0.812	0.0136	0.0588	0.0374	0.0292
0.273	0.829	0.0138	0.0579	0.0385	0.0303
0.321	0.84	0.0154	0.0545	0.0337	0.0249
0.374	0.862	0.0166	0.0528	0.0372	0.028
0.43	0.876	0.0156	0.0511	0.0366	0.028
0.491	0.896	0.0155	0.0482	0.0332	0.0262
0.556	0.912	0.0165	0.0458	0.0332	0.0229
0.626	0.927	0.0157	0.0427	0.0284	0.0214
0.626	0.928	0.0139	0.0413	0.0307	0.0229
0.701	0.944	0.0158	0.0386	0.0289	0.0198
0.701	0.943	0.0148	0.0395	0.0291	0.0206
0.78	0.964	0.0163	0.0334	0.0231	0.0162
0.78	0.969	0.016	0.0343	0.0258	0.019
0.863	0.975	0.0177	0.0306	0.0221	0.0162
0.863	0.976	0.0198	0.0296	0.0213	0.014
0.952	0.986	0.0167	0.0258	0.019	0.0128
0.952	0.985	0.0159	0.0276	0.0197	0.0128
1.046	0.995	0.0142	0.0191	0.0149	0.0081
1.046	0.996	0.0157	0.0193	0.0158	0.0081
1.145	1.001	0.0132	0.0145	0.0124	0.0057
1.145	1.001	0.0135	0.015	0.0134	0.0081
1.247	1.001	0.0119	0.0153	0.0091	0.0081
1.355	1.007	0.0099	0.0099	0.0096	0
1.468	1.004	0.0078	0.0083	0.0084	0
1.585	0.997	0.0015	0.0105	0.009	0
1.708	0.992	0.0018	0.0097	0.0083	0
1.964	0.998	-0.0048	0.0129	0.0104	0

**Table 4.5** Boundary layer data:  $x/L = 0.872$ ,  $U = 5.23$  m/s,  $\delta = 112.4$  mm

$y/\delta$	$u/U$	$v/U$	$u'/U$	$v'/U$	$(u'v')^{1/2}/U$
0.0009	0.329	0.063	0.0876	0.0409	0.0277
0.0053	0.436	0.087	0.0691	0.0472	0.0132
0.0125	0.482	0.097	0.074	0.045	0.0196
0.0231	0.541	0.106	0.0751	0.0461	0.0257
0.0365	0.565	0.113	0.0654	0.0451	0.0295
0.0525	0.596	0.119	0.0652	0.0485	0.0301
0.0721	0.637	0.122	0.0659	0.0505	0.0323
0.0943	0.653	0.12	0.062	0.0427	0.0221
0.119	0.679	0.126	0.0581	0.0393	0.0277
0.148	0.71	0.133	0.056	0.0411	0.0295
0.179	0.731	0.135	0.0566	0.0389	0.0295
0.213	0.753	0.133	0.0541	0.0391	0.0301
0.25	0.771	0.134	0.0505	0.0358	0.0264
0.29	0.796	0.131	0.0498	0.0364	0.0277
0.333	0.815	0.13	0.0481	0.0352	0.0229
0.379	0.833	0.128	0.0442	0.0349	0.0243
0.428	0.857	0.127	0.0456	0.034	0.0243
0.48	0.869	0.125	0.0434	0.0322	0.0213
0.535	0.884	0.124	0.0403	0.0313	0.0221
0.593	0.903	0.121	0.0387	0.0296	0.0196
0.653	0.926	0.119	0.0382	0.0266	0.0196
0.717	0.943	0.116	0.0332	0.0227	0.0167
0.784	0.963	0.114	0.0273	0.0199	0.0118
0.853	0.97	0.112	0.0247	0.0189	0.0102
0.926	0.981	0.107	0.0207	0.0167	0.0059
1.002	0.99	0.106	0.0136	0.0139	0
1.08	0.99	0.099	0.0129	0.0122	0
1.162	0.992	0.095	0.0109	0.0111	0
1.246	0.995	0.092	0.0101	0.0105	0
1.334	0.994	0.087	0.0097	0.0097	0
1.467	0.996	0.083	0.0095	0.01	0
1.601	0.997	0.077	0.0096	0.0095	0
1.734	0.997	0.071	0.01	0.0096	0
1.867	0.997	0.069	0.0097	0.0095	0
2.001	1	0.064	0.0081	0.0091	0
2.134	1.002	0.062	0.0092	0.0089	0
2.268	0.999	0.058	0.0091	0.0098	0
2.401	1.001	0.055	0.0089	0.0095	0
2.535	0.998	0.049	0.0101	0.0097	0



**Table 4.6** Boundary layer data:  $x/L = 0.895$ ,  $U = 5.15$  m/s,  $\delta = 142.9$  mm

$y/\delta$	$u/U$	$v/U$	$u'/U$	$v'/U$	$(u'v')^{1/2}/U$
0.0014	0.359	0.051	0.0835	0.033	-0.0134
0.0049	0.42	0.089	0.059	0.0387	0.017
0.0105	0.465	0.097	0.0711	0.0405	0.0147
0.0189	0.51	0.108	0.0676	0.0424	0.0134
0.0294	0.55	0.114	0.0715	0.0459	0.019
0.042	0.578	0.119	0.0633	0.0452	0.0208
0.0574	0.607	0.127	0.0628	0.0461	0.0134
0.0749	0.624	0.129	0.0591	0.0454	0.0208
0.0944	0.644	0.132	0.0618	0.045	0.0232
0.117	0.672	0.135	0.0576	0.0419	0.019
0.141	0.699	0.132	0.0586	0.0417	0.019
0.168	0.719	0.134	0.0545	0.0388	0.019
0.197	0.735	0.131	0.051	0.037	0.018
0.229	0.763	0.135	0.0502	0.0378	0.019
0.262	0.778	0.132	0.0499	0.0375	0.018
0.299	0.798	0.131	0.0468	0.0354	0.018
0.337	0.821	0.131	0.0463	0.0356	0.019
0.378	0.835	0.128	0.0454	0.0332	0.017
0.421	0.858	0.125	0.0426	0.0331	0.019
0.467	0.876	0.124	0.0414	0.0316	0.019
0.514	0.897	0.121	0.0402	0.0302	0.017
0.565	0.906	0.115	0.0378	0.0292	0.0159
0.617	0.922	0.114	0.0345	0.0263	0.012
0.672	0.94	0.11	0.0325	0.0256	0.0159
0.729	0.956	0.105	0.0274	0.0229	0.012
0.788	0.97	0.102	0.0244	0.019	0.0104
0.85	0.982	0.099	0.0169	0.0161	0.006
0.914	0.985	0.0972	0.0171	0.0164	0.006
0.981	0.989	0.0944	0.0109	0.0147	0
1.049	0.992	0.0915	0.0123	0.0131	0
1.154	0.992	0.0884	0.014	0.0134	0
1.259	0.994	0.0844	0.0144	0.013	0
1.364	0.999	0.0838	0.0136	0.0136	0
1.469	0.997	0.0772	0.013	0.013	0
1.574	0.997	0.0673	0.0127	0.0125	0
1.679	0.998	0.0607	0.0127	0.0124	0
1.784	0.998	0.0576	0.0118	0.013	0
1.889	1	0.054	0.0114	0.0123	0
1.994	1.002	0.0484	0.0112	0.0129	0
2.099	1.001	0.0426	0.0122	0.013	0

**Table 4.7** Wall pressure data for boundary layer measurements

x/L	C <sub>p</sub> (U = 1.05 m/s)	C <sub>p</sub> (U = 2.62 m/s)	C <sub>p</sub> (U = 10.3 m/s)
-0.476	0.0034	0.0003	-0.0007
-0.444	0.0021	-0.0005	-0.0013
-0.414	0.0025	0.0005	-0.0008
-0.3	0.0034	0.0005	-0.0012
-0.269	0	-0.0011	-0.0019
-0.237	-0.0029	-0.0024	-0.0024
-0.188	-0.0084	-0.0072	-0.0089
-0.158	-0.0097	-0.0086	-0.008
-0.128	-0.0076	-0.0084	-0.0078
-0.013	-0.0248	-0.0253	-0.0237
0.017	-0.0344	-0.0352	-0.035
0.049	-0.0415	-0.0431	-0.0429
0.098	-0.055	-0.056	-0.0557
0.128	-0.065	-0.0677	-0.0711
0.158	-0.0701	-0.0699	-0.0718
0.273	-0.0835	-0.0829	-0.0845
0.305	-0.086	-0.0868	-0.0893
0.335	-0.0864	-0.0865	-0.09
0.384	-0.089	-0.0885	-0.0907
0.414	-0.0885	-0.0887	-0.0895
0.444	-0.0864	-0.0873	-0.0892
0.561	-0.0978	-0.0975	-0.0995
0.591	-0.0986	-0.0973	-0.0994
0.621	-0.0948	-0.0963	-0.0983
0.67	-0.0961	-0.0963	-0.0985
0.7	-0.0915	-0.0909	-0.0895
0.73	-0.0869	-0.0868	-0.0892
0.877	-0.0726	-0.0685	-0.0671
0.956	-0.0579	-0.0566	-0.056
1.018	-0.0533	-0.0507	-0.0477
0.847	-0.0755	-0.0742	-0.0765
0.907	-0.0676	-0.0653	-0.0643
0.986	-0.0571	-0.0539	-0.053
1.193	-0.0529	-0.0506	-0.0498

## 5. COMPARISON OF COMPUTATIONAL AND EXPERIMENTAL RESULTS

### 5.1 Drag

The results of the computational studies, the small-scale experimental studies, and the LCC large-scale experimental studies for the drag coefficient of the bare submarine hull geometry are shown in Figure 5.1. Figure 5.1a compares all of the results, and Figure 5.1b concentrates on the LCC model scale results. The reasons for the large uncertainty bars on the MSU test results have been discussed previously. Figure 5.1b is essentially a reproduction of Figure (B)4.2. However, it should be pointed out that when Figure (B)4.2 was prepared, the pressure-gradient correction had not been applied to the LCC drag coefficient data. When the correction is added, the computations and experiments are in somewhat better agreement.

The particular feature to note in Figure 5.1 is the difference between the continual decrease in the drag coefficient predicted by the computations and the leveling off of the drag coefficient at a Reynolds number around  $10^8$ . If the conjecture presented in Chapter 4 is correct, this is the point where the pressure drag caused by the separation on the stern of the model becomes comparable to the skin friction drag caused by the viscous stresses. There was no indication in the computational results that separation occurred anywhere. Figure 5.2 (which is Figure (A)4.11 repeated) shows a very small region of low-velocity flow at the stern of the model but no apparent reversed flow. Other figures in Appendix A (including those listed in Table (A)4.2 on p. 46 of Appendix A) also indicate no reversed flow. It appears from these results that perhaps the small but critical separated regions were not captured or not computed accurately in the numerical simulations, and so the contribution to the total drag from the pressure drag was less than it should have been. Thus, in the computational simulations, the drag behavior appears to have been dominated over the entire Reynolds number range by the skin friction drag arising from the viscous stresses. It is possible that either the grid resolution for the computational simulations was not sufficient to capture the separated region or that the absence in the computational solutions of a separated flow region with reversed flow is due to a problem with the turbulence model.

An additional feature to note in Figure 5.1 is that despite the large uncertainty bars, the mean values of the drag coefficient obtained from the experiments on the small-scale model are reasonably consistent with the computational results. This agreement helps to confirm the validity of the wake profile method obtained in this study and suggests that the uncertainty in the value of the drag coefficient may have been overestimated.

## 5.2 Propeller thrust

The results for the computational and experimental studies of propeller thrust are shown in Figures 5.3 and 5.4. Figure 5.3 shows all of the computational and experimental results, and Figure 5.4 separates the results for different values of the Reynolds number. As was pointed out earlier, the computational results are in very good agreement with the experimental measurements. This is a tribute to the capability of the computational scheme to simulate a very complex, unsteady flow field. The computational studies were not extended to the Reynolds number corresponding to a full-scale prototype. However, the results for thrust coefficient plotted against advance ratio seem to be relatively independent of Reynolds number, suggesting that the computations would be equally as accurate at larger Reynolds number. The one caveat to keep in mind in considering the results of the computational simulations of the propelled model is the difficulty experienced by one of the turbulence models discussed in Section 4.2 of Appendix A. Both the “q- $\omega$ ” and Spalart-Allmaras models performed well for the isolated propeller studies. However, when the propelled model study was attempted using the “q- $\omega$ ” model, the model became unstable. This instability was attributed to the need to have a more refined grid in the vicinity of the sharp propeller blade edges.

In the calculations of both bare hull drag and propeller thrust, there were indications that further refinements in the computational methods were needed. Either a higher grid resolution or a better (but probably more complex) turbulence model was required. It is possible that both were required. Grid refinement and turbulence model studies would probably answer this question, but in a sense the lack of an answer is actually what the current study was looking for. The idea was to take an existing computational method, use it “as is” over a large range of Reynolds number, and then examine the results in the context of experimental measurements. The fact that has to be kept in mind when considering these results is that at the largest Reynolds number, there would be no experimental results with which to compare. What we can learn about the computational method at the lower values of Reynolds number has to be carried over into the higher Reynolds number range.

As just explained, it is possible that this flow required a computational grid with a higher resolution than the grid actually used. The greater grid refinement seemed to be needed, in the case of the drag studies, to capture the separated flow to produce the correct drag behavior and, in the case of the propeller thrust studies, to capture accurately the propeller edge geometry so that one of the two turbulence models would work properly. The need for a highly-refined grid on a (relatively) large geometry is a common problem in computational fluid dynamics, because it implies the need for a very large number of grid points, increasing the computational time and effort required to obtain a solution. This issue would have to be monitored in attempting to simulate flows at very large Reynolds number.

## 6. CONCLUSIONS

In order for computational solutions to simulate accurately flows at very large Reynolds number, the computational grid must have sufficient resolution to capture very small phenomena in the flow field, because these phenomena can still have a significant impact on the overall flow. Care must also be taken in the choice and implementation of a turbulence model. The computational methods used in this study produced results for the drag that did not agree with the experimental results, and this was attributed to the inability of the computational method as implemented to resolve accurately the separated flow behind the submarine, as a result of insufficient grid resolution, or difficulties with the turbulence model, or both. The computational method did an excellent job of predicting the thrust produced by the propeller, as long as the grid resolution did not interfere with the turbulence model. Because the large Reynolds number is usually the result of a "large" geometry, the computational grids will be correspondingly "large." The large grid with high resolution will have a very large number of points, requiring a considerable amount of computational time and memory. In other words, little things count.

## References

- Boswell, R. J. 1971 Design, cavitation Performance, and open-water performance of a series of research skewed propellers. *Naval Ship Research and Development Center Report No. 3339, March 1971.*
- Bridges, D. H. 2001 A detailed study of the flow field of a submarine at large angle of drift. *Office of Naval Research Grant No. N00014-96-1-0911 Final Report, Department of Aerospace Engineering, Mississippi State University, Report No. MSSU-ASE-01-1, May 2001.*
- Bridges, D. H. 2004 A detailed study of the flowfield of a submarine propeller during a crashback maneuver. *Office of Naval Research Grant No. N00014-97-1-1069 Final Report, Dept. of Aerospace Engineering, Mississippi State University, Report No. MSSU-ASE-04-01, August 2004.*
- Cash, A. N. 2001 Computational studies of fully submerged bodies, propulsors, and body/propulsor interactions. *M. S. Thesis, Department of Aerospace Engineering, Mississippi State University, December 2001.*
- Coakley, T. J. and Hsieh, T. 1985 A comparison between implicit and hybrid methods for the calculation of steady and unsteady inlet flows. *AIAA/SAE/ASME/ASEE 21<sup>st</sup> Joint Propulsion Conference, Paper no. 85-1125, July 1985.*
- Coleman, H. W. and Steele, W. G., Jr. 1999 Experimentation and uncertainty analysis for engineers. *New York: John Wiley & Sons, Inc..*
- Dimotakis, P. E. 1977 Laser Doppler velocimetry momentum defect measurements of cable drag at low to moderate Reynolds numbers. *Naval Construction Battalion Center Contract No. N62583/77-M-R541 Final Report, August 1977.*
- Etter, R. and Wilson, M. 1992 The large cavitation channel. *In Proceedings of the 23rd American Towing Tank Conference, Univ. of New Orleans, New Orleans, LA, 1992, pp. 243-252.*
- Etter, R. and Wilson, M. 1993 Testing ship designs in a water tunnel. *Mechanical Engineering, vol. 13, no. 10 (October 1993), pp. 74-80.*
- Fox, R. W. and McDonald, A. T. 1998 Introduction to Fluid Mechanics, 5<sup>th</sup> ed.. *New York: John Wiley & Sons, Inc.*
- Freudenthal, J. L. 2002 Experimental studies of the drag of an axisymmetric submarine hull. *M. S. Thesis, Department of Aerospace Engineering, Mississippi State University, December 2002.*
- Hecker, R. and Remmers, K. 1971 Four quadrant open-water performance of propellers 3710, 4024, 4086, 4381, 4382, 4383, 4384 and 4426. *Naval Ship Research and Development Center Report 417-H01.*
- Hyams, D. G. 2000 An investigation of parallel implicit solution algorithms for incompressible flows on unstructured topologies. *Ph. D. dissertation, Mississippi State University, May 2000.*
- Hyams, D. G., Sreenivas, K., Sheng, C., Nichols, S., Taylor, L. K., Briley, W. R., Marcum, D. L., and Whitfield, D. L. 2000 An unstructured multielement solution algorithm for complex geometry hydrodynamic simulations. *Presented at the 23<sup>rd</sup> Symposium on Naval Hydrodynamics, Val de Reuil, France, September 2000.*
- Lindsey, M. L. 1998 Renovation and initial operation of a high-speed water tunnel. *M. S. Thesis, Department of Aerospace Engineering, Mississippi State University, December 1998.*
- Park, J. T., Cutbirth, J. M., and Brewer, W. H. 2002 Hydrodynamic performance of the Large Cavitation Channel. *Naval Surface Warfare Center Carderock Division Report No. NSWCCD-50-TR-2002/068, December 2002.*
- Spalart, P. R. and Allmaras, S. R. 1992 A one-equation turbulence model for aerodynamic flows. *AIAA Paper No. 92-0439, 1992.*

Wells, W. G. 1964 Design principles for a high-speed fiberglass water tunnel. *Department of Aerophysics, Mississippi State University, Research Report No. 51, April 1964.*

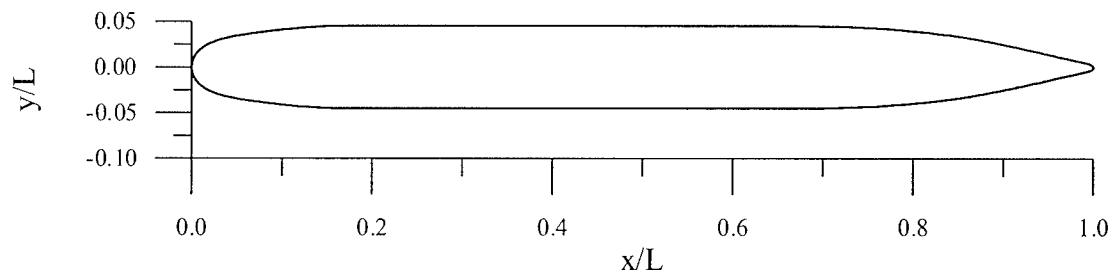


**Figure 1.1** Submarine hull geometry

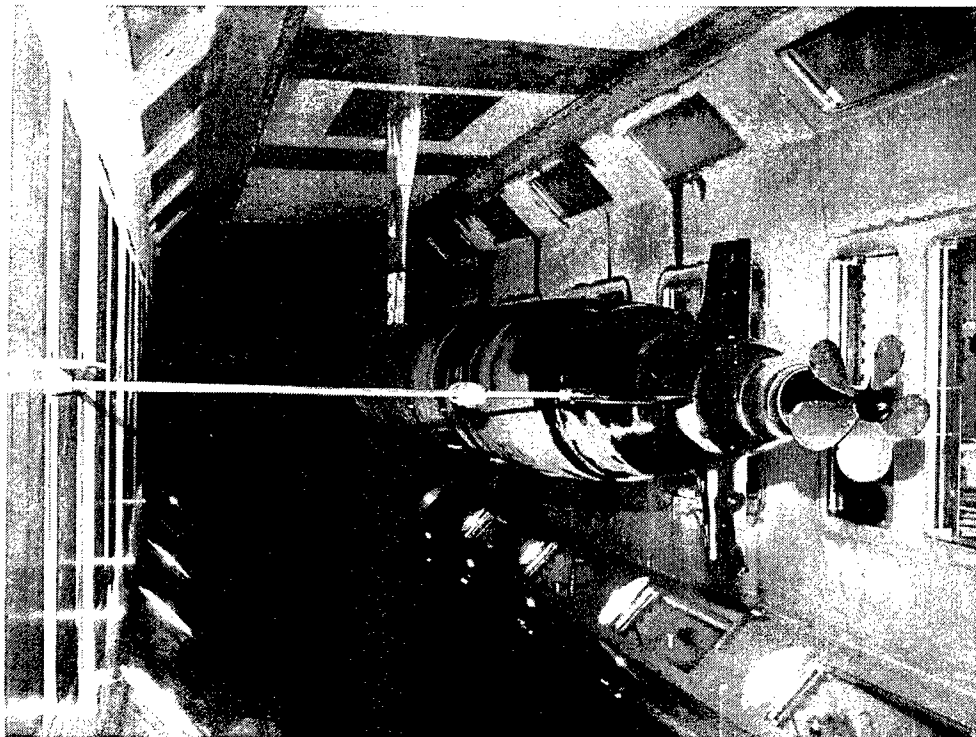
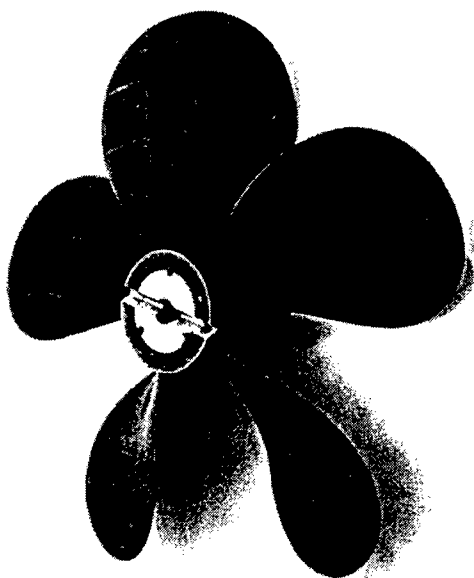


**Figure 1.2** Submarine model mounted in LCC (view shows location of stern appendages)





PROPELLER 4381

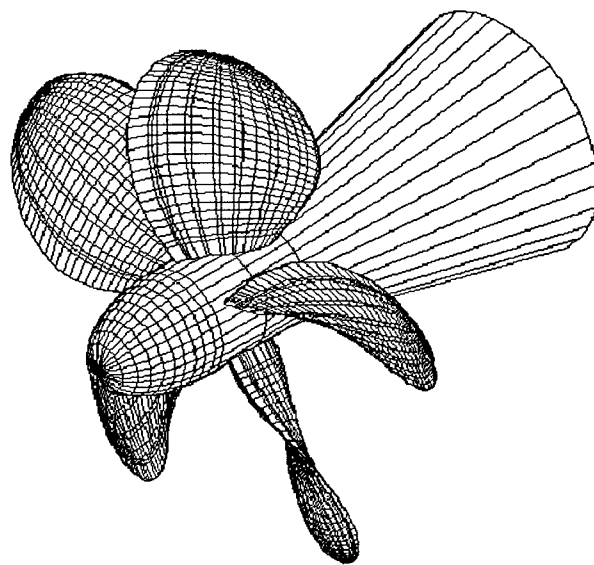
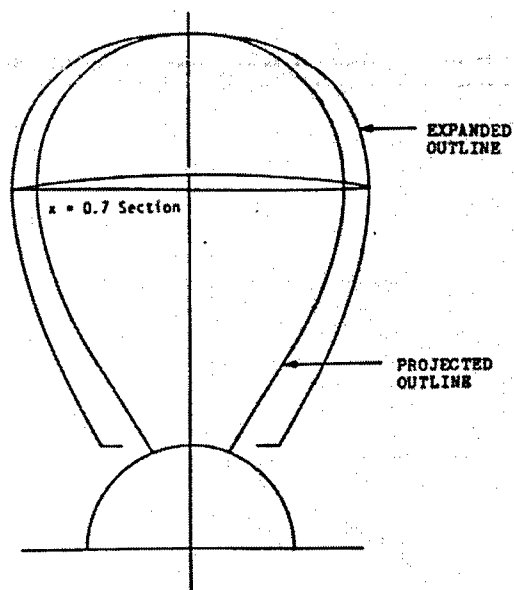
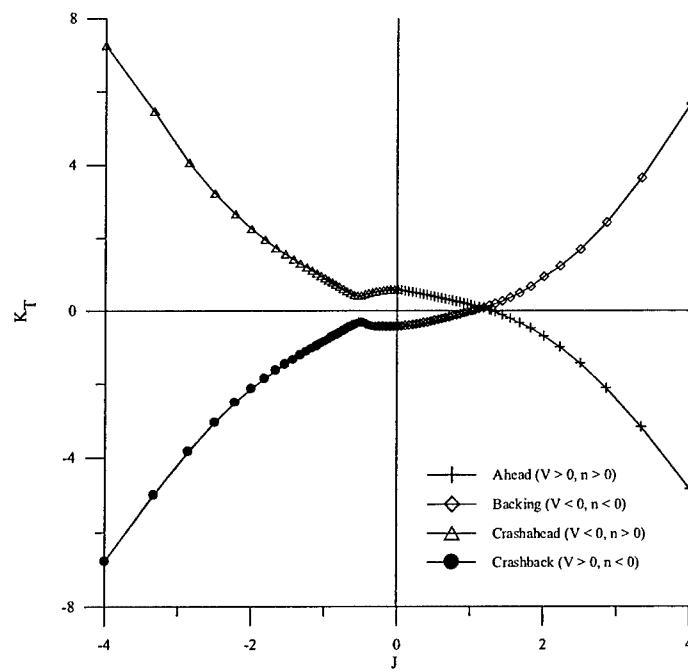
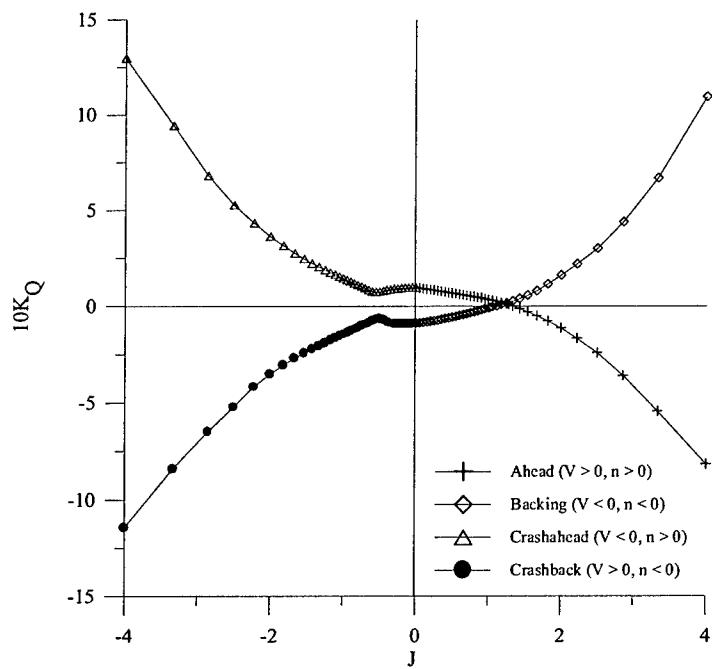


Figure 1.3 Propeller 4381 geometry



a. Thrust data



b. Torque data

Figure 1.4 Open-water data for Propeller 4381 (from Hecker and Remmers 1971)

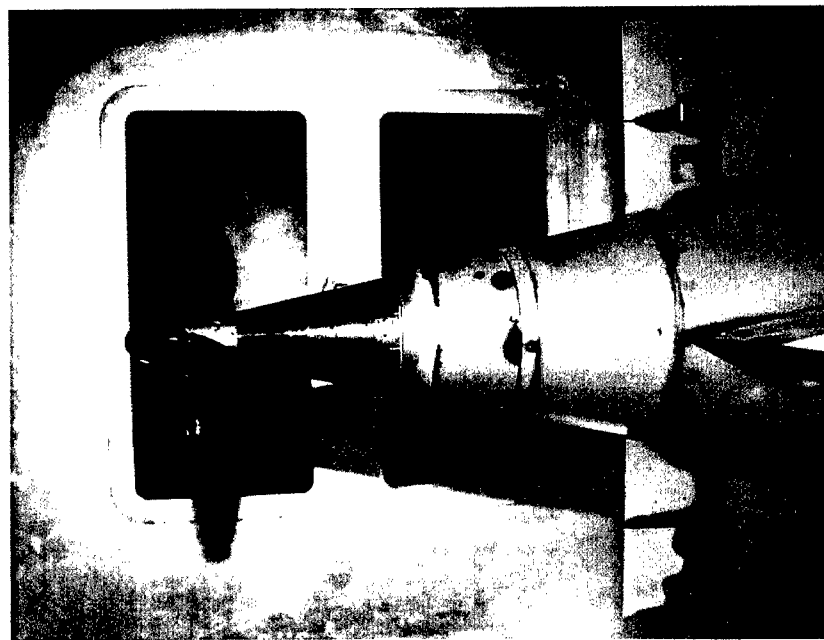
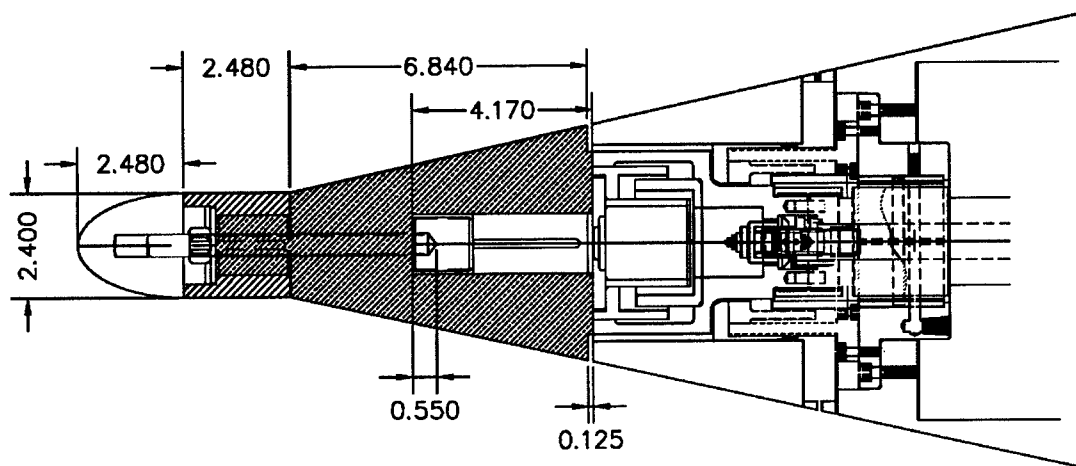


**Figure 1.5** Hull extension and Propeller 4381 mounted on submarine hull (P4381 omitted from drawing)

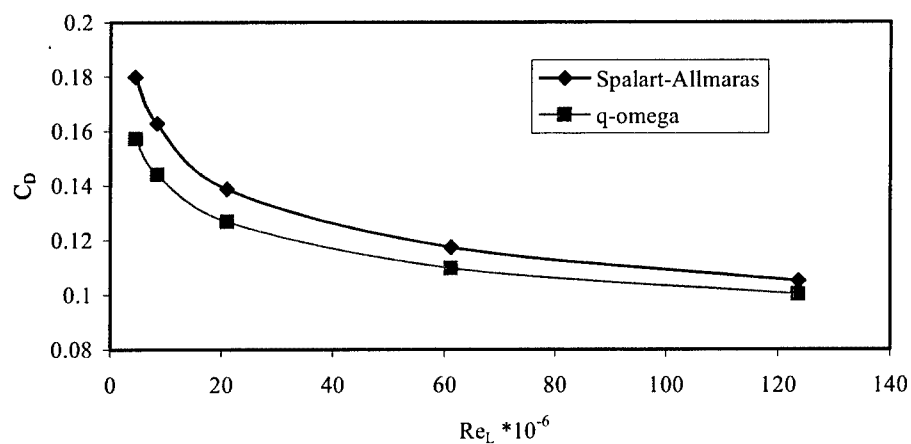


**Figure 2.1** Computational results for bare hull (LCC model scale); comparison between turbulence models

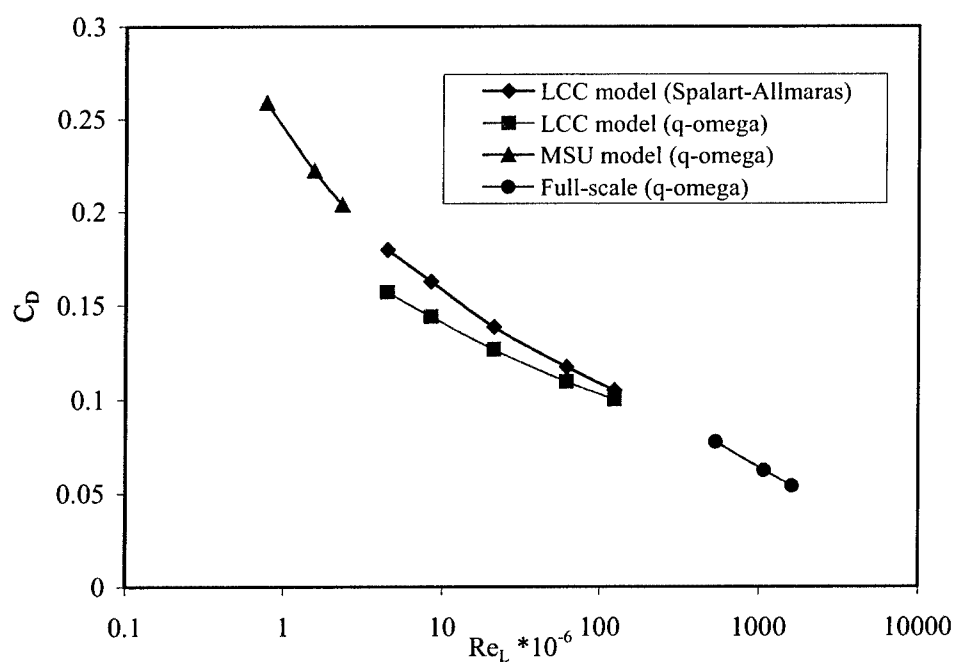
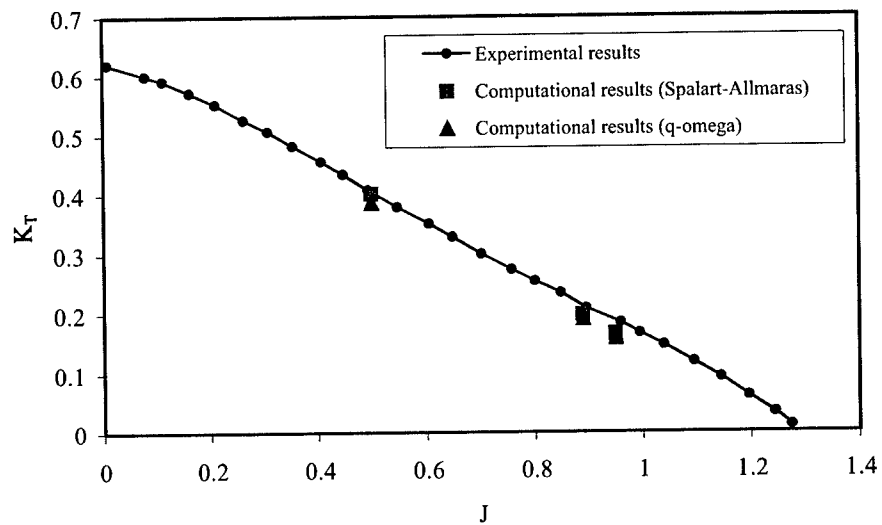
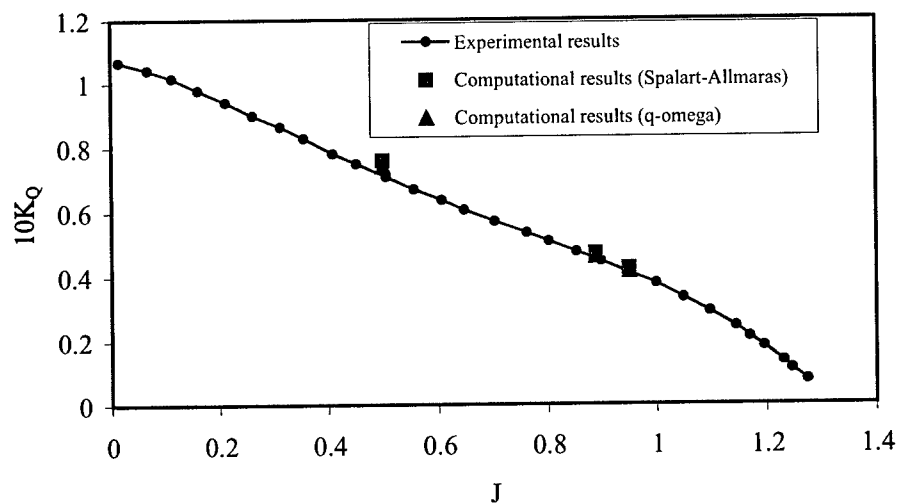


**Figure 2.2** Computational results for bare hull geometry and all scales

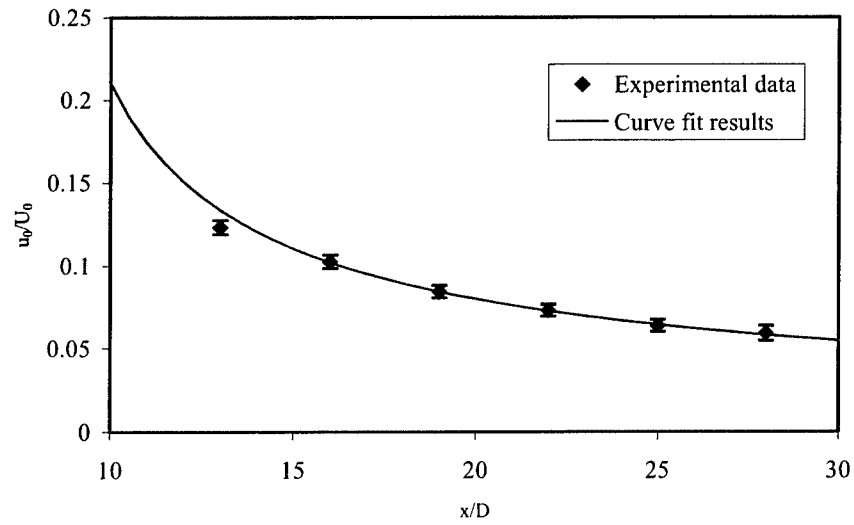


(a) Thrust coefficient

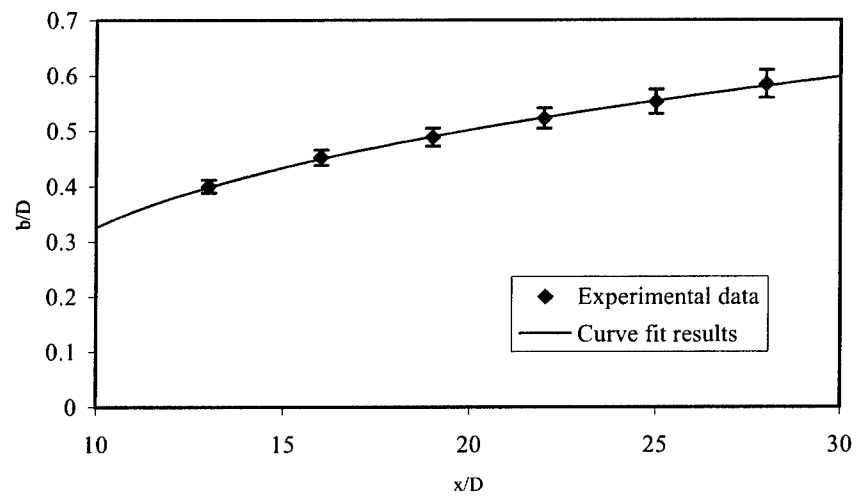


(b) Torque coefficient

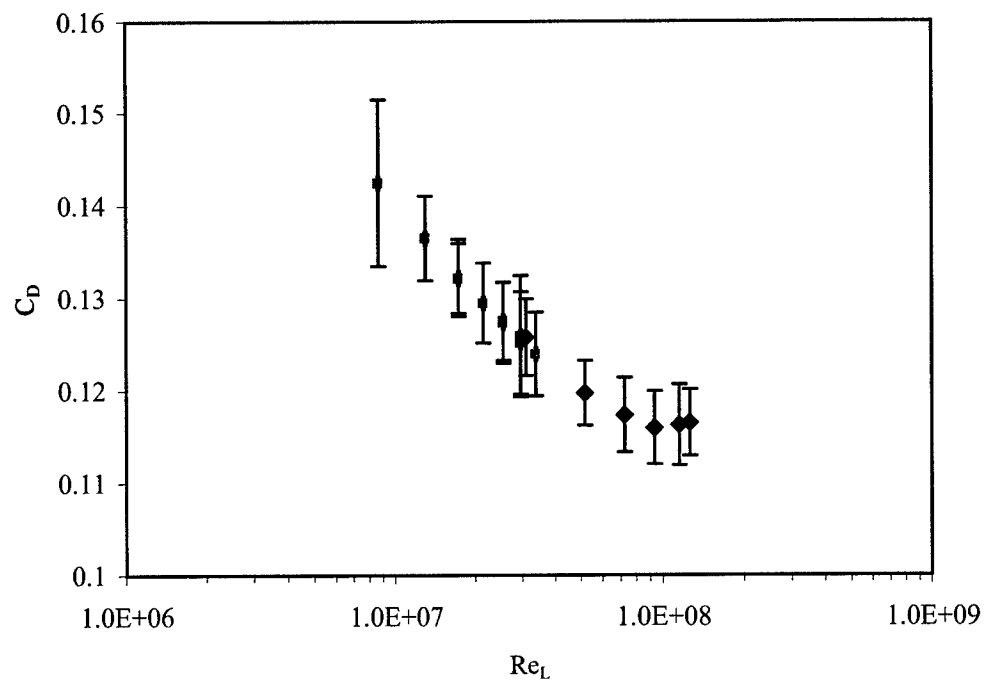
**Figure 2.3** Results of computations for isolated propeller (P4381); propeller thrust and torque coefficients as functions of advance ratio (experimental data from Hecker and Remmers 1971; see Figure 1.4)



**Figure 3.1** Streamwise variation of velocity deficit with uncertainties included

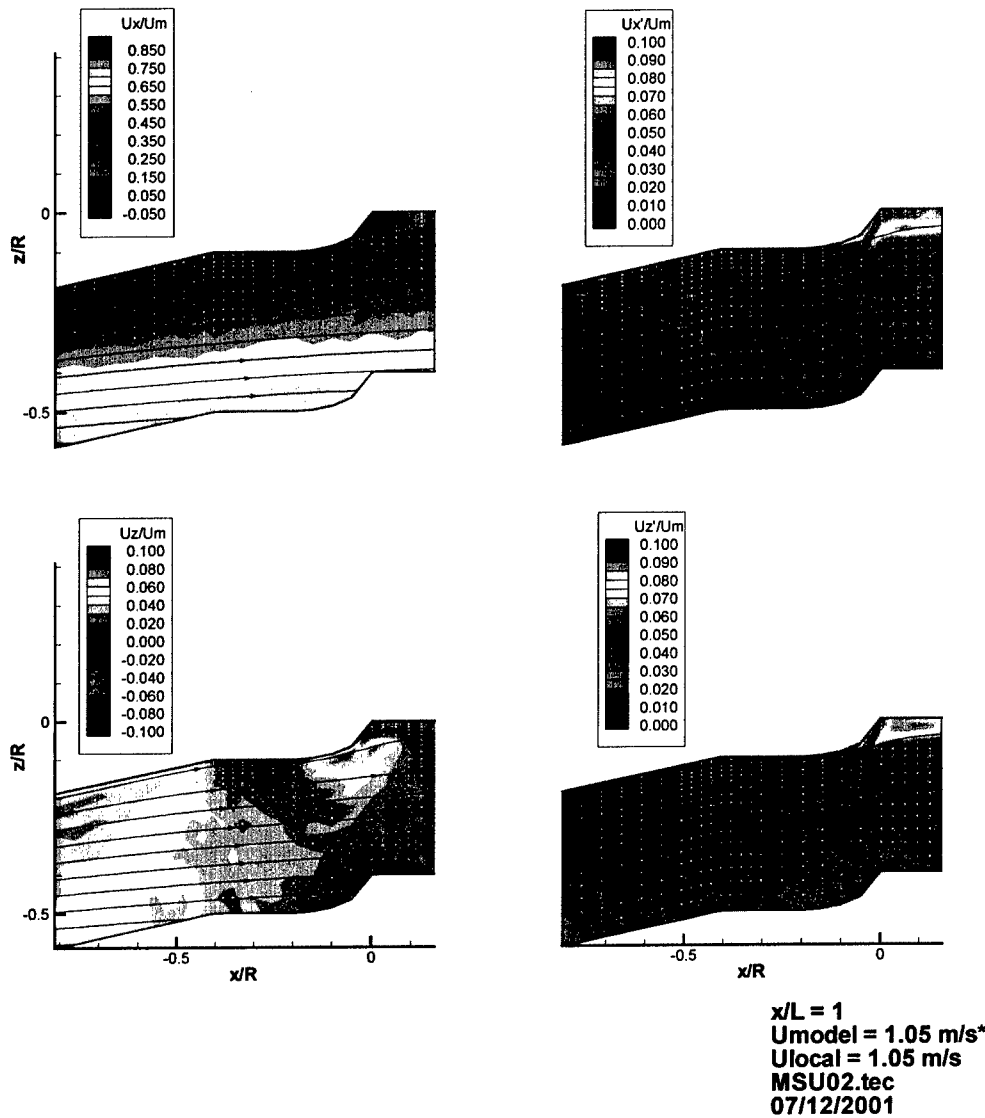


**Figure 3.2** Streamwise variation of wake width parameter with uncertainties included



**Figure 4.1** Experimental drag coefficient results obtained in the LCC

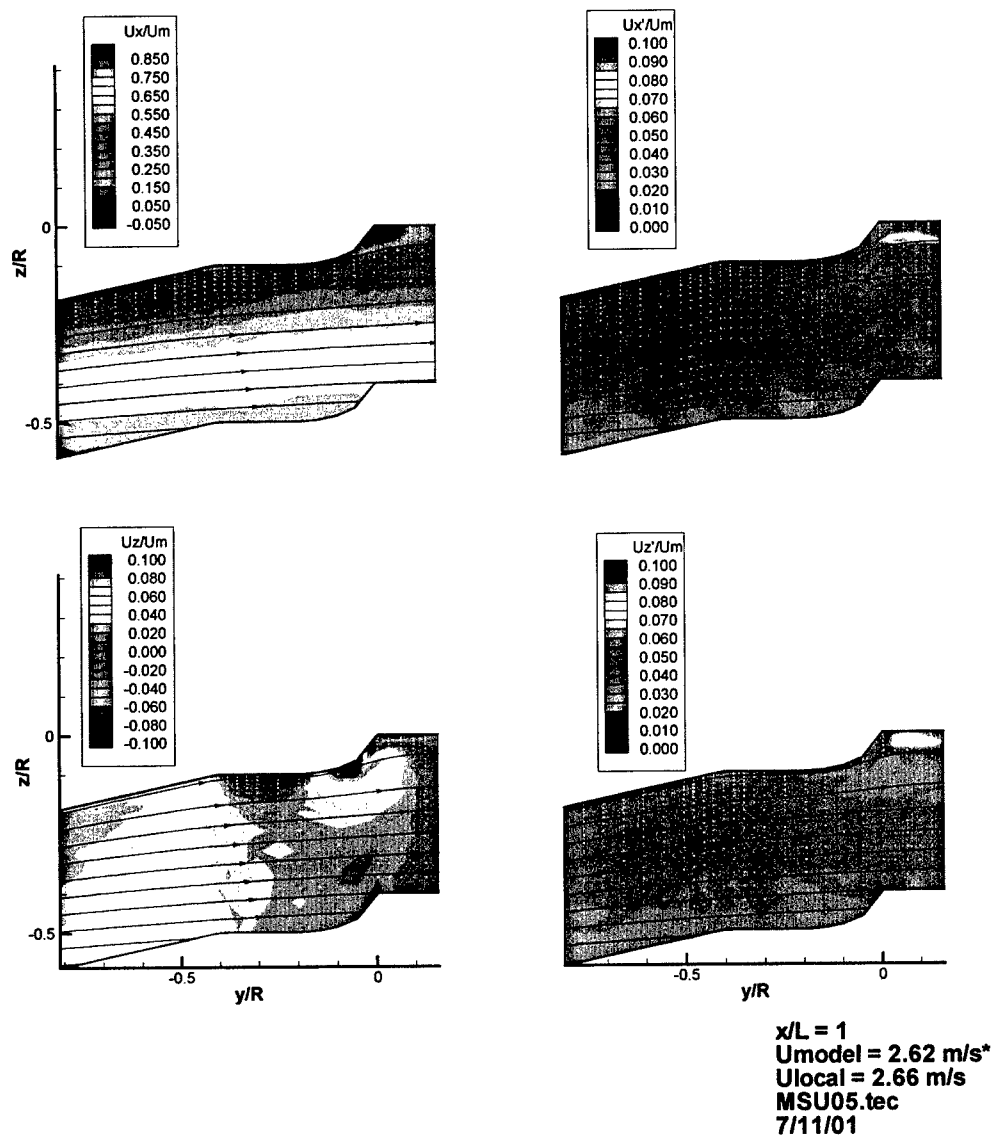
**Mississippi State University  
Submarine Near Wake & Aft Boundary Layer  
Tunnel Velocity 1.05 m/s**



**Figure 4.2** Results of LDV surveys of velocity flow field at stern of model at a tunnel set speed of 2 kts (upper bounding contour is hull outline and tunnel centerline)

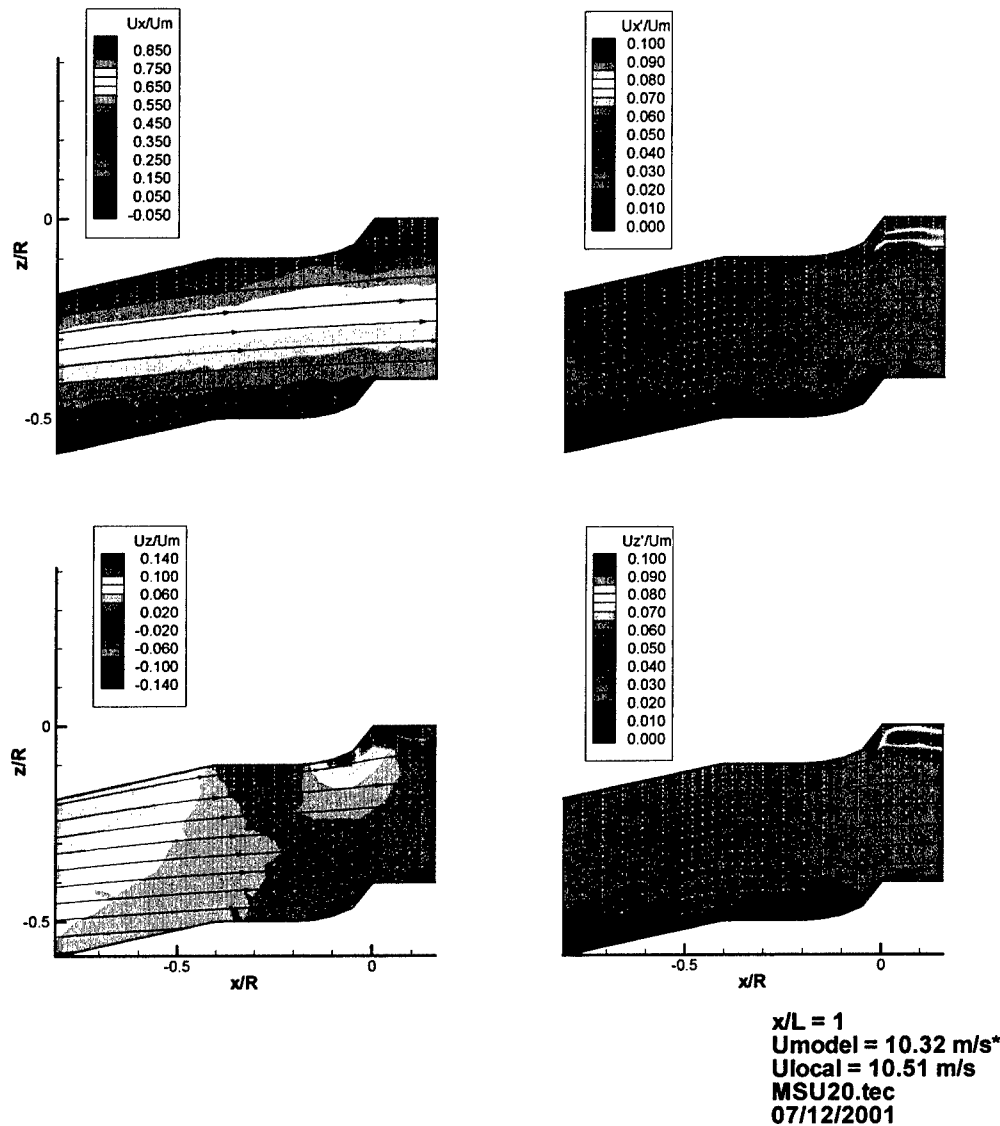


**Mississippi State University  
Submarine Near Wake & Aft Boundary Layer  
Tunnel Velocity 2.62 m/s**



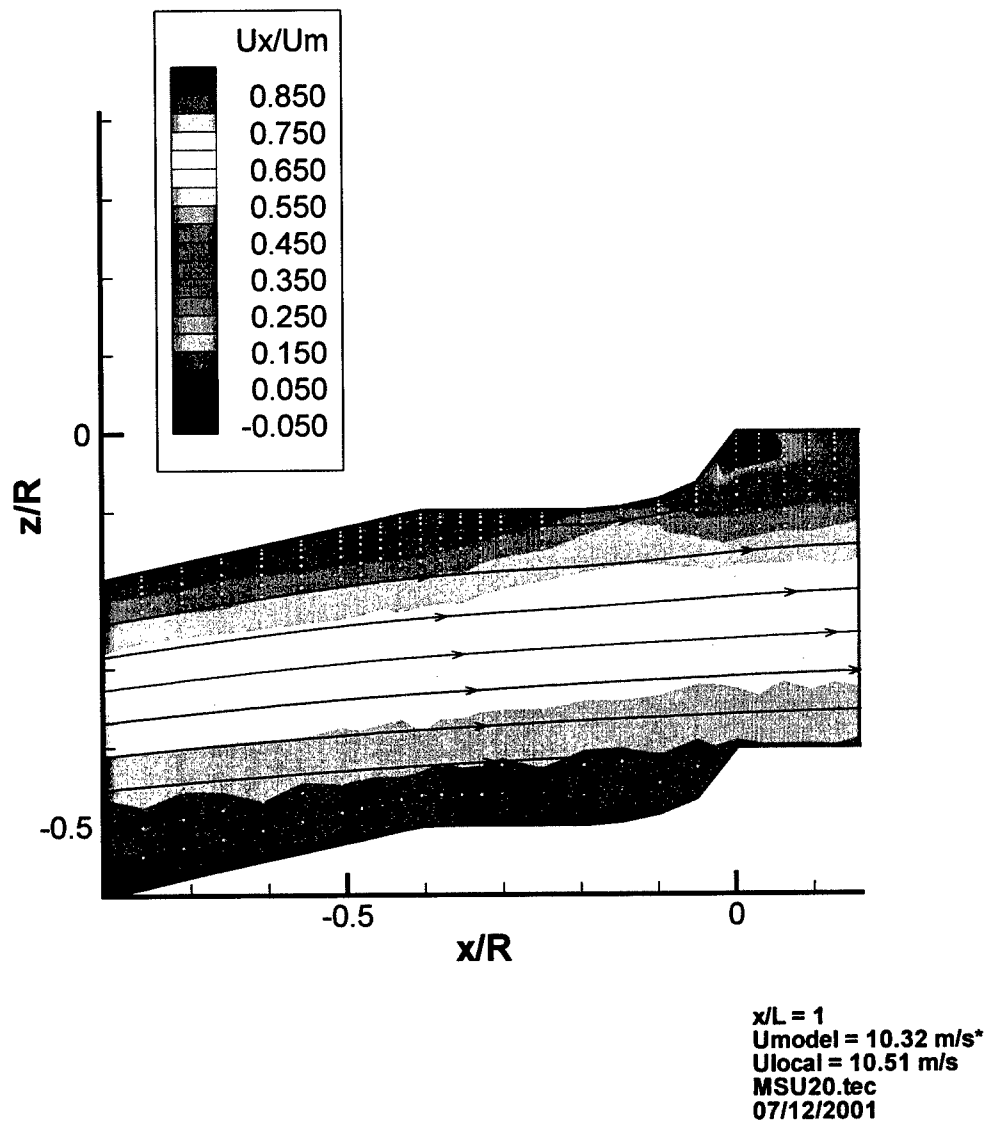
**Figure 4.3** Results of LDV surveys of velocity flow field at stern of model at a tunnel set speed of 5 kts (upper bounding contour is hull outline and tunnel centerline)

**Mississippi State University  
Submarine Near Wake & Aft Boundary Layer  
Tunnel Velocity 10.32 m/s**



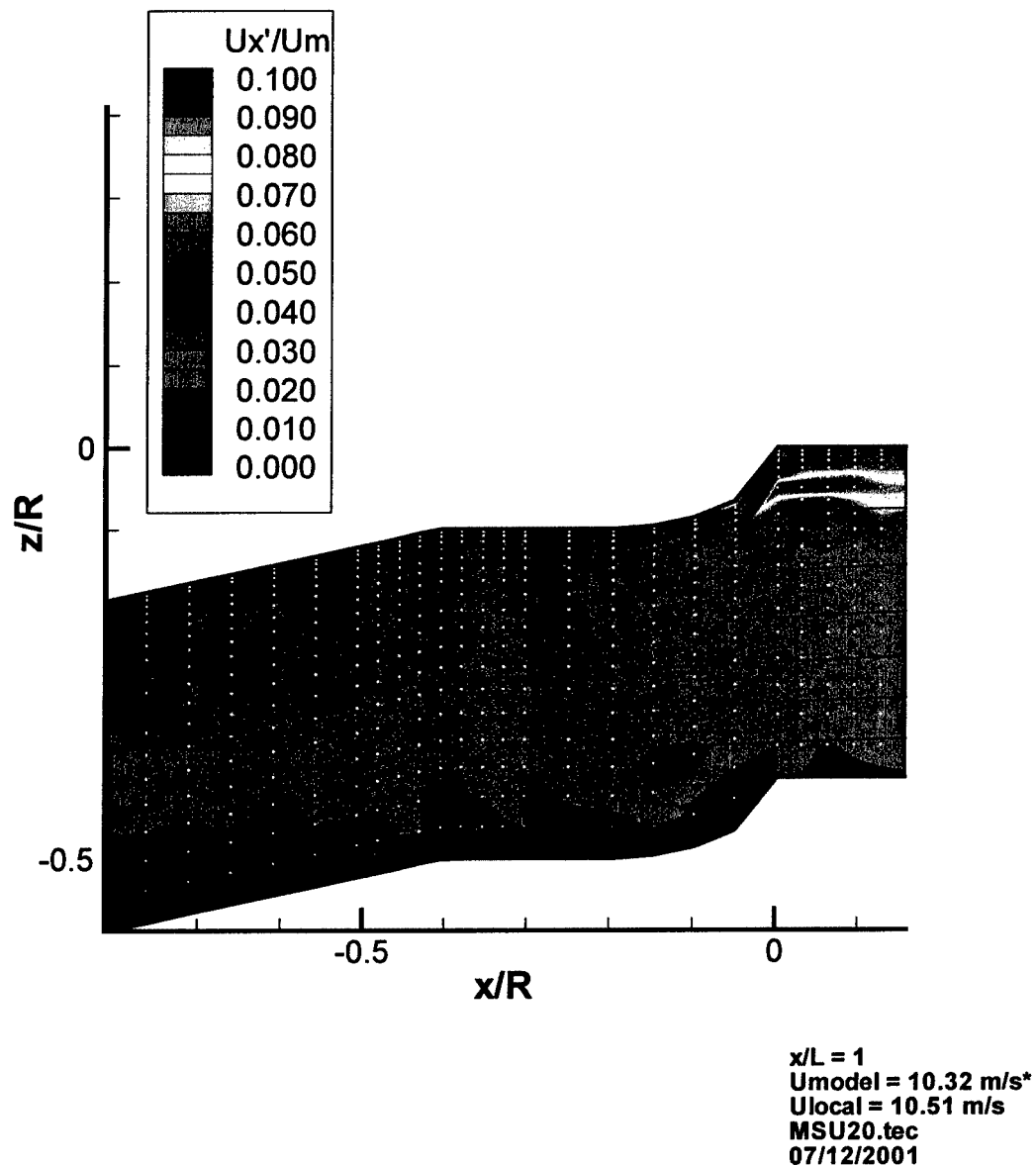
**Figure 4.4** Results of LDV surveys of velocity flow field at stern of model at a tunnel set speed of 20 kts (upper bounding contour is hull outline and tunnel centerline)

**Mississippi State University  
Submarine Near Wake & Aft Boundary Layer  
Tunnel Velocity 10.32 m/s**



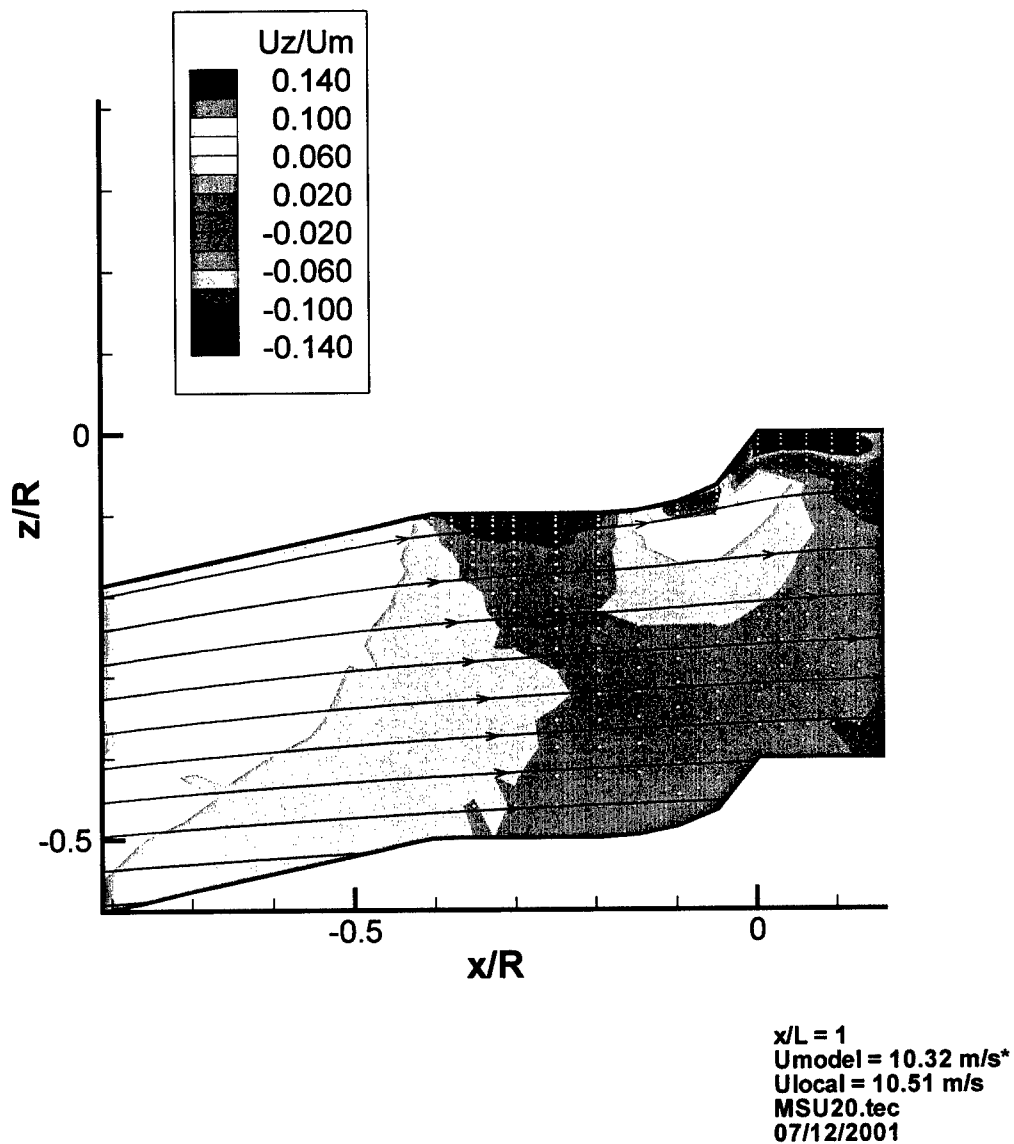
**Figure 4.5** Detail of mean streamwise velocity component at stern of model at a tunnel set speed of 20 kts  
(upper bounding contour is hull outline and tunnel centerline)

**Mississippi State University  
Submarine Near Wake & Aft Boundary Layer  
Tunnel Velocity 10.32 m/s**



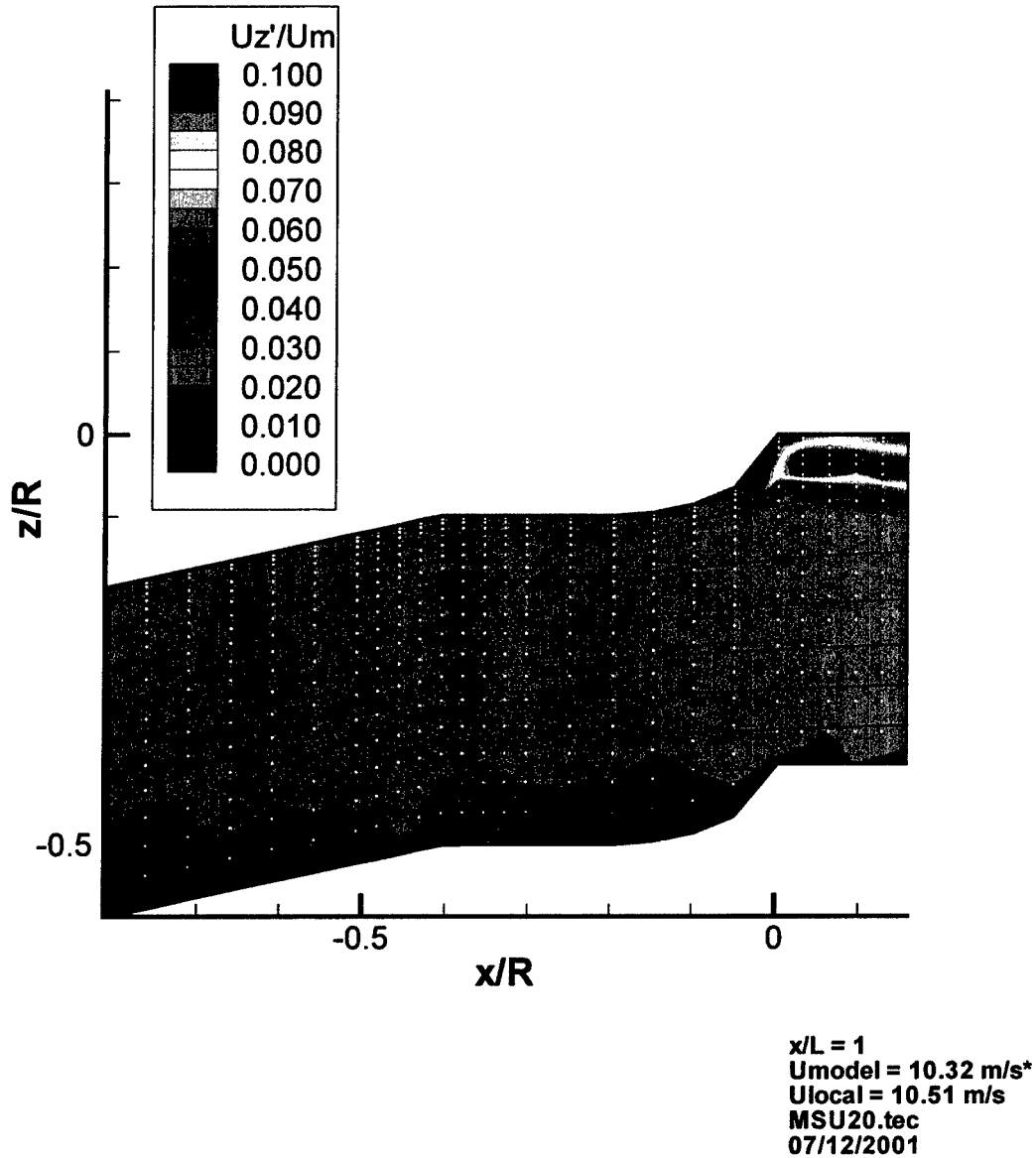
**Figure 4.6** Detail of fluctuating streamwise velocity component at stern of model at a tunnel set speed of 20 kts (upper bounding contour is hull outline and tunnel centerline)

**Mississippi State University  
Submarine Near Wake & Aft Boundary Layer  
Tunnel Velocity 10.32 m/s**

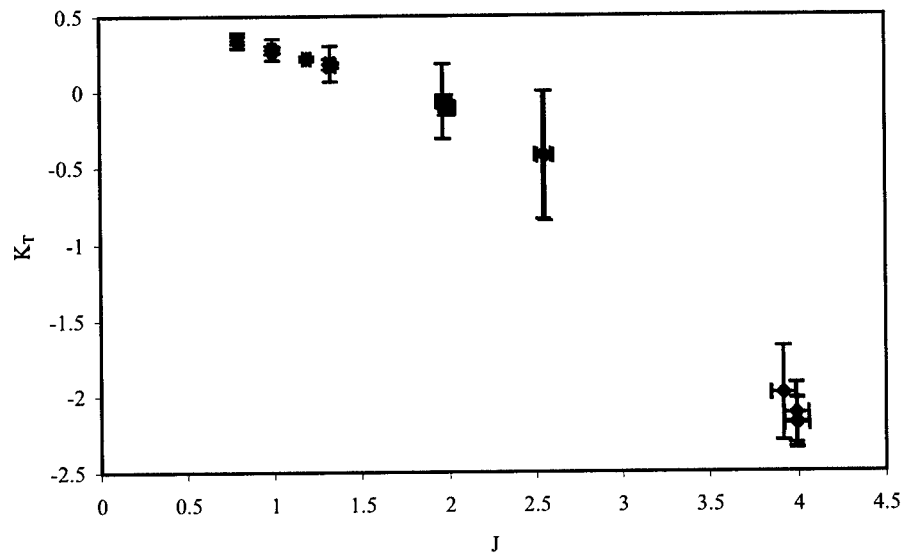


**Figure 4.7** Detail of mean transverse velocity component at stern of model at a tunnel set speed of 20 kts  
(upper bounding contour is hull outline and tunnel centerline)

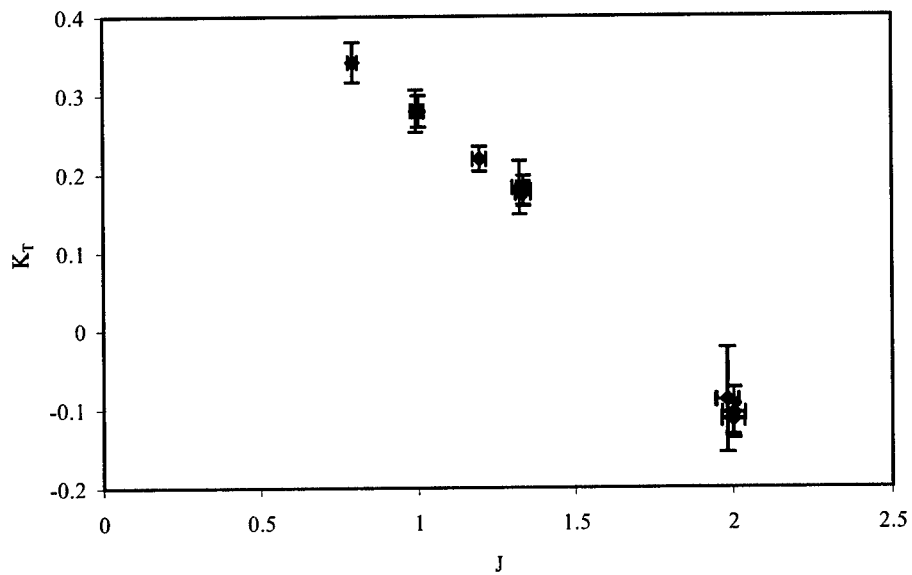
**Mississippi State University  
Submarine Near Wake & Aft Boundary Layer  
Tunnel Velocity 10.32 m/s**



**Figure 4.8** Detail of fluctuating transverse velocity component at stern of model at a tunnel set speed of 20 kts (upper bounding contour is hull outline and tunnel centerline)



(a) Entire data set

(b) Results with data acquired at 5 kts removed and range in  $J$  reduced**Figure 4.9** Propeller thrust coefficient variations with advance ratio

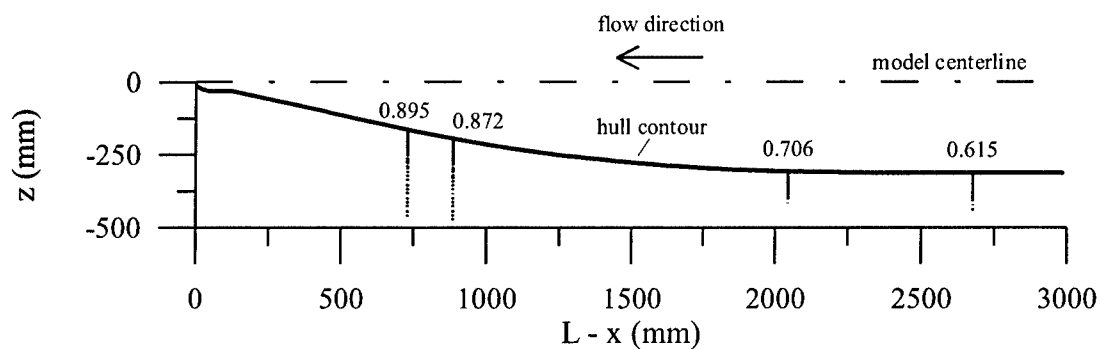


**Figure 4.10** Locations of boundary layer surveys ( $L$  = model length; numbers indicate  $x/L$  positions of boundary layer traverses)

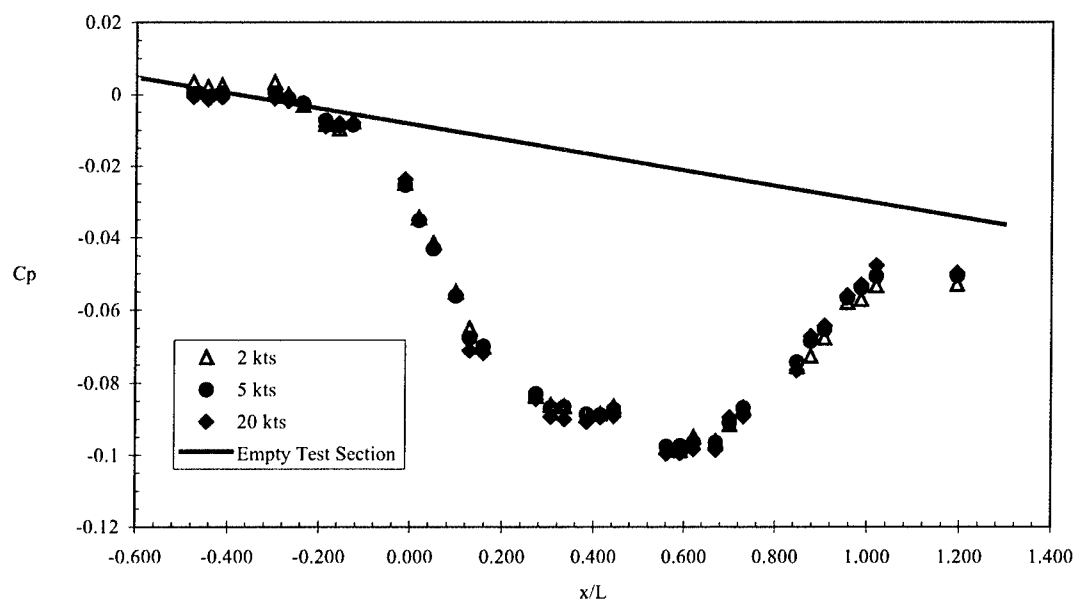
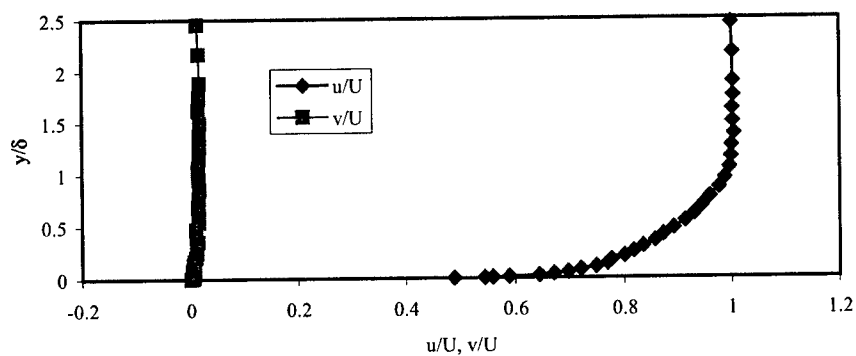
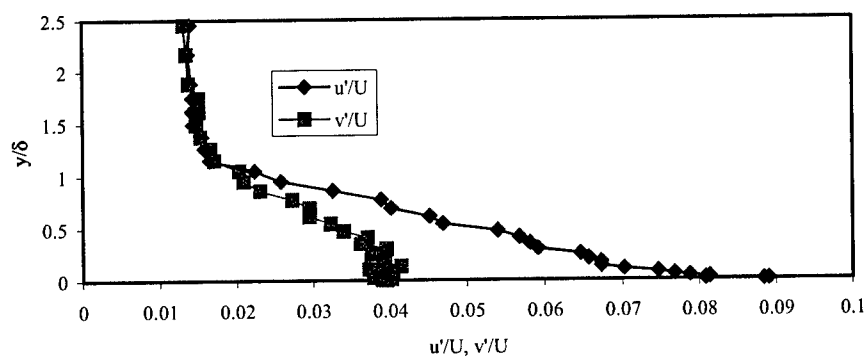


**Figure 4.11** LCC free stream pressure distribution obtained from test section wall taps

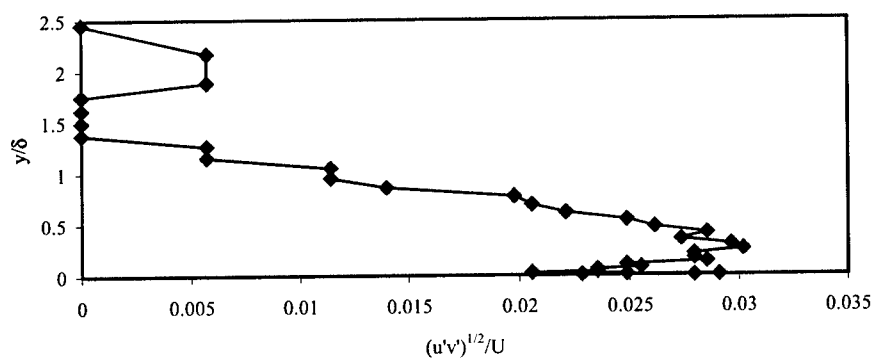




(a) Mean velocity components

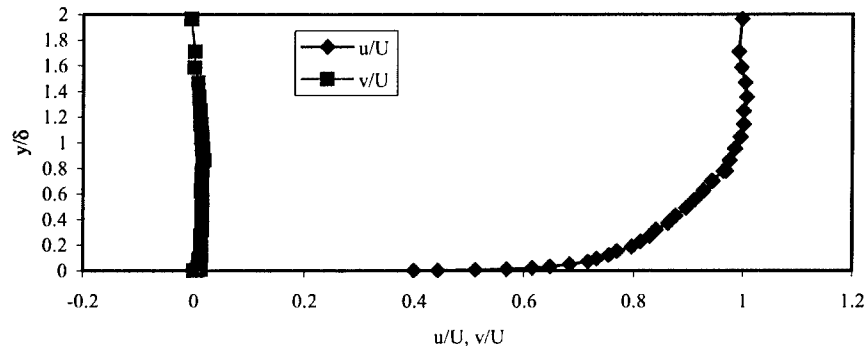


(b) Fluctuating components

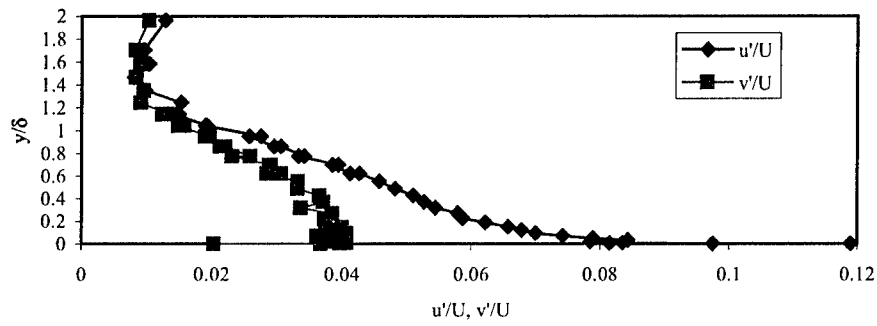


(c) Reynolds stresses

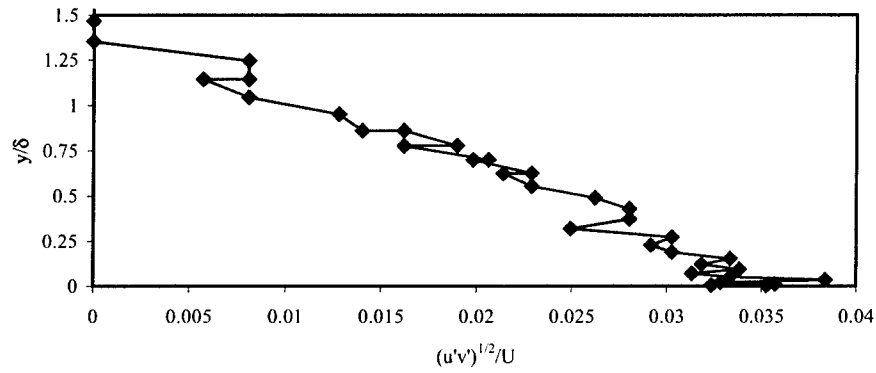
**Figure 4.12** Boundary layer profiles for  $x/L = 0.615$  ( $U = 5.42$  m/s,  $\delta = 53.0$  mm,  $\delta/R_{local} = 0.17$ )



(a) Mean velocity components

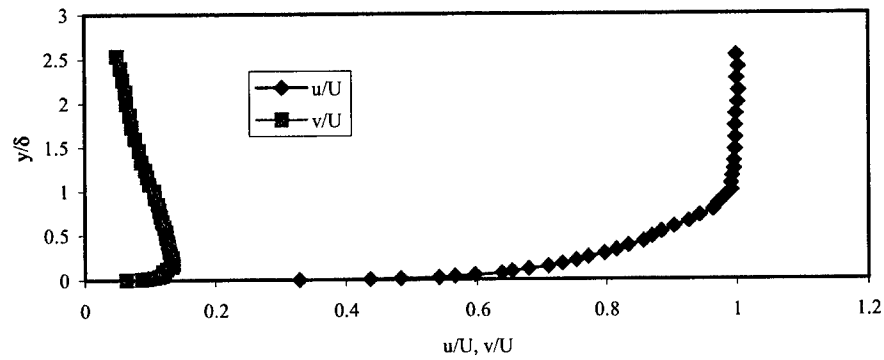


(b) Fluctuating velocity components

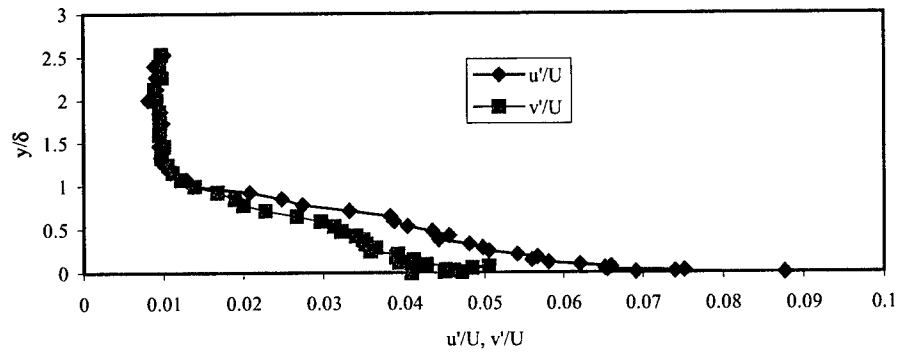


(c) Reynolds stresses

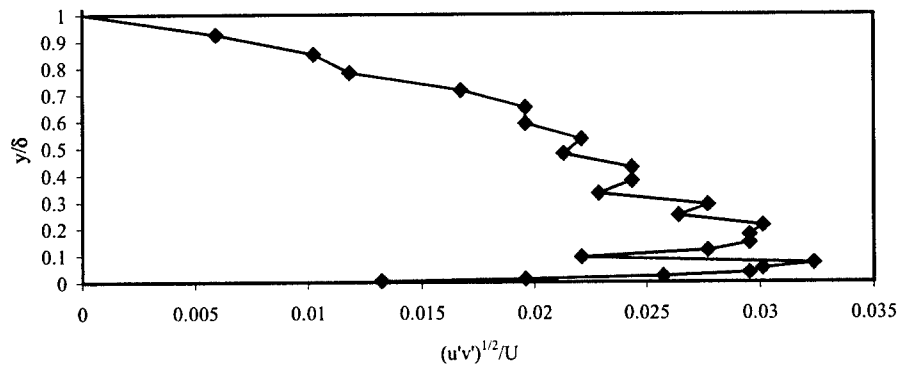
**Figure 4.13** Boundary layer profiles for  $x/L = 0.706$  ( $U = 5.41$  m/s,  $\delta = 58.6$  mm,  $\delta/R_{local} = 0.19$ )



(a) Mean velocity components

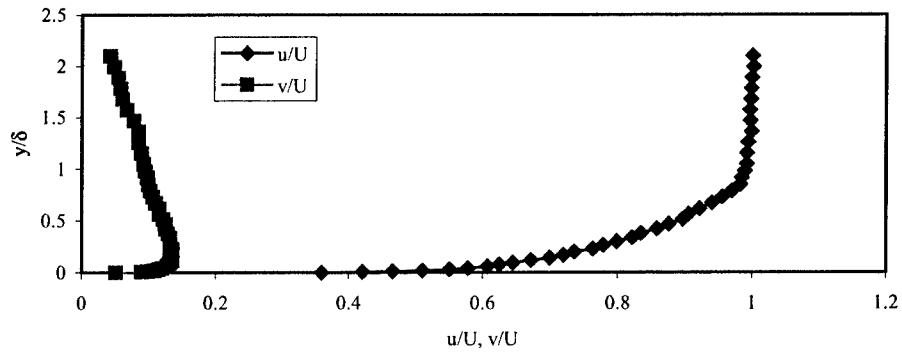


(b) Fluctuating velocity components

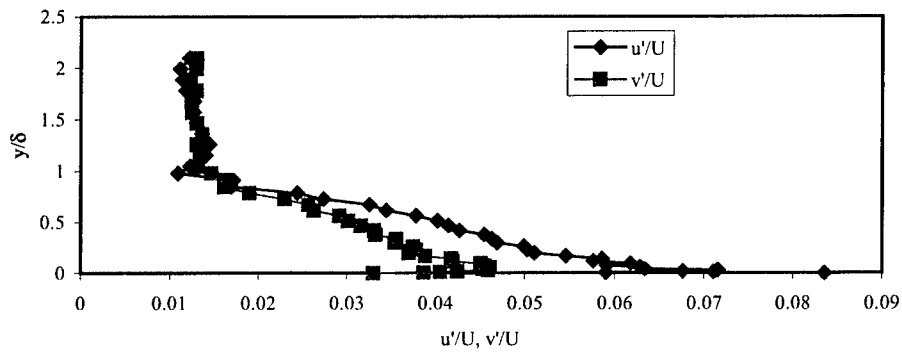


(c) Reynolds stresses

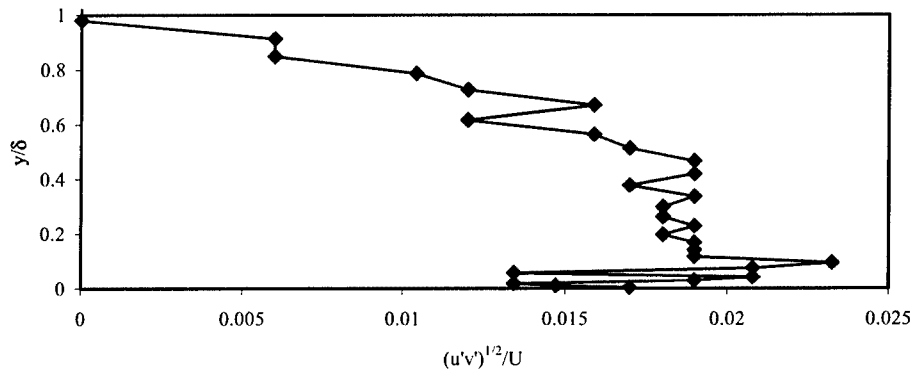
**Figure 4.14** Boundary layer profiles for  $x/L = 0.872$  ( $U = 5.23$  m/s,  $\delta = 112.4$  mm,  $\delta/R_{local} = 0.59$ )



(a) Mean velocity components

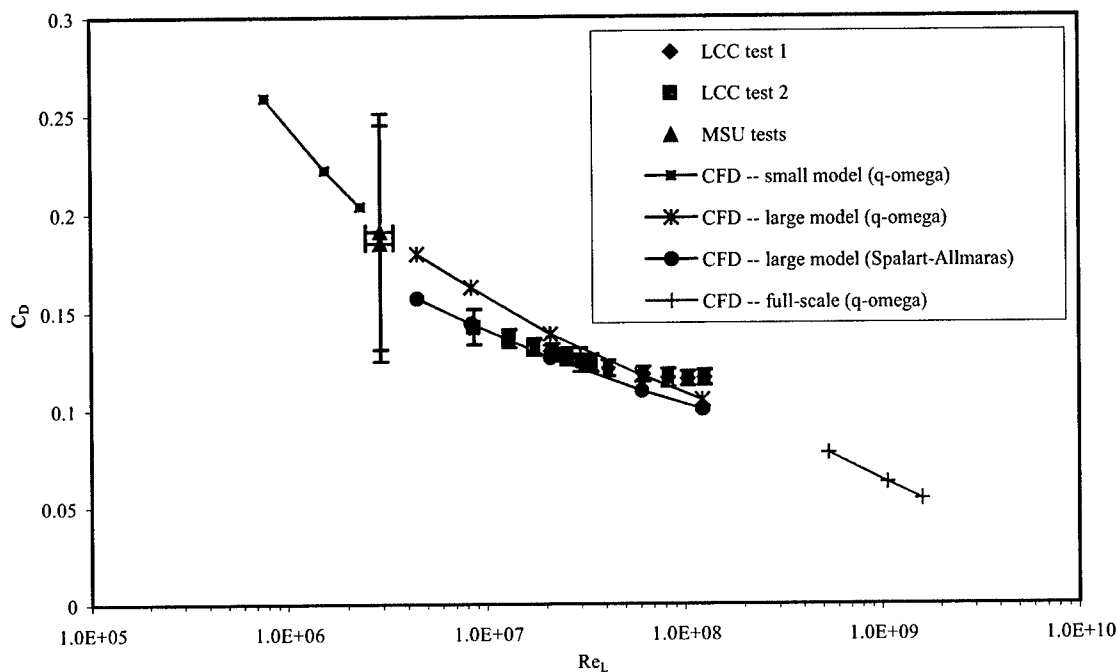


(b) Fluctuating velocity components

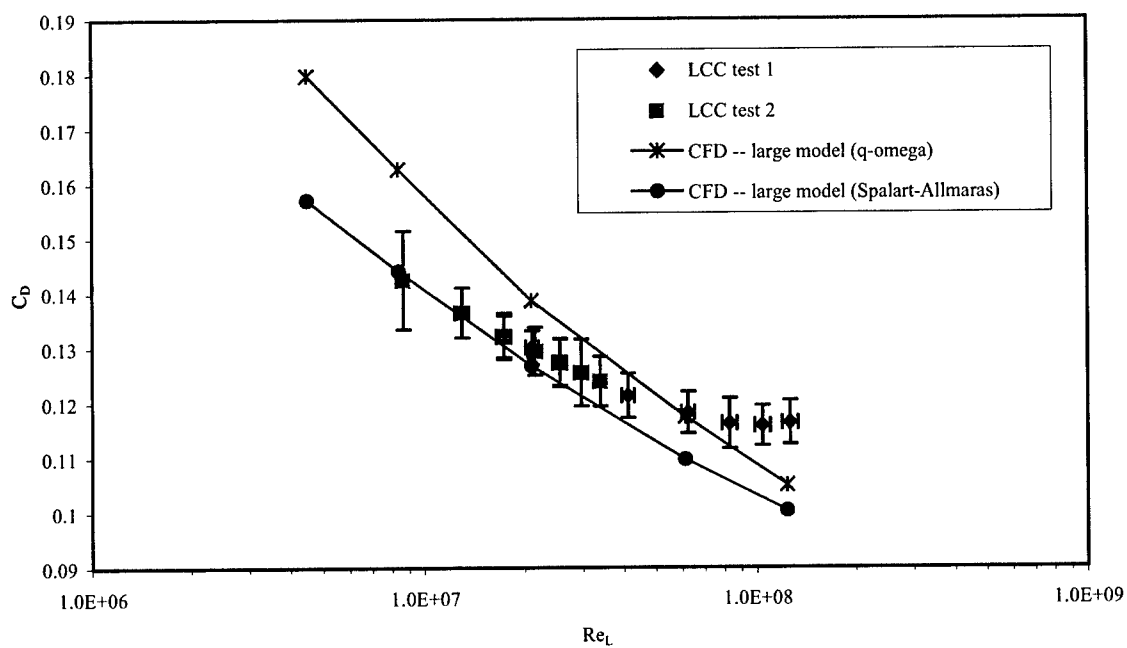


(c) Reynolds stresses

**Figure 4.15** Boundary layer profiles for  $x/L = 0.895$  ( $U = 5.15$  m/s,  $\delta = 142.9$  mm,  $\delta/R_{local} = 0.89$ )



(a) Comparison of all results



(b) Comparison of LCC model scale results

**Figure 5.1** Comparison of computational and experimental results for drag

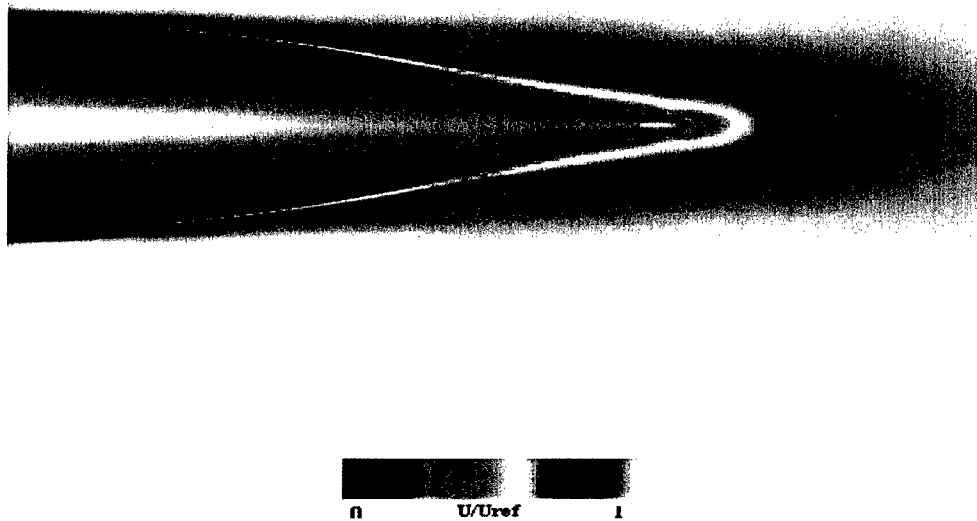
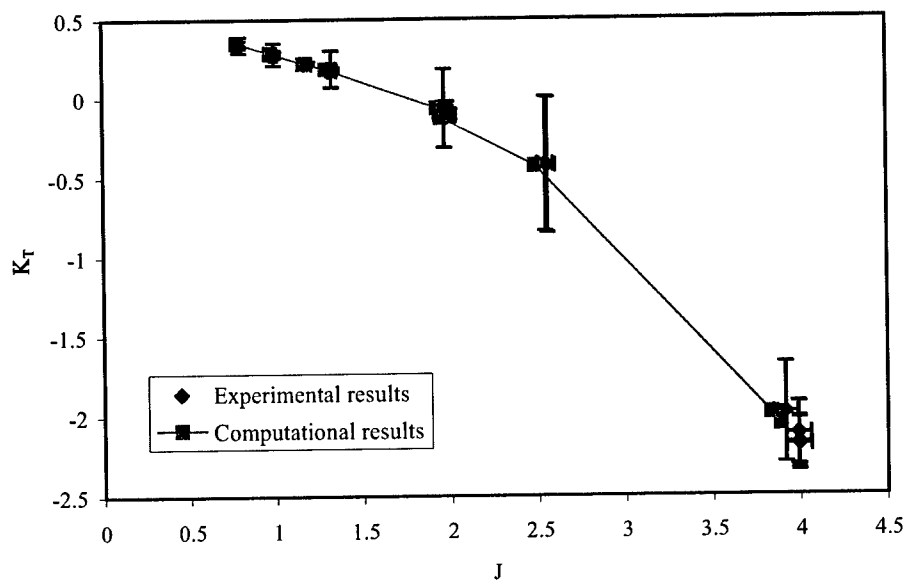
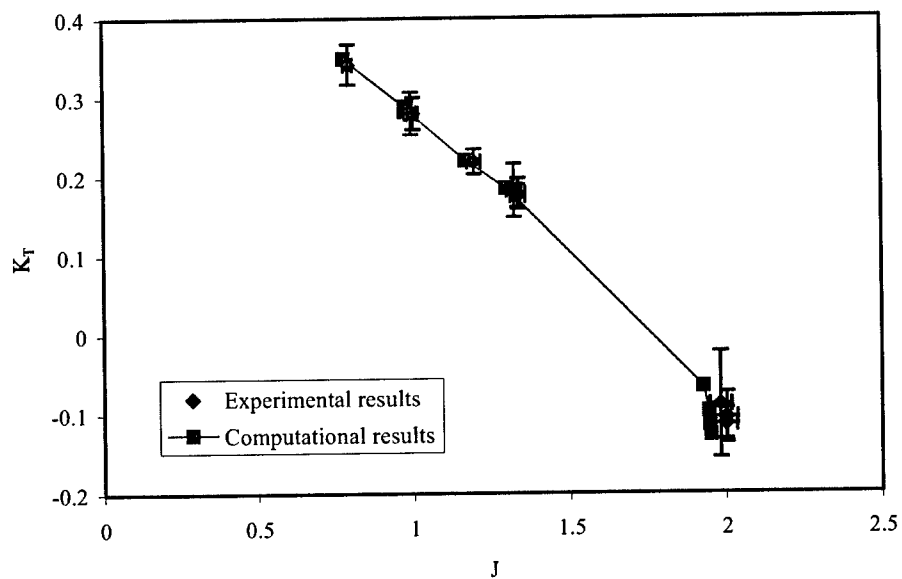


**Figure 5.2** Computed axial velocity contours for  $Re_L = 32$  million

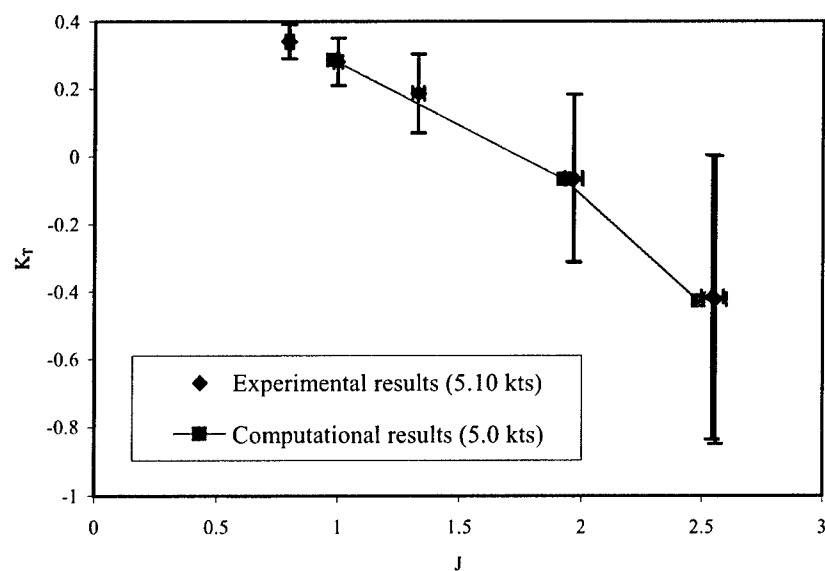


(a) All data

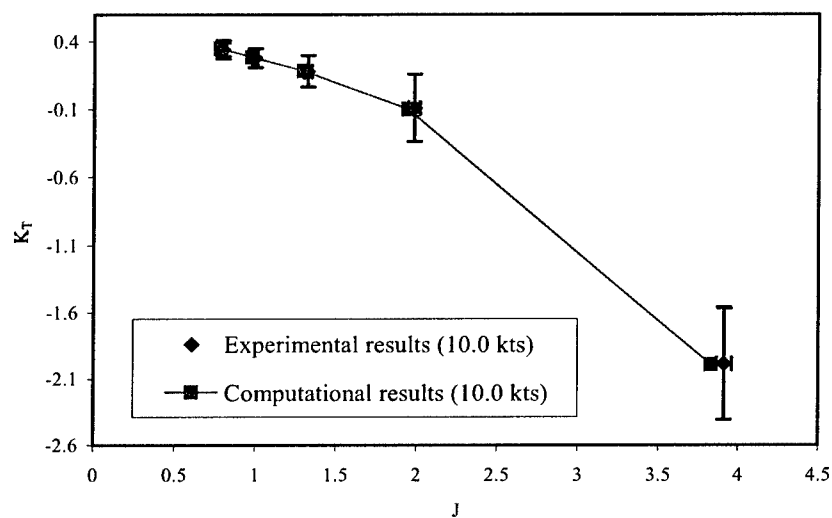


(b) Expanded scale in advance ratio

**Figure 5.3** Comparison of experimental and computation results for propeller thrust coefficient (all values of Reynolds number)



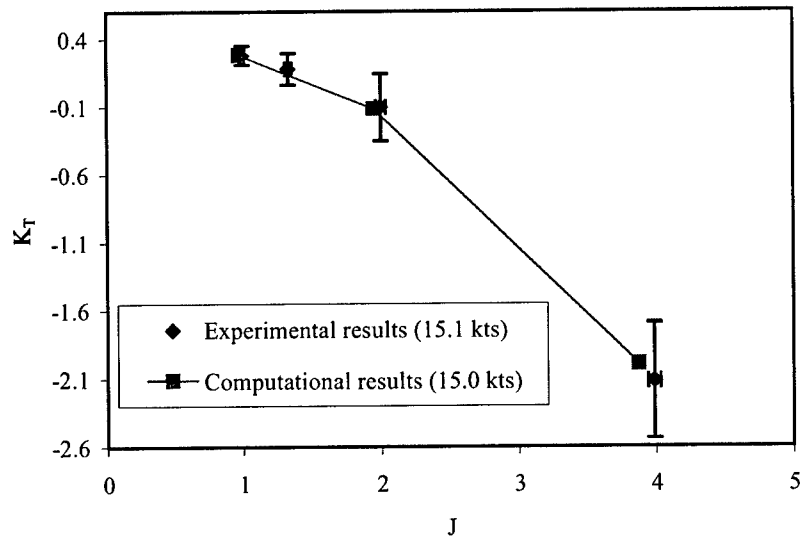
(a)  $Re_{L,exp} = 18.1(10^6)$ ,  $Re_{L,comp} = 16(10^6)$



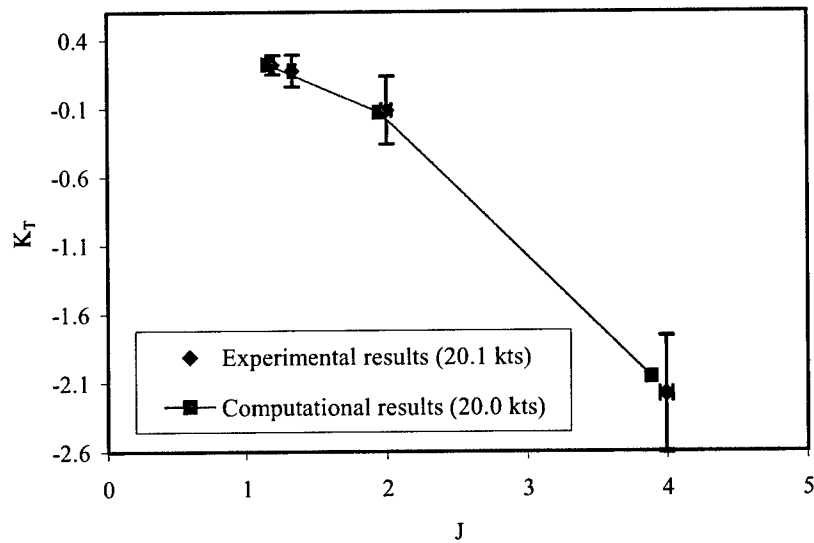
(b)  $Re_{L,exp} = 35.6(10^6)$ ,  $Re_{L,comp} = 32(10^6)$

**Figure 5.4** Comparison of experimental and computational results for propeller thrust at different values of the Reynolds number (continued)





(c)  $Re_{L, exp} = 53.4(10^6)$ ,  $Re_{L, comp} = 48(10^6)$



(d)  $Re_{L, exp} = 71.2(10^6)$ ,  $Re_{L, comp} = 64(10^6)$

**Figure 5.4** Comparison of experimental and computational results for propeller thrust at different values of the Reynolds number (concluded)

This page intentionally left blank.

Appendix A

COMPUTATIONAL STUDIES OF FULLY SUBMERGED BODIES,  
PROPULSORS, AND BODY/PROPULSOR INTERACTIONS

By

Allison Nicole Cash

A Thesis  
Submitted to the Faculty of  
Mississippi State University  
in Partial Fulfillment of the Requirements  
for the Degree of Master of Science  
in Aerospace Engineering  
in the Department of Aerospace Engineering

Mississippi State, Mississippi

December 2001

COMPUTATIONAL STUDIES OF FULLY SUBMERGED BODIES,  
PROPULSORS, AND BODY/PROPULSOR INTERACTIONS

By

Allison Nicole Cash

Approved:

---

David H. Bridges  
Associate Professor of Aerospace  
Engineering (Director of Thesis  
and Major Professor)

---

John C. McWhorter III  
Professor, Head, and Graduate  
Coordinator of the Department of  
Aerospace Engineering

---

Keith Koenig  
Professor of Aerospace Engineering  
(Committee Member)

---

Lafayette K. Taylor  
Associate Research Professor of  
Computational Engineering  
(Committee Member)

---

Wayne Bennett  
Dean of the College of Engineering

Name: Allison N. Cash

Date of Degree: December 14, 2001

Institution: Mississippi State University

Major Field: Aerospace Engineering

Major Professor: Dr. David Bridges

Title of Study: COMPUTATIONAL STUDIES OF FULLY SUBMERGED BODIES,  
PROPULSORS, AND BODY/PROPULSOR INTERACTIONS

Pages in Study: 85

Candidate for Degree of Master of Science

Difficulties exist with designing and testing on a model scale. The purpose of this study is to examine variations in the flow field of a submarine due to hull/propulsor interaction and Reynolds scaling. The scope of this study includes the simulation of the flow past a 1) five-bladed marine propeller with  $0^\circ$  skew, 2) unappended submarine hull, 3) forward propelled submarine with asymmetrical stern appendages, and 4) submarine in crashback with asymmetrical stern appendages. The bare hull simulations are conducted for three different length scales: small model scale, large model scale, and full scale. The isolated propeller and appended submarine simulations are conducted on the large model scale. It is of interest how sensitive the various flow characteristics are to Reynolds number and the turbulence model. All simulations are at  $0^\circ$  angle of attack, and validated with experimental data where available.

## DEDICATION

*To my husband*

## ACKNOWLEDGEMENTS

First, I wish to thank Dr. David Bridges for the opportunity to work on such an interesting project and for his support throughout this endeavor. A personal thanks is extended to Dr. Lafe Taylor for his invaluable guidance and support, and to Dr. Keith Koenig for his advice and calming influence. For being a vital source of information and a patient guide, a great deal of appreciation goes to Kidambi Sreenivas. Also, I would like to extend a heartfelt thanks to Brent Mitchell for all of his help.

Funds for this research were provided by the Office of Naval Research DEPSCoR Grant No. N00014-99-1-0534 with Dr. L. Patrick Purtell serving as program monitor. This support is gratefully acknowledged.

I would like to thank my husband for his compassion and understanding. I also wish to thank my closest friend, Heather Tinney, for her support and encouragement. To my family, thank you for all the years of science fair, without which I may not have found my path. Last, but hardly least, I would like to thank God for being the light through many a dark hour.

## TABLE OF CONTENTS

	Page
DEDICATION .....	ii
ACKNOWLEDGMENTS .....	iii
LIST OF TABLES .....	vi
LIST OF FIGURES .....	vii
 CHAPTER	
I. INTRODUCTION .....	1
1.1 Previous Studies .....	2
1.2 Present Study .....	3
1.3 Chapter Overview .....	4
II. BACKGROUND .....	5
2.1 Description of the Experiments .....	5
2.1.1 Isolated Propeller .....	5
2.1.2 Submarine Models .....	5
2.2 Description of the Flow Solver .....	8
2.2.1 Governing Equations .....	9
2.2.2 Numerical Method .....	10
2.2.3 Boundary Conditions .....	11
2.2.4 Turbulence Models .....	11
III. DESCRIPTION OF COMPUTATIONAL CASE PREPARATION .....	13
3.1 Bare Hull .....	14
3.2 Isolated Propeller .....	21
3.3 Forward Propelled Appended Submarine .....	24
3.4 Appended Submarine in Crashback .....	27
IV. DISCUSSION OF RESULTS .....	29



CHAPTER	Page
4.1 Validation of Computational Results.....	29
4.2 Turbulence Model Comparisons.....	37
4.3 Reynolds Scaling Analysis .....	44
4.4 Hull/Propulsor Interaction .....	52
4.5 Submarine Crashback .....	63
4.6 Possible Sources of Error.....	67
V. CONCLUSIONS AND RECOMMENDATIONS	
5.1 Conclusions.....	71
5.2 Recommendations.....	73
REFERENCES .....	74
APPENDIX	
A. TABLE OF CONDITIONS FOR EACH COMPUTATIONAL CASE.....	76
B. VELOCITY CONTOURS FOR FORWARD PROPELLED SIMULATIONS.....	80

## LIST OF TABLES

TABLE	Page
3.1 Grid statistics .....	18
4.1 Drag coefficient comparison between grids and turbulence models .....	32
4.2 Xy-plane axial velocity contours .....	46
4.3 Yz-plane axial velocity contours .....	47
4.4 Comparison of isolated propeller and installed propeller yz-plane axial velocity fields showing the influence of the appendage wakes and hull boundary layer .....	55
4.5 Comparison of isolated propeller and installed propeller xy-plane axial velocity fields showing the influence of the appendage wakes and hull boundary layer .....	61

## LIST OF FIGURES

FIGURE	Page
2.1 Schematic showing orientation and mounting of submarine model .....	6
3.1 Bare LCC hull.....	15
3.2 Composite unstructured/structured surface grid.....	16
3.3 Volume element distribution about LCC stern.....	17
3.4 Convergence history by scale for $q-\omega$ turbulence model.....	19
3.5 Convergence history by grid type and turbulence model .....	20
3.6 Volume element distribution in the vicinity of stern appendages.....	21
3.7 Geometry and surface grid of the isolated P4381 .....	22
3.8 Force history for isolated propeller thrust coefficient. J = 0.95 correlates to experimental data; J = 0.97 correlates to hull/propulsor study. ....	23
3.9 Appended LCC Hull with P4381 Propeller .....	24
3.10 Volume grid in the vicinity of the stern appendages .....	25
3.11 Force history for forward propelled submarine, $J \approx 1$ .....	26
3.12 Force history for crashback showing total force in the x-direction, case cbsub.2b.....	28
4.1 Drag coefficient versus Reynolds number with 15% error bars. LCC model scale = 22.964 feet. Normalized by length.....	30

FIGURE	Page
4.2 Drag coefficient versus Reynolds number. LCC model scale. Normalized by projected frontal area.....	31
4.3 Validation of thrust coefficient for isolated propeller .....	33
4.4 Validation of torque coefficient for isolated propeller .....	33
4.5 Thrust coefficient for installed propeller versus advance coefficient. Tunnel speed is 5 knots. Reynolds number = 16 million .....	35
4.6 Thrust coefficient for installed propeller versus advance coefficient. Tunnel speed is 10 knots. Reynolds number = 32 million .....	35
4.7 Thrust coefficient for installed propeller versus advance coefficient. Tunnel speed is 15 knots. Reynolds number = 48 million .....	36
4.8 Thrust coefficient for installed propeller versus advance coefficient. Tunnel speed is 20 knots. Reynolds number = 64 million .....	36
4.9 Pressure coefficient distribution across bare hull .....	39
4.10 Skin friction coefficient distribution across bare hull.....	39
4.11 Xy-plane axial velocity contour, case bare.4d; Spalart-Allmaras .....	40
4.12 Xy-plane axial velocity contour, case bare.2d; $q-\omega$ .....	40
4.13 Velocity contour at $x/L = 0.9987$ in yz-plane, case bare.4d; Spalart-Allmaras .....	41
4.14 Velocity contour at $x/L = 0.9987$ in yz-plane, case bare.2d; $q-\omega$ .....	41
4.15 Xy-plane axial velocity contour, $J = 0.95$ ; Spalart-Allmaras .....	42

FIGURE	Page
4.16 Xy-plane axial velocity contour, $J = 0.95$ ; $q-\omega$ .....	43
4.17 Yz-plane axial velocity contour, $J = 0.95$ ; Spalart-Allmaras .....	43
4.18 Yz-plane axial velocity contour, $J = 0.95$ ; $q-\omega$ .....	44
4.19 Computational drag coefficient versus Reynolds number, three length scales. Normalized by length .....	45
4.20 Skin friction coefficient distribution along bare hull for various Reynolds numbers .....	48
4.21 (a) $J = 0.95$ , $Re = 2.4$ million (b) $J = 0.98$ , $Re = 32$ million .....	49
4.22 (a) $J = 0.95$ , $Re = 2.4$ million (b) $J = 0.98$ , $Re = 32$ million .....	50
4.23 (a) Pressure contours for stern region at $Re = 16$ million (b) Pressure contours for stern region at $Re = 64$ million .....	51
4.24 Influence of stern appendages and propeller on the hull velocity field .....	53
4.25 Upstream influence of the stern appendages and propeller .....	53
4.26 Downstream influence of the stern appendages and propeller .....	54
4.27 Thrust coefficient comparison between P4381 mounted on appended LCC hull and isolated P4381; $Re = 32$ million .....	62
4.28 Validation of crashback computations cback1.x and cback2.x. Experimental has 15% error bars .....	63
4.29 Swirl parameter isosurface showing the instantaneous ring vortex structure .....	64

FIGURE	Page
4.30 Ring vortex in relation to submarine .....	65
4.31 Particle trace of ring vortex.....	65
4.32 Yz-plane axial velocity contour comparison .....	66
4.33 Xy-plane axial velocity contour comparison .....	66
4.34 Numerical artifact in high Reynolds number flow boundary layer. $Re = 1$ billion .....	68
4.35 Hull curve and 2 <sup>nd</sup> derivative. Large plot is close up of stern region. ....	69
B.1 Velocity contours; 5 knot tunnel speed $Re = 16$ million .....	81
B.2 Velocity contours; 10 knot tunnel speed; $Re = 32$ million .....	82
B.3 Velocity contours; 15 knot tunnel speed; $Re = 48$ million .....	84
B.4 Velocity contours; 20 knot tunnel speed; $Re = 64$ million .....	85

## CHAPTER I

### INTRODUCTION

Today's submarines travel at speeds in excess of 25 knots and practice extreme maneuvers that push the very limit of their design and structural integrity. It is important to understand the forces encountered when such speeds and maneuvers are executed. There are two ways to obtain this information: experimentation and computation.

One of the difficulties associated with experimentation is the inability to effectively test a full-scale submarine. Experiments must be carried out on a smaller scale and Reynolds scaling used to determine full-scale forces. The largest scale model is a quarter-scale model, but the data from those tests are classified. The largest model scale data available for this study is from a 6% scale model tested at the Large Cavitation Channel (LCC) in Memphis, Tennessee. Reynolds scaling does not account for all the differences in the flow, and with such a large jump between the scales, small uncertainties can create large inaccuracies on the full-scale level.

Another method to determine the forces on a submarine at extreme conditions is to computationally simulate the maneuvers. Computationally simulating such conditions is a relatively new avenue of pursuit and pushes current numerical algorithms to their limits.

### 1.1 Previous Studies

Studies have been performed on both the experimental side and the computational side for fully submerged bodies or submarines. A recent experimental venture used to validate many CFD methods is the Defense Advanced Research Projects Agency (DARPA) funded study of the SUBOFF model [1]. Experiments on the SUBOFF model were performed in the David Taylor Model Basin in 1990. The SUBOFF hull is 14.3 feet long and was tested at a Reynolds number of  $1.4 \times 10^7$ . Force and moment data, as well as pressure and skin friction coefficient distributions, were recorded. The model was tested in several configurations, but all were unpropelled.

The computational investigation of complex hydrodynamic configurations has evolved from CFD studies involving aerodynamic bodies that began in the 1980s. These studies have focused on fully submerged prolate spheroids and SUBOFF configurations because of the availability of the experimental data for validation. Such studies have included force and moment validation [2], and full-scale studies [3]. Little has been done with propelled simulations, and even less with the validation of those simulations. Only within the past five years have propelled studies with the SUBOFF model been investigated. Some work has even involved six-degree-of-freedom simulations [4], but these are still in the development stages. This study is one of the first to validate fully submerged and propelled body simulations with experimental data.



## 1.2 Present Study

This study will focus on several aspects of the problem described above. The propulsor and body interaction will be investigated, as well as the differences in computed flow fields as Reynolds number varies. Turbulence model effects and the integrity of the flow solver to run long duration unsteady problems will also be noted.

There are four major parts to this study: 1) simulation of the flow past an isolated marine propeller with  $0^\circ$  skew, 2) simulation of the flow past a unappended submarine at three different length scales with large corresponding differences in Reynolds number, 3) simulation of the flow past a forward propelled submarine with asymmetric stern appendages at various advance coefficients, and 4) simulation of the flow past a submarine with asymmetric stern appendages in crashback. Reynolds numbers for this study are based on the length of the hull. All simulations are validated by experimental data where available.

The bare hull and isolated propeller studies provide the groundwork to analyze the propulsor and body interaction. The forward propelled and appended submarine cases will be compared against the component cases in order to analyze what effect the impingement of hull boundary layer and appendage wakes on the propeller flow field have on the overall flow field. This relationship is important because it can provide information to better design a quieter submarine.

### **1.3 Chapter Overview**

The next chapter will discuss the experiments and the flow solver that are pertinent to the sufficiency of this study. Chapter III discusses the methodology behind the four major components of this study. Chapter IV presents the results of the study and discusses the relevancy of each. The last chapter discusses the study as a whole. Concluding remarks and recommendations for future work are made.

## CHAPTER II

### BACKGROUND

#### **2.1 Description of the Experiments**

##### 2.1.1 Isolated Propeller

The isolated propeller tests were carried out in the Naval Ship Research and Development Center's (NSRDC) deep-water basin in 1971 [5]. Open water propulsion tests were conducted on four marine propellers with varying degrees of skew. The propeller of interest to the current study is the P4381. The P4381 propeller has five blades with  $0^\circ$  skew.

Forward and backing propulsion tests were performed. The forward tests are of primary interest to this study. A propeller boat was instrumented with a gravity dynamometer for the forward tests. All forward tests were run at a rotational speed of 7.8 rotations per second (rps) with the speed of advance varying from 2.75 fps to 10.14 fps. Thrust and torque data were recorded.

##### 2.1.2 Submarine Models

The 6% scale model submarine experiments were conducted at the Large Cavitation Channel (LCC) in Memphis, Tennessee. Three sets of experiments were performed: bare hull, forward propelled, and crashback. All of these experiments used an existing axisymmetric hull (referred to as the LCC hull), which totaled 22.964 feet in length.

Figure 2.1 shows the layout of the model in the test chamber. The view of Figure 2.1 is from the side. The submarine model was suspended from the ceiling of the test chamber by a strut.

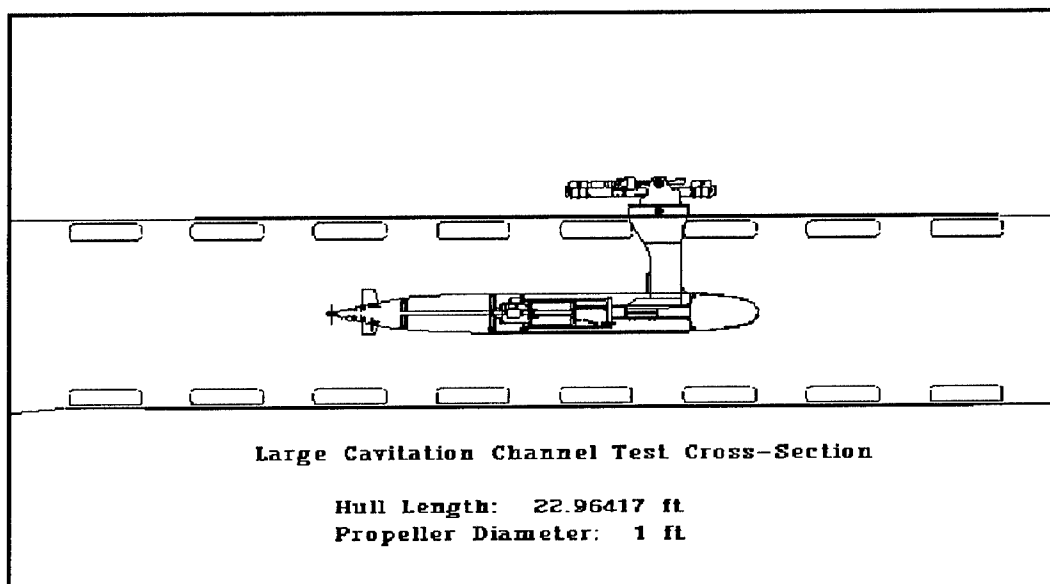


Figure 2.1: Schematic showing orientation and mounting of submarine model.

For the propelled cases, the LCC hull was outfitted with a one-foot diameter P4381 propeller and four asymmetric stern appendages set in a conventional cruciform pattern. The bare hull tests were conducted on the LCC hull without the propeller and stern appendages.

Although the P4381 is a marine propeller designed for surface ships, it was chosen for these experiments because it was readily available, unclassified and previous data were available. The P4381 still maintains many of the characteristics

associated with a submarine propeller. Importantly, it is designed to operate within the boundary layer and wake of a much larger body.

For this particular hull, the one-foot P4381 is slightly undersized and mounted further downstream from the stern appendages than is typical. This does not significantly affect the experiments, but must be considered in analysis.

For the bare hull, 61 runs were made at various Reynolds numbers (based on body length) ranging from  $4.5 \times 10^6$  to  $1.23 \times 10^8$ . A Laser Doppler Velocimeter (LDV) was used to measure the tunnel velocities with the reference velocity taken at  $x/L$  of 0.866, where  $x$  is the axial position and  $L$  is the length of the body. Force and moment data were also recorded.

The forward propelled cases were run at various values of the advance coefficient ( $J$ , defined as  $J = V/nD$  where  $V$  is the forward speed,  $n$  is the propeller rotational speed and  $D$  is the propeller diameter) for four different tunnel speeds: 5, 10, 15, and 20 knots. These speeds yield Reynolds numbers (based on body length) of  $1.6 \times 10^7$ ,  $3.2 \times 10^7$ ,  $4.8 \times 10^7$ , and  $6.4 \times 10^7$ . Thrust and drag measurements were taken for each case. A total of 35 runs were made for the forward propelled submarine. Fourteen of those cases are investigated in this study.

Thirty-one runs were made for the submarine in crashback. The crashback simulation involves forward tunnel speed, but with the submarine propeller rotating in reverse. These cases were run at various advance coefficients for four different tunnel speeds: 2.5, 5, 7.5, 10 knots. These speeds yield Reynolds numbers of  $8 \times 10^6$ ,  $1.6 \times 10^7$ ,  $2.4 \times 10^7$ , and  $3.2 \times 10^7$ . Force and moment data were recorded for the crashback

experiments. Two cases at a Reynolds number of  $1.6 \times 10^7$  and three cases at a Reynolds number of  $3.2 \times 10^7$  are investigated in this study.

Additional bare hull experiments are currently being carried out on a LCC hull model that is 11.278 inches in length and is identical in hull contour to the model used in the LCC tests. These tests are performed in the water tunnel located in Patterson Engineering Laboratories at Mississippi State University. The Reynolds numbers from these tests range from  $7 \times 10^5$  to  $2.5 \times 10^6$ . The purpose of these experiments is to provide an additional Reynolds number range for comparison purposes.

The previous descriptions are intended to provide context for the computational simulations. A complete description of the experiments can be found in [6].

## 2.2 Description of the Flow Solver

The flow solver used in this study is **U<sup>2</sup>NCLE** (*Unstructured Unsteady Computation of Field Equations*). **U<sup>2</sup>NCLE** is a Reynolds-averaged Navier-Stokes (RANS) incompressible flow solver capable of performing viscous, high Reynolds number flow simulations using unstructured grids. In [7] the **U<sup>2</sup>NCLE** solver is demonstrated for large scale meshes, and is shown to be an effective solver for complex hydrodynamic applications.

In this section, the fundamentals behind the flow solver are explained. If greater detail is desired, [8] explains the finer points.

### 2.2.1 Governing Equations

The pseudo-compressibility method is used to put the governing equations into a time-dependent form. This transforms the equations into a hyperbolic system and allows for the use of compressible flow algorithms [9]. The integral form of the Navier-Stokes equations is the basis for finite volume flow solvers [10]. Written below is the conservative integral form of the RANS equations

$$V \frac{\partial \bar{Q}}{\partial t} + \int_{\partial \Omega} F \cdot \hat{n} dl = \int_{\partial \Omega} G \cdot \hat{n} dl \quad (2.1)$$

where  $\hat{n}$  is the outward unit normal to the control volume  $V$ .

Given below are the vector of dependent variables and the components of the inviscid and viscous flux vectors with the pseudo-compressibility factor ( $\beta$ ).

$$Q = \begin{bmatrix} P \\ u \\ v \\ w \end{bmatrix} \quad (2.2)$$

$$F \cdot \hat{n} = \begin{bmatrix} \beta \Theta \\ u \Theta + \hat{n}_x P \\ v \Theta + \hat{n}_y P \\ w \Theta + \hat{n}_z P \end{bmatrix} \quad (2.3)$$

$$G \cdot \hat{n} = \begin{bmatrix} 0 \\ \hat{n}_x \tau_{xx} + \hat{n}_y \tau_{xy} + \hat{n}_z \tau_{xz} \\ \hat{n}_x \tau_{yx} + \hat{n}_y \tau_{yy} + \hat{n}_z \tau_{yz} \\ \hat{n}_x \tau_{zx} + \hat{n}_y \tau_{zy} + \hat{n}_z \tau_{zz} \end{bmatrix} \quad (2.4)$$

The variables in the above equations are normalized by the characteristic length and free stream values of velocity, density, and viscosity. The dependent variables  $u$ ,  $v$ , and  $w$  are the velocity components in the  $x$ ,  $y$ , and  $z$  directions

respectively.  $P$  is the pressure. The unit normal,  $\hat{n}$ , is broken into its  $x$ ,  $y$ , and  $z$  components for the inviscid and viscous flux vectors. The term  $\beta$  in the inviscid flux vector is the pseudo-compressibility factor and is equal to 15 for this study.  $\Theta$  is the velocity normal to the control volume face. The viscous stresses from Equation 2.4 are given as

$$\tau_{ij} = (\mu + \mu_t) \frac{1}{\text{Re}} \left( \frac{\partial u_i}{\partial x_j} + \frac{\partial u_j}{\partial x_i} \right) \quad (2.5)$$

where  $\mu$  is the molecular viscosity and  $\mu_t$  is the eddy viscosity. The Reynolds number is denoted  $\text{Re}$  and is defined as  $LV/v$ , where  $L$  is the length of the body,  $V$  is the forward velocity and  $v$  is the kinematic viscosity of water.

### 2.2.2 Numerical Method

The basic flow solver is a node-centered, finite volume, implicit scheme applied to general unstructured grids with non-simple elements. The solver is based on domain decomposition for concurrent solution within subdomains assigned to multiple processors. This parallelization allows for quick turnaround of a solution.

The basic numerical method involves reconstruction of the solution states, evaluation of the residuals, and time evolution of the solution in each control volume [11]. Reconstruction is done by extrapolating the solution at the vertices to the faces of the surrounding control volume using a higher-order spatial method. The gradients at the vertices are computed using the unweighted least squares method and then the variables at the interface are computed using a first-order Taylor series. The governing equations are discretized using a finite volume technique. The surface integrals from Equation 2.1 are approximated by a quadrature over the surface of the



control volume of interest. The evaluation of the discrete residual is performed separately for the inviscid and viscous terms. After the spatial terms have been discretized, the time derivative is approximated. For the time evolution, a Newton iterative scheme is used. It requires the solution of a sparse linear system at each nonlinear subiteration. A bi-directional Gauss-Seidel algorithm is used to solve the system.

### 2.2.3 Boundary Conditions

All the boundary conditions are dealt with in an implicit manner. The farfield conditions are managed by a characteristic variable reconstruction. Viscous conditions are enforced by modifying the linear system such that no change is allowed in the velocity, and the pressure is driven according to the imbalance in the continuity equation in the boundary control volume.

A symmetry plane boundary condition is dealt with by creating a layer of phantom cells that is a mirror image of the cells inside and connected to the symmetry plane. The control volumes on the symmetry plane are closed and behave just as interior control volumes.

### 2.2.4 Turbulence Models

There are two turbulence models available: 1) the one-equation Spalart-Allmaras model [12], and 2) the two-equation  $q-\omega$  model [13]. The Spalart-Allmaras model formulates a transport equation for the turbulent Reynolds number, which is then related to the turbulent viscosity. The  $q-\omega$  model uses a transport equation each for the velocity scale and length scale to specify the distribution of the eddy viscosity.

Although the two equation  $q-\omega$  model is very robust and more accurate, it is also more expensive to run due to the number of equations to be solved. The  $q-\omega$  model is also very sensitive to the surface grid, while the Spalart-Allmaras model is more forgiving. For this study, both turbulence models are employed.

## CHAPTER III

### DESCRIPTION OF COMPUTATIONAL CASE PREPARATION

The flow around a powered submarine is very complex due to the interactions among the hull boundary layer, appendage boundary layers and wakes, and the propulsor. This study breaks the problem down into bare hull, isolated propeller and appended and powered simulations. The flow fields about the bare hull and isolated propeller will be analyzed to determine which flow characteristics are unique to the components. The flow field about the powered and appended submarine will be compared against the component flow fields to determine what effect the impingement of the hull/appendage flow on the propeller flow has on the overall flow field.

Another aspect of this study is the comparison of the hull (bare as well as appended) flow field at three different length scales to examine differences in flow characteristics. It has been observed in previous studies that significant differences in the submarine flow fields exist between model and full scale flows [14][15]. It is also noted that the differences are widespread and not localized to a specific location. This leads to the need to fully simulate the full scale Reynolds number flow in order to investigate the flow in its entirety.

Several simulations are computed to provide the groundwork for the above analyses. The LCC model and isolated propeller simulations are corroborated with available experimental data, thus serving to further validate the flow solver.

The simulation of a submarine in crashback serves as the ultimate test case for this study. It demonstrates the integrity of the code to run long duration unsteady simulations yielding results in good agreement with experimental data. It also underscores the level of complexity the interaction of the component flows can attain. It is hoped that the information gleaned from the crashback simulations will yield new insight into the nature of the flow. It should be noted that for this study, all simulations are computed at zero angle of attack.

The table in Appendix A breaks down all of the cases and gives the conditions for each. In the remainder of this report, the cases will be referred to by the designation given to them in Appendix A. Multiple cases are referred to by their root case name, followed by an x that represents the alphanumeric that designates a specific case, i.e. case.1x stands for case.1a, case.1b, case.1c, etc.

### **3.1 Bare Hull**

The bare hull simulations provide a baseline flow field for the propulsor and hull interaction study. These cases are also computed for three different length scales for the scaling analysis. The three length scales correspond to the 11.278-inch small model tested in Patterson labs, the 22.9614-foot large model tested in the LCC, and a 383.5-foot full-scale submarine [16]. Figure 3.1 shows the bare hull geometry configuration.

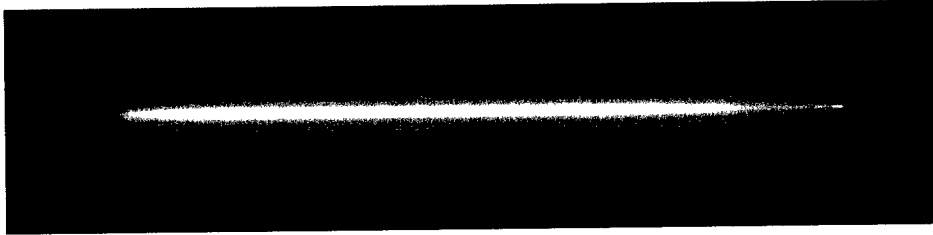


Figure 3.1: Bare LCC hull.

The first step in performing these simulations is to build an accurate computational model for the hull. Geometry preparation and surface grid generation are performed using SolidMesh [17] with AFLR (Advancing Front/Local Reconnection) surface grid generation [18]. The computational grids are multielement unstructured meshes generated with an advancing normal methodology for the boundary layer elements, and an AFLR methodology for the isotropic volume elements as given in [18]. For clarity of discussion, the axis orientation for the submarine is as follows: x-axis is from nose to tail, y-axis is through the dorsal (top) of the hull and the z-axis is through the port side (left looking forward).

A composite unstructured/structured surface grid is generated for the LCC hull and a multielement unstructured mesh is generated for the volume. A composite grid is often used in cases where there is a large axisymmetric section that does not require high resolution. Usually, with a reasonable aspect ratio (less than 5) for the structured elements, the point spacing will be broader than with all unstructured elements.

Figure 3.2 shows the surface grid with the structured grid elements making up most of the hull. The sections in red represent the unstructured portions, and the section in blue represents the structured portion of the surface grid.

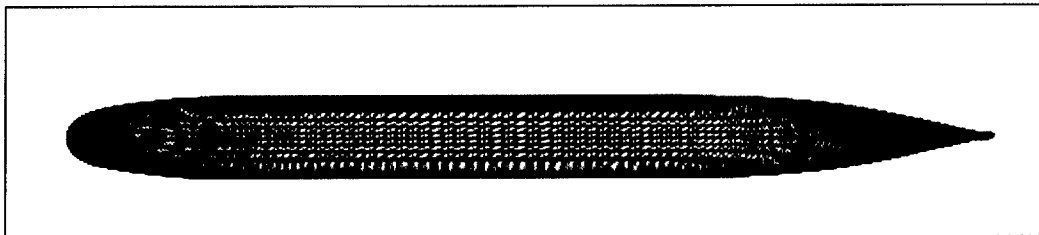


Figure 3.2: Composite unstructured/structured surface grid.

The symmetry of the body is exploited to save points, and consequently, computational time. A symmetry plane is used to solve for only half of the hull. The force and moment data are multiplied by a factor of two to take this into consideration.

One grid is used for all Reynolds numbers for each of the three length scales. The initial absolute off-wall spacing of the volume grid from the body is  $5 \times 10^{-7}$ , which yields a  $y^+$  distribution of approximately 1 over the entire hull for the high Reynolds number cases. This indicates good viscous sublayer resolution. The volume grid around the stern of the sub body is shown in Figure 3.3.

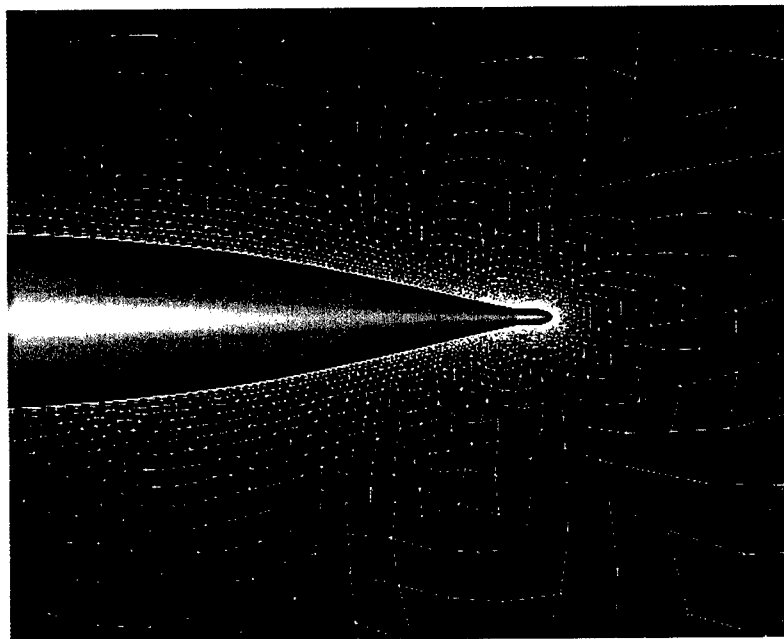


Figure 3.3: Volume element distribution about the LCC stern.

For the Reynolds scaling analysis, the axial force coefficient or drag coefficient is of major concern. For the bare.2x cases, the drag coefficient is validated with experimental data [Bridges]. The sensitivity of axial force (drag) to the streamwise grid density is explored by building two additional grids: a fully structured grid and a fully unstructured grid. These grids, along with the structured/unstructured composite grid, provide three different axial densities and topologies to examine the sensitivity of axial drag. Table 3.1 gives a breakdown of the grid statistics. It is noted that the fully unstructured and the unstructured/structured composite grid have about the same number of points.

Table 3.1: Grid statistics.

<i>Grid Type</i>	<i>Nodes</i>	<i>Tetrahedra</i>	<i>Pyramids</i>	<i>Prisms</i>	<i>Hexahedra</i>
<b>Unstructured</b>	397302	410857	419	617760	0
<b>Unstructured/Structured</b>	410715	363008	434	662984	0
<b>Structured</b>	1181037	0	120	8160	1143780

All bare hull simulations were run using local time stepping and converged to obtain steady-state solutions. Runs are made with both turbulence models. Specific run details are outlined by case in Appendix A.

The bare hull cases were typically run for 1500 time steps. As seen in the figures below, convergence was apparent by 500 time steps, but the solution was run further for insurance. All simulations were carried out using Lakota, a super cluster of 256 dual gigahertz processor Pentium III computers. The average computation time for the bare hull computations was approximately 10 hours.



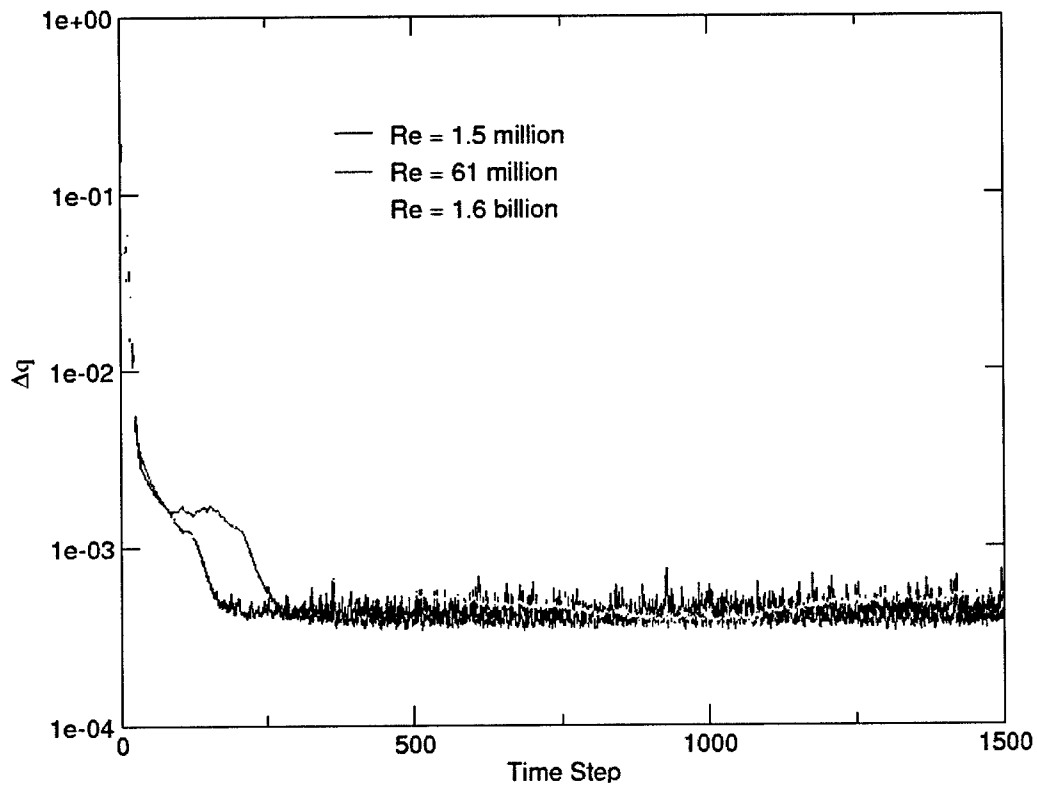


Figure 3.4: Convergence history by scale for  $q$ - $\omega$  turbulence model.

Figure 3.4 shows the  $q$ -vector convergence histories that were obtained for the various Reynolds numbers using the  $q$ - $\omega$  turbulence model. As Reynolds number increases, more time is required for convergence.

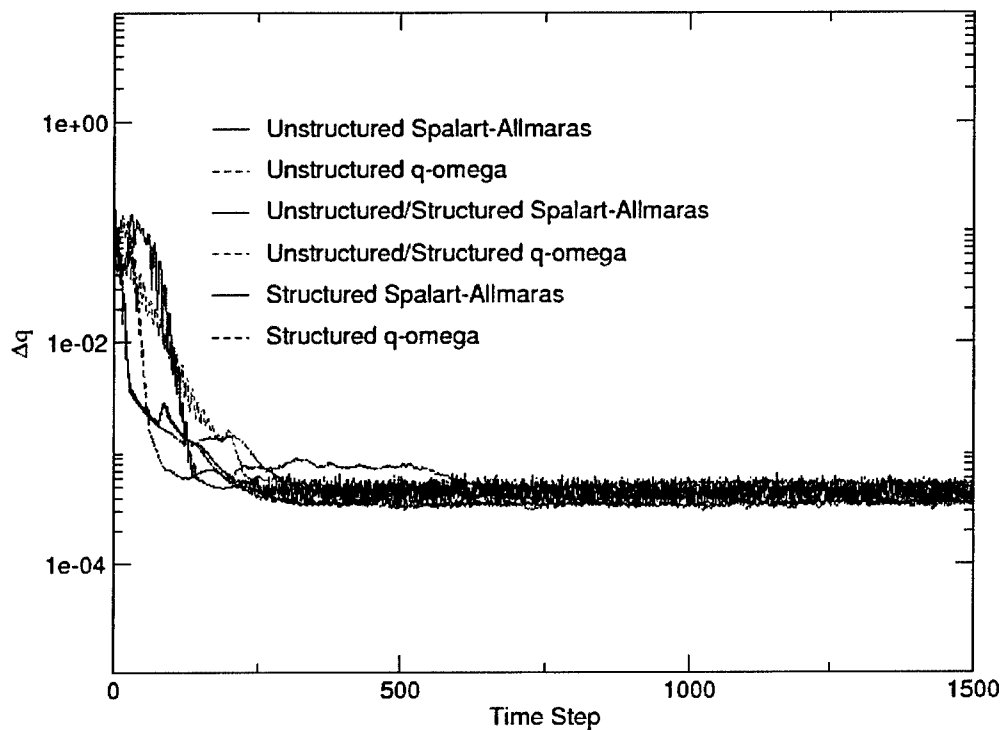


Figure 3.5: Convergence history by grid type and turbulence model.

It is noted from Figure 3.5 that all of the grids converge at about the same rate. The noise in each of the residuals is due to the use of a mean flow limiter to help with solver stability. It is also noted that there is no significant difference in the convergence between turbulence models. Although convergence appears to be relatively better with the structured grid, it requires more computational resources. The typical load per processor is approximately 100,000 grid points. The structured grid requires 12 processors as opposed to the four required by the unstructured/structured and unstructured grids.

An additional case, denoted apphull.1, was run to isolate the effects of the stern appendages on the flow field. Figure 3.6 shows the volume grid in the vicinity of the stern appendages. From this picture, the asymmetry of the rudders can be seen. Boundary layer clustering is also clearly visible.

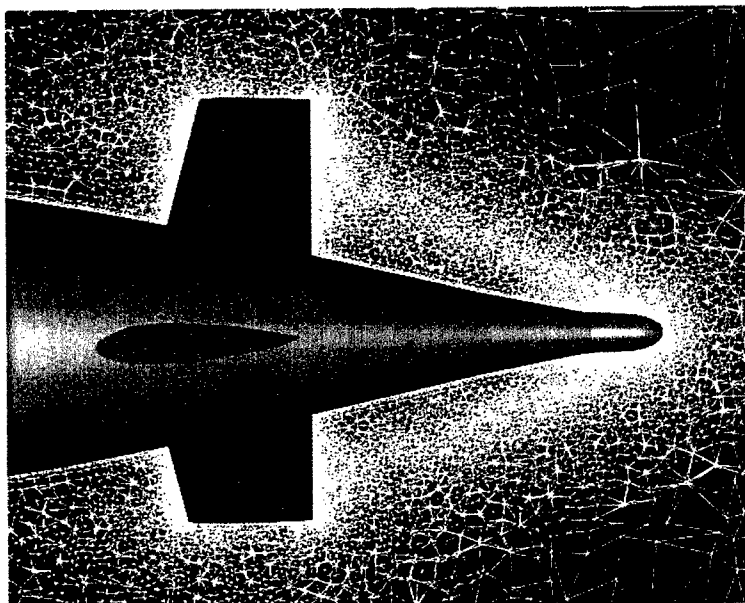


Figure 3.6: Volume element distribution in the vicinity of stern appendages.

### 3.2 Isolated Propeller

Isolated propeller studies are performed using the P4381 marine propulsor. The five bladed propeller is mounted on a generic hub. Figure 3.7 shows the geometry used for the isolated simulations. An unstructured, multielement mesh is generated for the propeller geometry. This mesh consists of 2.4 million nodes, 16,000 pyramids, 2.1 million prisms, and 7.9 million tetrahedra.

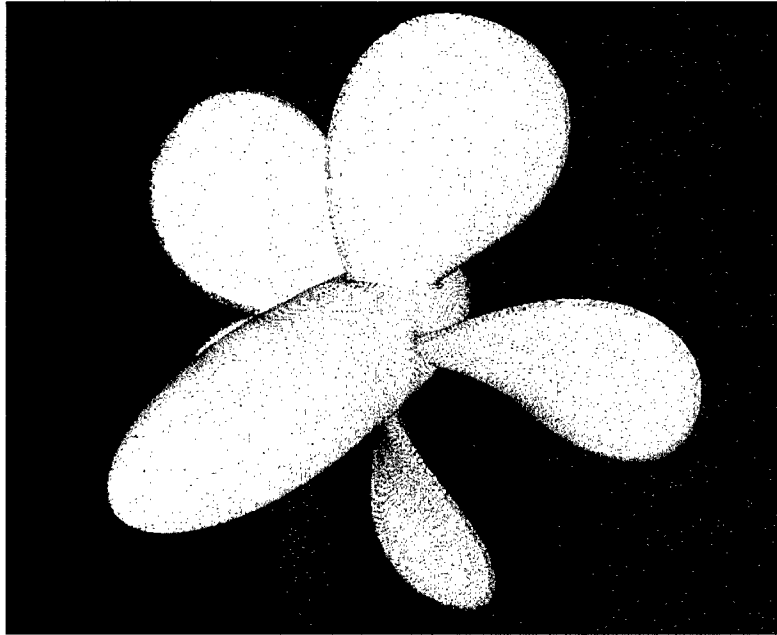


Figure 3.7: Geometry and surface grid of the isolated P4381.

The isoprop1.x and isoprop2.x cases are used to validate the simulation and compare the turbulence models. The isoprop3.x cases are run at a Reynolds number of 32 million for the advance coefficients that correspond to the 10-knot forward propelled cases from the LCC experiments. The thrust coefficients and velocity profiles from these cases will be compared to the fwdsbub.xx cases.

The reference velocity used for non-dimensionalization of variables for flow solver input is typically the free stream velocity,  $U_\infty$ . For the isolated propeller cases, the typical non-dimensionalization resulted in very large tip speeds with respect to the forward speed. This created stability problems with the solver. To make the input values more manageable for the solver, the rotational tip speed was used as the reference velocity.

The isolated propeller cases were run unsteady with local time stepping for approximately 300-400 time steps. The solver was then switched to minimum time stepping that corresponded to  $1.5^\circ$  of rotation per time step and run for an additional 600-700 time steps. As seen in the given force history (Figure 3.8), around time step 700 the solution has reached steady state. The average computational time required was approximately 23 hours.

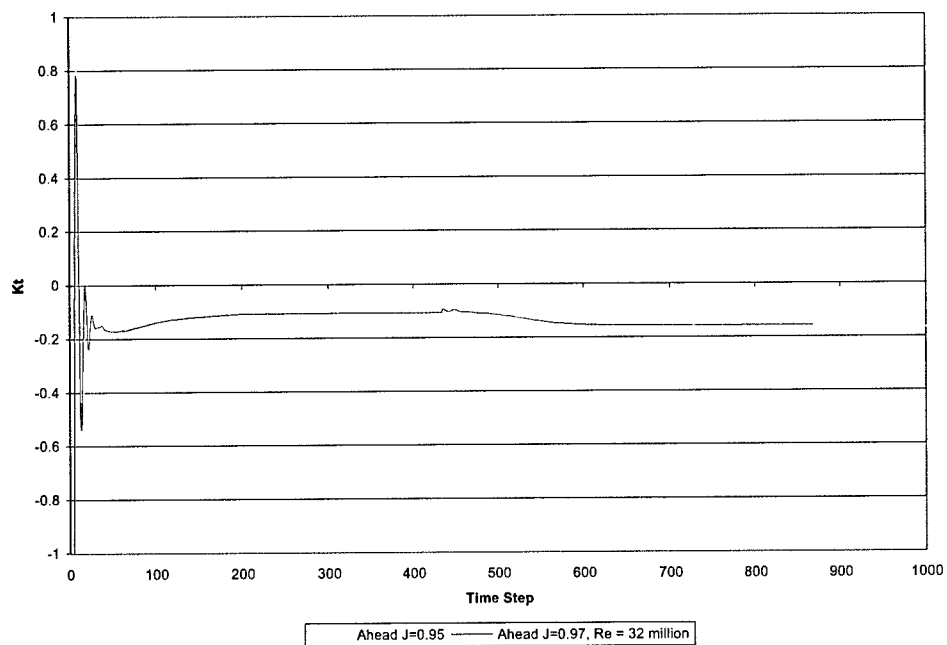


Figure 3.8: Force history for isolated propeller thrust coefficient.  $J = 0.95$  correlates to experimental data;  $J = 0.97$  correlates to hull/propulsor study.

### 3.3 Forward Propelled Appended Submarine

The forward propelled simulations model the composite flow field generated by an appended and propelled submarine in straight and level forward motion. The model for these simulations is the LCC hull with four asymmetric stern appendages and a one-foot P4381 propeller. Figure 3.9 depicts the geometry just described.

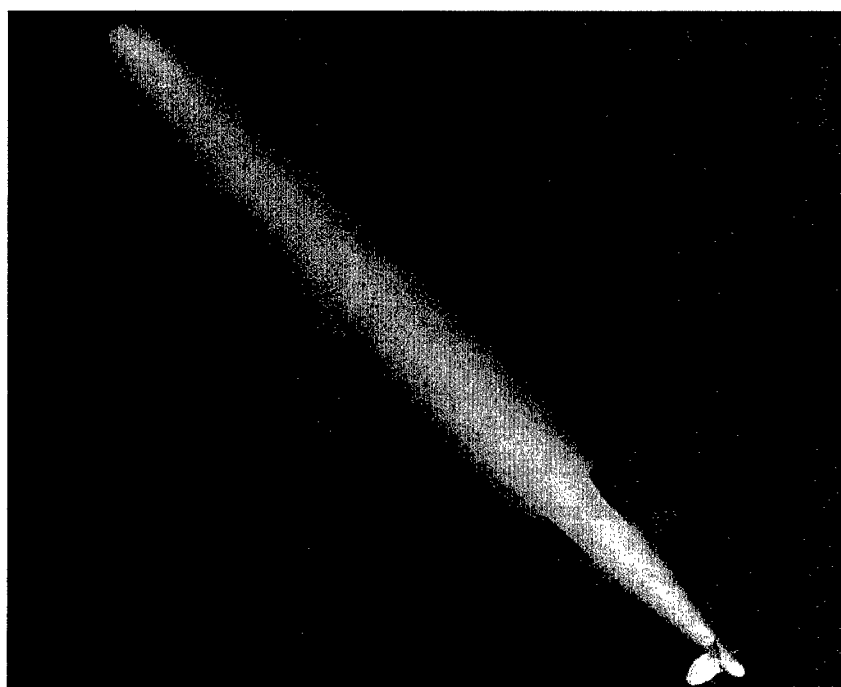


Figure 3.9: Appended LCC Hull with P4381 Propeller

An unstructured grid is generated to model the geometry used in the LCC experiments minus the support strut. The grid is approximately 3.1 million points and yields a viscous sublayer resolution for all four Reynolds numbers of  $y^+$  of approximately 1. The unstructured mesh consists of 19500 pyramids, 4.3 million prisms, and 5 million tetrahedra. The volume grid in the vicinity of the stern

appendages is shown in Figure 3.10. This figure shows the point clustering in the boundary layer region.



Figure 3.10: Volume grid in the vicinity of the stern appendages.

Typical nondimensionalization by free stream quantities is used for flow solver inputs. The propelled submarine cases are run with local time stepping for approximately the first 400 time steps. Time stepping is then switched to minimum with step size set to  $1.5^\circ$  rotation per time step. The rotating propeller is handled by locally regenerating the grid in the vicinity of the propeller for each time step. This simulates an actual rotating propeller on a fixed body. Three Newton iterations are used to ensure time accurate solutions. These cases are run for 800-1000 time steps where a periodic state has been well attained. The force history given in Figure 3.10 shows convergence to a periodic state for cases fwdsub.1c, fwdsub.2d, fwdsub.3c and fwdsub.4c. The cases are all for an advance coefficient of  $J \approx 1$ . Note that at a similar advance coefficient, the solutions converge to a similar thrust coefficient.

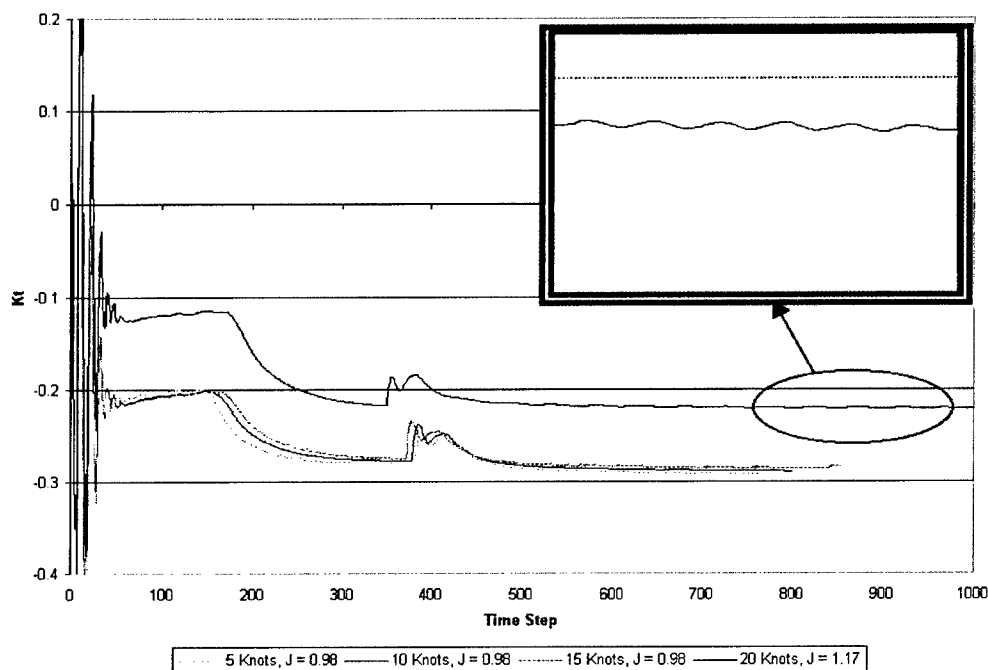


Figure 3.11: Force history for forward propelled submarine,  $J \approx 1$ .

The inset depicts what is meant by periodic state. Due to the unsteady nature of a rotating propeller, the thrust coefficient will not converge to a constant value but will converge to a periodic pattern about a mean value. To allow for this, force coefficients are averaged over the last propeller revolution.

It should be noted that due to the orientation of the computational model (x-axis from nose to tail), thrust is shown as negative and drag is shown as positive. Typical sign designations of thrust as positive and drag as negative are applied for the results section.

Utilizing 31 processors, the computation time required per time step averaged 1.25 minutes. This totaled to 23-26 hours of total run time for a converged solution.



### 3.4 Appended Submarine in Crashback

The crashback maneuver in this study is a forward moving submarine with the propeller rotating in reverse. This results in a very unsteady flow with the establishment of an asymmetric ring vortex around the propeller and a nonuniform pressure distribution on the propeller blades. The complexity and the unsteadiness of this flow make it a particular challenge to model numerically.

Of utmost importance is the accuracy of modeling this flow. Crashback maneuvers put the submarine under large forces and high stress, and complicate the issue of controllability. The understanding of these forces and stresses, and the physics of the ring vortex can greatly aid in the effective design and safety of a submarine.

Crashback is difficult to analyze experimentally. The flow's unsteadiness makes Fourier analysis difficult, and complicates long duration testing. It is also hard to simulate the deceleration that occurs during crashback. If computational simulation can yield accurate results, it simplifies the problem of data acquisition and generates more data.

The grid used for the forward propelled cases is used for the crashback simulations. The major difference between the crashback and forward propelled simulations is the direction of propeller rotation. The crashback cases also require a considerable amount of time to converge to a quasi-periodic state, if they ever converge. These cases are run long duration for 18-20 propeller revolutions. Previous studies have only run 8-10 propeller revolutions, so this pushes the limits of the flow

solver. Computation time per time step averages 1.25 minutes. The total run time for a crashback simulation is approximately 120 hours for the super cluster described previously. Figure 3.12 shows the force history for a representative crashback solution. Notice that the switch from local to minimum time stepping occurs around time step 400 and convergence is apparent after 3000 time steps.

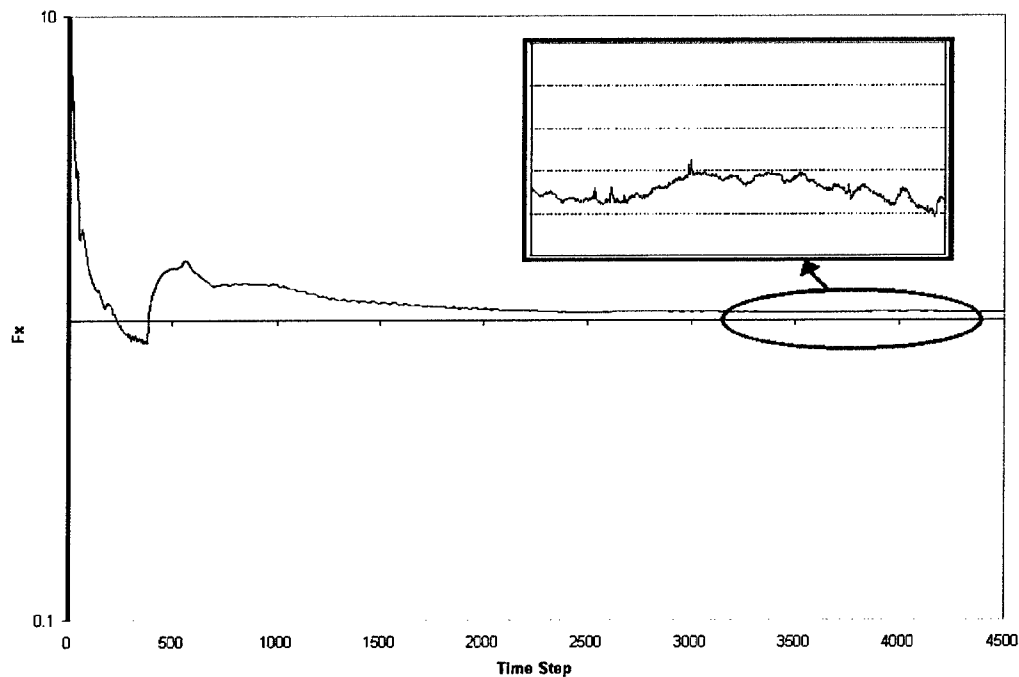


Figure 3.12: Force history for crashback showing total force in the x-direction, case cbsub.2b.

## CHAPTER IV

### DISCUSSION OF RESULTS

The first step in evaluating the computational results is to validate them with available experimental data. The next section presents the validation of the bare hull, isolated propeller, and forward propelled simulations with the available experimental data described in Section 2.1. A comparison of the two turbulence models is then given. The real essence of this chapter lies in Sections 4.3 and 4.4 where Reynolds scaling and hull/propulsor flow interaction is discussed. Section 4.5 discusses the results of the crashback simulation and presents a few of the more interesting flow characteristics. The last section of this chapter discusses possible sources of error for the computational results.

#### **4.1 Validation of Computational Results**

Drag coefficient is of paramount interest in the bare hull simulations. Theoretically, as the Reynolds number increases, the drag coefficient should decrease. This occurs because the boundary layer becomes thinner with increase in Reynolds number, thus diminishing the effective contour the flow sees. As shown in Figure 4.1, this trend holds true for the computational as well as the experimental results.

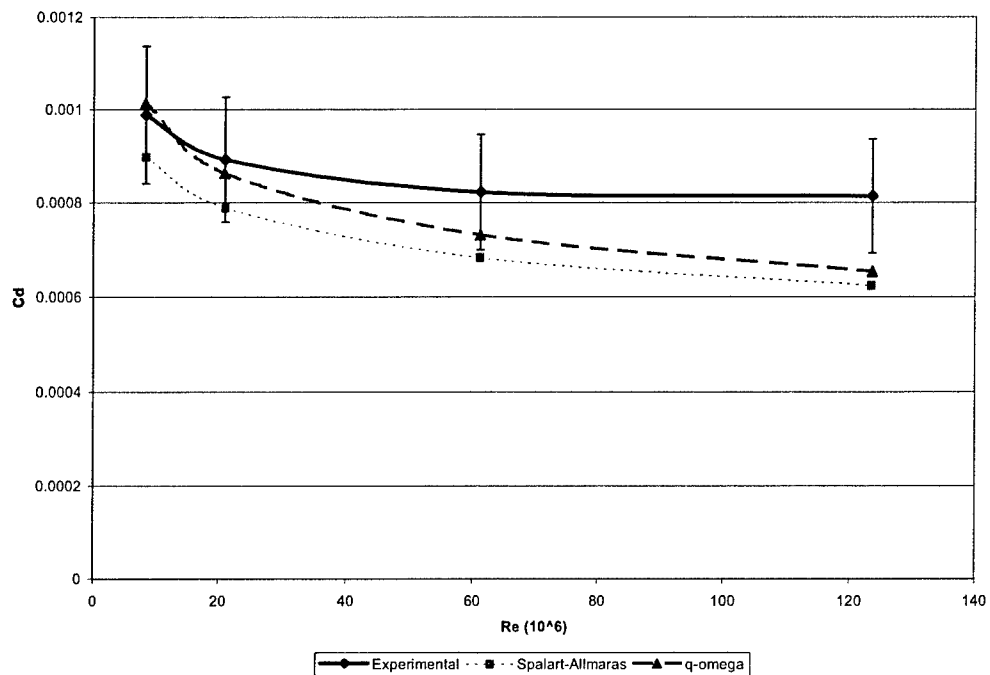


Figure 4.1: Drag coefficient versus Reynolds number with 15% error bars. LCC model scale = 22.964 feet. Normalized by length.

It is also noted from Figure 4.1 that the agreement between the computational results and the experimental results degrades with the increase in Reynolds number. A potential explanation for this is discussed at the end of this chapter with possible sources of error.

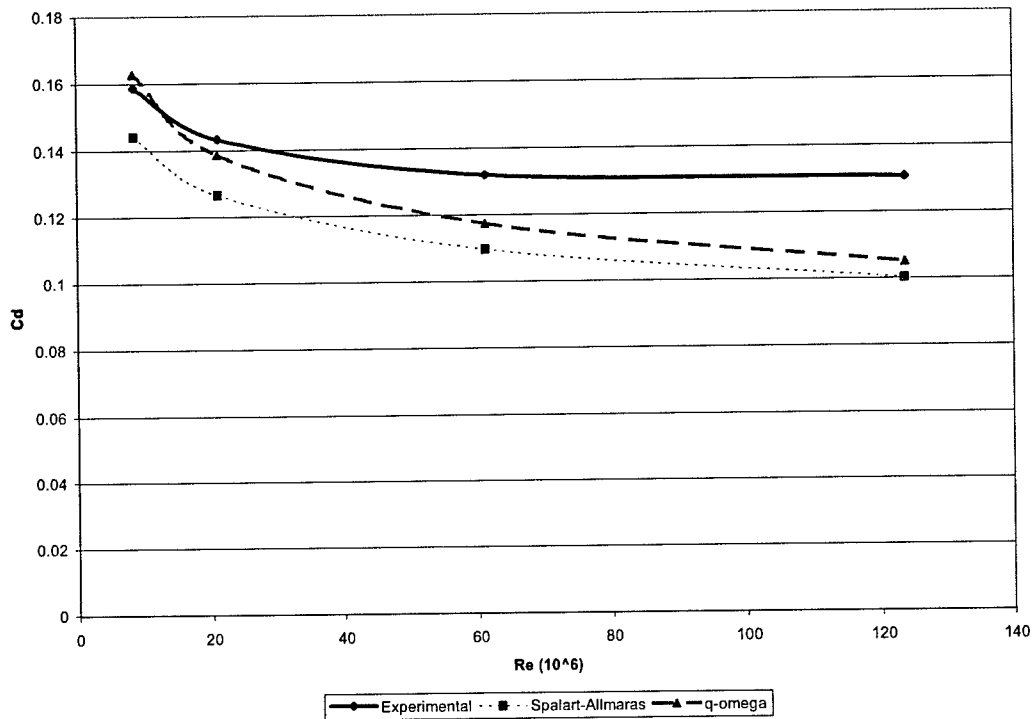


Figure 4.2: Drag coefficient versus Reynolds number. LCC model scale. Normalized by projected frontal area.

Figure 4.2 is similar to Figure 4.1, except that the drag coefficient is normalized by projected frontal area rather than hull length. The same trend is apparent in both Figures. Drag coefficient decreases with Reynolds number, and the agreement between the experimental and computational results degrades with increase in Reynolds number.

The drag coefficients from the bare.2f, bare.4f, bare.5a, bare.5b, bare.6a, and bare.6b cases are compared against the experimental drag coefficient in Table 4.1. The drag coefficients are normalized by hull length. The percent contribution from viscous forces to the drag coefficient is also given. The large viscous contribution

illustrates the need to include the viscous terms in the computation of these simulations despite the increased computational cost.

Table 4.1: Drag coefficient comparison between grids and turbulence models.

<i>Case Name</i>	<i>Drag Coefficient</i>	<i>% Viscous Forces</i>
Experimental	0.0008274	-----
bare.2f	0.0006546	84
bare.4f	0.0006254	83.5
bare.5a	0.0005838	89.5
bare.5b	0.0005816	88
bare.6a	0.0006252	82
bare.6b	0.0006458	83.5

The tightest axial spacing and boundary layer resolution is with the structured grid, although it is noted that the structured grid had the poorest agreement with the experimental data. The structured grid was also run with a structured flow solver using the k- $\epsilon$  turbulence model [ramesh]. The drag coefficient computed was 0.00056. The computational drag coefficients are consistently low. Three different grid topologies and densities, three different turbulence models, and two different flow solvers were used to investigate this phenomenon. Further investigation is warranted, but is beyond the scope of this study. The unstructured/structured results had the best agreement and will be used in further analyses.

The next two plots show the agreement between the computational and experimental results for thrust and torque coefficients for the isolated propeller.

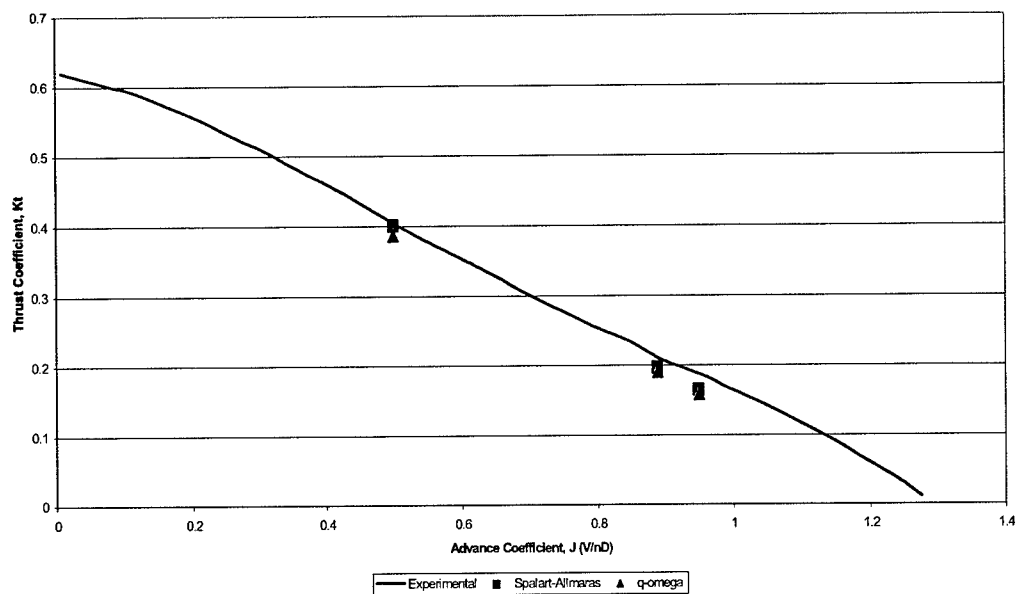


Figure 4.3: Validation of thrust coefficient for isolated propeller.

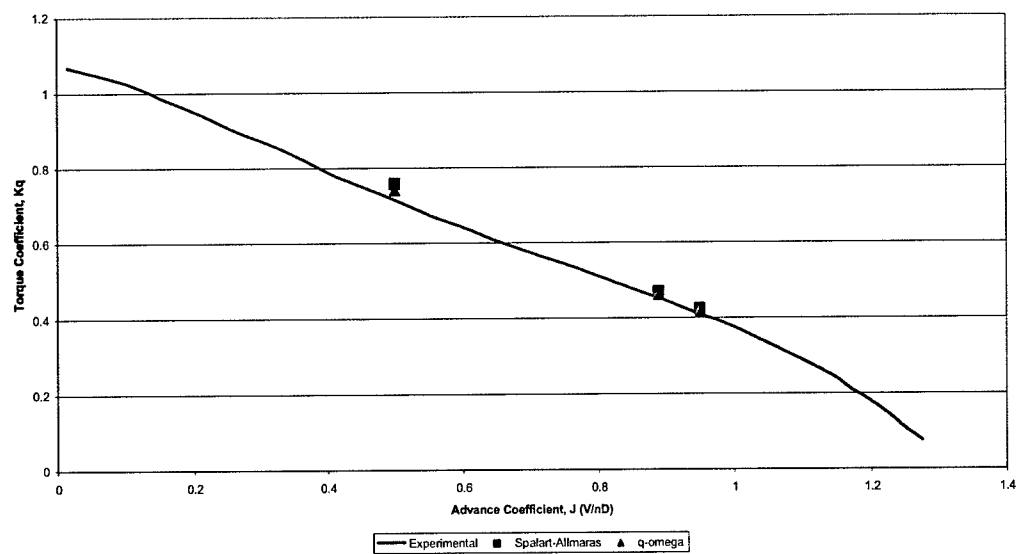


Figure 4.4: Validation of torque coefficient for isolated propeller.

Although, a discussion on the turbulence models follows later, it is noted from these plots that the Spalart-Allmaras one equation turbulence model maintains better agreement with the experimental data for the thrust coefficient. For the torque coefficient, the  $q-\omega$  two-equation turbulence model has better agreement with the experimental data. However, there is not a significant difference between either turbulence model.

With good agreement for the bare hull and isolated propeller computations, the forward propelled cases are next. Excellent agreement with the experimental data is exhibited by all forward cases. Some difference is noted for the higher advance coefficients.

The next four plots show the propeller thrust coefficient. The computational data are plotted against the experimental data. Four tunnel speeds are given with varying advance coefficients for each. The design advance coefficient for the P4381 is  $J = 0.889$ . It is clear that performance degrades with increase in advance coefficient, and for advance coefficients less than the design advance coefficient, no real advantage is gained because the thrust curve begins to flatten out. It is noted that the propeller actually produces drag at the higher advance coefficients. Axial velocity contours can be found in Appendix B for each speed and advance coefficient.



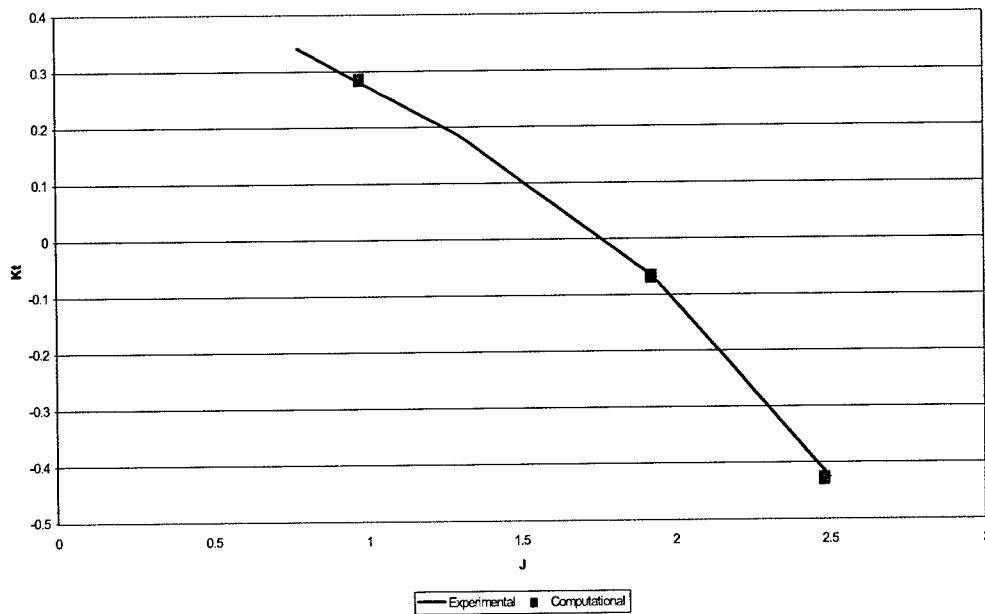


Figure 4.5: Thrust coefficient for installed propeller versus advance coefficient. Tunnel speed is 5 knots. Reynolds number = 16 million.

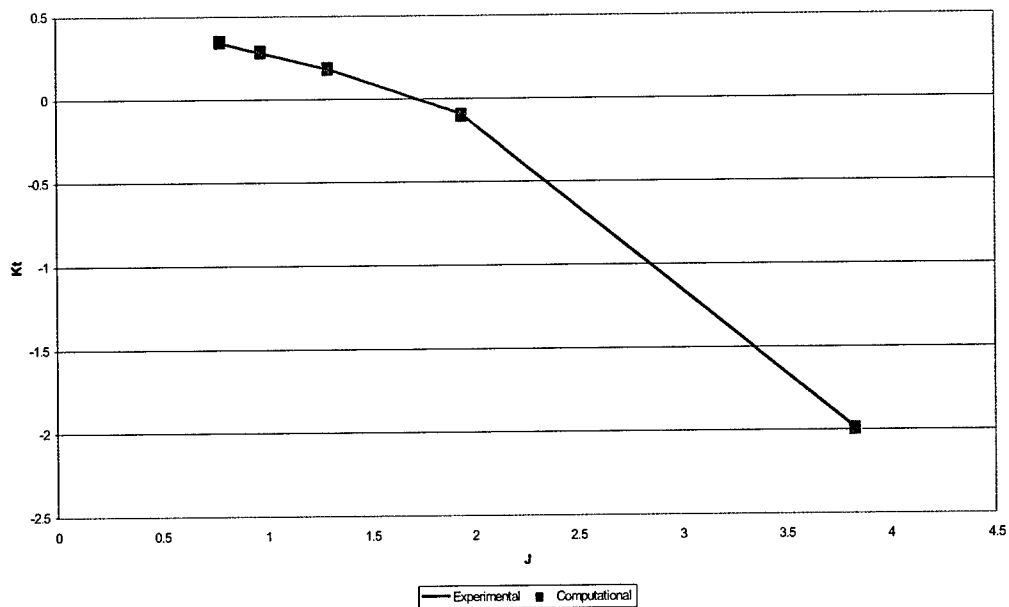


Figure 4.6: Thrust coefficient for installed propeller versus advance coefficient. Tunnel speed is 10 knots. Reynolds number = 32 million.

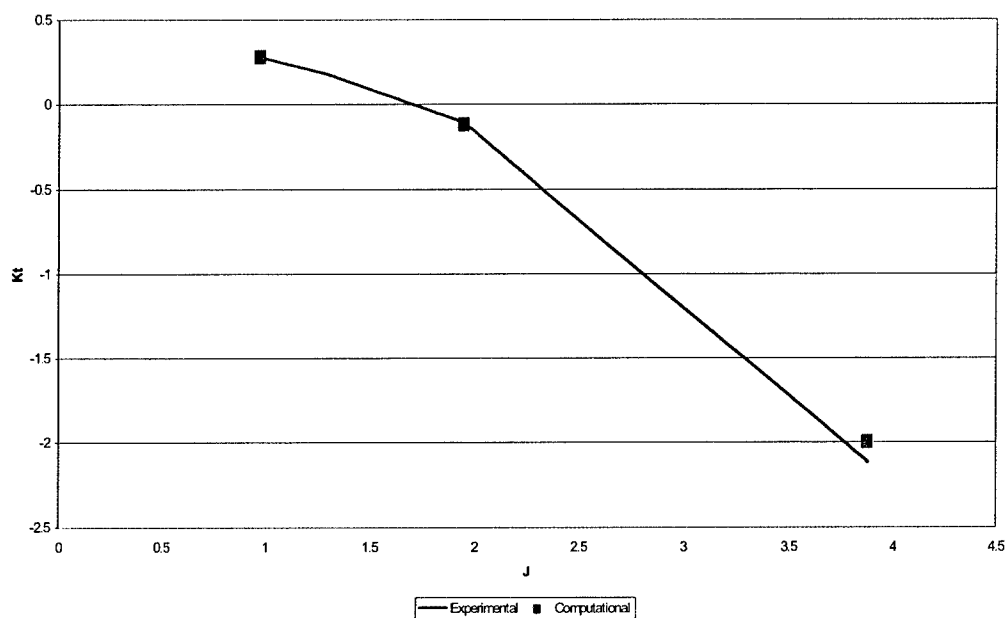


Figure 4.7: Thrust coefficient for installed propeller versus advance coefficient. Tunnel speed is 15 knots. Reynolds number = 48 million.

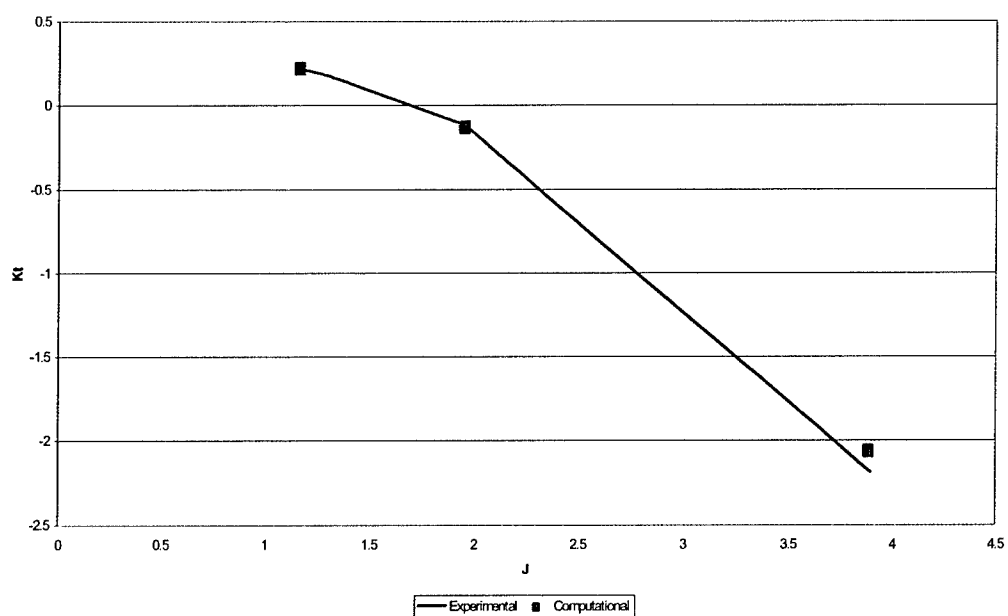


Figure 4.8: Thrust coefficient for installed propeller versus advance coefficient. Tunnel speed is 20 knots. Reynolds number = 64 million.

## 4.2 Turbulence Model Comparisons

The choice of turbulence model has a direct effect on the accuracy of the solution. Chapter 2 gave a description of the two turbulence models available for use. In general, the Spalart-Allmaras turbulence model is more forgiving in relation to the computational geometry. The  $q-\omega$  model is more accurate, but due to number of equations to be solved is more expensive. It also tends to be very sensitive to the quality of the surface grid.

It was found that the propelled simulations would not run using the  $q-\omega$  model. It is thought that the surface grid on the propeller is the culprit. The propeller blade tips are very fine and require many points for resolution. Surface triangulation by the grid generator sometimes creates minute 'divots' in the surface topology, particularly for sharp edges. Due to the sensitivity of the  $q-\omega$  model, these 'divots' appear to be part of the geometry itself. In trying to account for these geometry characteristics, the turbulence model becomes unstable and blows up in relatively short order. With special attention paid to the propeller tips, the geometry could be refined so the  $q-\omega$  model could be used. This was deemed unnecessary since the Spalart-Allmaras model yielded accurate results. Also, the amount of time required, and the additional computational resources that would be needed were considered too great for this study. As shown in the previous section, there is not a significant difference between the results from either model. The agreement between computational and experimental results for the forward propelled solutions is extraordinary.

Both models were used for the isolated propeller and bare hull simulations. As stated earlier, both models show excellent agreement with the experimental data for the isolated propeller. For the bare hull simulations, the  $q-\omega$  has slightly better agreement with the experimental results, particularly at the lower Reynolds numbers. This agreement degrades with the increase in Reynolds number. For the higher Reynolds numbers, the results from both turbulence models are off by 15-20%.

It is important to understand the differences in the flow field due to the turbulence models. The Reynolds scaling study uses the  $q-\omega$  model since it had the best agreement with the experimental data. The hull/propulsor interaction study uses the Spalart-Allmaras model because of its use in the propelled simulations. Given below are the pressure and skin coefficient distributions across the hull for each turbulence model. The first plot, Figure 4.9, shows that both turbulence models yield approximately the same pressure distribution. Although in Figure 4.10, it is clear that the Spalart-Allmaras model has a lower skin friction distribution than does the  $q-\omega$  model.

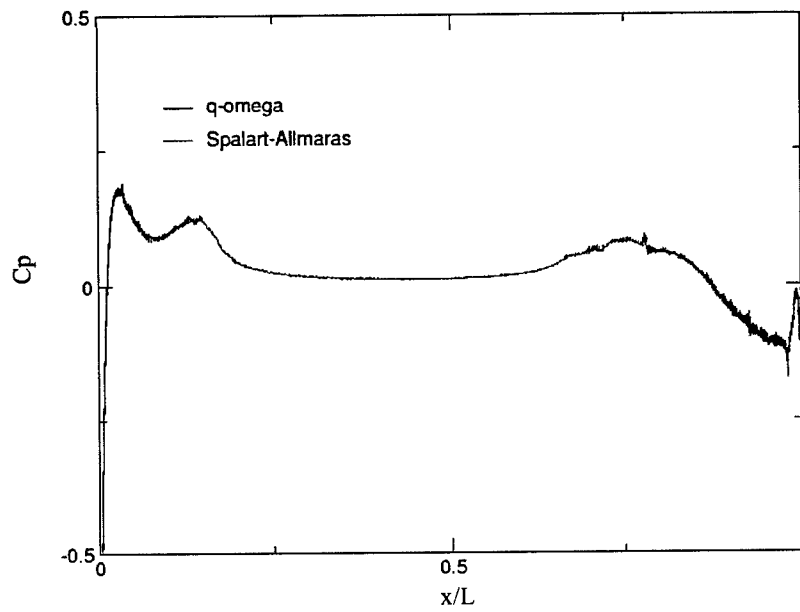


Figure 4.9: Pressure coefficient distribution across bare hull.

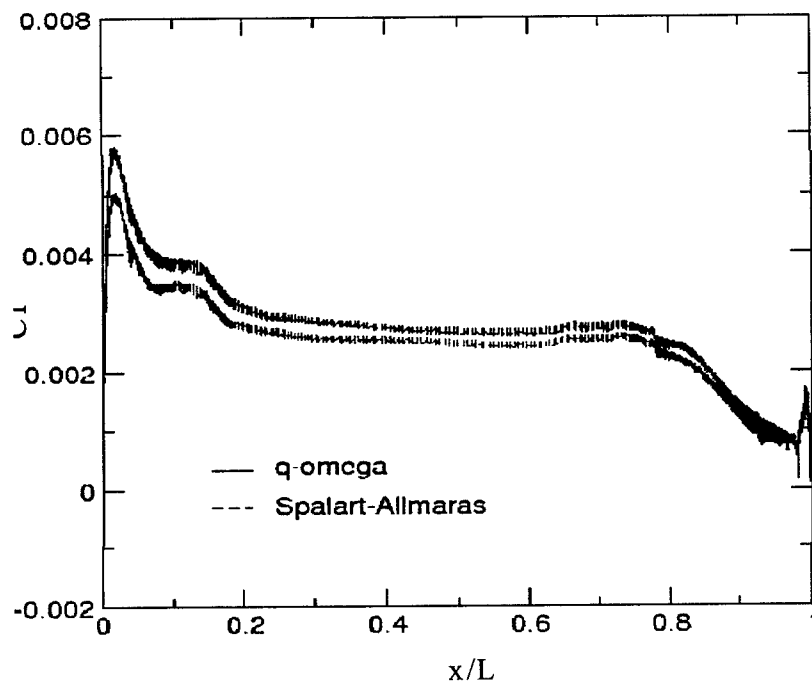


Figure 4.10: Skin friction coefficient distribution across bare hull.

Figures 4.11 and 4.12 show the xy-plane axial velocity contours at a Reynolds number of 32 million for each turbulence model.

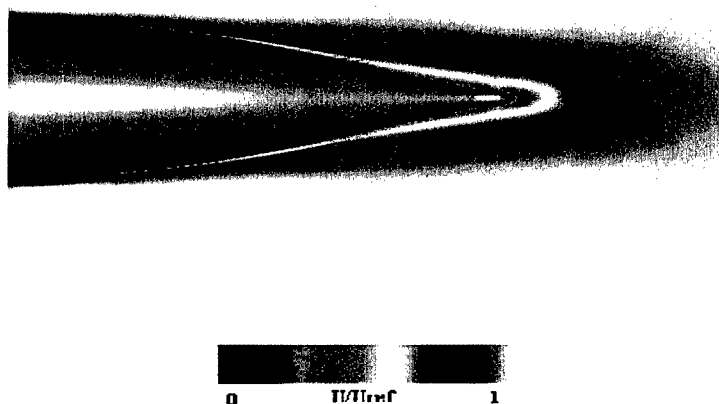


Figure 4.11: Xy-plane axial velocity contour, case bare.4d; Spalart-Allmaras.

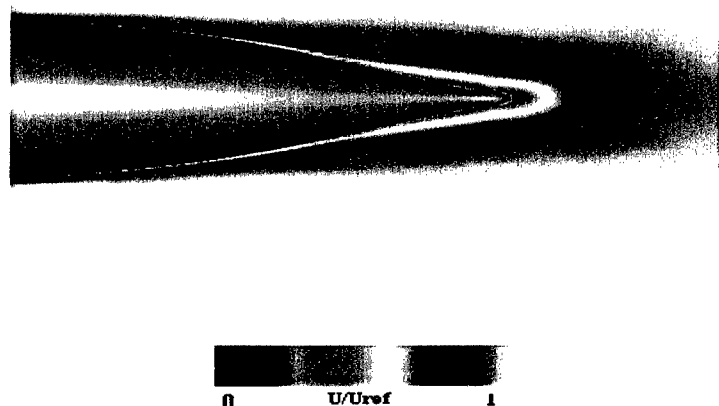


Figure 4.12: Xy-plane axial velocity contour, case bare.2d;  $q-\omega$ .

The xy-plane axial velocity contours for both turbulence models are very similar. Upon close inspection, it is found that the  $q-\omega$  solution has a thicker boundary layer. The next two figures are velocity contours in the yz-plane at an  $x/L$  location of 0.9987. The view is from the rear of the submarine looking forward.

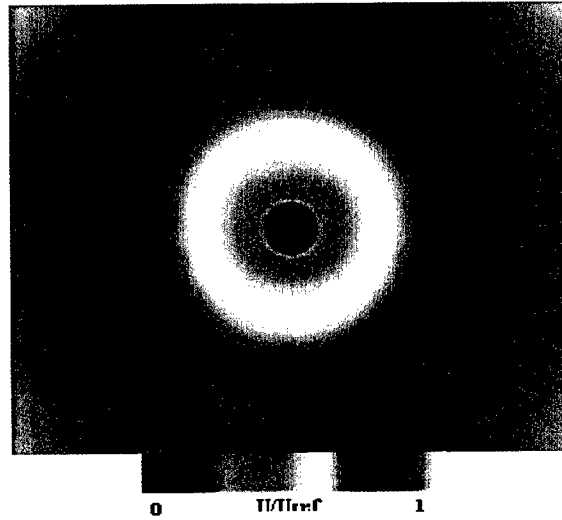


Figure 4.13: Velocity contour at  $x/L = 0.9987$  in yz-plane, case bare.4d; Spalart-Allmaras.

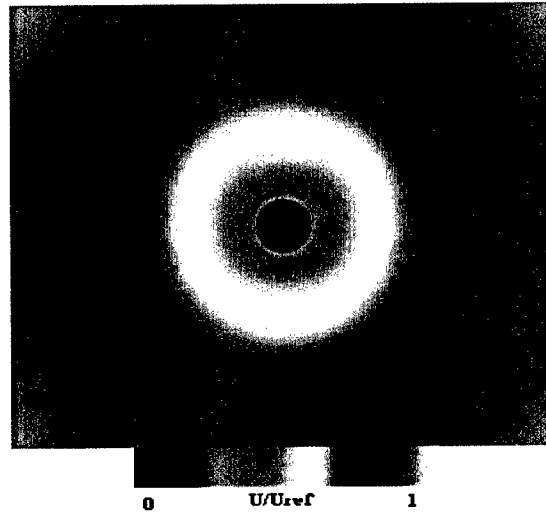


Figure 4.14: Velocity contour at  $x/L = 0.9987$  in yz-plane, case bare.2d;  $q-\omega$ .

The difference in the boundary layer thickness can more easily be seen in the yz-plane axial velocity contours than in the xy-plane axial velocity contours. This difference is small, but consistent with the drag coefficient plots. The thicker boundary layer would produce more drag.

The isolated propeller cases were also run with the two turbulence models. The next few plots show the xy-plane and yz-plane axial velocity contours for the isolated P4381 at an advance coefficient of  $J = 0.95$ . Flow field differences are minute at best. This is consistent with Figures 4.3 and 4.4; there is not much difference between the two turbulence models.

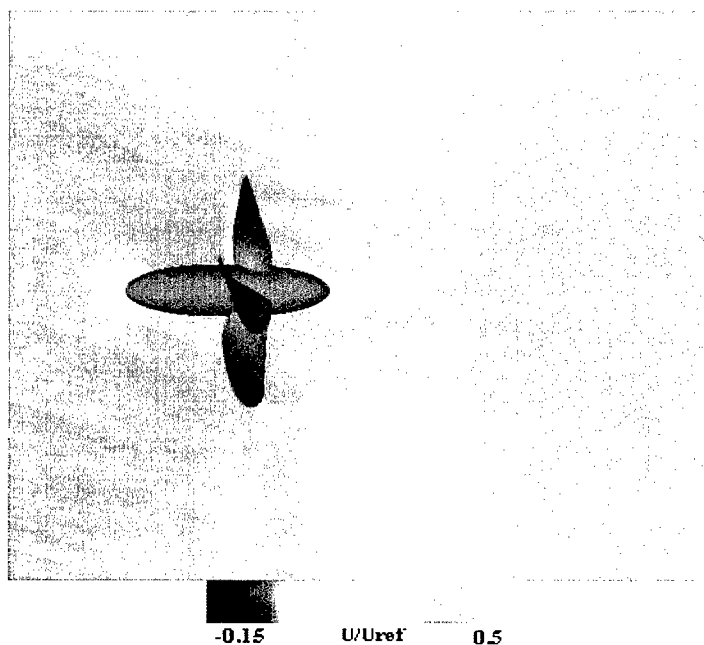


Figure 4.15: Xy-plane axial velocity contour,  $J = 0.95$ ; Spalart-Allmaras.



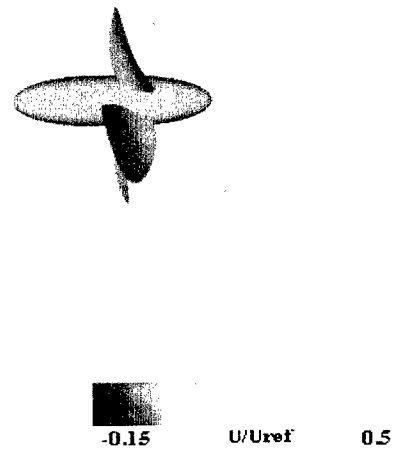


Figure 4.16: Xy-plane axial velocity contour,  $J = 0.95$ ;  $q-\omega$ .

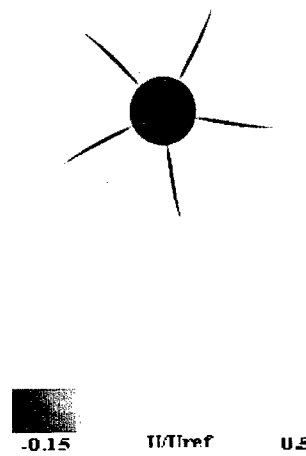


Figure 4.17: Yz-plane axial velocity contour,  $J = 0.95$ ; Spalart-Allmaras.

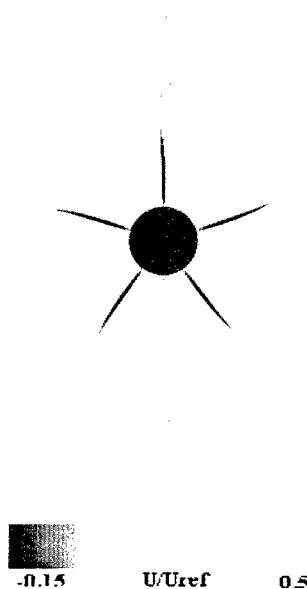


Figure 4.18: Yz-plane axial velocity contour,  $J = 0.95$ ;  $q-\omega$ .

As can be seen in Figures 4.11 – 4.18, the differences in specific flow characteristics between the turbulence models are small. The most noticeable difference overall is with the skin friction distribution. It is decided that consistency in the use of a turbulence model is more important than which particular model is used.

### 4.3 Reynolds Scaling Analysis

This section aims to explore some of the particular differences in flow characteristics between Reynolds scales. The three scales under investigation are the small model scale (11.278 inches), the LCC model scale (22.964 feet), and full scale (383.5 feet). These three scales generate Reynolds numbers from 770,000 to 1.6 billion. It has previously been discussed that simply applying Reynolds scaling principles to the force components is not sufficient because it does not take into account localized differences [paper]. The first plot (Figure 4.19) given is drag

coefficient versus Reynolds number. This is similar to Figure 4.1, but includes only the computational results and covers a broader range of Reynolds numbers. As expected, the same trend of drag coefficient decreasing with Reynolds number increase is readily seen. It is noted that the most significant drop happens across the lower Reynolds numbers.

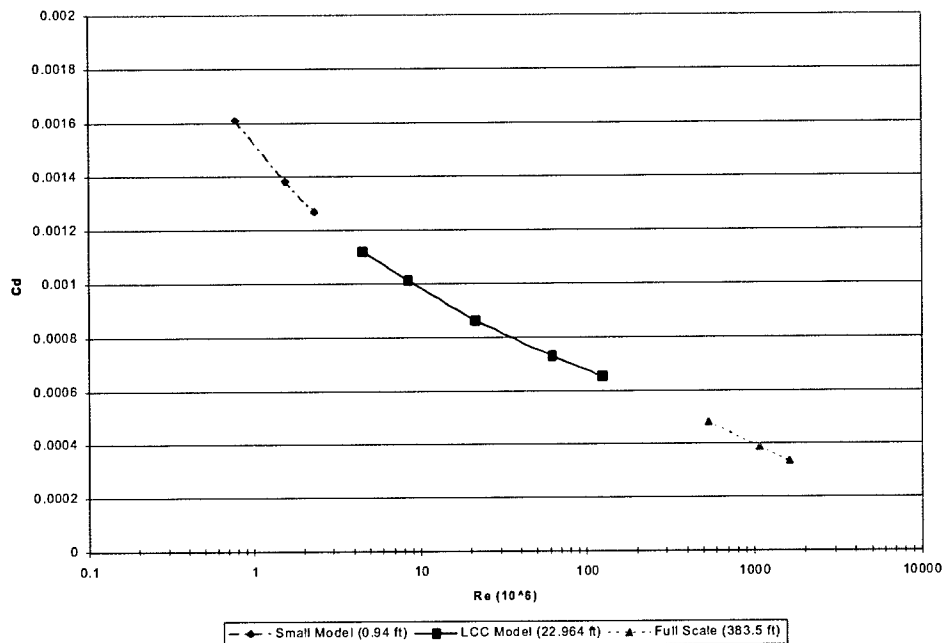


Figure 4.19: Computational drag coefficient versus Reynolds number, three length scales. Normalized by length.

Table 4.2 is a table of bare hull xy-plane axial velocity contours. Presenting these contours side by side makes it easier to see the differences between the Reynolds scales. As the Reynolds number increases, the boundary layer becomes thinner. The Reynolds number and case number are given below the contour. It is noted that the bare.3x contours have some peculiar characteristics. An explanation is offered in Section 4.5.

Table 4.2: Xy-plane axial velocity contours.

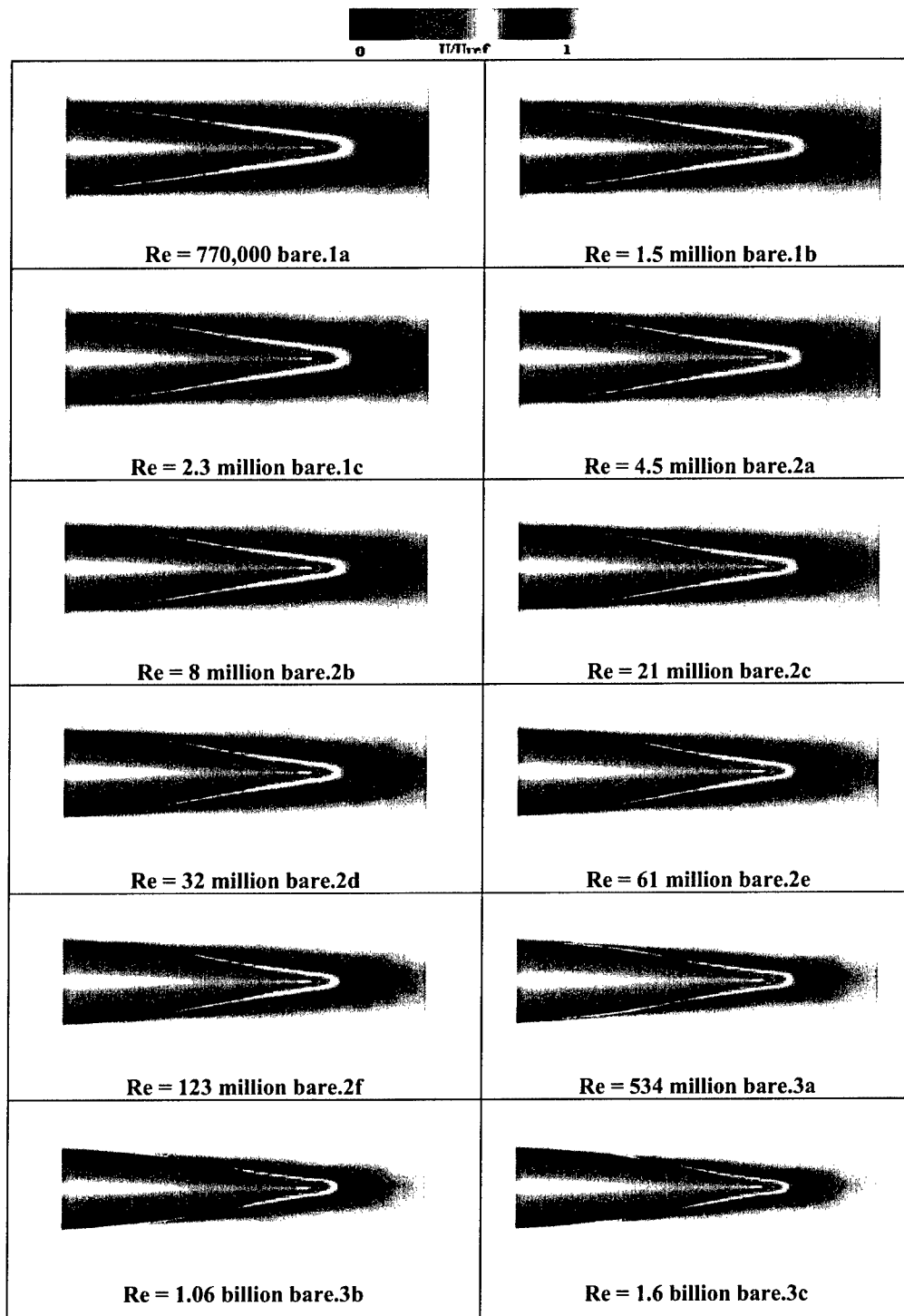
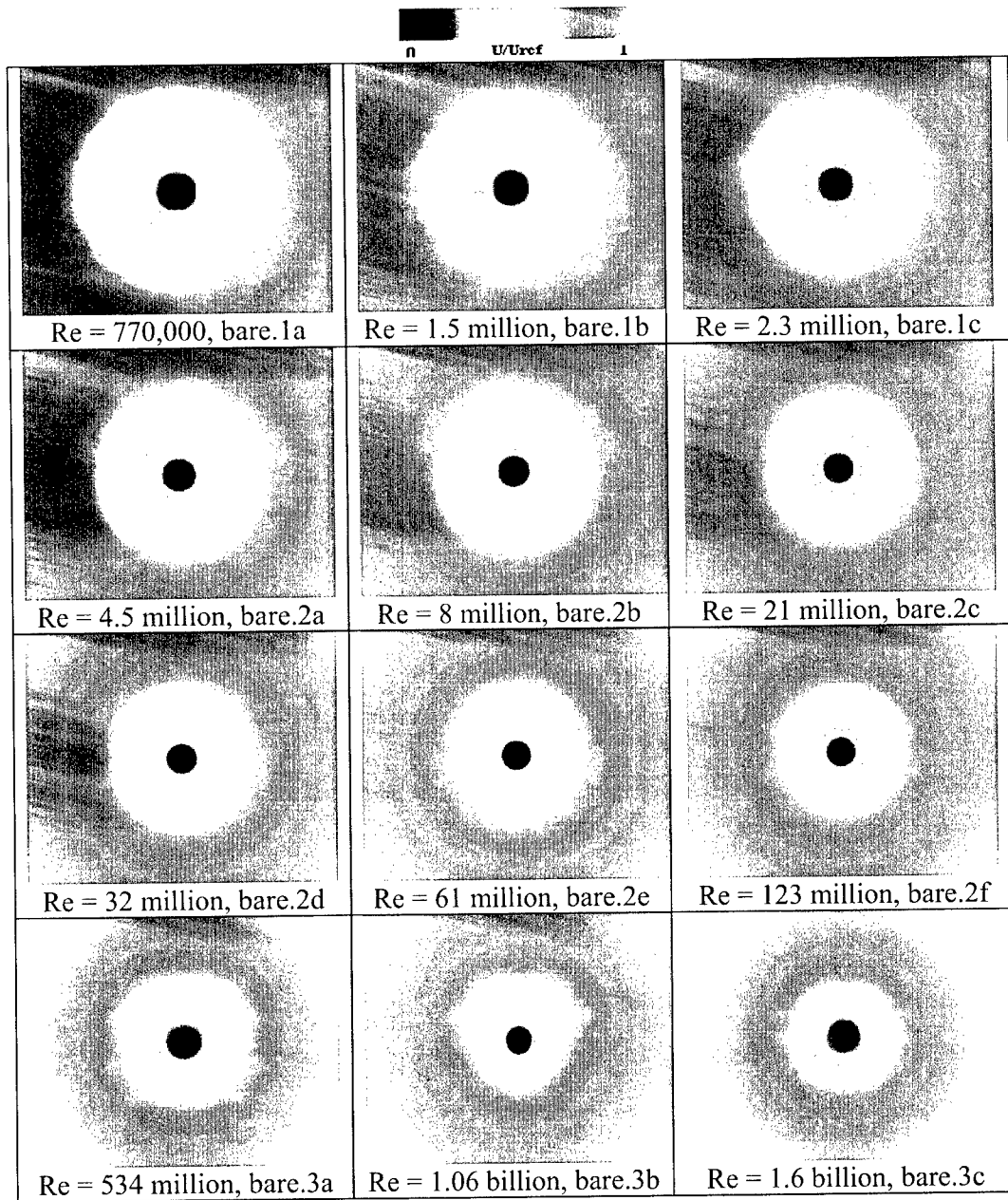


Table 4.3 compares the yz-plane axial velocity contours for all the Reynolds numbers. Again, the progressive diminishing of the boundary layer can be seen across the Reynolds numbers. The view is aft looking forward.

Table 4.3: Yz-plane axial velocity contours.



The boundary layer diminishing process seems to become more rapid and more pronounced at the higher Reynolds numbers. This seems counter to the drag coefficient plot, Figure 4.19, where the decrease in drag coefficient is more rapid and pronounced at the lower Reynolds number. As stated previously, the diminishing boundary layer and decreasing drag coefficient go hand in hand.

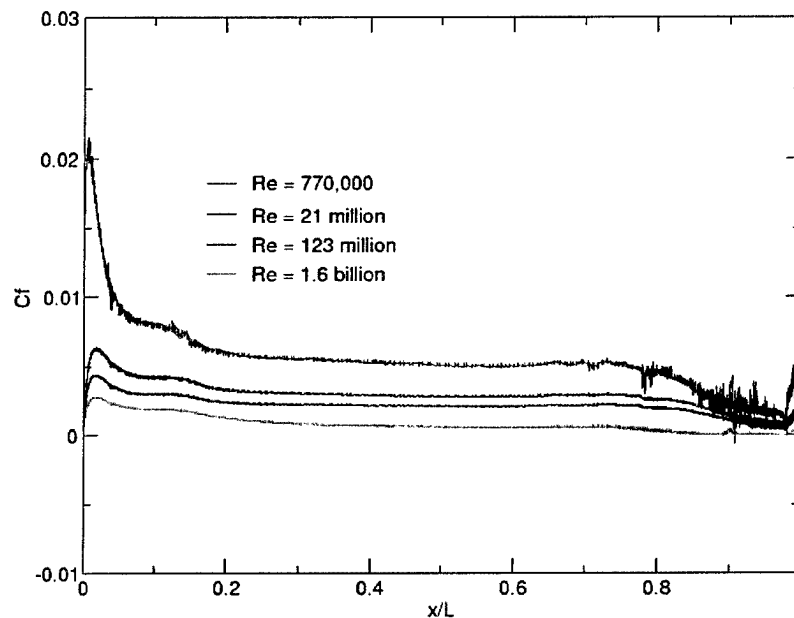


Figure 4.20: Skin friction coefficient distribution along bare hull for various Reynolds numbers.

As seen in Figure 4.20, the skin friction coefficient also decreases with increase in Reynolds number. The decrease in skin friction coefficient is indicative of the decrease in boundary layer thickness. This is related to the corresponding decrease in drag coefficient. Note that there is a lot of noise present at the lowest Reynolds number. This may be due to the off-wall grid spacing being too tight for that low of a

Reynolds number. Since one grid was used for all the Reynolds numbers, the lowest Reynolds numbers had the tightest off-wall spacing.

Next is to compare the propeller flow field at different Reynolds numbers, but for the same advance coefficient. It has been shown in Figure 3.10 that similar advance coefficients have similar thrust coefficients. The two xy-plane axial velocity contours and the two yz-plane axial velocity contours given below compare the propeller flow fields of an isolated P4381 propeller for an advance coefficient of  $J \sim 0.95$  at Reynolds numbers of 2.4 million and 32 million. For the yz-plane contour pictures, the view is aft looking forward. The cut is at an  $x/L$  of 0.9987, which is at the rear of the propeller blades.

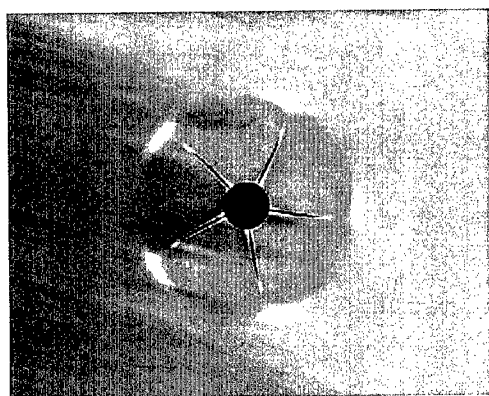


Figure 4.21(a):  $J = 0.95$ ,  
 $Re = 2.4$  million

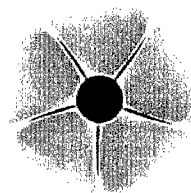


Figure 4.21(b):  $J = 0.98$ ,  
 $Re = 32$  million

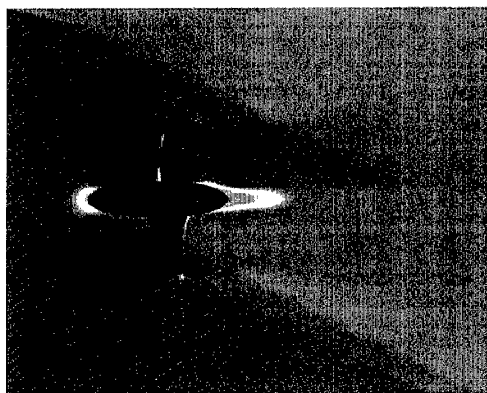


Figure 4.22(a):  $J = 0.95$ ,  
 $Re = 2.4$  million.

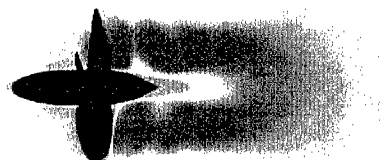


Figure 4.22(b):  $J = 0.98$ ,  
 $Re = 32$  million.

For the Reynolds number of 2.4 million, the propeller has a greater influence on the surrounding flow field. There is a 'bulge' of high-speed flow in between blade passages. The region of high-speed flow is more confined in the higher Reynolds number case. This confinement limits the propeller's region of influence. This effect is very similar to the reduction in boundary layer thickness of the bare hull cases.



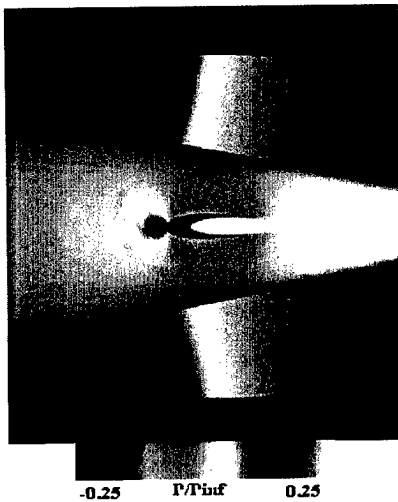


Figure 4.23(a): Pressure contours for stern region at  $Re = 16$  million.

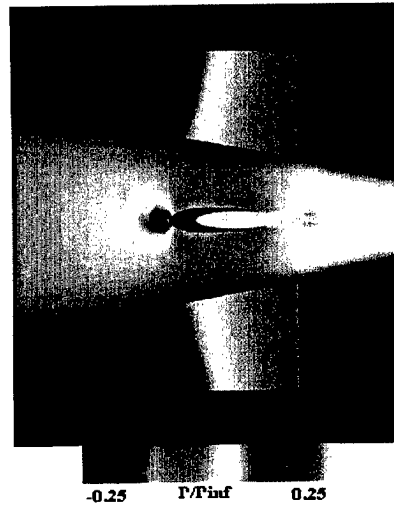


Figure 4.23(b): Pressure contours for stern region at  $Re = 64$  million.

Figures 4.23(a) and 4.23(b) show the differences in the region of influence of the stern appendages for two Reynolds numbers. The view is from the top looking down. The stagnation point on the rudder at a Reynolds number of 64 million exhibits a greater upstream influence than at a Reynolds number of 16 million. The downstream influence is also more pronounced. The effect of the stern appendages is more widely felt at the higher Reynolds number because of the decreased boundary layer thickness.

The results given in this section illustrate the concept of boundary layer thickness reduction, and thusly reduction in drag coefficient, with increase in Reynolds number. It has been shown that for the hull and the propeller, the Reynolds number has a localized effect on flow field characteristics.

#### 4.4 Hull/Propulsor Interaction

The complex flow surrounding a powered submarine is analyzed by breaking the flow up into its component pieces and examining the characteristics unique to each component. A discussion of the flow field interactions due to the hull, appendages and propeller ensues.

The three figures below show graphically the differences in the xy-plane axial flow field due to the stern appendages and the propeller at a Reynolds number of  $32 \times 10^6$ . The addition of the stern appendages thickens the boundary layer upstream, but lessens the influence of the hull boundary layer downstream of the submarine. The stern appendages increase the drag on the hull by 125%. The drag coefficient of the bare hull is 0.00074; with the addition of the stern appendages, the drag coefficient increases to 0.0017. In the third picture, the boundary layer can be seen “necking down” just before the propeller hub. The propeller drastically affects the submarine’s downstream influence, but doesn’t appear to have any influence upstream of the stern appendages. It is apparent that the propeller is immersed in the wake of the appendages.

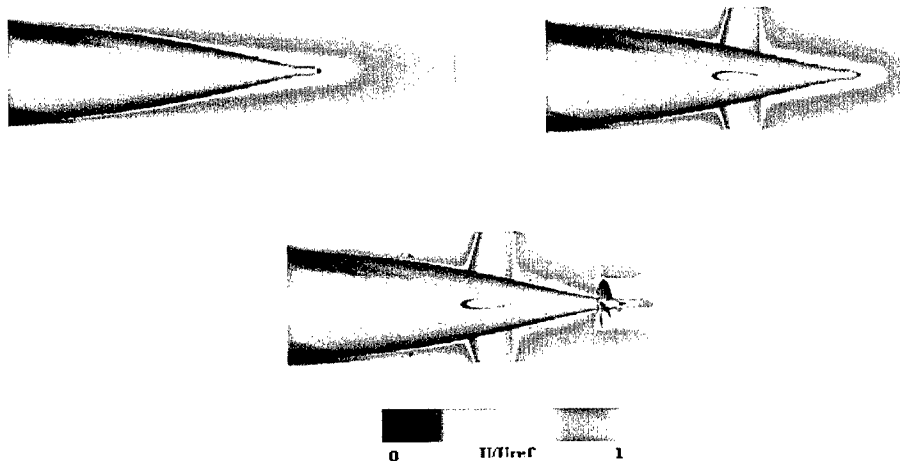


Figure 4.24: Influence of stern appendages and propeller on the hull velocity field.

The next figure shows the upstream influence of the stern appendages and the propeller. The view is a cut in the  $yz$ -plane just before the appendages. The axial location is  $x/L = 0.887$ . The view is forward looking aft.

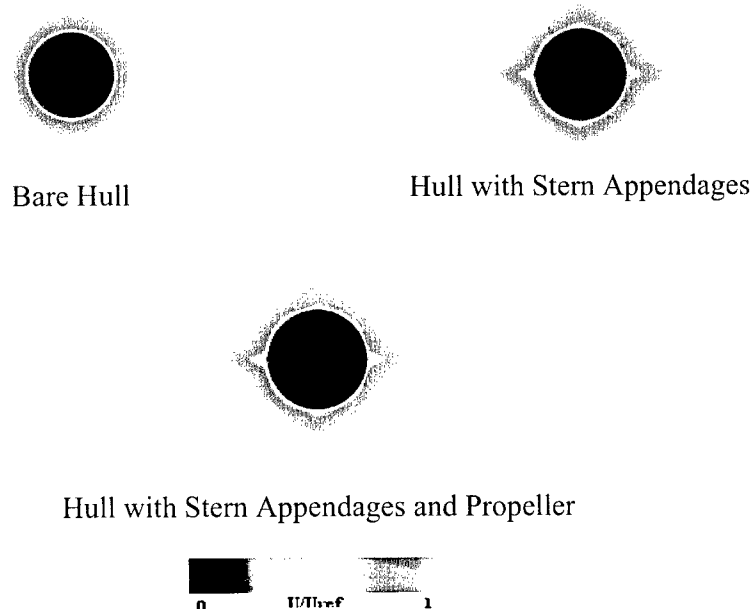


Figure 4.25: Upstream influence of the stern appendages and propeller.

It is clearly seen in Figure 4.25 that the stern appendages have an upstream influence. The lack of noticeable differences in the flow field of the hull with appendages and the hull with appendages and propeller shows that the appendages are the predominant upstream influence. The propeller has little, if any, effect on the flow upstream from the appendages. This may be due to the propeller being slightly undersized and further downstream than is typical.

Figure 4.26 shows that the stern appendages maintain a significant influence downstream of their position. This view is at approximately the middle of the propeller. The axial location is  $x/L = 0.986$  and the view is aft looking forward.

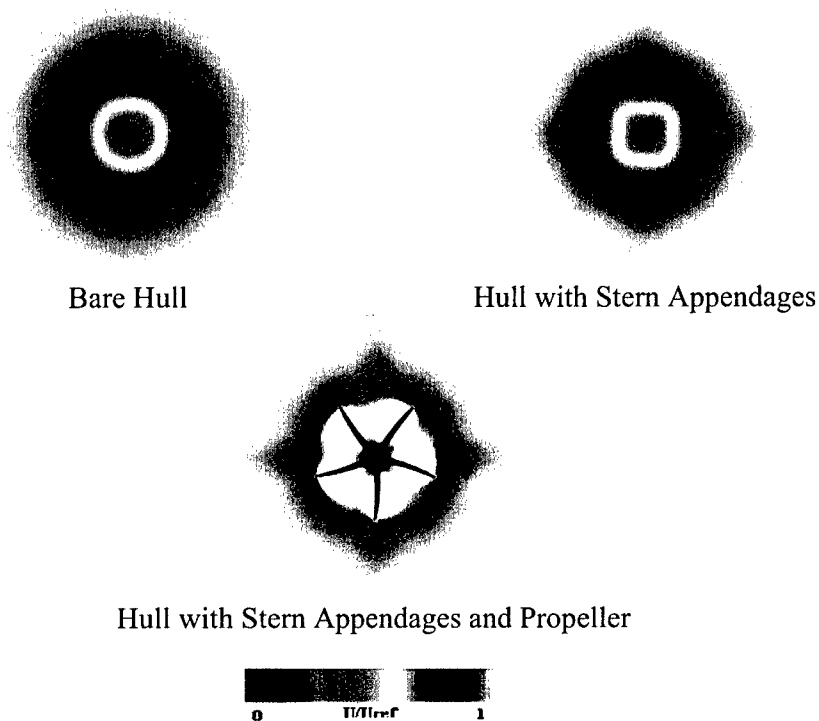


Figure 4.26: Downstream influence of the stern appendages and propeller.

The wake from the stern appendages squares off the interior velocity field downstream. Their location can be identified by the cross pattern in the flow field. The swirl pattern seen in the third picture is due to the propeller blade passages. The white area is the accelerated flow that provides the thrust.

The next series of graphics are a side-by-side comparison of the velocity fields for the isolated propeller and the installed propeller. Figure 4.26 shows yz-plane axial contours at the rear of the propeller blades with the view aft looking forward. Both solution sets were run at the same conditions for a Reynolds number of  $32 \times 10^6$ . The contour scales have been adjusted to show the most flow characteristics. The advance coefficient and case name are given below each picture.

Table 4.4: Comparison of isolated propeller and installed propeller yz-plane axial velocity fields showing the influence of the appendage wakes and hull boundary layer.

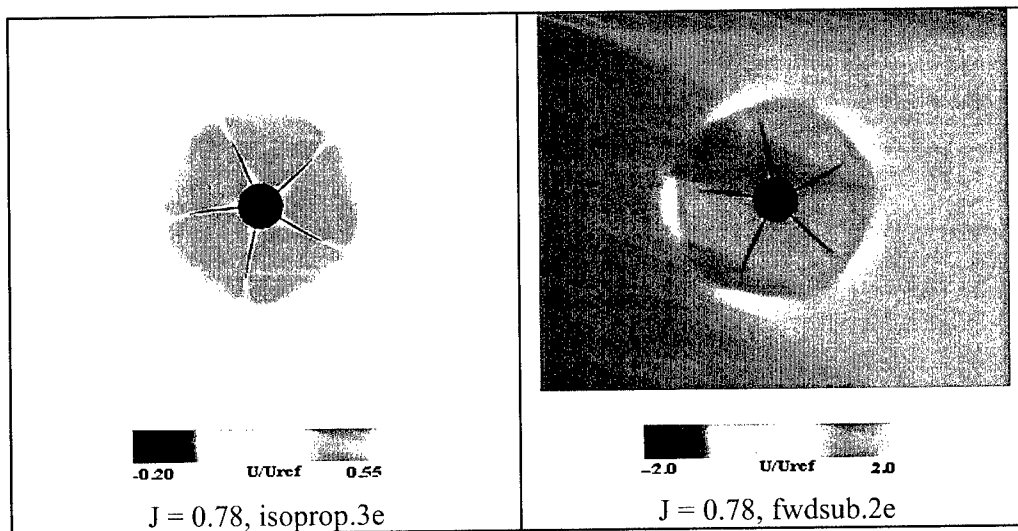


Table 4.4 (continued): Comparison of isolated propeller and installed propeller yz-plane axial velocity fields showing the influence of the appendage wakes and hull boundary layer.

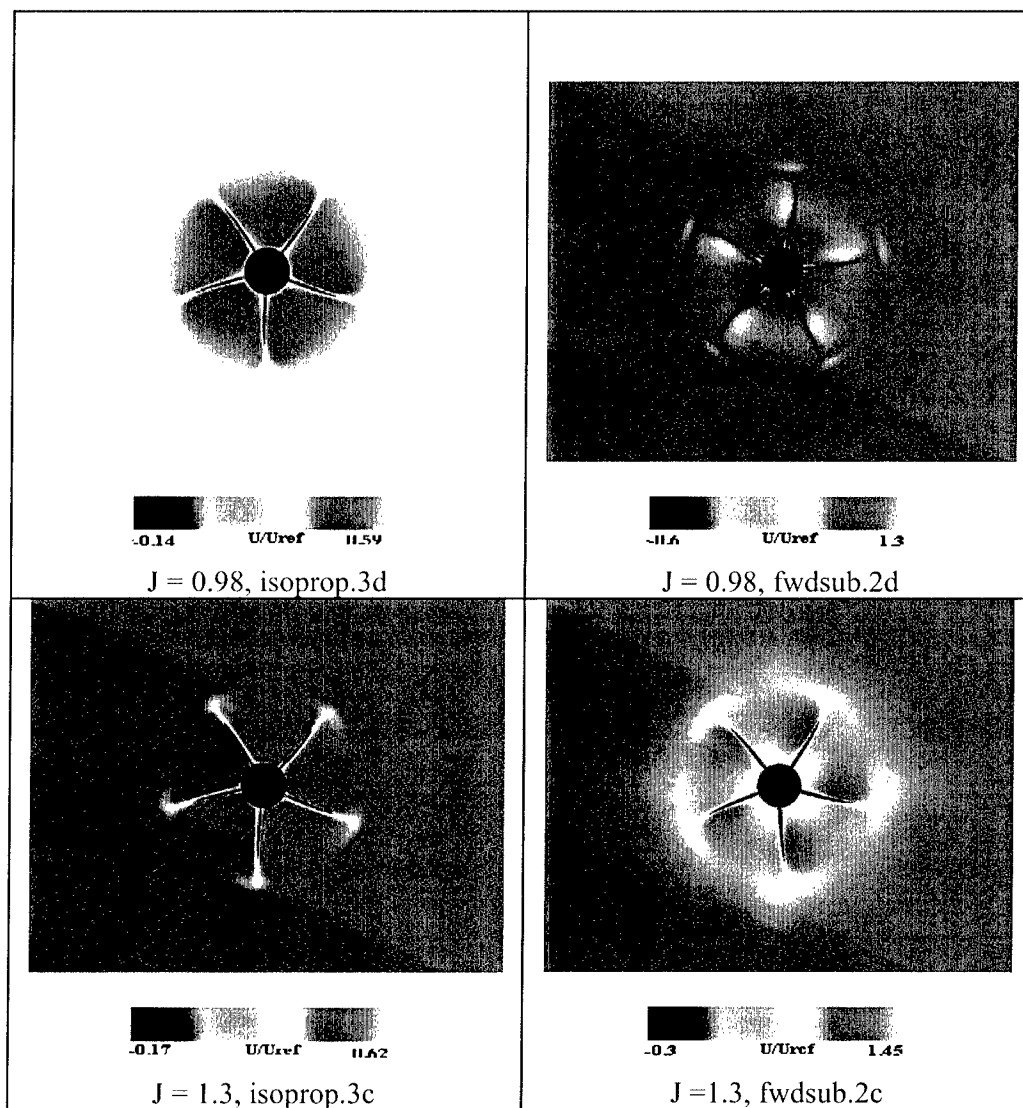
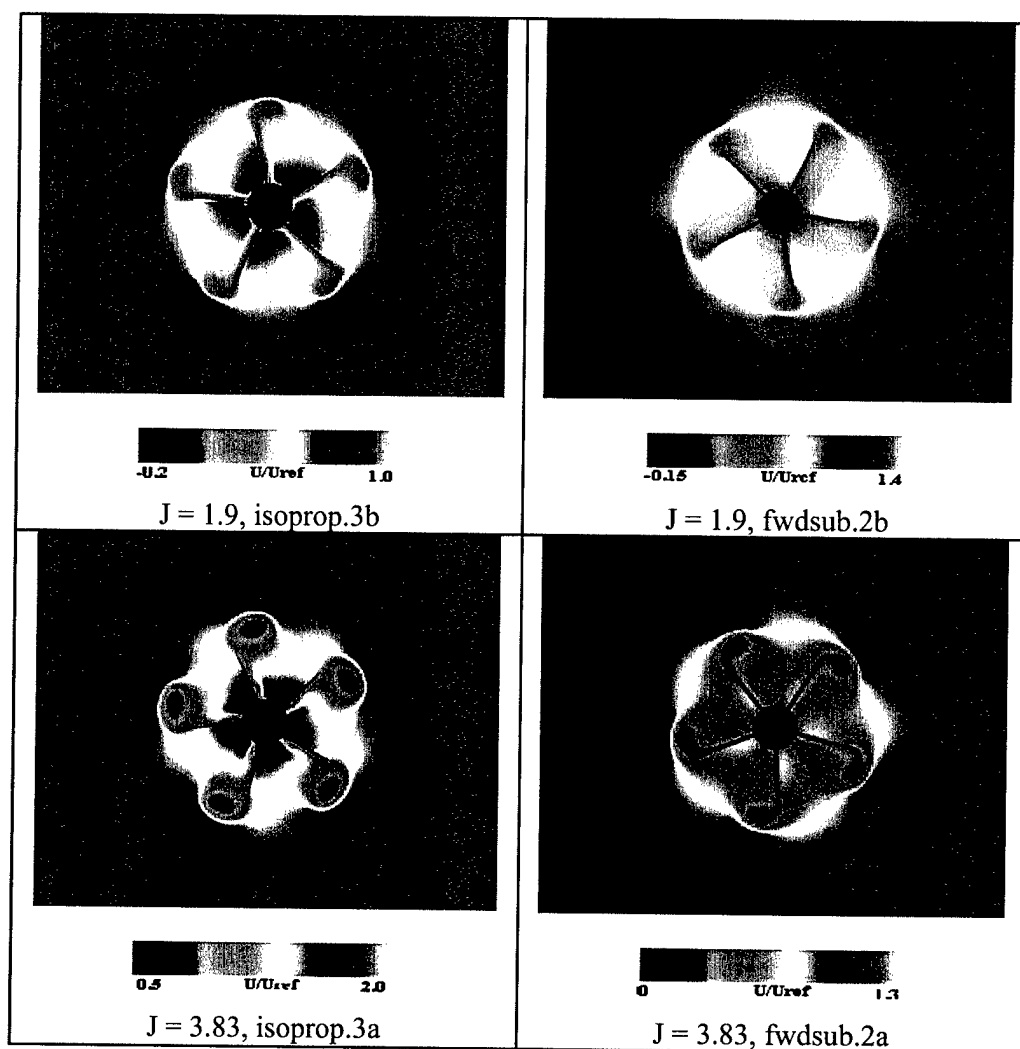


Table 4.4 (concluded): Comparison of isolated propeller and installed propeller yz-plane axial velocity fields showing the influence of the appendage wakes and hull boundary layer.



The cross pattern due to the appendage wakes is apparent in several of the above contours. For  $J = 1.3$ , the appendage wakes and hull boundary layer create almost a low velocity ring around the propeller. This phenomenon is not present in the corresponding isolated propeller contour. The combination of the wakes and the

hull boundary layer confine the flow field generated by the propeller. All cases show similar flow characteristics between the two configurations. The tip vortices are very noticeable in both cases for  $J = 3.83$ . The big difference between the two  $J = 3.83$  contours is the immersion of the installed propeller in the hull and appendage boundary layers. The interior propeller flow field is mostly low velocity. On the other hand, the isolated propeller interior flow field has pockets of high velocity flow. Notice for  $J = 1.3$ , the impingement of the appendage wakes on the propeller flow field smears out the low velocity pockets to a blurred low velocity ring. The presence of the appendage wakes is less apparent at the lower advance coefficients, but it still has an effect. The isolated propeller contour for  $J = 0.78$  is fairly round. The appendage wakes and hull boundary layer constrain the propeller flow field, which is exhibited by the flattened sides of the high velocity region.

Table 4.5 is a side-by-side comparison of the xy-plane axial velocity contours for the isolated propeller and the installed propeller. It is interesting to note that many of the same flow characteristics appear in both sets of cases.



Table 4.5: Comparison of isolated propeller and installed propeller xy-plane axial velocity fields showing the influence of the appendage wakes and hull boundary layer.

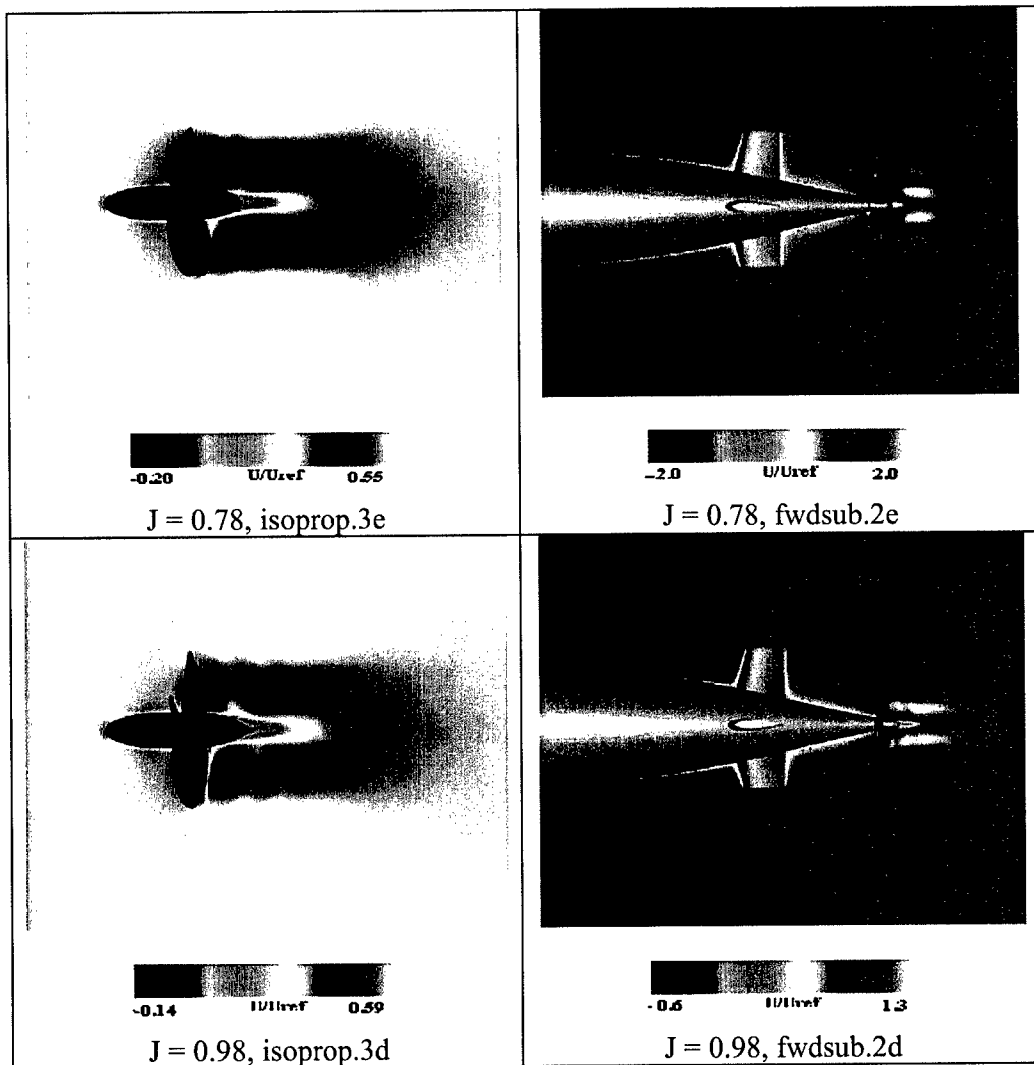


Table 4.5 (continued): Comparison of isolated propeller and installed propeller xy-plane axial velocity fields showing the influence of the appendage wakes and hull boundary layer.

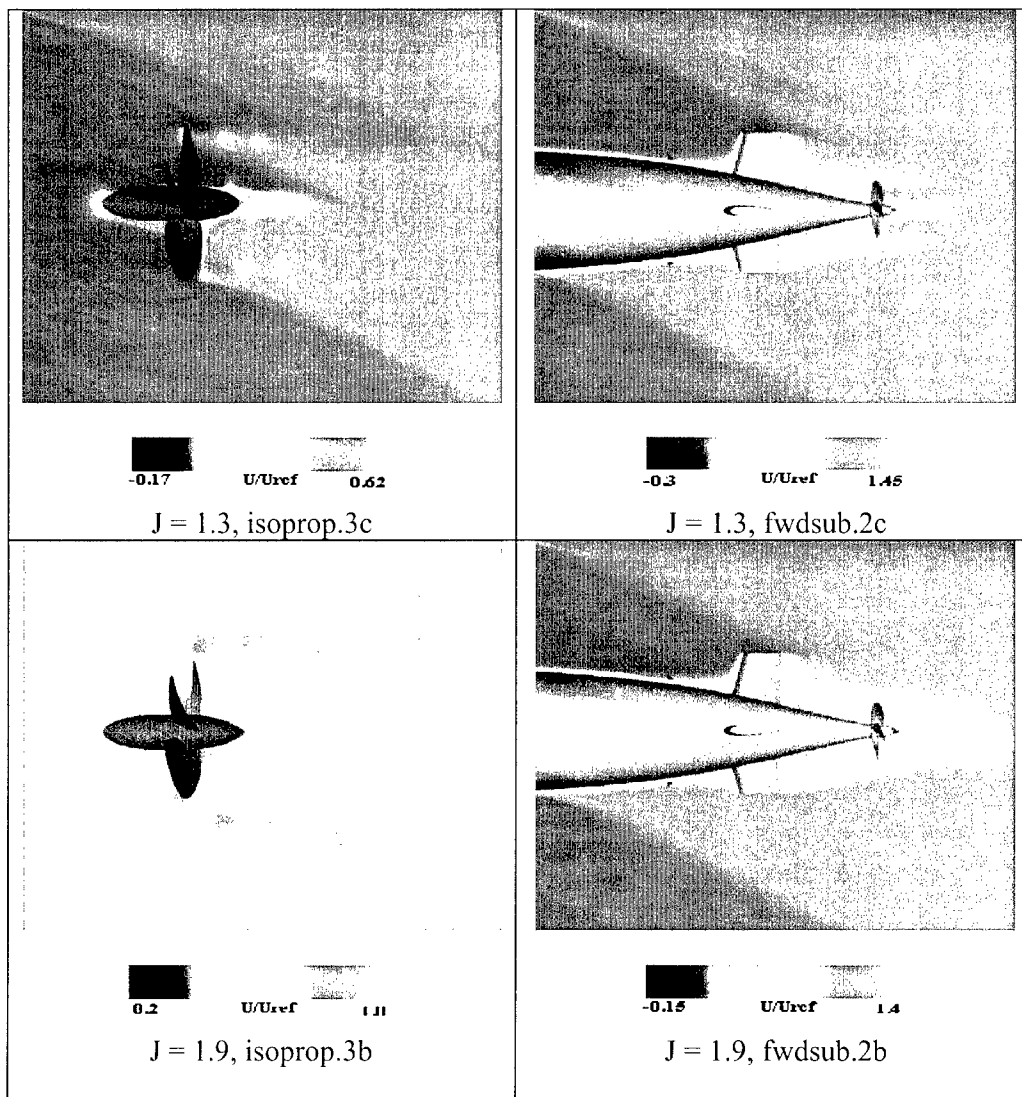
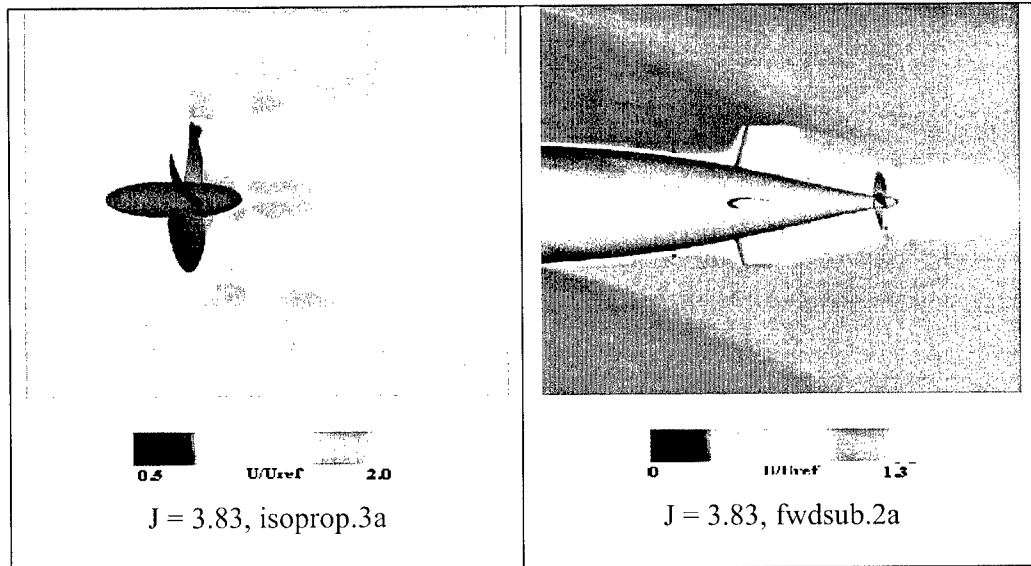


Table 4.5(concluded): Comparison of isolated propeller and installed propeller xy-plane axial velocity fields showing the influence of the appendage wakes and hull boundary layer.



The predominant difference between the two flow fields is the inflow conditions. The isolated propeller has close to free stream inflow conditions while the propeller on the body has the benefit of a reduced inflow due to the hull and appendage boundary layers. Another note is that the isolated propeller, even at the lower advance coefficients never generates a concentrated jet of flow. The reduced inflow and the containment by the body and appendage boundary layers allow for the body-mounted propeller to produce that jet of flow.

It is becoming clear that rather than hurting the performance of the propeller, the hull and appendage boundary layers actually provide the necessary environment for the propeller to do its job. This makes sense given that marine propellers are designed for optimum performance with a body.

To support the previous statement further, Figure 4.27 compares the thrust coefficients computed from the isoprop.3x and fwdsub.2x cases. As shown in Appendix B, both sets of cases are run at identical conditions.

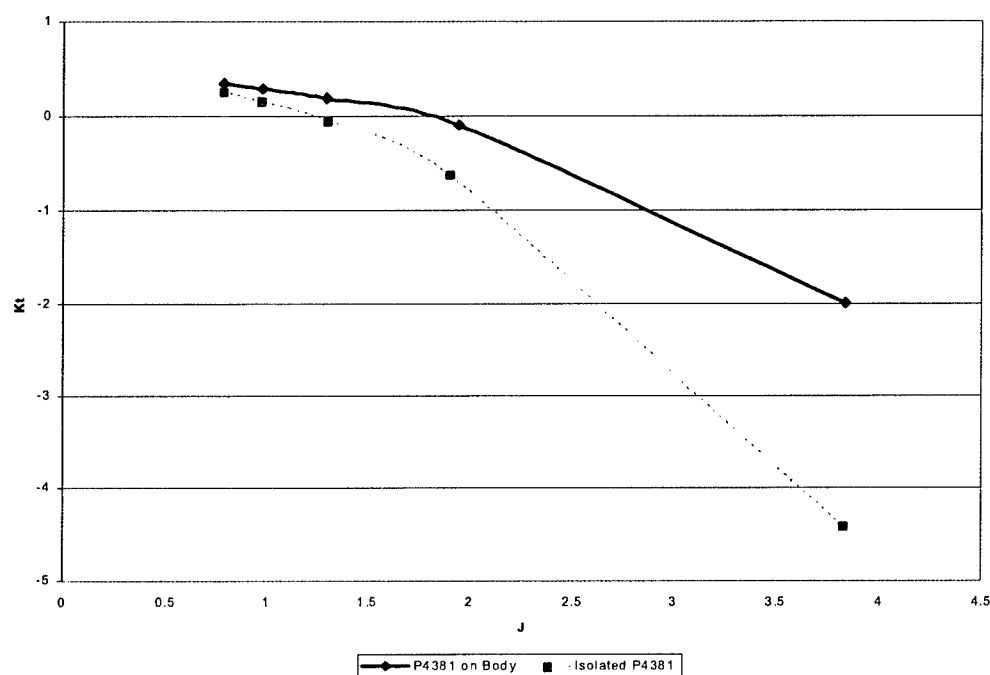


Figure 4.27: Thrust coefficient comparison between P4381 mounted on appended LCC hull and isolated P4381;  $Re = 32$  million.

Note in Figure 4.27, the propeller mounted on the body performs better than the isolated propeller. At first, this may seem backwards, but as stated previously, marine propulsors are designed to operate mounted to a larger body. The propeller on the appended LCC hull is buried in the boundary layer from the hull and the appendages. Due to this, the effective inflow that the mounted propeller sees is less than that of the isolated propeller. The reduced inflow velocity increases the lift and

therefore the thrust produced by the propeller blades. This graph illustrates the point that the hull and appendage boundary layers actually aid the propeller in performing its function.

#### 4.4 Submarine Crashback

In this section, the crashback computations will be shown to be valid and a few of the more interesting flow characteristics will be examined. The first plot is of the total axial force versus advance coefficient for both the cback.1x and cback.2x cases.

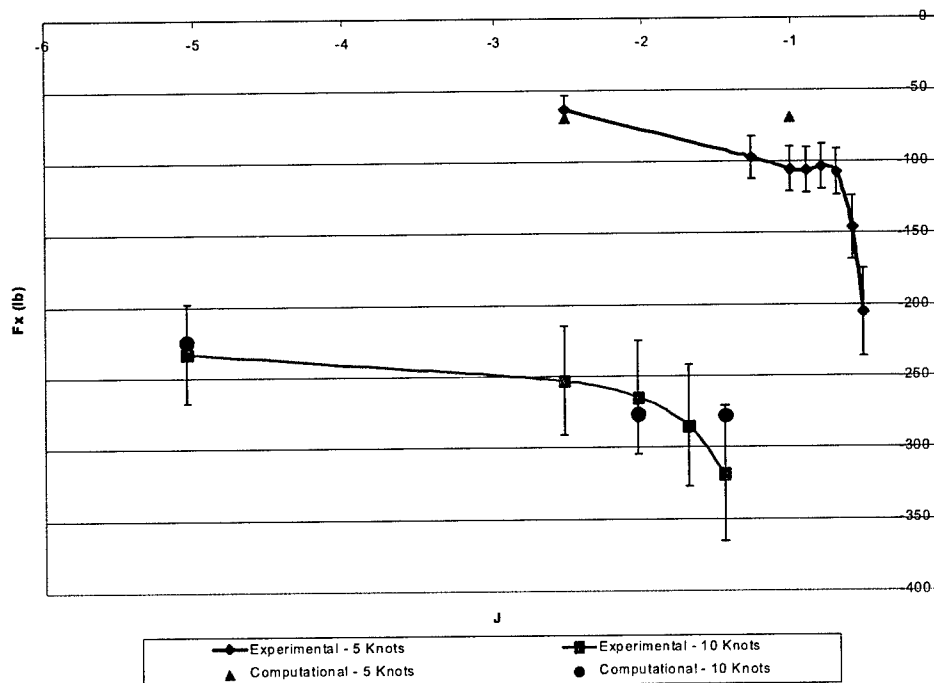


Figure 4.28: Validation of crashback computations cback.1x and cback.2x. Experimental has 15% error bars.

The results for the ten knot cases are much better than the results for the five knot cases. The computational results were averaged over two propeller revolutions in an attempt to attain the best possible force representation. Most of the results are

within the 15% error bound which is very good agreement for such an unsteady case.

The ring vortex presents a unique challenge in simulating this flow; it is constantly changing. Figure 4.29 is an intrinsic swirl isosurface of value  $\sim 2$  [19]. The propeller blades are colored by pressure. Notice the asymmetry of the ring vortex. Some of the asymmetry is due to the nature of the ring vortex itself, but it is believed that the asymmetry of the stern appendages and resulting wakes have some influence on the ring vortex structure as well.

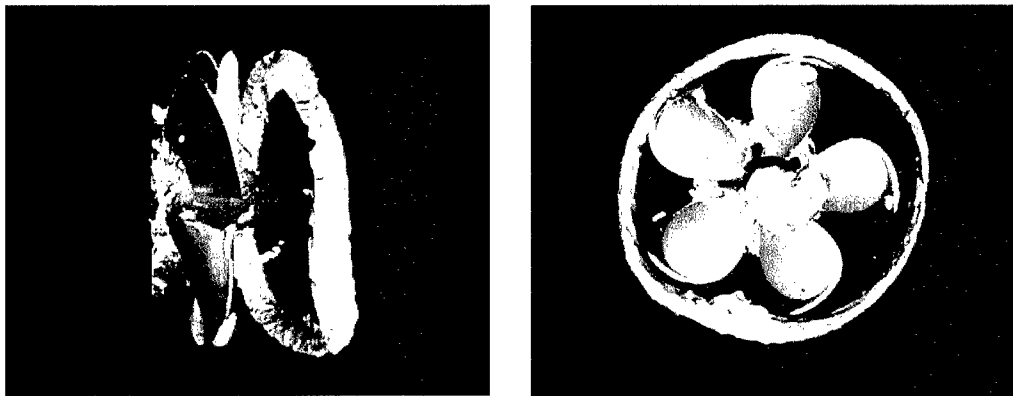


Figure 4.29: Swirl parameter isosurface showing the instantaneous ring vortex structure.

Figures 4.30 and 4.31 show the ring vortex in relation to the entire submarine. Figure 4.30 is another isosurface picture showing the establishment of the ring vortex at the rear of the submarine. Figure 4.31 is a particle trace. The swirl in the trace is very descriptive of the nature of the ring vortex.

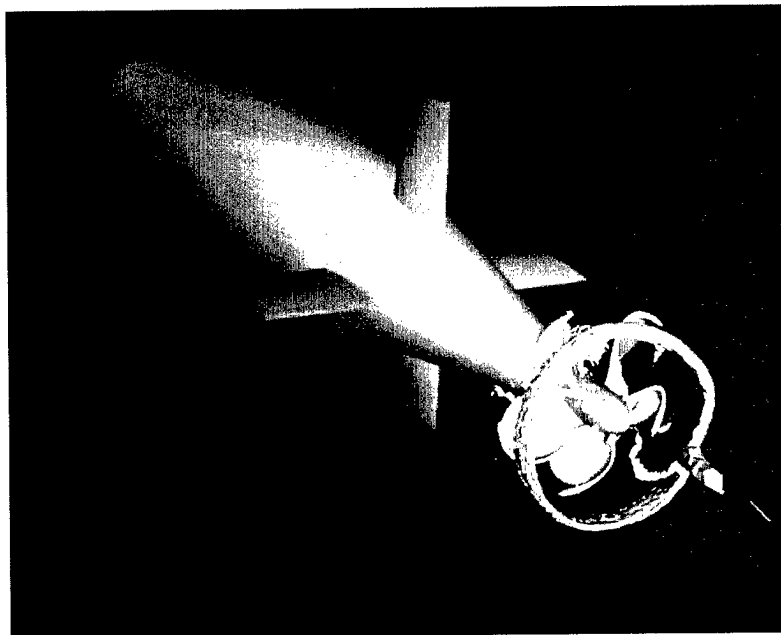


Figure 4.30: Ring vortex in relation to submarine.

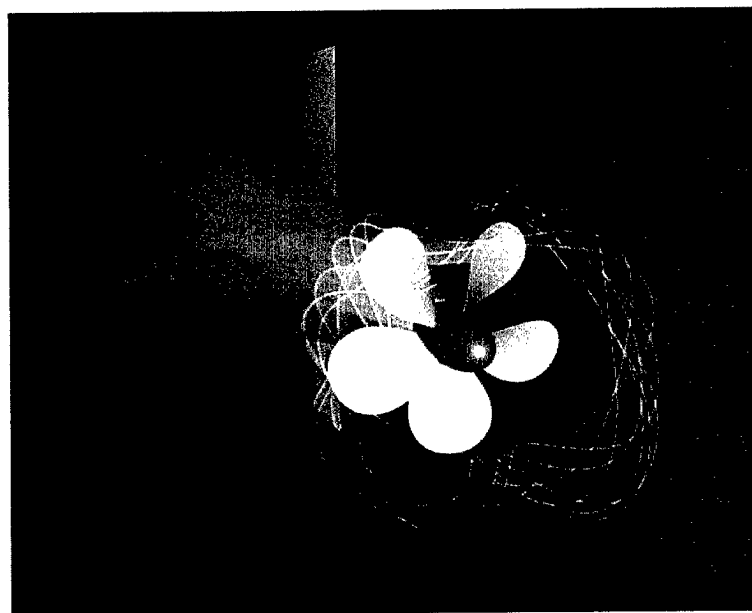
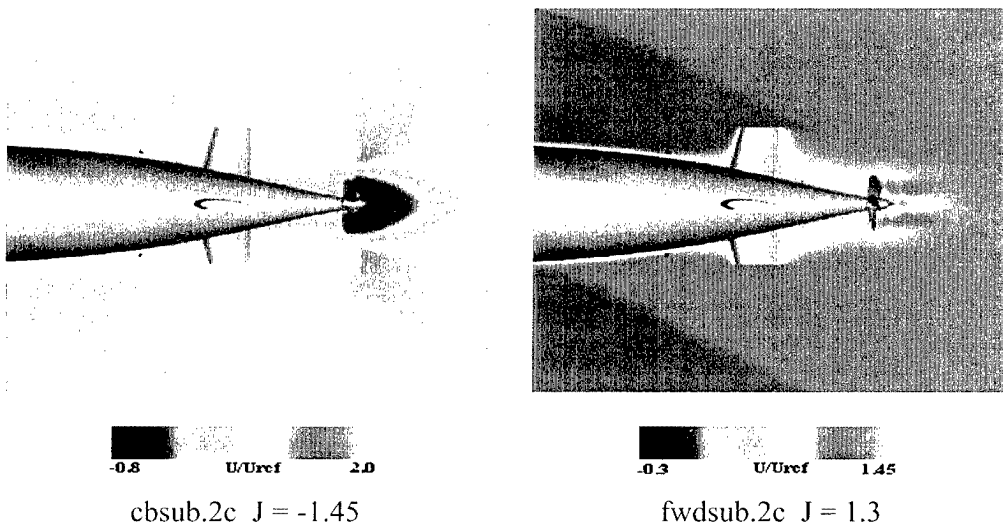
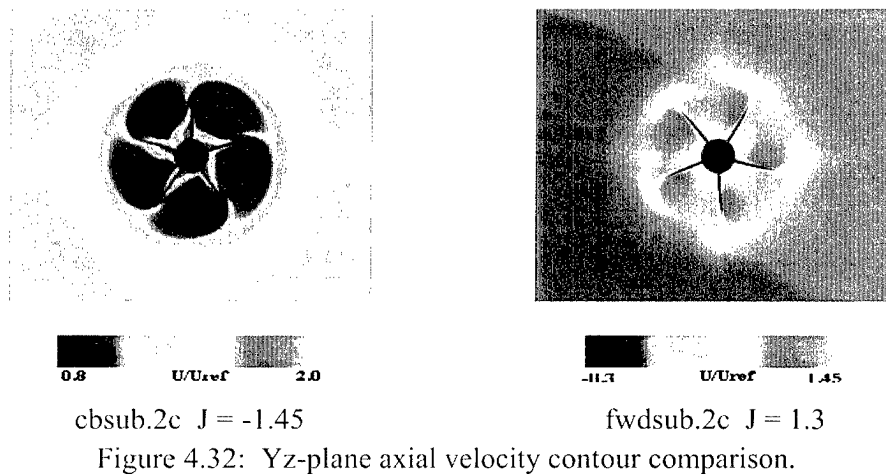


Figure 4.31: Particle trace of ring vortex.

The next set of figures is a comparison between the crashback velocity contours and a similar set of forward propelled contours. The crashback velocity contours are for the cbsub.2c case. The related forward case is the fwdsb.2c case. The first two pictures, Figure 4.32, are yz-plane axial velocity contours of the propeller. Figure 4.33 is a set of xy-plane axial velocity contours showing the reversed flow region around the propeller of the crashback case.





There are several things to note in the above velocity contours. The impingement on the boundary layer upstream of the propeller is clearly shown in the crashback contour of Figure 4.33. In the crashback contour of Figure 4.32, the instability of the flow field and resulting asymmetry can be seen. The propeller in crashback also has a much larger region of influence than does the propeller rotating forward. The crashback flow field is very complex and is an intriguing flow to model. The results presented in this section show good agreement with the experimental results and several of the pictures clearly show the physical phenomenon associated with crashback flow.

#### **4.6 Possible Sources of Error**

There are a couple of possible sources of error. As with any study, the results are not infallible, but considering the good to excellent agreement with the experimental results, the overall quality of the computations is felt to be very high.

Considering the bare hull drag, one source of error might be the absence of the test strut. At the onset of the study, it was decided that the strut was probably a negligible source of drag. But it is recognized that the strut would have a contribution to the recorded drag. Also, the tunnel walls were not modeled. All of the computations were run as open water simulations. It was decided that the tunnel blockage was not sufficient as to warrant the computational resources that would be required for such a large-scale simulation.

Another possible source would be the geometry definition for the hull. This possibility did not show up until the full-scale simulations were run. As shown in

Figure 4.34, with the highest Reynolds numbers (as in those for the full scale submarine), a numerical artifact is present in the velocity flow field. This artifact is represented as the dark blue area in the boundary layer region. Although this artifact affects the boundary layer region of the velocity flow field, it doesn't seem to have a major effect on the overall flow field.



Figure 4.34: Numerical artifact in high Reynolds number flow boundary layer.  
 $Re = 1$  billion.

When the curve definition for the hull is analyzed by taking the second derivative, it is noted that the curve is not entirely smooth. The top line is the hull definition and the bottom line is the second derivative.

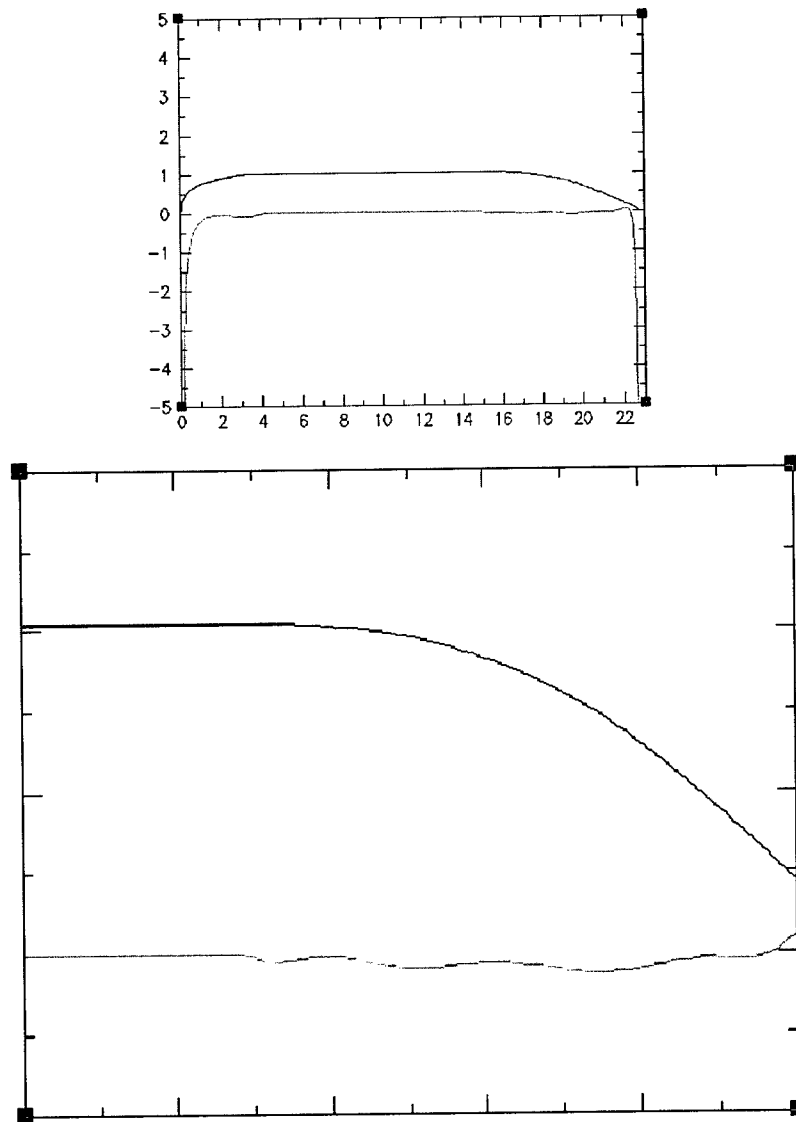


Figure 4.35: Hull curve and 2<sup>nd</sup> derivative. Large plot is close up of stern region.

The ‘wiggles’ apparent in the hull definition may have caused some bumps in the computational model of the hull. While at the lower Reynolds number this didn’t seem to have much of an effect, it did affect the boundary layer for the higher Reynolds numbers. At the higher Reynolds numbers, the boundary layer is so thin that the flow becomes much more sensitive to the computational geometry. To prove

that the hull definition is the culprit, the curve would need to be smoothed, a new computational model generated, and the solution run again.

The last source to be discussed is the grid resolution behind the stern appendages. Grid refinement to the rear of the stern appendages would help resolve the wakes. The tighter resolution of the wakes might yield some more interesting flow interactions with the propeller.

## CHAPTER V

### CONCLUSIONS AND RECOMMENDATIONS

#### 5.1 Conclusions

Computational simulation is growing by leaps and bounds. Technological advances are making it easier and faster to model complex geometries and physics. This study has shown that the flow solver,  $U^2NCLE$ , can produce valid results for isolated propeller, bare hull, forward propelled, and crashback submarine simulations. With the exception of the bare hull configuration, all simulations produced solutions with excellent agreement to experimental data. Although the agreement between the experimental drag coefficient and the computational drag coefficient for the bare hull would not be considered excellent, it would still be considered good agreement.

The flow solver has also been shown to run long duration unsteady problems, such as 18-20 propeller revolutions for a submarine in crashback. Previous propelled studies have only run 8-10 revolutions.

With respect to the turbulence models, it has been determined that the consistency of turbulence model use is more important than which particular model is used. While the  $q-\omega$  turbulence model generally produced better agreement with experimental data, it was also more difficult to run. Its sensitivity to the surface grid can make it difficult to work with depending upon the type of geometry being modeled.

The importance of the computational geometry itself has also been pointed out.

The Spalart-Allmaras model has been shown to be both forgiving and reliable. The results, particularly for the forward propelled simulations, produced with the Spalart model all had good to excellent agreement with the experimental results.

The Reynolds scaling study showed that the drag coefficient for the bare hull decreased with the increase in Reynolds number. Related to this, the boundary layer became increasingly thin with Reynolds number as well. The change in the velocity profiles is something that cannot be taken into consideration with Reynolds scaling of forces. Depending on which flow characteristics are of great importance, computationally simulating the entire flow field becomes essential, particularly with respect to the propeller. Reynolds number affects the extent of the propeller's influence on the surrounding flow. The propeller flow field has some localized flow characteristics that cannot be accounted for through basic Reynolds scaling. Thus, the need to computationally simulate the entire flow field for higher Reynolds numbers has been supported.

It has been shown that the stern appendages have the greatest influence on both the hull and propeller flow fields. The propeller is more efficient mounted on a submarine than isolated by itself. By itself, it actually creates more drag because of the effective inflow. The boundary layer interaction between the hull, appendages and propeller is actually a good thing. It allows the propeller to take advantage of a reduced inflow thereby increasing its thrust production.

The submarine crashback has been discussed and pictorially described.

Specific flow characteristics have been pointed out, and insights gained in the nature of this very complex, and unsteady flow. The validation of the code to run crashback simulations is also very important.

This study has made a significant advance towards the accurate prediction of forces and flow characteristics for a fully submerged body. It is one of the first studies to validate fully submerged and propelled simulations with experimental data. This study has hopefully shed a little light on understanding the physics associated submarine flow fields. This understanding might help with the design of a faster, quieter submarine.

## **5.2 Recommendations**

Several recommendations are made:

- Complete a grid topology and density study on the bare hull drag coefficient to determine why the agreement with experimental data degrades with increase in Reynolds number.
- Smooth hull definition and re-run full-scale bare hull simulations.
- Run additional crashback simulations to see if agreement is consistent.
- Refine the propeller tips to run a full-scale propelled simulation.

## REFERENCES

- [1] Roddy, R.F., "Investigation of the Stability and Control Characteristics of Several Configurations of the DARPA SUBOFF Model from Captive-Model Experiments", Technical Report DTRC/SHD-1298-08, David Taylor Research Center, Bethesda, Maryland, September 1990.
- [2] Jonnalagadda, Ramanadham, "Reynolds Averaged Navier-Stokes Computation of Forces and Moments for Appended SUBOFF Configurations at Incidence", M.S. Thesis, Department of Aerospace Engineering, Mississippi State University, May 1996.
- [3] Bull, P.W. and Watson, S.J.P., "The Prediction of Flow Around Submarines at Full Scale", Twenty-Second Symposium on Naval Hydrodynamics, Washington, August 1998.
- [4] Gorski, J.J., Briley, R.J., and Whitfield, D.L., "Large-Scale Simulations for Maneuvering Submarines and Propulsors," AIAA 29<sup>th</sup> Fluid Dynamics Conference, Paper No. 98-2930, 1998.
- [5] Boswell, R.J., "Design Cavitation Performance and Open-Water Performance of a Series of Research Skewed Propellers," Ship Performance Department Research and Development Report No. 3339, Naval Ship Research and Development Center, Washington D.C., March 1971.
- [6] Freudenthal, J., "Experimental Studies of the Drag of an Axisymmetric Submarine Hull," M.S. Thesis, Department of Aerospace Engineering, Mississippi State University, May 2002.
- [7] Hyams, D.G., Sreenivas, K., Sheng, C., Nichols, S., Taylor, L.K., Briley, W.R., Marcum, D.L., and Whitfield, D.L., "An Unstructured Multielement Solution Algorithm for Complex Geometry Hydrodynamic Simulations," 23<sup>rd</sup> Symposium of Naval Hydrodynamics, Val de Reuil, France, September, 2000.
- [8] Hyams, D.G., "An Investigation of Parallel Implicit Solution Algorithms for Incompressible Flows on Unstructured Topologies," PhD Dissertation, Mississippi State University, May 2000.



- [9] Taylor, L.K., "Unsteady Three-Dimensional Incompressible Algorithm Based on Artificial Compressibility," PhD Dissertation, Mississippi State University, 1991.
- [10] Hirsch, C., Numerical Computation of Internal and External Flows. Volume 2. John Wiley & Sons, New York, 1990.
- [11] Hyams, D.G., Sreeniva, K., Sheng, C., Briley, W.R., Marcum, D.L., and Whitfield, D.L., "An Investigation of Parallel Implicit Solution Algorithms for Incompressible Flows on Multielement Unstructured Topologies," AIAA 38<sup>th</sup> Aerospace Sciences Meeting, Paper No. 2000-0271, January 2000.
- [12] Spalart, P.R. and Allmaras, S.R., "A One Equation Turbulence Model for Aerodynamic Flows," AIAA Paper No. 92-0439, 1992.
- [13] Coakley, T.J. and Hsieh, T., "A Comparison Between Implicit and Hybrid Methods for the Calculation of Steady and Unsteady Inlet Flows," AIAA/SAE/ASME/ASEE 21<sup>st</sup> Joint Propulsion Conference, Paper No. 85-1125, July 1985.
- [14] Watson, S.J.P. and Bull, P.W., "The Scaling of High Reynolds Number Viscous Flow Predictions Using CFD Techniques," Third Colloquium on Advanced CFD Applications to Ship Flow and Hull Form Design, Osaka, May 1998.
- [15] Sreenivas, K., Hyams, D., Mitchell, B., Taylor, L., Briley, W.R., and Whitfield, D.L., "Physics Based Simulations of Reynolds Number Effects in Vortex Intensive Incompressible Flows," Computational Simulation and Design Center Report, Mississippi State University, 2001.
- [16] Bridges, D.H., "Private Conversation," Department of Aerospace Engineering, Mississippi State University, September 2001.
- [17] Gaither, J.A., "A Solid Modeling Topology Data Structure for General Grid Generation," M.S. Thesis, Mississippi State University, 1997.
- [18] Marcum, D.L., and Gaither, J.A., "Mixed Element Type Unstructured Grid Generation for Viscous Flow Applications," 14<sup>th</sup> AIAA CFD Conference, Paper No. 99-3252, June 1999.
- [19] Berdahl, C.H. and Thompson, D.S., "Eduction of Swirling Structure Using the Velocity Gradient Tensor," AIAA Journal, Vol. 31, No. 1, January 1993.

## APPENDIX A

### TABLE OF CONDITIONS FOR EACH COMPUTATIONAL CASE

Case Name	Scale*	Reynolds #	Velocity (fps)	Propeller rps	Turbulence Model
<b><i>Bare Hull (nonappended, unpropelled LCC hull)</i></b>					
bare.1a	small	$7.77 \times 10^5$	10	-----	q- $\omega$
bare.1b	small	$1.55 \times 10^6$	20	-----	q- $\omega$
bare.1c	small	$2.33 \times 10^6$	30	-----	q- $\omega$
bare.2a	LCC	$4.49 \times 10^6$	1.86	-----	q- $\omega$
bare.2b	LCC	$8.41 \times 10^6$	3.41	-----	q- $\omega$
bare.2c	LCC	$21.05 \times 10^6$	8.55	-----	q- $\omega$
bare.2d	LCC	$32 \times 10^6$	13.58	-----	q- $\omega$
bare.2e	LCC	$61.15 \times 10^6$	25.58	-----	q- $\omega$
bare.2f	LCC	$12.3 \times 10^7$	51.21	-----	q- $\omega$
bare.3a	Full	$5.35 \times 10^8$	16.87	-----	q- $\omega$
bare.3b	Full	$1.07 \times 10^9$	33.73	-----	q- $\omega$
bare.3c	Full	$1.6 \times 10^9$	50.6	-----	q- $\omega$
bare.4a	LCC	$4.49 \times 10^6$	1.86	-----	Spalart Allmaras
bare.4b	LCC	$8.41 \times 10^6$	3.41	-----	Spalart Allmaras
bare.4c	LCC	$21.05 \times 10^6$	8.55	-----	Spalart Allmaras
bare.4d	LCC	$32 \times 10^6$	13.58	-----	Spalart Allmaras
bare.4e	LCC	$61.15 \times 10^6$	25.58	-----	Spalart Allmaras
bare.4f	LCC	$12.3 \times 10^7$	51.21	-----	Spalart Allmaras
bare.5a structured grid	LCC	$12.3 \times 10^7$	51.21	-----	Spalart Allmaras
bare.5b structured grid	LCC	$12.3 \times 10^7$	51.21	-----	q- $\omega$
bare.6a unstructured grid	LCC	$12.3 \times 10^7$	51.21	-----	Spalart Allmaras
bare.6b unstructured grid	LCC	$12.3 \times 10^7$	51.21	-----	q- $\omega$
<b><i>Hull with Fins (appended, unpropelled LCC hull)</i></b>					
apphull.1	LCC	$32 \times 10^6$	13.58	-----	Spalart Allmaras
<b><i>Isolated P4381 Propeller</i></b>					
isoprop.1a	-----	$2.4 \times 10^6$	3.9	7.8	q- $\omega$

Case Name	Scale*	Reynolds #	Velocity (fps)	Propeller rps	Turbulence Model
isoprop.1b	-----	$2.4 \times 10^6$	6.93	7.8	q- $\omega$
isoprop.1c	-----	$2.4 \times 10^6$	7.41	7.8	q- $\omega$
isoprop.2a	-----	$2.4 \times 10^6$	3.9	7.8	Spalart Allmaras
isoprop.2b	-----	$2.4 \times 10^6$	6.93	7.8	Spalart Allmaras
isoprop.2c	-----	$2.4 \times 10^6$	7.41	7.8	Spalart Allmaras
isoprop.3a	LCC	$32 \times 10^6$	16.87	4.25	Spalart Allmaras
isoprop.3b	LCC	$32 \times 10^6$	16.87	8.5	Spalart Allmaras
isoprop.3c	LCC	$32 \times 10^6$	16.87	12.75	Spalart Allmaras
isoprop.3d	LCC	$32 \times 10^6$	16.87	17	Spalart Allmaras
isoprop.3e	LCC	$32 \times 10^6$	16.87	21.25	Spalart Allmaras
<b><i>Submarine (appended and propelled LCC hull – P4381)</i></b>					
fwdsb.1a	LCC	$16 \times 10^6$	8.42	3.33	Spalart Allmaras
fwdsb.1b	LCC	$16 \times 10^6$	8.42	4.32	Spalart Allmaras
fwdsb.1c	LCC	$16 \times 10^6$	8.42	8.63	Spalart Allmaras
fwdsb.2a	LCC	$32 \times 10^6$	16.87	4.25	Spalart Allmaras
fwdsb.2b	LCC	$32 \times 10^6$	16.87	8.5	Spalart Allmaras
fwdsb.2c	LCC	$32 \times 10^6$	16.87	12.75	Spalart Allmaras
fwdsb.2d	LCC	$32 \times 10^6$	16.87	17	Spalart Allmaras
fwdsb.2e	LCC	$32 \times 10^6$	16.87	21.25	Spalart Allmaras
fwdsb.3a	LCC	$48 \times 10^6$	25.32	6.35	Spalart Allmaras
fwdsb.3b	LCC	$48 \times 10^6$	25.32	12.68	Spalart Allmaras
fwdsb.3c	LCC	$48 \times 10^6$	25.32	25.38	Spalart Allmaras

Case Name	Scale*	Reynolds #	Velocity (fps)	Propeller rps	Turbulence Model
fwdsb.4a	LCC	$64 \times 10^6$	33.75	8.43	Spalart Allmaras
fwdsb.4b	LCC	$64 \times 10^6$	33.75	16.88	Spalart Allmaras
fwdsb.4c	LCC	$64 \times 10^6$	33.75	28.33	Spalart Allmaras
cbsb.1a	LCC	$16 \times 10^6$	8.42	-3.35	Spalart Allmaras
cbsb.1b	LCC	$16 \times 10^6$	8.42	-8.33	Spalart Allmaras
cbsb.2a	LCC	$32 \times 10^6$	16.87	-3.33	Spalart Allmaras
cbsb.2b	LCC	$32 \times 10^6$	16.87	-8.33	Spalart Allmaras
cbsb.2c	LCC	$32 \times 10^6$	16.87	-11.67	Spalart Allmaras

\* Small: hull length is 11.278 inches, LCC: hull length is 22.964 feet, Full: hull length is 383.5 feet

## APPENDIX B

### VELOCITY CONTOURS FOR FORWARD PROPELLED SIMULATIONS

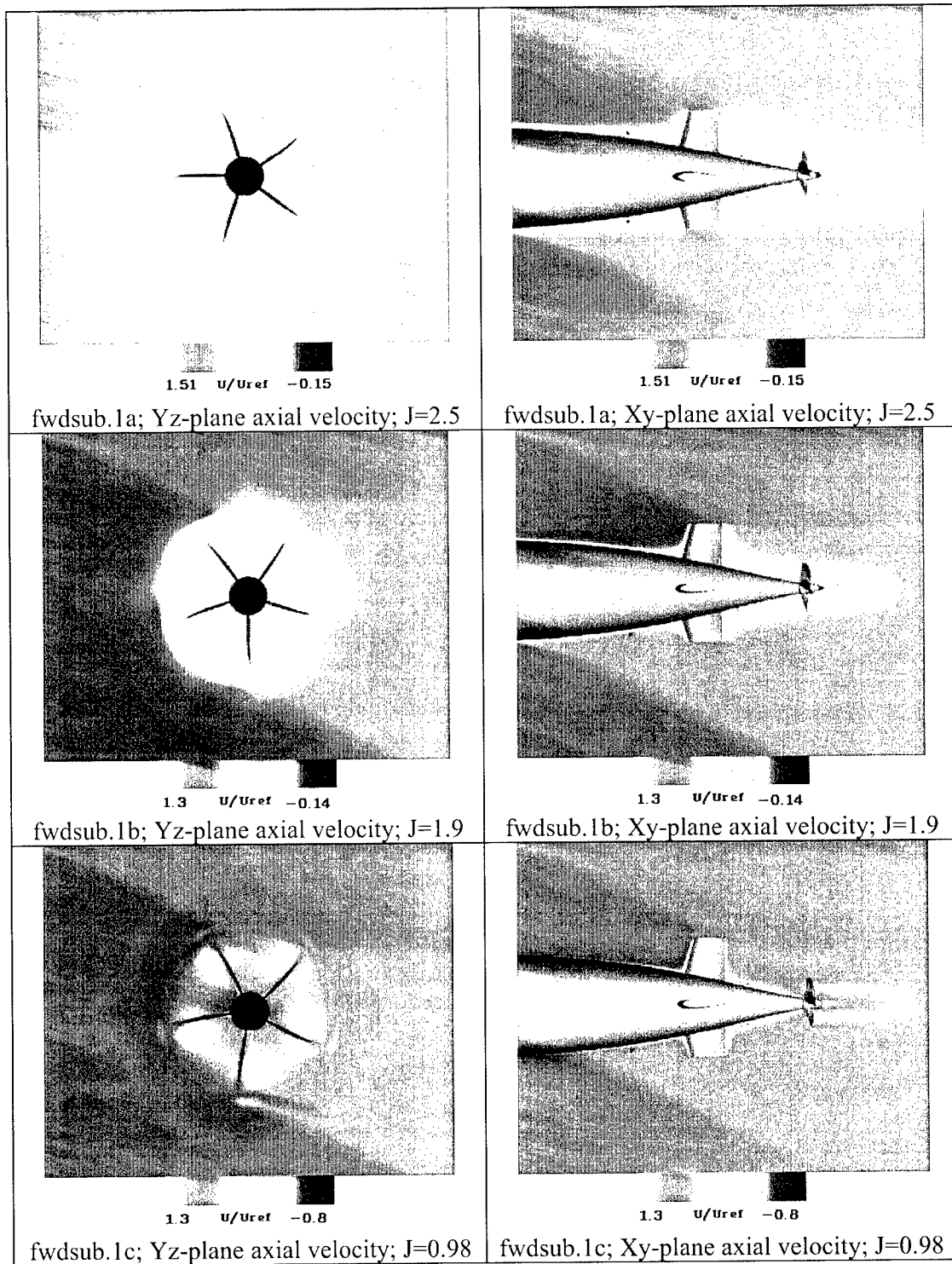
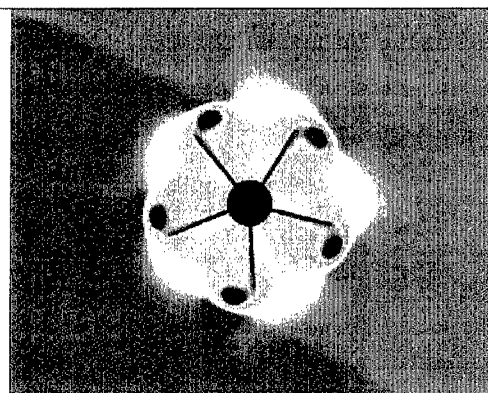
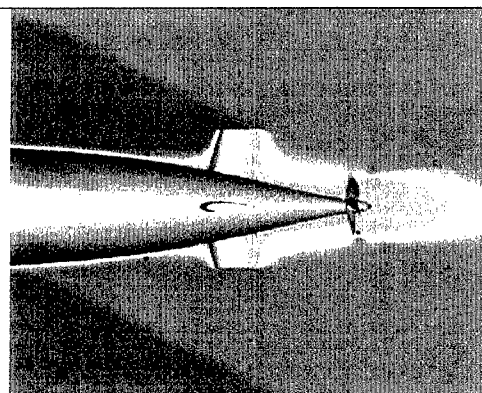
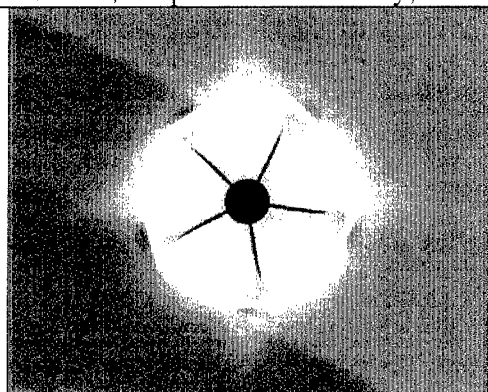
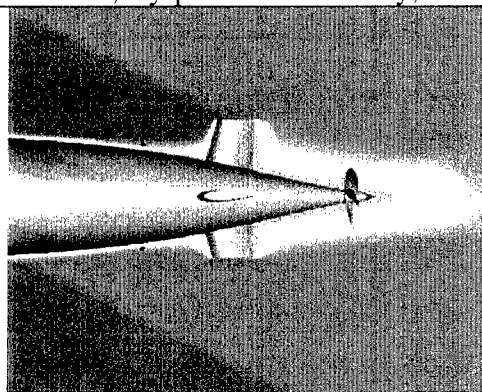
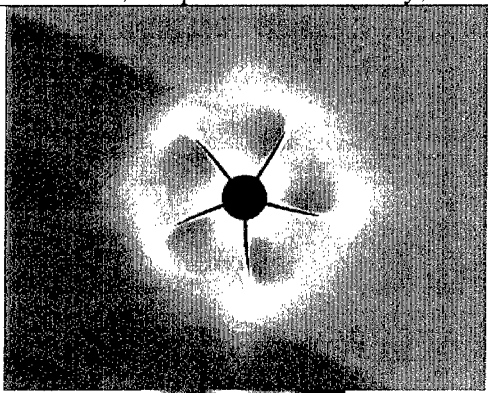
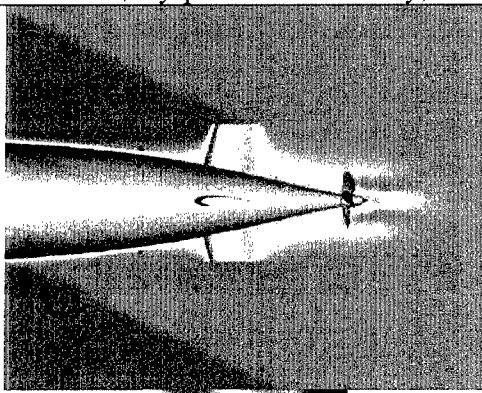
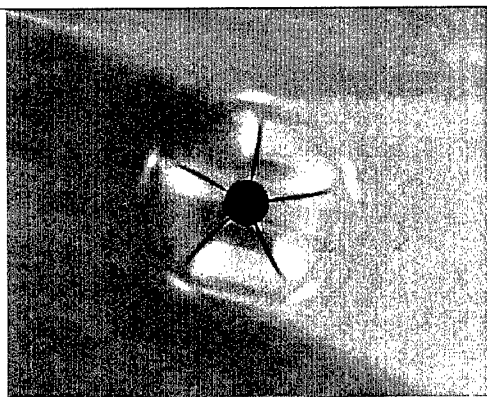


Figure B.1: Velocity contours; 5 knot tunnel speed;  $Re = 16$  million.

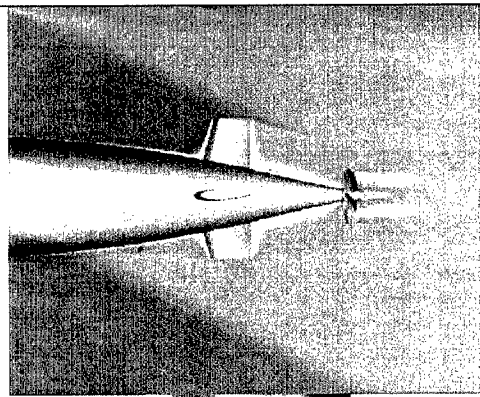
1.3  $u/u_{ref}$  0fwdsb.2a; Yz-plane axial velocity;  $J=3.83$ 1.3  $u/u_{ref}$  0fwdsb.2a; Xy-plane axial velocity;  $J=3.83$ 1.4  $u/u_{ref}$  -0.15fwdsb.2b; Yz-plane axial velocity;  $J=1.9$ 1.4  $u/u_{ref}$  -0.15fwdsb.2b; Xy-plane axial velocity;  $J=1.9$ 1.45  $u/u_{ref}$  -0.3fwdsb.2c; Yz-plane axial velocity;  $J=1.3$ 1.45  $u/u_{ref}$  -0.3fwdsb.2c; Xy-plane axial velocity;  $J=1.3$ Figure B.2: Velocity contours; 10 knot tunnel speed;  $Re = 32$  million.





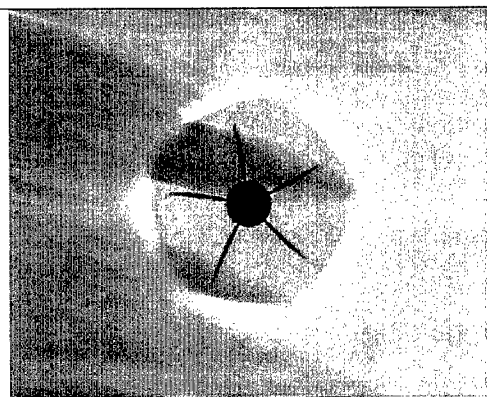
1.3  $u/u_{ref}$  -0.6

fwdsub.2d; Yz-plane axial velocity;  $J=0.98$



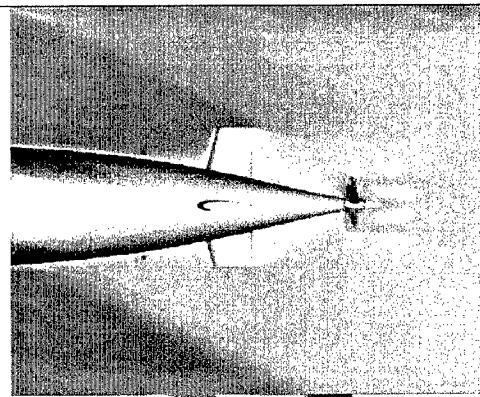
1.3  $u/u_{ref}$  -0.6

fwdsub.2d; Xy-plane axial velocity;  $J=0.98$



2  $u/u_{ref}$  -2

fwdsub.2e; Yz-plane axial velocity;  $J=0.78$



2  $u/u_{ref}$  -2

fwdsub.2e; Xy-plane axial velocity;  $J=0.78$

Figure B.2 (concl'd): Velocity contours; 10 knot tunnel speed;  $Re = 32$  million.

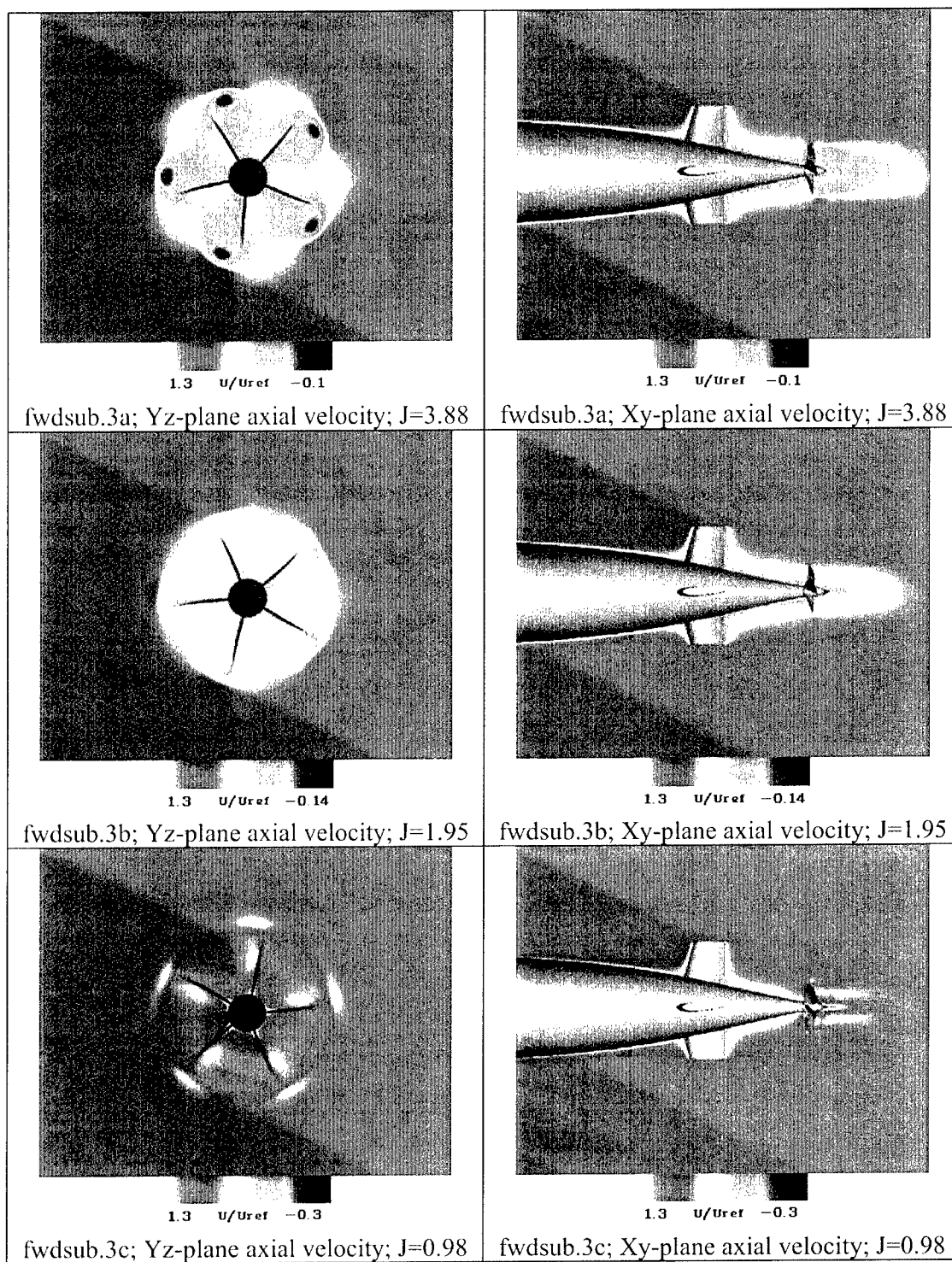


Figure B.3: Velocity profiles; 15 knot tunnel speed;  $Re = 48$  million.

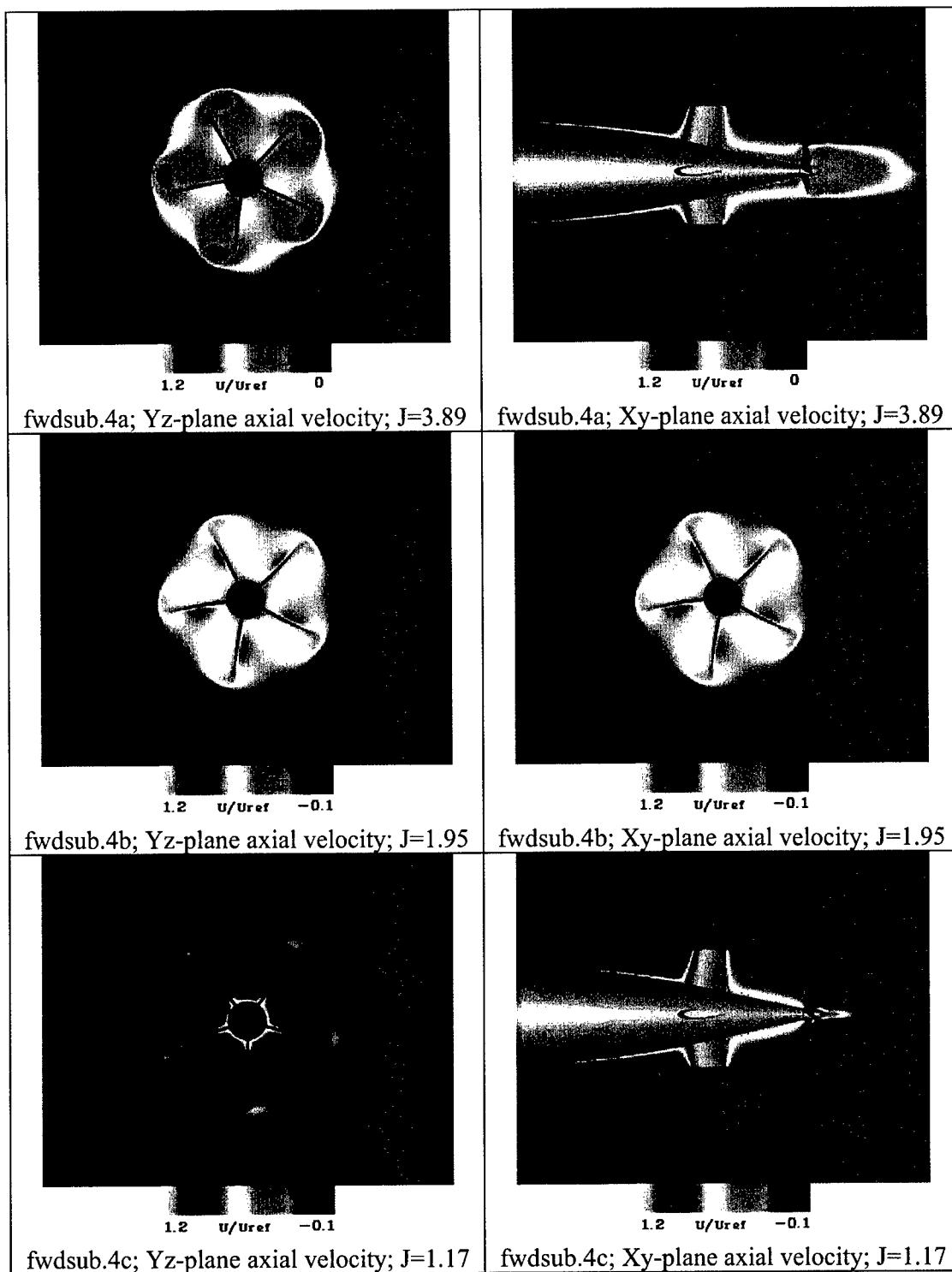


Figure B.4: Velocity contours; 20 knot tunnel speed;  $Re = 64$  million.

This page intentionally left blank.

APPENDIX B

EXPERIMENTAL STUDIES OF THE DRAG OF AN  
AXISYMMETRIC SUBMARINE HULL

By

John Lindsley Freudenthal

A Thesis  
Submitted to the Faculty of  
Mississippi State University  
in Partial Fulfillment of the Requirements  
for the Degree of Master of Science  
in Aerospace Engineering  
in the Department of Aerospace Engineering

Mississippi State, Mississippi

December 2002

EXPERIMENTAL STUDIES OF THE DRAG OF AN  
AXISYMMETRIC SUBMARINE HULL

By

John Lindsley Freudenthal

Approved:

---

David H. Bridges  
Associate Professor of Aerospace  
Engineering (Director of Thesis)

---

Boyd Gatlin  
Associate Professor, Interim Head and  
Graduate Coordinator of the  
Department of Aerospace Engineering

---

Keith Koenig  
Professor of Aerospace Engineering  
(Committee Member)

---

Z. U. A. Warsi  
Professor of Aerospace Engineering  
(Committee Member)

---

A. Wayne Bennett  
Dean of the College of Engineering

Name: John Lindsley Freudenthal

Date of Degree: December 13, 2002

Institution: Mississippi State University

Major Field: Aerospace Engineering

Major Professor: Dr. David H. Bridges

Title of Study: EXPERIMENTAL STUDIES OF THE DRAG OF AN  
AXISYMMETRIC SUBMARINE HULL

Pages in Study: 79

Candidate for Degree of Master of Science

The purpose of these studies was to measure the drag coefficient of a small model submarine to add data to a Reynolds number study. First, a laser Doppler velocimeter (LDV) was used to measure the flow characteristics of the Mississippi State University water tunnel. The velocity and turbulence intensity profiles were measured for a range of freestream velocities of 8.6 m/s to 10.7 m/s. Several wake velocity profiles were taken for a model submarine at downstream distances of  $x/d = 10$  to  $x/d = 28$ , with a freestream velocity of 8.6 m/s. A formula for the drag coefficient that uses only mean velocity measurements in the wake was derived for an axisymmetric body using the assumptions of a self-similar wake and a power law behavior of the wake scales. The experimental drag coefficient results are compared to computational fluid dynamic (CFD) solutions.

## DEDICATION

To Mom and Dad



## ACKNOWLEDGEMENTS

I wish to express my gratitude to Dr. David Bridges for his guidance and support throughout this project. I would also like to recognize Dr. Keith Koenig's support in both the theoretical and practical aspects of this research. I also would like to thank Jim Schrock for his extensive help with reassembling the water tunnel and troubleshooting all of its problems. A number of students (whether they worked for the Department or not) helped out along the way. In particular, I would like to thank Viva Austin for her enthusiastic willingness to help in any possible way.

This research would not have been possible without the funding by the Office of Naval Research DEPSCoR Grant No. N00014-99-1-0534. Dr. L. Patrick Purtell was the program monitor.

I would like to thank my fiancé, Sharon Johnston, for her encouragement and inspiration. I cannot imagine having finished this thesis without her influence. She helped me to see that I could not carry my burdens alone, but that I must give them to God. God has used my time at MSU to bring me back into a closer relationship with Him. This is the greatest lesson that I carry from this place.

I would like to thank my parents and Sharon's parents for their support and encouragement. Also, the support of the entire Aerospace Department "family" has been great—I have many new friends.

## TABLE OF CONTENTS

	Page
DEDICATION.....	ii
ACKNOWLEDGEMENTS.....	iii
LIST OF TABLES.....	vi
LIST OF FIGURES .....	vii
LIST OF SYMBOLS .....	x
 CHAPTER	
I. INTRODUCTION.....	1
II. BACKGROUND .....	3
2.1 Total-Head Loss Measurement of the Drag of a Body.....	3
2.2 Momentum Defect Measurement of the Drag of an Axisymmetric Body .....	5
2.2.1 Derivation of Drag Coefficient .....	5
2.2.2 Self-Preserving Flow .....	14
III. EXPERIMENTAL APPARATUS .....	18
3.1 Water Tunnel .....	18
3.1.1 Water Tunnel History and Description .....	18
3.1.2 Repainting of Corners, Turning Vanes, and Drive Section.....	20
3.1.3 Drive Bearing Modifications .....	21
3.1.4 Other Tunnel Modifications.....	23
3.1.5 Propeller Knocking .....	24
3.2 Laser Doppler Velocimeter .....	24
3.3 LDV Calibration Apparatus .....	26
3.3.1 Calibration Apparatus Description .....	26
3.3.2 Uncertainty of Disk Radius Measurement.....	27
3.3.3 Uncertainty in Radial Positioning During Calibration.....	29

CHAPTER	Page
3.3.4 Positioning the Measurement Volume in $z$ .....	30
3.3.5 Uncertainty in Angular Velocity Measurement .....	30
3.3.6 Random Uncertainty of LDV Velocity Measurement .....	31
3.3.7 Calibration Results .....	32
3.4 Submarine Model and Mount .....	35
IV. EXPERIMENTAL PROCEDURE AND RESULTS .....	37
4.1 LDV Configuration .....	37
4.1.1. LDV Alignment with Water Tunnel .....	37
4.1.2 Laser Beam Refraction Correction .....	39
4.2 Test Section Flow Characteristics .....	39
4.3 Submarine Model Wake Experiments .....	49
4.3.2 Curve Fits to Wake Profile Data .....	59
4.3.3 Drag Coefficient of Model .....	64
V. CONCLUSIONS AND RESULTS .....	75
5.1 Conclusions .....	75
5.2 Recommendations .....	77
BIBLIOGRAPHY .....	79

## LIST OF TABLES

TABLE		Page
4.1	PMT high voltage settings for test section regions.....	40
4.2	Curve fit results for each day's experiment. ....	65
4.3	Curve fit results from composite data sets.....	72

## LIST OF FIGURES

FIGURE	Page
2.1 Control volume representation.....	6
3.1 Diagram of MSU water tunnel (from Wells <sup>5</sup> ).....	19
3.2 Random uncertainties of LDV mean velocity measurements.....	32
3.3 LDV calibration plot with upper and lower uncertainty bands.....	34
3.4 Calibration plot of expected water tunnel test speed range, with uncertainty bands and error bars on the data points.....	34
3.5 Submarine model drawing showing mounting details.....	35
4.1 Velocity profiles in the test section at motor input speed of 500 rpm. ....	41
4.2 Velocity profiles in the test section at motor input speed of 550 rpm. ....	41
4.3 Velocity profiles of the water tunnel at motor input speed of 600 rpm. ....	42
4.4 Velocity profiles of the water tunnel at motor input speed of 630 rpm. ....	42
4.5 Velocity profiles taken at $x/L = 0.492$ , 500 rpm, showing typical velocity shift and non-uniform profile. ....	43
4.6 Local turbulence intensity factors at $x/L = 0.492$ , 500 rpm. ....	45
4.7 Local turbulence intensity factors at $x/L = 0.492$ , 550 rpm. ....	45
4.8 Local turbulence intensity factors at $x/L = 0.492$ , 600 rpm. ....	46
4.9 Typical velocity profile with error bars, $x/L = 0.492$ , 500 rpm. ....	46
4.10 Typical velocity profile with error bars, $x/L = 0.492$ , 550 rpm. ....	47
4.11 Typical velocity profile with error bars, $x/L = 0.492$ , 600 rpm. ....	47

FIGURE	Page
4.12 Typical velocity profile with error bars, $x/L = 0.492$ , 600 rpm, repeated with full velocity scale to show relative magnitude of errors. ....	48
4.13 Mean test section velocity at $x/L = 0.125$ versus motor input speed. Error bars are shown on the data points, and uncertainty bands are shown around the curve fit. ....	48
4.14 Mean velocity profiles from 5/16/02. ....	51
4.15 Turbulence intensity from 5/16/02.....	51
4.16 Mean velocity profiles from 5/17/02. ....	52
4.17 Turbulence intensity from 5/17/02.....	52
4.18 Mean velocity profiles from 5/22/02. ....	53
4.19 Turbulence intensity from 5/22/02.....	53
4.20 Mean velocity profiles from 5/30/02. ....	54
4.21 Turbulence intensity from 5/30/02.....	54
4.22 Mean velocity profiles from 6/4/02. ....	55
4.23 Turbulence intensity from 6/4/02.....	55
4.24 Velocity profile with typical uncertainties, 5/22/02, $x/d = 10$ . ....	57
4.25 Velocity profile with typical uncertainties, 5/22/02, $x/d = 16$ . ....	58
4.26 Velocity profile with typical uncertainties, 5/22/02, $x/d = 25$ . ....	58
4.27 Similarity profiles for 5/22/02 data.....	61
4.28 Similarity profiles for 6/4/02 data.....	61
4.29 Freestream velocity $U_0$ outside of wake. ....	62
4.30 Velocity deficit $u_0/U_0$ .....	63
4.31 Wake width parameter $b/d$ .....	63
4.32 Comparison of wakes profiles at $x/d = 16$ for all five data sets. ....	66

FIGURE	Page
4.33 Test section freestream velocity behavior over a period of decreasing static pressure.....	67
4.34 Test section freestream velocity behavior over a period of constant static pressure of 46 psi.....	68
4.35 Comparison of averaged velocity deficit parameter from the first three days' experiments to the power law.....	70
4.36 Comparison of averaged wake width parameter from the first three days' experiments to the power law.....	70
4.37 Comparison of averaged velocity deficit parameter from the last two days' experiments to the power law.....	71
4.38 Comparison of averaged wake width parameter from the last two days' experiments to the power law.....	71
4.39 Comparison of experimental results with computational results of Cash.....	73
4.40 Averaged experimental results for MSU model and computational results of Cash for three different submarine lengths. ....	74

## LIST OF SYMBOLS

$B$	systematic uncertainty
$b$	wake half-width parameter
$C_D$	drag coefficient
$\Delta C_{D,p}$	drag coefficient contribution of pressure gradient
$c_l$	power law constant of proportionality for wake length scale
$c_p$	pressure coefficient
$c_{p_0}$	pressure coefficient outside of wake
$c_{p_w}$	pressure coefficient within wake
$c_u$	power law constant of proportionality for wake velocity scale
$D$	drag force
$d$	maximum body diameter
$d\vec{S}$	surface element vector
$\hat{e}$	unit vector
$F_p$	pressure reaction force
$H$	total head
$L$	length of test section
$L_{sub}$	length of submarine model
$l_0$	wake length scale
$P$	random uncertainty
$p$	pressure
$p_\infty$	pressure in freestream
$p_0$	pressure outside of wake
$R$	radius of control volume, disk, test section
$t$	time



$U, V, W$	cartesian velocity components
$u, v, w$	polar cylindrical velocity components
$u', v', w'$	polar cylindrical velocity fluctuating components
$U$	total uncertainty
$U_0$	velocity outside of wake
$U_\infty$	velocity in freestream
$\underline{u}$	velocity vector
$u_0$	wake velocity scale
$\nabla$	control volume
$\nabla_{body}$	volume of body
$x, \theta, r$	polar cylindrical coordinates
$x, y, z$	cartesian coordinates
$x_0$	curve fit origin
$z_{cl}$	centerline of test section, traverse coordinate system
$z_0$	centerline of wake, from curve fit
$\delta_1$	wake displacement thickness
$\Omega$	motor input speed
$\mu$	absolute viscosity
$\nu$	kinematic viscosity
$\rho$	density
$\underline{\tau}$	viscous stress tensor

## CHAPTER I

### INTRODUCTION

In recent years, the study of Reynolds number effects has become an increasingly important area of research. The extrapolation of data from a large experimental model to a full-scale prototype is extremely critical in predicting the performance of the prototype. Often the large model is still much smaller than the prototype. This is particularly true of naval vessels, including submarines. The Office of Naval Research funded a Reynolds number study to examine the capability of computational fluid dynamics (CFD) solutions to track large changes in Reynolds number. Three length scales of submarine hull forms were to be used in this study. A small model was to be constructed and tested in a water tunnel facility located at Mississippi State University. This model was to be identical in shape to a model tested in the U. S. Navy's Large Cavitation Channel (LCC), but the LCC model was to be over twenty times larger. The flow conditions of speed and pressure were to be the same in both experiments. CFD solutions were to be obtained for the small and large models, as well as for the full-scale submarine, which is over twenty times larger than the LCC model. It was hoped that the information obtained concerning how well the CFD solutions tracked the changes in Reynolds number when going from small model to large model would be useful in predicting how well the CFD solutions would track the next jump in order of Reynolds number magnitude when going from the

large LCC model to the full-scale submarine. The objective of the current experiment was to obtain drag coefficient measurements of the smaller model submarine.

The Mississippi State University Department of Aerospace Engineering has performed hydrodynamic research in conjunction with the United States Navy for several years. The water tunnel in the Mississippi State Patterson Engineering Laboratories has been renovated to perform research work with the LCC. The first phase of research studied the effect of pressure tap hole size on static pressure measurements. After this first phase of testing, the water tunnel needed many repairs. The protective coating was replaced in many sections of the water tunnel. Also, the modification of the interior drive shaft bearing assembly and the addition of a reverse thrust bearing solved a problem that had developed with the bearings being burned out during operation. These modifications were completed before the current experiment was undertaken.

The Aerospace Engineering Department acquired a Laser Doppler Velocimeter (LDV) for use with the water tunnel, among other things. A calibration device consisting of a precisely controlled rotating disk was built for the LDV. Once the water tunnel was operational, the LDV was used to measure the flow characteristics of the water tunnel test section. After these tests were completed, a submarine model was mounted in the test section and wake velocity profiles were measured at several stations downstream. The drag coefficient of the submarine model was then computed using these wake velocity profiles. The calculated drag coefficients of the model submarine were in fairly good agreement with the CFD solutions. During the final stages of the experiment, a section of the water tunnel failed under pressure, effectively ending the experiment.

## CHAPTER II

### BACKGROUND

#### 2.1 Total-Head Loss Measurement of the Drag of a Body

The classical approach to the drag measurement of a body has been to use a pitot probe to measure the total pressure distribution of the wake behind an experimental model. Two of the earliest methods were derived by Betz and by Jones, as discussed in *Modern Developments in Fluid Dynamics*<sup>1</sup>. Betz was the first to develop the technique of determining the drag of an airplane wing by measuring the pressure distribution of the wake at a short distance behind the wing's trailing edge. From the momentum equation, the drag of a wing can be calculated using the flow properties through two parallel planes at right angles to the mean flow:

$$D = \iint (p_1 + \rho U_1^2) dS_1 - \iint (p_2 + \rho U_2^2) dS_2, \quad (2.1)$$

where the subscripts 1 and 2 denote the front plane and rear plane respectively. Betz introduced the total-head equations and a hypothetical flow to transform the above equation to an integral requiring measurements on the rear plane only:

$$D = \iint_r (H_1 - H_2) dS + \frac{1}{2} \rho \iint_r (U_2^* - U_2)(U_2^* + U_2 - 2U_0) dS + \frac{1}{2} \rho \iint \{ (V_2^2 + W_2^2) - (V_1^2 + W_1^2) \} dS, \quad (2.2)$$

where

$$U_2 = \sqrt{\frac{2(H_2 - p_2)}{\rho}}, \quad (2.3)$$

and

$$U_2^* = \sqrt{\frac{2(H_1 - p_2)}{\rho}}, \quad (2.4)$$

and the region  $T$  is the region of the wake only. The sum of the first two integrals of equation (2.2) yields the profile drag, and the third integral yields the induced drag. The second term in equation (2.2) is a correction factor that is important in regions close to the body. It is small when the measurement plane is at a considerable distance from the body. If there is no lift being produced by the body and the measurement plane is at a certain distance downstream of the body, the profile drag is simply the integration of the head deficit of the wake:

$$D = \iint_T (H_1 - H_2) dS. \quad (2.5)$$

B. M. Jones developed a similar method using measurements in a plane far downstream of a body. For a body at zero-lift conditions, at a certain distance downstream the pressure is uniformly equal to the freestream pressure  $p_\infty$  and the velocity is uniformly equal to the freestream velocity  $U_\infty$ , except in the wake. The profile drag of the body is simply an integration over the wake region:

$$D = \rho \iint U_3 (U_\infty - U_3) dS_3, \quad (2.6)$$

where  $U_3$  is the velocity in area element  $dS_3$  of the wake. The total head at this downstream plane is

$$H_2 = \frac{1}{2} \rho U_3^2 + p_\infty. \quad (2.7)$$

Defining the function  $g$  such that

$$g = \left[ 1 - \frac{(H_\infty - H_2)}{\frac{1}{2} \rho U_\infty^2} \right], \quad (2.8)$$

equation (2.6) reduces to the form

$$D = \frac{1}{2} \rho U_\infty^2 \iint 2g^{1/2} (1 - g^{1/2}) dS_3. \quad (2.9)$$

At a certain distance downstream of the body,  $H_2 \rightarrow H_\infty$  and  $g \rightarrow 1$ , and the above equation (2.9) can be written approximately

$$D = \frac{1}{2} \rho U_\infty^2 \iint (1 - g) dS_3 = \iint (H_\infty - H_2) dS_3, \quad (2.10)$$

which is the same form as equation (2.5).

## 2.2 Momentum Defect Measurement of the Drag of an Axisymmetric Body

### 2.2.1 Derivation of Drag Coefficient

In the current experiments, it was not possible to make pressure measurements in the wake of the test model. Only velocity measurements were possible with the LDV system, which makes local velocity measurements at the intersection of two crossed laser beams. Because the test section of the water tunnel was cylindrical, the LDV was only able to measure points lying on the horizontal transverse plane that bisected the test

section through the sides. This limitation was imposed by the requirement that the each laser beam must have the same incidence angle when entering the cylindrical test section. Since a full velocity field cannot be measured with the cylindrical test section, the flow was necessarily assumed to be axially symmetric. Because of these limitations, it was necessary to derive a formula for the drag coefficient of an axisymmetric body that only made use of velocity measurements to compute the drag coefficient. The following derivation closely follows the procedure used by Dimotakis<sup>2</sup> for a Cartesian coordinate system and a nominally two-dimensional flow.

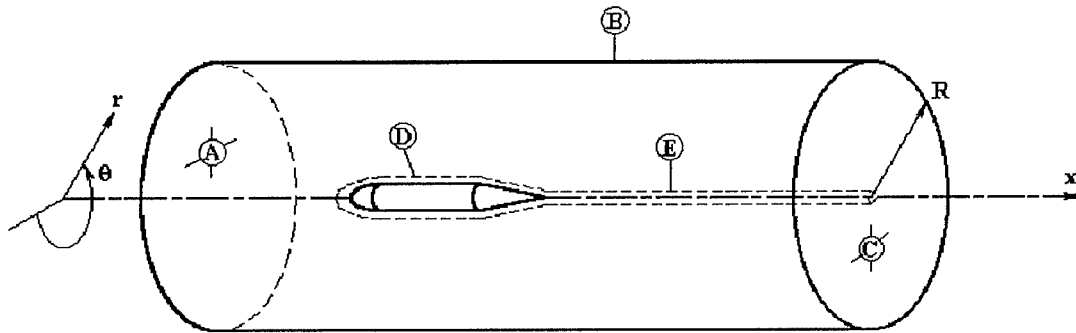


Figure 2.1: Control volume representation.

Consider an axisymmetric body located along the  $x$ -axis. The body is surrounded by a cylindrical volume  $\mathcal{V}$  along the  $x$ -axis whose surfaces are  $ABCDE$ , as shown in Figure 2.1. Surface  $A$  is the transverse plane upstream of the submerged body, where uniform freestream conditions are assumed to apply. Surface  $B$  is a streamtube surrounding the submerged body; surface  $C$  is the transverse plane downstream of the

body; surface D is the fluid surface adjacent to the body; and surface E is a cylindrical surface of infinitesimally small diameter extending along the x-axis from surface D to surface C.

The Navier-Stokes equations are

$$\text{div } \underline{u} = 0, \quad (2.11)$$

and

$$\frac{\partial}{\partial t} \underline{u} + \nabla \cdot \underline{uu} + \frac{1}{\rho} (\nabla p - \nabla \cdot \underline{\tau}) = 0, \quad (2.12)$$

where  $\underline{u}$  is the velocity vector,  $\rho$  is the fluid density,  $p$  is the pressure, and  $\underline{\tau}$  is the viscous stress tensor. Integrating the momentum equation with respect to the interior volume  $V$  and applying Gauss' theorem, this becomes

$$\frac{\partial}{\partial t} \int_V \underline{u} dV + \int_S \underline{uu} \cdot d\underline{S} + \frac{1}{\rho} \int_S (p - p_\infty) d\underline{S} - \frac{1}{\rho} \int_S \underline{\tau} \cdot d\underline{S} = 0, \quad (2.13)$$

where  $d\underline{S}$  is a vector directed along the outward surface normal, of magnitude equal to the surface element  $dS$ ; and the freestream pressure  $p_\infty$  is chosen as the origin in pressure. The various operators and vectors in equation (2.13) are defined in cylindrical coordinates:

$$\text{Gradient operator} \quad \nabla \equiv \hat{e}_x \frac{\partial}{\partial x} + \frac{\hat{e}_\theta}{r} \frac{\partial}{\partial \theta} + \hat{e}_r \frac{\partial}{\partial r} \quad (2.14)$$

$$\text{Velocity vector} \quad \underline{u} = \hat{e}_x u + \hat{e}_\theta v + \hat{e}_r w \quad (2.15)$$

$$\text{Surface element vector} \quad d\underline{S} = \hat{e}_x dS_x + \hat{e}_\theta dS_\theta + \hat{e}_r dS_r \quad (2.16)$$



The surface element magnitudes are further defined:

$$dS_x = r d\theta dr; \quad (2.17)$$

$$dS_\theta = dr dx; \quad (2.18)$$

$$dS_r = r d\theta dx. \quad (2.19)$$

The viscous stress tensor  $\underline{\underline{\tau}}$  is defined for incompressible flow as

$$\underline{\underline{\tau}} = \mu \left[ \nabla \underline{u} + (\nabla \underline{u})^T \right], \quad (2.20)$$

where  $\mu$  is the absolute viscosity. When  $\underline{\underline{\tau}}$  is expanded in cylindrical coordinates, it is written as:

$$\begin{aligned} \underline{\underline{\tau}} = \mu \left\{ 2 \frac{\partial w}{\partial r} \hat{e}_r \hat{e}_r + \left( \frac{1}{r} \frac{\partial w}{\partial \theta} + \frac{\partial v}{\partial r} \right) \hat{e}_r \hat{e}_\theta + \left( \frac{\partial w}{\partial x} + \frac{\partial u}{\partial r} \right) \hat{e}_r \hat{e}_x + \left( \frac{\partial v}{\partial r} + \frac{1}{r} \frac{\partial w}{\partial \theta} \right) \hat{e}_\theta \hat{e}_r + \right. \\ \left. + \left( \frac{2}{r} \frac{\partial v}{\partial \theta} \right) \hat{e}_\theta \hat{e}_\theta + \left( \frac{\partial v}{\partial x} + \frac{1}{r} \frac{\partial u}{\partial \theta} \right) \hat{e}_\theta \hat{e}_x + \left( \frac{\partial u}{\partial r} + \frac{\partial w}{\partial x} \right) \hat{e}_x \hat{e}_r + \right. \\ \left. + \left( \frac{1}{r} \frac{\partial u}{\partial \theta} + \frac{\partial v}{\partial x} \right) \hat{e}_x \hat{e}_\theta + 2 \frac{\partial u}{\partial x} \hat{e}_x \hat{e}_x \right\} \end{aligned} \quad (2.21)$$

When the cylindrical coordinate operators and vectors are substituted into equation (2.13) and dotted with  $\hat{e}_x$ , the x-component of the momentum equation is obtained:

$$\begin{aligned} \frac{\partial}{\partial t} \int_V u dV + \int_S u w dS_r + \int_S u v dS_\theta + \int_S u u dS_x + \frac{1}{\rho} \int_S (p - p_\infty) dS_x + \\ - \nu \int_S \left( \frac{\partial u}{\partial r} + \frac{\partial w}{\partial x} \right) dS_r - \nu \int_S \left( \frac{1}{r} \frac{\partial u}{\partial \theta} + \frac{\partial v}{\partial x} \right) dS_\theta - \nu \int_S \left( 2 \frac{\partial u}{\partial x} \right) dS_x = 0 \end{aligned} \quad (2.22)$$

Taking the time average of the equation eliminates the time derivative term:

$$\begin{aligned} \int_S \overline{u} w dS_r + \int_S \overline{u} v dS_\theta + \int_S \overline{u} u dS_x + \frac{1}{\rho} \int_S (\bar{p} - p_\infty) dS_x - \nu \int_S \left( \frac{\partial \overline{u}}{\partial r} + \frac{\partial \overline{w}}{\partial x} \right) dS_r + \\ - \nu \int_S \left( \frac{1}{r} \frac{\partial \overline{u}}{\partial \theta} + \frac{\partial \overline{v}}{\partial x} \right) dS_\theta - \nu \int_S \left( 2 \frac{\partial \overline{u}}{\partial x} \right) dS_x = 0 . \end{aligned} \quad (2.23)$$

At this point it is helpful to decompose each surface integral to the sum of the integrals over each sub-surface A, B, C, D, E; i.e.,

$$\int_S = \int_A + \int_B + \int_C + \int_D + \int_E . \quad (2.24)$$

The integrals over surface E are zero because surface E has been chosen to be a streamtube of infinitesimally small diameter across which there is no flux. The integral over surface D represents the drag force per unit mass per unit volume that the fluid control volume  $\mathcal{V}$  exerts on the body in the x-direction. The resulting equation is:

$$\begin{aligned} \frac{D}{\rho} = - \int_B \overline{u} w R d\theta dx - \left\{ \int_A + \int_C \right\} \overline{u}^2 r d\theta dr - \frac{1}{\rho} \left\{ \int_A + \int_C \right\} (\bar{p} - p_\infty) r d\theta dr + \\ + \nu \int_B \left( \frac{\partial \overline{u}}{\partial r} + \frac{\partial \overline{w}}{\partial x} \right) R d\theta dx + 2\nu \left\{ \int_A + \int_C \right\} \frac{\partial \overline{u}}{\partial x} r d\theta dr , \end{aligned} \quad (2.25)$$

where  $R$  is the radius of the cylindrical control volume. If the maximum body diameter  $d$  is the characteristic length of the submerged body, and equation (2.25) is divided by

$$\frac{1}{2} U_\infty^2 \frac{\pi}{4} d^2 , \text{ then:}$$

$$\begin{aligned}
\frac{D}{\frac{1}{2}\rho U_\infty^2 \frac{\pi}{4} d^2} = & \frac{-8}{\pi d^2 U_\infty^2} \int_B \overline{uw} R d\theta dx - \frac{8}{\pi d^2 U_\infty^2} \left\{ \int_A + \int_C \right\} \overline{u^2} r d\theta dr + \\
& - \frac{1}{\frac{1}{2}\rho U_\infty^2 \frac{\pi}{4} d^2} \left\{ \int_A + \int_C \right\} (\bar{p} - p_\infty) r d\theta dr + \\
& + \frac{8\nu}{\pi d^2 U_\infty^2} \int_B \left( \frac{\partial \bar{u}}{\partial r} + \frac{\partial \bar{w}}{\partial x} \right) R d\theta dx + \frac{16\nu}{\pi d^2 U_\infty^2} \left\{ \int_A + \int_C \right\} \frac{\partial \bar{u}}{\partial x} r d\theta dr.
\end{aligned} \tag{2.26}$$

The drag coefficient of the body is defined as

$$C_D = \frac{D}{\frac{1}{2}\rho U_\infty^2 \frac{\pi}{4} d^2}, \tag{2.27}$$

and the time averaged pressure coefficient  $\bar{c}_p$  is defined as

$$\bar{c}_p = \frac{\bar{p} - p_\infty}{\frac{1}{2}\rho U_\infty^2}. \tag{2.28}$$

Applying these definitions, equation (2.26) becomes:

$$\begin{aligned}
C_D = & \frac{-8}{\pi d^2} \int_B \frac{\overline{uw}}{U_\infty^2} R d\theta dx - \frac{8}{\pi d^2} \left\{ \int_A + \int_C \right\} \frac{\overline{u^2}}{U_\infty^2} r d\theta dr - \frac{4}{\pi d^2} \left\{ \int_A + \int_C \right\} \bar{c}_p r d\theta dr + \\
& + \frac{8\nu}{\pi d^2 U_\infty^2} \int_B \left( \frac{\partial \bar{u}}{\partial r} + \frac{\partial \bar{w}}{\partial x} \right) R d\theta dx + \frac{16\nu}{\pi d^2 U_\infty^2} \left\{ \int_A + \int_C \right\} \frac{\partial \bar{u}}{\partial x} r d\theta dr.
\end{aligned} \tag{2.29}$$

Equation (2.11) is integrated over the control volume  $\mathcal{V}$ , and Gauss' Theorem is applied to obtain:

$$\int_{\mathcal{V}} \nabla \cdot \underline{u} d\mathcal{V} = \int_S \underline{u} \cdot d\underline{S} = 0. \tag{2.30}$$

Expanding equation (2.30) and multiplying by a factor of  $\frac{8}{\pi d^2 U_\infty}$ , the continuity

equation is written in terms of integrals over the sub-surfaces A, B, and C:

$$\frac{8}{\pi d^2 U_\infty} \left\{ \int_A + \int_C \right\} \bar{u} r d\theta dr + \frac{8}{\pi d^2 U_\infty} \int_B \bar{w} R d\theta dx = 0 \quad (2.31)$$

Equation (2.31) can be subtracted from the  $C_D$  equation (2.29):

$$\begin{aligned} C_D = & \frac{-8}{\pi d^2} \int_B \frac{\bar{u}\bar{w} - U_\infty \bar{w}}{U_\infty^2} R d\theta dx - \frac{8}{\pi d^2} \left\{ \int_A + \int_C \right\} \frac{\bar{u}^2 - U_\infty \bar{u}}{U_\infty^2} r d\theta dr + \\ & - \frac{4}{\pi d^2} \left\{ \int_A + \int_C \right\} \bar{c}_p r d\theta dr + \frac{8\nu}{\pi d^2 U_\infty^2} \int_B \left( \frac{\partial \bar{u}}{\partial r} + \frac{\partial \bar{w}}{\partial x} \right) R d\theta dx + \\ & + \frac{16\nu}{\pi d^2 U_\infty^2} \left\{ \int_A + \int_C \right\} \frac{\partial \bar{u}}{\partial x} r d\theta dr . \end{aligned} \quad (2.32)$$

Surface A has been chosen to be far enough upstream of the body such that the velocity and pressure are assumed to be uniform across the surface and equal to the freestream values  $U_\infty$  and  $p_\infty$ , respectively. Thus the second and third terms of equation (2.32) are equal to zero on surface A.

The velocity components  $u$  and  $w$  can be separated into a mean value and a fluctuating part, i.e.:

$$u = \bar{u} + u' ; \quad (2.33)$$

$$w = \bar{w} + w' ; \quad (2.34)$$

$$\overline{u^2} = \bar{u}^2 + \overline{u'^2} ; \quad (2.35)$$

$$\overline{uw} = \bar{u}\bar{w} + \overline{u'w'} . \quad (2.36)$$

The product  $\overline{uw}$  appears only in the integrals over surface B. Surface B has been defined to be a streamtube that lies outside of the regions where disturbances from the wall or the

body are assumed negligible, which implies

$$\bar{w} = \overline{u'w'} = \frac{\partial \bar{w}}{\partial x} = 0 \quad (2.37)$$

on surface B.

Applying the conditions on surfaces A and B, and assuming that the surfaces are far enough away from the body that all mean velocity gradients are negligible, equation (2.32) is reduced to:

$$\begin{aligned} C_D = & \frac{8}{\pi d^2} \left\{ \int_C \right\} \frac{\bar{u}}{U_\infty} \left( 1 - \frac{\bar{u}}{U_\infty} \right) r d\theta dr - \frac{8}{\pi d^2} \left\{ \int_C \right\} \frac{\overline{u'^2}}{U_\infty^2} r d\theta dr + \\ & - \frac{4}{\pi d^2} \left\{ \int_C \right\} \bar{c}_p r d\theta dr. \end{aligned} \quad (2.38)$$

Now define the displacement thickness  $\delta_1$  at the downstream surface C such that

$$(\pi R^2 - \pi \delta_1^2) U_0 \equiv \int_C \bar{u} r d\theta dr; \quad (2.39)$$

$$\delta_1^2 = \frac{1}{\pi} \int_C \left( 1 - \frac{\bar{u}}{U_0} \right) r d\theta dr; \quad (2.40)$$

where  $U_0$  is defined as the velocity outside of the wake at surface C. Since there is no mass flux through surface B, the flow rate through surfaces A and C must be equal:

$$\pi R^2 U_\infty = (\pi R^2 - \pi \delta_1^2) U_0. \quad (2.41)$$

Equation (2.41) can be rearranged to the form:

$$\frac{U_0}{U_\infty} = \frac{1}{1 - \left( \frac{\delta_1}{R} \right)^2}. \quad (2.42)$$

The effects of freestream acceleration due to displacement thickness  $\delta_1$  on the pressure coefficient can be separated from the pressure differences across the wake by dividing the pressure coefficient into two separate components:

$$\bar{c}_p = \frac{\bar{p} - p_\infty}{\frac{1}{2} \rho U_\infty^2} = \frac{p_0 - p_\infty}{\frac{1}{2} \rho U_\infty^2} + \frac{\bar{p} - p_0}{\frac{1}{2} \rho U_\infty^2} = c_{p_0} + \bar{c}_{p_w}, \quad (2.43)$$

where  $c_{p_0}$  is the pressure coefficient of the flow outside of the wake, and  $\bar{c}_{p_w}$  is the time-averaged pressure coefficient of the flow within the wake. Bernoulli's equation can be applied outside of the wake between surfaces A and C:

$$p_0 + \frac{1}{2} \rho U_0^2 = p_\infty + \frac{1}{2} \rho U_\infty^2. \quad (2.44)$$

Using equation (2.42) with equation (2.44),  $c_{p_0}$  can be defined in terms of the displacement thickness:

$$c_{p_0} = -\left(\frac{\delta_1}{R}\right)^2 \frac{2 - \left(\frac{\delta_1}{R}\right)^2}{\left[1 - \left(\frac{\delta_1}{R}\right)^2\right]^2}. \quad (2.45)$$

Using equations (2.45), (2.40), and (2.42) in equation (2.38), the equation for the drag coefficient becomes:

$$C_D = \frac{8}{\pi d^2 \left[1 - \left(\frac{\delta_1}{R}\right)^2\right]^2} \left\{ \int_c^{\bar{u}} \frac{\bar{u}}{U_0} \left(1 - \frac{\bar{u}}{U_0}\right) r d\theta dr - \int_c^{\bar{u}^2} \frac{\bar{u}^2}{U_0^2} r d\theta dr - \frac{\pi \delta_1^4}{2 d^2 R^2} \right\} + \frac{4}{\pi d^2} \int_c^{\bar{c}_{p_w}} \bar{c}_{p_w} r d\theta dr. \quad (2.46)$$

### 2.2.2 Self-Preserving Flow

The generation of a wake behind a body is an example of a developing flow. The velocity deficit of the wake is greater and the width of the wake is smaller near the body, but as the flow moves downstream the velocity deficit decreases and the wake width increases as the wake turbulence dies out. An assumption of self-preserving flow stipulates that the transverse velocity profiles retain the same functional forms at points further downstream of the body, but that the length scales and mean flow property values scale according to the distance downstream of the body. According to Townsend<sup>3</sup>, the definition of a self preserving flow is one in which the variation of a mean value quantity  $M$  in the flow direction must be of the form:

$$M = M_l + m_0(x) \text{func}(r/l_0(x)), \quad (2.47)$$

where the length scale  $l_0$  and the scale of quantity  $m_0$  are functions of  $x$ , and  $M_l$  is the reference mean value.

Assume  $\bar{u}$ ,  $\overline{u'^2}$ , and  $\bar{p}$  have the forms:

$$\bar{u}(r) = U_0 - u_0(x)f(r/l_0(x)); \quad (2.48)$$

$$\overline{u'^2} = u_0^2(x)g(r/l_0(x)); \quad (2.49)$$

$$\bar{p} = p_0 + \frac{1}{2} \rho u_0^2(x) \Pi(r/l_0(x)). \quad (2.50)$$

Introduce the non-dimensional coordinate  $\eta$ :

$$\eta = \frac{r}{l_0(x)}. \quad (2.51)$$

Then,

$$\bar{u}(r) = U_0 - u_0(x)f(\eta), \quad (2.52)$$

$$\overline{u'^2} = u_0^2(x)g(\eta), \text{ and} \quad (2.53)$$

$$\bar{p} = p_0 + \frac{1}{2} \rho u_0^2(x) \Pi(\eta). \quad (2.54)$$

Applying these forms to equation (2.40) and integrating in  $\theta$  results in the displacement thickness in terms of the length and velocity scales, and an integration of the function

$f(\eta)$ :

$$\delta_1^2 = 2 \frac{u_0(x) l_0^2(x)}{U_0} \int_0^{R/l_0} f(\eta) \eta d\eta. \quad (2.55)$$

Now consider the time averaged pressure coefficient of the wake  $\bar{c}_{p_w}$ :

$$\bar{c}_{p_w} = \frac{\bar{p} - p_0}{\frac{1}{2} \rho U_\infty^2}. \quad (2.56)$$

Substituting the equations (2.42) and (2.54) into equation (2.56) yields

$$\bar{c}_{p_w} = \frac{1}{\left[1 - \left(\delta_1/R\right)^2\right]^2} \frac{u_0^2(x)}{U_0^2} \Pi(\eta). \quad (2.57)$$

When the functional forms of equations (2.51) through (2.55), and equation (2.57) are applied to the drag coefficient equation (2.46), the resulting equation is:



$$\begin{aligned}
C_D = \frac{8}{\pi d^2} & \left\{ \int_c l_0^2 \eta d\eta d\theta - \int_c \frac{u_0^2 l_0^2}{U_0^2} f(\eta) \eta d\eta d\theta - \frac{2\pi u_0^2 l_0^4}{R^2 U_0^2} \left( \int_0^{R/l_0} f(\eta) \eta d\eta \right) + \right. \\
& - \int_c \left( 1 - 2 \frac{u_0}{U_0} f(\eta) + \frac{u_0^2}{U_0^2} f^2(\eta) \right) l_0^2 \eta d\eta d\theta - \pi \frac{u_0^2 l_0^2}{U_0^2} \int_0^{R/l_0} \Pi(\eta) \eta d\eta + \\
& \left. - \frac{u_0^2 l_0^2}{U_0^2} \int_c g(\eta)^2 \right\} \left[ 1 - \frac{2}{R^2} \frac{u_0^2 l_0^2}{U_0^2} \int_0^{R/l_0} f(\eta) \eta d\eta \right]^{-2}, \quad (2.58)
\end{aligned}$$

where  $u_0$  and  $l_0$  are implicitly functions of  $x$ .

White<sup>4</sup> states that the velocity defect of a circular wake can be expressed as a Gaussian distribution. The function  $f(\eta)$  is assumed to have the Gaussian form:

$$f(\eta) = e^{-(\ln 2)\eta^2}. \quad (2.59)$$

The presence of the  $(\ln 2)$  factor in the exponent of equation (2.59) references the length scale to the wake half width  $b$ , which is defined as the width of the wake where the velocity deficit is half of the maximum velocity deficit. Substitution for  $f(\eta)$  in equation (2.58) and integration results in:

$$\begin{aligned}
C_D = \frac{16}{d^2} & \left\{ \frac{u_0^2 l_0^2}{2U_0 (\ln 2)} - \frac{u_0^2 l_0^2}{4U_0^2 (\ln 2)} + \frac{u_0^2 l_0^4}{4R^2 U_0^2 (\ln 2)^2} + \right. \\
& \left. - \frac{u_0^2 l_0^2}{U_0^2} \int_c g(\eta) \eta d\eta - \frac{u_0^2 l_0^2}{2U_0^2} \int_0^{R/l_0} \Pi(\eta) \eta d\eta \right\} \left[ 1 - \frac{u_0^2 l_0^2}{R^2 U_0 (\ln 2)} \right]^{-2}. \quad (2.60)
\end{aligned}$$

According to White<sup>4</sup>, the self-similarity parameters  $u_0$  and  $l_0$  of a circular wake with small velocity defect are described by the power law relations  $u_0 \propto x^{-2/3}$  and  $l_0 \propto x^{1/3}$ . A further fit is introduced such that

$$\frac{u_0}{U_0} = c_u \left( \frac{x - x_0}{d} \right)^{-2/3}, \text{ and} \quad (2.61)$$

$$\frac{l_0}{d} = c_l \left( \frac{x - x_0}{d} \right)^{1/3}, \quad (2.62)$$

where  $x_0$  is the origin from the curve fitting process. The drag coefficient equation becomes:

$$C_D = 16 \left[ 1 - \frac{c_u c_l^2}{(\ln 2)} \left( \frac{d}{R} \right)^2 \right]^{-2} \left\{ \frac{c_u c_l^2}{2(\ln 2)} \left[ 1 + \frac{c_u c_l^2}{2(\ln 2)} \left( \frac{d}{R} \right)^2 \right] + \right. \\ \left. - c_u^2 c_l^2 \left( \frac{x - x_0}{d} \right)^{-2/3} \left[ \frac{1}{4(\ln 2)} + \int_c g(\eta) \eta d\eta - \frac{1}{2} \int_0^{R/l_0} \Pi(\eta) \eta d\eta \right] \right\}. \quad (2.63)$$

By extrapolating far enough downstream, the terms containing  $\left( \frac{x - x_0}{d} \right)^{-2/3}$  vanish, and

the equation for drag coefficient becomes:

$$C_D = 16 \left[ 1 - \frac{c_u c_l^2}{(\ln 2)} \left( \frac{d}{R} \right)^2 \right]^{-2} \left\{ \frac{c_u c_l^2}{2(\ln 2)} \left[ 1 + \frac{c_u c_l^2}{2(\ln 2)} \left( \frac{d}{R} \right)^2 \right] \right\}. \quad (2.64)$$

If it is assumed that the body diameter  $d$  is much less than the control volume radius  $R$ , the terms containing  $(d/R)^2$  may be neglected, and the equation for  $C_D$  reduces to

$$C_D \cong \frac{8 c_u c_l^2}{(\ln 2)}. \quad (2.65)$$

## CHAPTER III

### EXPERIMENTAL APPARATUS

#### 3.1 Water Tunnel

##### 3.1.1 Water Tunnel History and Description

The Aerospace Engineering Department Water Tunnel is located in Patterson Engineering Laboratories on the Mississippi State University main campus. A layout drawing of the water tunnel is shown in Figure 3.1. The preliminary design of the water tunnel was begun in 1961 by Dr. Graham Wells <sup>5</sup>. The tunnel was constructed from fiberglass by Aerospace Engineering Department shop technicians, with the largest section diameter being 40 inches, the limit of shop capabilities. The test section is a 4-ft length of 11-inch inner diameter Plexiglas® tube. This results in a contraction ratio of 13.22:1. The length of the contraction is 5 feet, and the contraction was designed for minimal adverse pressure gradient and a uniform exit velocity profile. The original drive system was a Buick V-8 automotive engine with belt drive, but this was later changed to an electric motor retaining the old belt drive, and finally to an efficient direct-drive electric motor. The drive section is located on the first floor of Patterson Laboratory, and the test section is located on the second floor. The current motor has a remote control panel so that the tunnel can be operated from the second floor. The 3-bladed propeller

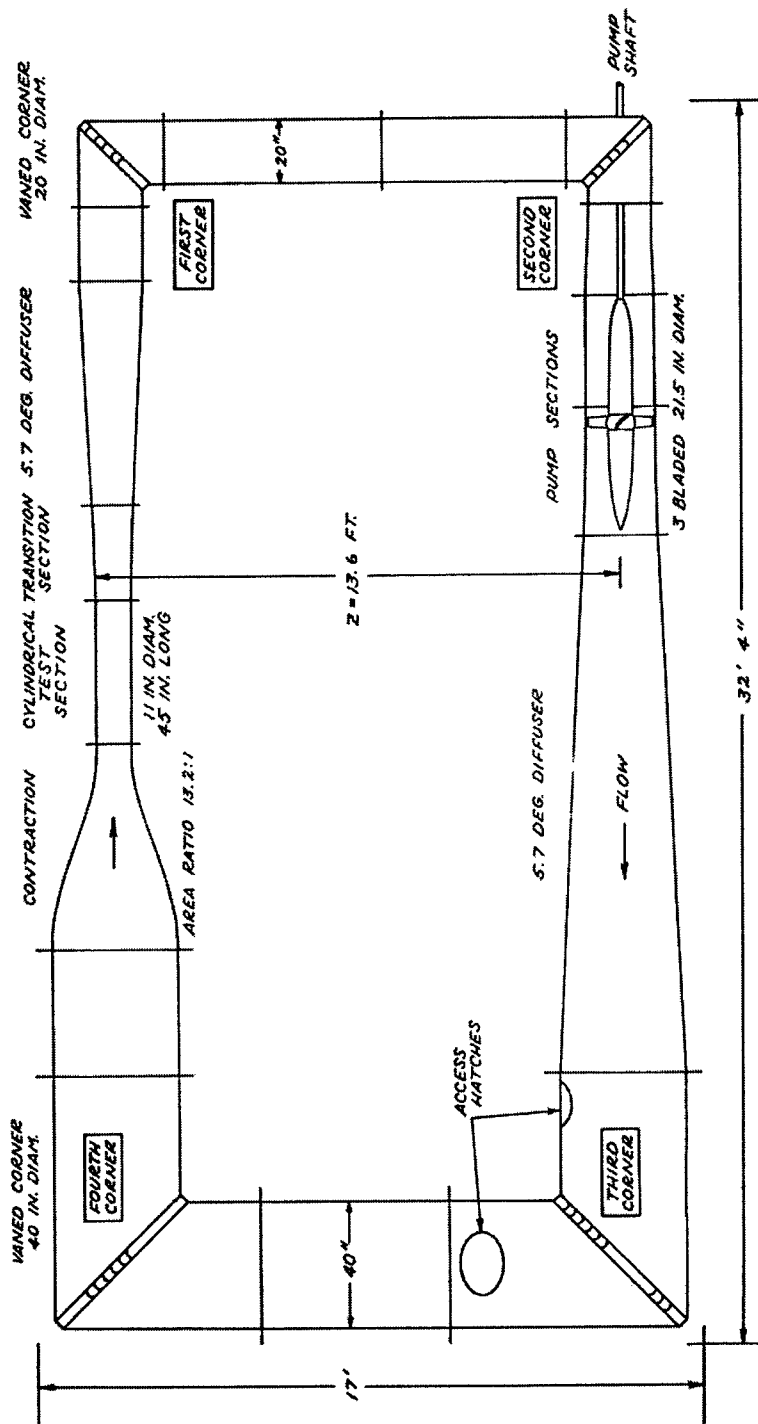


Figure 3.1: Diagram of MSU water tunnel (from Wells<sup>5</sup>).

was reportedly taken from a Second World War amphibious assault vehicle. The water fill line is located on the second floor. The valve to this water line is opened to pressurize the water tunnel to the line pressure, which is usually about 50 psig. The tunnel pressurization and the hydrostatic head suppress cavitation from occurring in the tunnel drive section. The tunnel contains no flow straighteners, but does have turning vanes on each of the corners. Another set of tunnel segments consisting of contraction, test section, and diffuser were built to study nominally two-dimensional flows, but these sections were never fitted into the tunnel and are in storage.

The primary motivation for the construction of the water tunnel at MSU was to attract hydrodynamic research from the submarine and shipbuilding industries, which were booming in the 1950's and 1960's as the modern nuclear submarine was being developed. The facility never saw any of this research, and for most of the 1980's and the 1990's the tunnel was not operated nor maintained. It was renovated in the late 1990's to support research at the new U.S. Navy Large Cavitation Channel (LCC) in Memphis, Tennessee. The first experiments performed after the renovation studied the effect of tap hole size on static pressure measurements in the test section <sup>6</sup>. During these experiments a number of problems developed with the tunnel that required further work, and the tunnel was taken apart.

### 3.1.2 Repainting of Corners, Turning Vanes, and Drive Section

At the end of the previous testing on the water tunnel, it was noticed that certain things had to be repaired. Although the entire tunnel interior had received a new finish of four coats of Duratec® vinyl ester, the finish on the tunnel corners, turning vanes, and

drive section had peeled off. It was necessary to recoat these corner sections to protect the fiberglass structure from water penetration. Additional coats of Interlux InterProtect® epoxy paint were applied to the tunnel drive section and the third corner downstream of the test section. InterProtect® is formulated to prevent water penetration into fiberglass boat hulls.

### 3.1.3 Drive Bearing Modifications

A more serious problem that developed during the previous testing of the tunnel was bearing overheating and burnout. The water-cooled Cutless bearing inside the drive section of the tunnel was completely burned out. When the drive section was disassembled, it was discovered that the step of the drive shaft had been cut into by the edge of the brass Cutless bearing. It was determined that the location of the shaft had shifted downstream relative to the support bearings, causing the step to butt against the brass Cutless bearing. This not only cut off the water flow through the bearing, but damaged the stainless steel shaft as well. To ensure adequate water flow, a Little Giant® 1/40 hp water pump was placed into the bearing cooling water feed line. Previously, water was forced through the feed line by the differential pressure between the third corner (where the water is picked up) and the drive section.

It was also noted that a hydraulic press was needed to press the Cutless bearing into and out of its stainless steel holder. Measurement of the holder inner diameter and the Cutless bearing outer diameter showed that the holder diameter was 0.015 inch too small, and out of round. It was speculated that local buckling of the bearing as it was pressed into the holder caused the inner diameter to shrink enough to cause the bearing to

grip the drive shaft too tightly. A new bearing slipped onto the shaft easily, but after being pressed into the bearing holder it could only be forced onto the shaft. It was decided to bore out the bearing holder to a diameter that was 0.002 inch less than the bearing outer diameter. The parts were prepared for installation by placing the bearing in a freezer and by heating the bearing holder in an oven. The chilled bearing was quickly inserted into the heated holder. Afterwards, as the temperatures equalized, the bearing expanded and the holder shrunk, providing a solid grip on the bearing.

Other modifications were made to the bearing to ensure adequate water flow. First, the bearing length was reduced by 0.4 inch to fit completely within the holder sleeve. Previously, the bearing had protruded from the holder end and had severely restricted the flow into the holder from the feed line outlets on either side of the holder end. Another minor modification to the bearing was the filing of ramps into the brass and rubber, to aid the water flow into the rubber/shaft interface. Furthermore, the drive shaft steps in this region were moved back 0.875 inch to insure no further contact with the bearing end.

Later, during tunnel assembly, it was finally determined why the drive shaft had drifted downstream and caused the Cutless bearings to fail. During the last renovation and upgrade of the tunnel, a new 50 hp electric motor was installed. Power was directly transmitted to the shaft by means of a flexible connection. It was discovered during tunnel assembly that the previous power train lacked a reverse thrust bearing. The power system before that had a belt drive system that incorporated a reverse thrust bearing. A thrust bearing and locking collar were fitted onto the shaft so that the new thrust bearing

worked against the existing outer bearing casing. This prevented the shaft from shifting longitudinally when reverse thrust was applied. Although the motor was not run in reverse, reverse thrust was applied when the tunnel was slowed or stopped, causing the propeller to work against the water flow. It was speculated that in the previous power train, the shaft was pulled downstream just enough to bind the shaft step against the Cutless bearing during these transitional phases of operation.

#### 3.1.4 Other Tunnel Modifications

Several other modifications were made to the tunnel to improve tunnel installation and maintenance. A new and larger drain line was placed into the bottom of the third corner. A Culligan® HF-150 water filter rated at 125 psi was fitted into the fill line of the water tunnel. Culligan® S1A 20-micron sediment water filter cartridges were used to filter out the great amounts of rust and sediment in the fill line, providing cleaner water in the tunnel. To further aid in keeping the tunnel clean, common pool algaecide was added to the tunnel to prevent organic pollution. Ball valves were added onto the percolator domes, which are installed on each corner of the water tunnel to collect air that is pressurized out of solution with the water during operation. Algaecide and seeding particles can be added to the filled water tunnel by use of the funnel on the percolator on the first corner.

The bearing bolts that hold the bearing holder in the drive section of the tunnel were modified. Previously, these bolts were very short and difficult to reach. Also, the bolt had to pass through three separately threaded lugs. All but the bearing holder lug holes were stripped of their threads. 5/16 x 3-1/8 inch Allen head bolts were then used to



secure the holder. The extra length of these new bolts extended the bolt head to the outside of the drive fairing, which greatly simplified the assembly of the tunnel drive section. These bolts had to be custom made from 3/8 x 3-1/8 inch bolts. The ends of these bolts were turned down on a lathe to 5/16-inch diameter and threaded.

### 3.1.5 Propeller Knocking

After final assembly of the tunnel and initial run-up, a loud knocking noise was heard in the propeller area. Because the clearance between the propeller and the wall is less than a paper thickness, the most likely source of the noise was the propeller striking the wall. After running the tunnel unpressurized for some time, the noise was reduced at the higher normal operating pressures. It was speculated that the propeller had worn itself in during the unpressurized run. The reduced noise was deemed acceptable, and was ignored during further testing.

## 3.2 Laser Doppler Velocimeter

The laser Doppler velocimeter (LDV), which is also called a laser Doppler anemometer (LDA), employs the Doppler theory to measure particle velocities at a point in a fluid flow. The measurement probe of the system is a lens that focuses two laser beams of the same wavelength onto a point determined by the focal length of the probe lens. The intersection of the two beams forms an ellipsoid-shaped measurement volume where a distinct pattern of light is formed. The amplitudes of the two laser beams add together to form alternating regions of high amplitude and low amplitude light—this is called the fringe pattern. If a light-reflecting particle were to pass through this

measurement volume in a direction normal to the fringe pattern, it would reflect pulses of light as it passes through the high amplitude fringes of the measurement volume. The wavelength and the angle of intersection of the beams are known, which determines the distance between each fringe in the measurement volume. The LDV system thus measures the time interval between reflected bursts of light, and is able to calculate the particles speed through the measurement volume in the direction normal to the fringe pattern.

The above description assumes that the frequencies of the two beams are the same, and are in “sync”. This is achieved by optically splitting a single laser beam. However, it is undesirable to have both beams of the same frequency. If the frequency of one of the beams is shifted by a slight amount, the fringe pattern “scrolls” in one direction. This allows the LDV system to discern between negative and positive velocity directions. The LDV system does this through the use of a Bragg cell. The Bragg cell is a device that shifts one of the laser beams frequencies by directing the beam through a prism that is electro-mechanically vibrated at the desired frequency shift.

The laboratory LDV is a Dantec FiberFlow system. The laser source is a Spectra Physics Stabilite 2017 Argon-ion laser. This unit consists of a laser, a laser power supply, and a remote control module. The laser and the power supply run on 220 V and require water-cooling. The output beam of this system is directed into the FiberFlow transmitter, which contains the beam splitter and Bragg cell. The beam splitter splits the primary laser beam into up to three pairs of beams. The three pairs of beams may be 476.5 nm wavelength (violet), 488 nm (blue), or 514.5 nm (green). One pair of beams

represents one velocity component that can be measured. Currently, the optics are not installed on the violet beams, rendering the system capable of only two-component measurements. The Bragg cell puts a 40-Mhz frequency shift into one of the beams of each pair. The laser beams are then transmitted to a 2-D probe by means of fiber optic cables. The probe has a 80 mm diameter lens with a focal length of 800 mm. The probe is equipped with a 1.95 ratio beam expander. The system is computer-controlled and the data are collected and processed using the Dantec Flow Velocity Analyzer (FVA) and its associated software.

### **3.3 LDV Calibration Apparatus**

#### **3.3.1 Calibration Apparatus Description**

The LDV was calibrated by measuring the tangential velocity at a point of radius  $r$  on a disk with a rough surface rotating at a precisely controlled angular velocity. The disk was rough-cut from a sheet of 0.25-inch Plexiglas and was turned down on a lathe to a radius of 12 inches. An aluminum hub was attached to the backside of the disk by two screws. The disk assembly was not balanced, nor was the disk perfectly flat; the disk wobbled  $\pm 0.381$  mm perpendicular to the disk plane near the extreme radius. The wobble should not have affected the accuracy of the calibration measurements, but rather it just moved the disk surface back and forth in the axial direction through the measurement volume, which had a dimension of 4.303 mm. A rough disk surface was created by attaching a 12-inch diameter, 80-grit sandpaper disk with a spray-adhesive such as 3M

Super77®. This rough surface simulated a particle flow for the LDV system to measure. A pinhole was located in the center of the disk for laser alignment purposes.

The calibration disk was rotated by a Compumotor SM233BE-NTQN type servo motor. The motor was mounted onto aluminum T-stock, which was then clamped onto the lower water tunnel test section tie bars with four “c”-clamps. These tie bars were located just beneath the test section. This location allowed an LDV calibration to be performed without physically moving the traverse system out of alignment with the water tunnel. It was necessary to shim the motor mount 2.25 inches above the lower support bars in order to place the center of the disk within the vertical limits of the LDV traverse. The TQ10X Servo Controller was mounted on an aluminum beam, which acted as a heat sink and allowed the unit to hang from the lower tie bars.

### 3.3.2 Uncertainty of Disk Radius Measurement

The first task in the calibration process was to locate the LDV measurement volume on the center of the calibration disk. The current laboratory arrangement did not allow the LDV measurement volume to measure more than a few centimeters below the calibration disk center, so an alignment procedure was developed using only the top half of the disk surface. First, the LDV measurement volume was visually centered by positioning the probe so that the measurement volume “disappeared” into the pinhole on the calibration disk center. The centering accuracy of this visual method was only  $\pm 1.0$  mm. A more accurate centering alignment was achieved by using the LDV beam system and the traverse to measure the disk radius, and to center the traverse by measuring off of the top and sides of the calibration disk.

Designate the left side of the disk as  $x_1$ , and the right side as  $x_2$ . The radius  $R$  of the disk is then:

$$R = \frac{x_2 - x_1}{2}. \quad (3.1)$$

After the LDV measurement volume was visually centered as closely as possible, the blue beams were used to measure the radius of the disk at  $x_1$  and  $x_2$ .

According to the methods advocated by Coleman and Steele <sup>7</sup>, the uncertainty of the disk radius is given by the following equation:

$$U_R^2 = \left( \frac{\partial R}{\partial x_1} \right)^2 P_{x_1}^2 + \left( \frac{\partial R}{\partial x_2} \right)^2 P_{x_2}^2 + \left( \frac{\partial R}{\partial x_1} \right)^2 B_{x_1}^2 + \left( \frac{\partial R}{\partial x_2} \right)^2 B_{x_2}^2 + 2 \left( \frac{\partial R}{\partial x_1} \right) \left( \frac{\partial R}{\partial x_2} \right) B_{x_1 x_2}, \quad (3.2)$$

where  $P_{x_k}$  denotes the random uncertainty associated with  $x_k$ ,  $B_{x_k}$  denotes the systematic uncertainty associated with  $x_k$ , and  $B_{x_1 x_2}$  denotes the correlated systematic uncertainties of the variables  $x_1$  and  $x_2$ . Because the same procedure was used to measure both  $x_1$  and  $x_2$ , the same random and systematic uncertainties were applied to each x-coordinate.

Only one source of random uncertainty was found in the procedure, and that was the judgment of the operator as to the exact alignment of the beams onto the edge of the disk. The possible error in this alignment was estimated to be half of a beam diameter, or  $\pm 0.675$  mm. Possible random uncertainty of the traverse was considered negligible, as the traverse specification reported a resolution of  $6.25 \mu\text{m}$ .

There were a number of systematic uncertainty sources. One systematic uncertainty source was the specified accuracy of the traverse, which was  $\pm 0.2$  mm. Another systematic uncertainty was in the radius of the Plexiglas® disk itself. Using a

dial indicator, a variation in disk radius of  $\pm 0.3429$  mm was measured. The total systematic uncertainty of the location of  $x_1$  and  $x_2$  then was  $\pm 0.3967$  mm.

Because the measurement of  $x_1$  and  $x_2$  was by the same method, the systematic uncertainties of these two variables were completely correlated. The correlated systematic error term is

$$B_{x_1 x_2} = B_{x_1} B_{x_2} . \quad (3.3)$$

Using these uncertainty estimates, the uncertainty in the measurement of disk radius  $R$  was  $\pm 0.4773$  mm. The actual measured value of the calibration disk radius using this procedure was 152.9875 mm, or 6.023 inches.

### 3.3.3 Uncertainty in Radial Positioning During Calibration

All random and systematic uncertainties of the radial measurement used in the calibration procedure were associated with the centering of the measurement volume in the y-direction (vertical). This was done by visually locating the green laser beams on the top edge of the calibration disk, which introduced a random error of  $\pm 0.675$  mm, as discussed previously. The measurement volume was then moved down a distance equal to the disk radius, which introduced a systematic error of  $\pm 0.4773$  mm. Accounting for the additional systematic error introduced by the traverse accuracy ( $\pm 0.2$  mm) and the finite diameter of the measurement volume ( $\pm 0.0995$  mm), the total systematic uncertainty in the radial position measurement was  $\pm 0.5270$  mm. Because the traverse was able to resolve to within  $6.25 \mu\text{m}$  of a given position, and the step sizes during the calibration tests were on the order of millimeters, the total random uncertainty in the radial position measurement was  $\pm 0.675$  mm.

#### 3.3.4 Positioning the Measurement Volume in $z$

Before proceeding with the calibration, the measurement volume must be located such that its center is bisected by the surface of the calibration disk. After the measurement volume was centered in  $x$  and  $y$ , the volume was moved to a point close to the center of the disk, but not in the pinhole. With the calibration disk rotating, the  $z$  position was adjusted to maximize the LDV data rate. This was done by enabling the high voltage in the FVA software and connecting an oscilloscope to the appropriate channel on the FVA. The  $z$  position was then adjusted to maximize the signal-to-noise ratio as was seen on the oscilloscope. To further improve the calibration data, the high voltage settings were adjusted to increase the signal-to-noise ratio, again using the oscilloscope as a guide. It was found that a high voltage setting of 800-900 worked well for this purpose.

#### 3.3.5 Uncertainty in Angular Velocity Measurement

The angular velocity of the servo motor was precisely controlled and reported to the computer control software every few seconds. A stroboscopic tachometer was used to verify the accuracy of the rotational velocity at low and high speeds. There was no discrepancy between the angular velocity reported by the motor controller and the velocity measured by the tachometer. The systematic uncertainty of the rotational velocity was set at the resolution limits of the stroboscopic tachometer, which was  $\pm 0.05$  rad/s.

During the actual calibration measurements, data were only taken when the motor controller reported a stable reading of the target speed. However, at some speeds (especially lower speeds) a random fluctuation of disk speed was noticed in the digital readout of the motor control program. This flicker was on the order of 0.03 rev/s. Thus the random uncertainty for the disk speed was estimated to be  $\pm 0.03$  rev/s, or  $\pm 0.18$  rad/s.

### 3.3.6 Random Uncertainty of LDV Velocity Measurement

The random uncertainty of the mean velocities measured by the LDV was determined to be  $\pm 0.004$  m/s. This estimate was developed by taking 25 measurements of a reference speed, and determining the standard deviation of the mean velocities of these measurements. The random uncertainty of an LDV mean velocity measurement is twice the standard deviation. These measurements were done for several reference velocities, as shown in Figure 3.2.



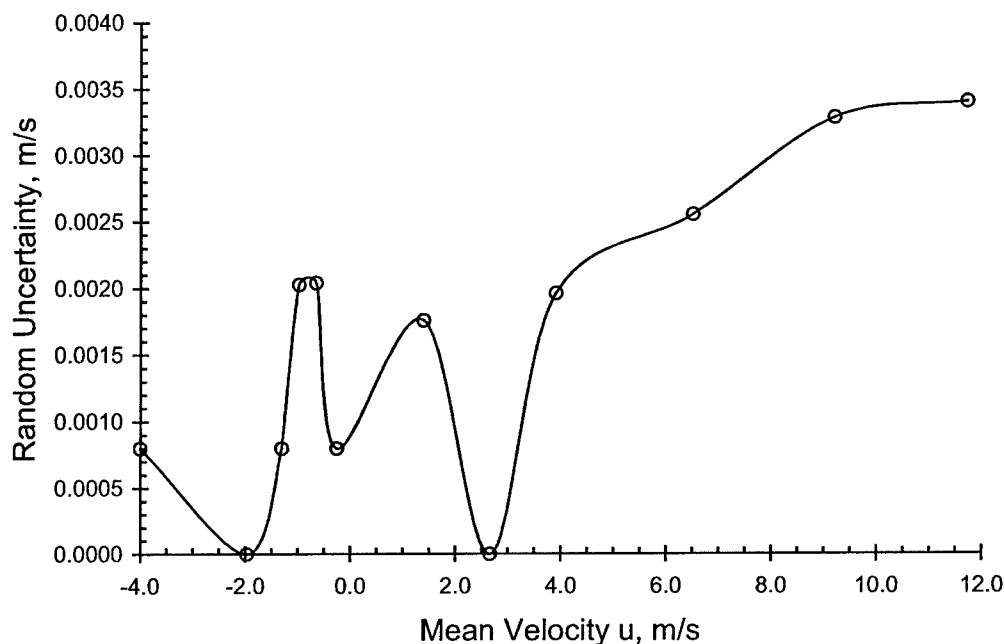


Figure 3.2: Random uncertainties of LDV mean velocity measurements.

### 3.3.7 Calibration Results

Several calibration tests were made. In one type of test, the measurement volume was placed at a specific radius and the disk angular velocity was stepped through a range of speeds. In a second type of test, the disk angular velocity was set to a specific speed and the measurement volume was moved through a range of radii using the traverse. Care was taken during these procedures to not overload the LDV system's photo multiplier tubes (PMT). As a guideline, FVA software high voltage settings of 800-900 worked well, with a low laser current such as 10 Amps.

The results for the series of four calibration tests from 1/25/02 are shown below. The method of constant angular velocity was used for these tests because it could be

executed quickly. The angular velocity was set at 15 revolutions per second to avoid velocity fluctuations. Tangential velocities were measured in a range of radii from -5 mm to 127 mm. These combinations of radius and angular velocity enveloped the range of expected velocities in the water tunnel, and included small negative velocities. The radii positions were stepped sequentially up and down, to detect any possible hysteresis. No hysteresis was detected in the measurements, and the results were very consistent.

The comprehensive data set consisted of 140 points. A linear regression was applied to the data to return a slope of  $m = 0.9681$  and an intercept of  $b = -0.0352$  m/s. An uncertainty analysis was performed analytically on the regression equation, and a second order curve fit was applied to the uncertainty to obtain an estimate of the regression uncertainty  $U_{u-regress}$  for new values of calibrated velocity  $u_c$ :

$$u_c = 0.9681u_{FVA} - 0.0352 \quad (3.4)$$

$$U_{u-regress} = 0.0507 + (-2.4825 \times 10^{-4})u_c + (2.4639 \times 10^{-5})u_c^2 \quad (3.5)$$

The linear regression with uncertainty bands is plotted in Figure 3.3 for the entire calibration range. The linear regression plot is repeated in Figure 3.4 for the range of expected water tunnel velocities. This second plot also includes the calibration data points with error bars.

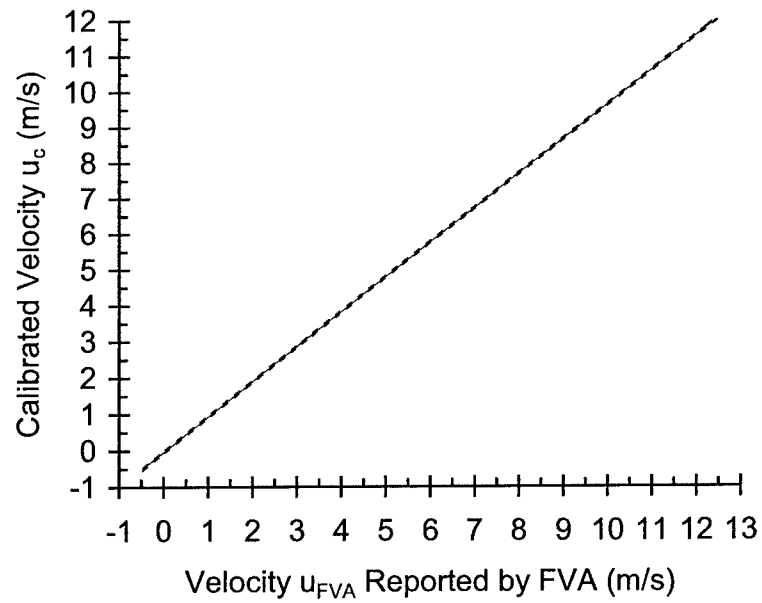


Figure 3.3: LDV calibration plot with upper and lower uncertainty bands.

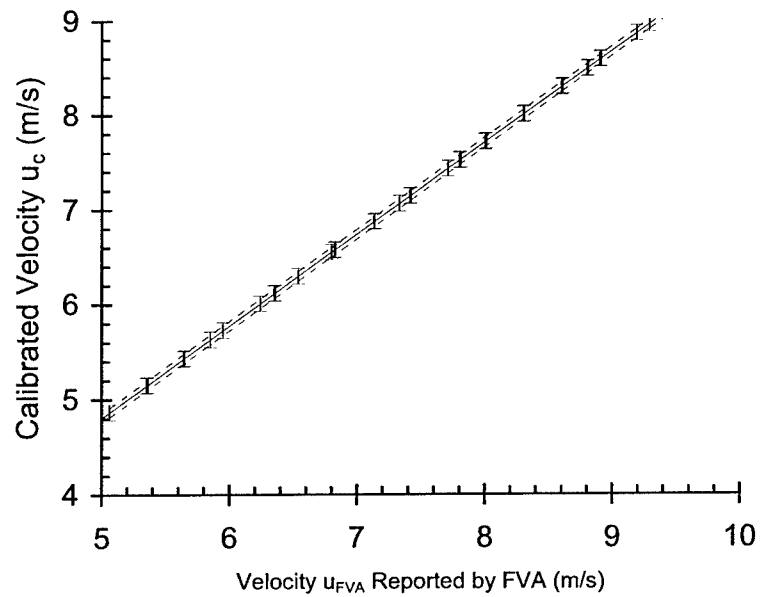


Figure 3.4: Calibration plot of expected water tunnel test speed range, with uncertainty bands and error bars on the data points.

### 3.4 Submarine Model and Mount

The submarine shape that was tested was identical to one that was used in a number of experiments at the LCC. The submarine hull shape is plotted in Figure 3.5. The model constructed for the current experiment was 286.47 mm (11.278 in) long with a diameter of 25.4 mm (1 in), which resulted in a fineness ratio of 11.278. The hull form had no appendages or fins, but did incorporate a propeller hub shape on the end. The model was constructed of two pieces of stainless steel bar stock. The hull shape was turned down on a CNC lathe in the MSU Mechanical Engineering shop. The two pieces were screwed together to form the complete single model.

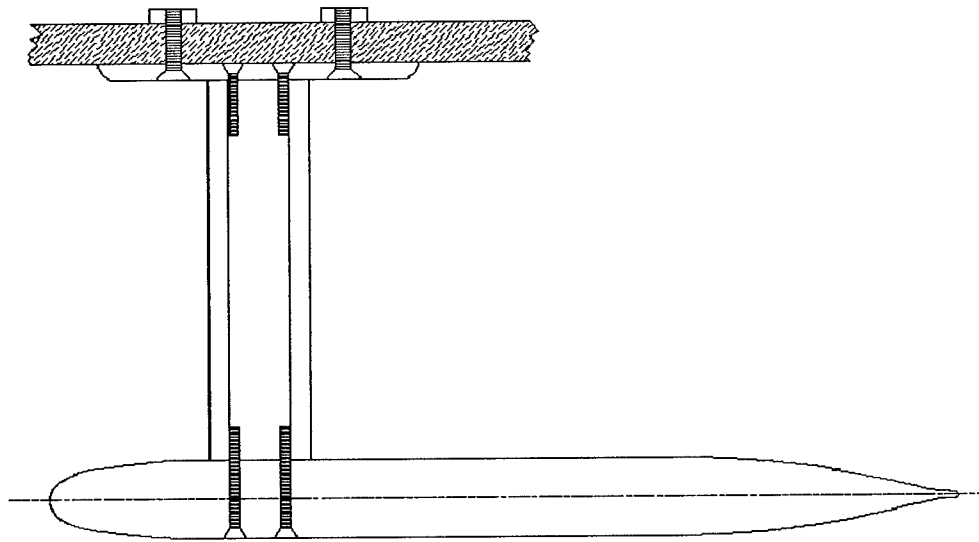


Figure 3.5: Submarine model drawing showing mounting details.

The model was mounted along the test section centerline by means of a single stainless steel strut. The strut was 1.25 inches wide and 0.125 inches thick, which was just wide enough for 4-40 size threads. Two 4-40 size flat head screws were used to mount the model on one end of the strut. Two more 4-40 size flat head screws were used to mount the other end of the strut onto a stainless steel mounting plate. This mounting plate was in turn mounted onto the inside of the test section wall by two flat head 10-32 screws, which were threaded into two holes in the test section wall. Nuts were put on the outside to further secure the mount. Silicon was used between the mounting plate and the test section wall to prevent water leakage. Also, all exposed countersunk screw heads in the mounting plate and in the model were filled with epoxy and sanded flush with 400-grit sandpaper. The model was mounted so that the nose of the submarine was approximately 6 body diameters (6 inches) downstream of the test section entrance. The strut was mounted on the submarine model in the position corresponding approximately to the position of the strut on the LCC submarine model. The leading edge of the strut was located at  $x/L_{sub} = 0.183$ .

## CHAPTER IV

### EXPERIMENTAL PROCEDURE AND RESULTS

#### 4.1 LDV Configuration

##### 4.1.1. LDV Alignment with Water Tunnel

The lightweight traverse that was used with the LDV had three axes at right angles. The x-direction was chosen to be the direction of flow; the y-direction was the vertical axis transverse to the direction of flow, and the z-direction was the horizontal axis transverse to the direction of flow. The first alignment was to position the traverse system so that the x-axis of the traverse was parallel to the centerline of the water tunnel. This was achieved by hanging plumb lines over the side of the test section and taping a length of string on the floor between the two points. A second length of string was then taped onto the floor so that it was parallel to the first string, with about 20 inches of distance between them. The traverse was then positioned so that plumb lines that were hung from the traverse were lined up on the second string. Next, the probe was aligned on the horizontal plane of the test section centerline. To do this, the green beams were first centered on the outside wall of the test section in the vertical direction (y-direction) by positioning the entering laser beams and the exiting reflected beams in a straight, horizontal line at a point near the middle of the test section. This adjustment was made by moving the probe with the traverse. The probe was then traversed in the x-direction to

the end of the test section. At this new position, the beams were adjusted in the y-direction by raising or lowering the traverse platform on that end, if it was necessary. This procedure accounted for any angular displacement the water tunnel may have had from the true horizontal.

The origin of the experiment coordinates was a point on the centerline of the outside test section wall and 7.5 body diameters downstream of the submarine body propeller hub. For the x-direction reference, the blue beams were touched to the aft end of the hub; the traverse was then moved downstream 7.5 body diameters, which was a distance of 190.5 mm. A piece of masking tape with a small black dot was placed at this point, so that when the measurement volume was on the origin, the laser beam “disappeared” when viewed through the laser safety goggles.

To center the measurement volume onto the outside wall in the z-direction, the following procedure was used. First the z-position was adjusted until the laser beams formed a fine point on the test section wall. The traverse coordinates were then set to zero. A refinement was necessary to insure that the middle of the measurement volume was on the outer wall surface. Using the green beams, the measurement volume was stepped in increments of 0.5 mm in the z-direction, starting from a point a short distance off the wall. The anode current reading in the LDV software output was recorded at each point. The point where the highest anode current was recorded was the point where the center of the measurement volume was on the outer surface of the wall. The data rate was a maximum at this point.

It was found that this alignment procedure had to be performed for every new experiment because the water tunnel shifted position under operation. The masking tape with the black dot aided in locating the  $x$  datum easily. The  $y$  and  $z$  datum had to be reconfirmed using the procedures outlined above.

#### 4.1.2 Laser Beam Refraction Correction

The refraction of the laser beams when changing media must be accounted for when positioning the measurement volume within the test section. Fortunately, the index of refraction for water and Plexiglas® are nearly the same, so that only one refraction index needed to be considered. The overall effect of the change in media from air to water was that the ratio of the travel distance of the probe volume within the test section to the travel distance of the probe traverse outside of the test section was equal to the index of refraction of the new medium. The index of refraction for water is  $4/3$ .

### 4.2 Test Section Flow Characteristics

A number of velocity measurements were made of the water tunnel test section with no model to determine the flow characteristics of the water tunnel. Three positions were selected for velocity profile measurements:  $x/L = 0.125$ ,  $x/L = 0.492$ ,  $x/L = 0.738$ ; where  $L$  is the length of the test section. At each of these positions, several velocity profiles were recorded for three different motor input speeds. For  $x/L = 0.492$ , the motor input speeds were 500, 550, and 600 rpm. It was noted during this time that the water tunnel was being excited near its natural frequency at motor input speeds that were multiples of 200 rpm. The water tunnel shook very badly at 600 rpm, so that for the



velocity profiles at  $x/L = 0.125$  and  $x/L = 0.738$ , the motor input speeds were 500, 550, and 630 rpm.

The water was seeded with 5-micron silicon carbide during these tests to increase data rates. A laser current of 16 Amps was used throughout the tests. The PMT high voltage setting had to be increased as the probe measurement volume was moved further into the test section. Table 4.1 below lists the optimum high voltage setting for a given range of  $z$  for a moderately seeded flow.

Table 4.1: PMT high voltage settings for test section regions.

Range in $z$ (mm)	PMT High Voltage
15-40	700
45-75	800
80-100	1000
105-120	1200

The plots of the water tunnel velocity profiles are shown below in Figure 4.1 through Figure 4.4 for each of the motor speeds. The presence of the wall boundary layer is noted on the right hand side of each plot. It is evident that the tunnel speeds are more consistent at higher velocities and near the entrance to the test section. At  $x/L = 0.125$ , all velocity profiles fall right on top of each other, even with the distinctive kinks in the profile. These kinks and shifts can be seen in other profiles as well. Figure 4.5 shows the representative velocity profile kinks and shifts for  $x/L = 0.492$  and a motor input speed of 500 rpm.

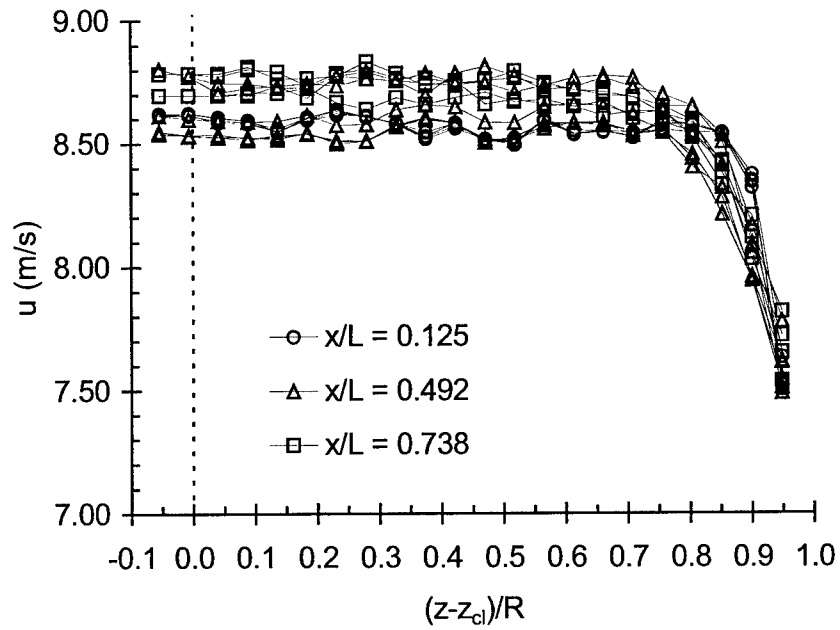


Figure 4.1: Velocity profiles in the test section at motor input speed of 500 rpm.

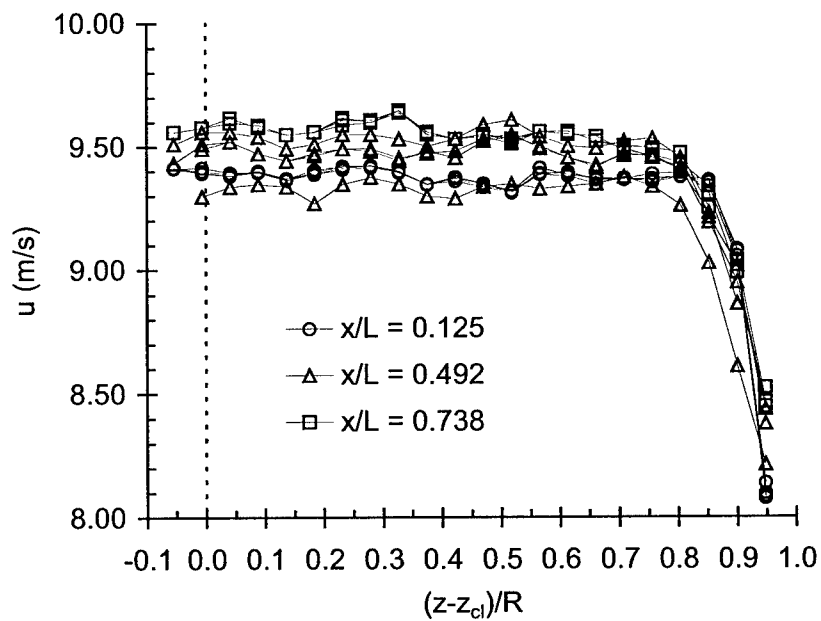


Figure 4.2: Velocity profiles in the test section at motor input speed of 550 rpm.

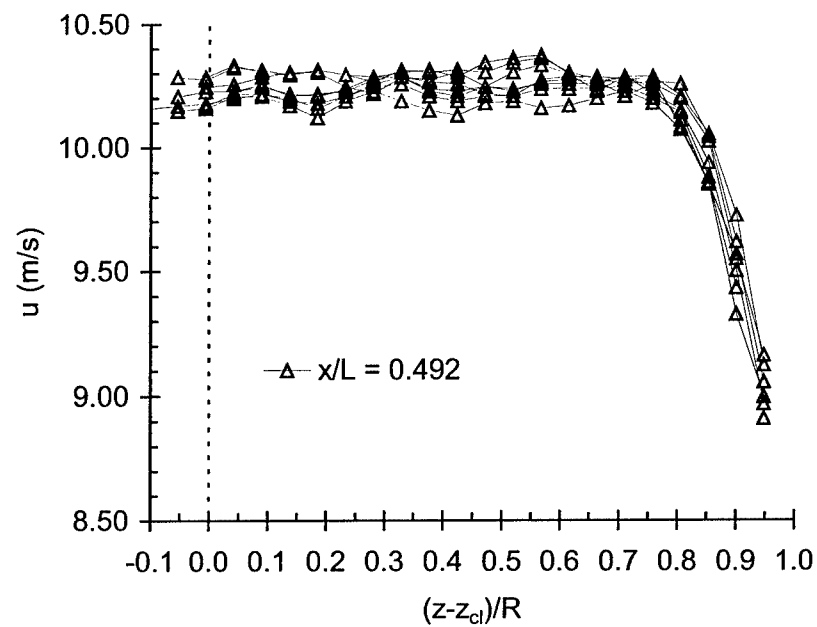


Figure 4.3: Velocity profiles of the water tunnel at motor input speed of 600 rpm.

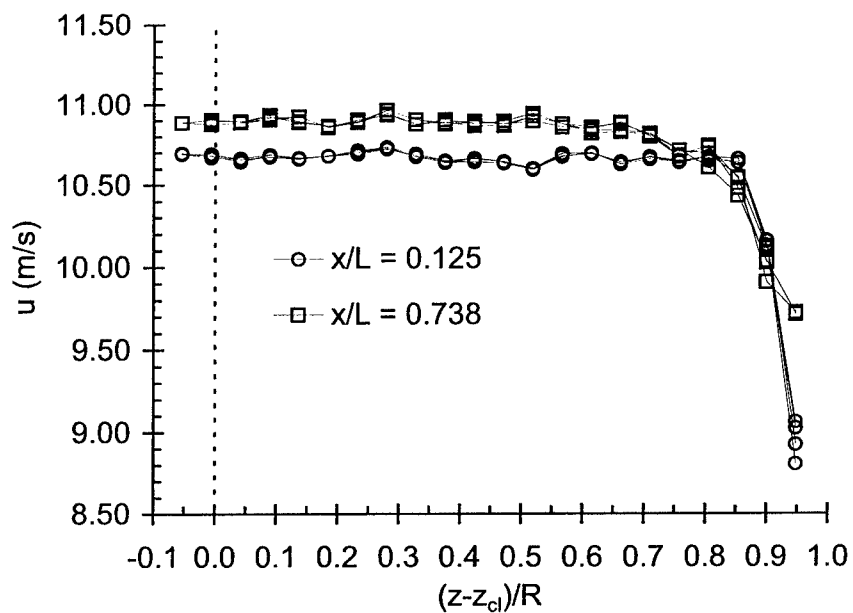


Figure 4.4: Velocity profiles of the water tunnel at motor input speed of 630 rpm.

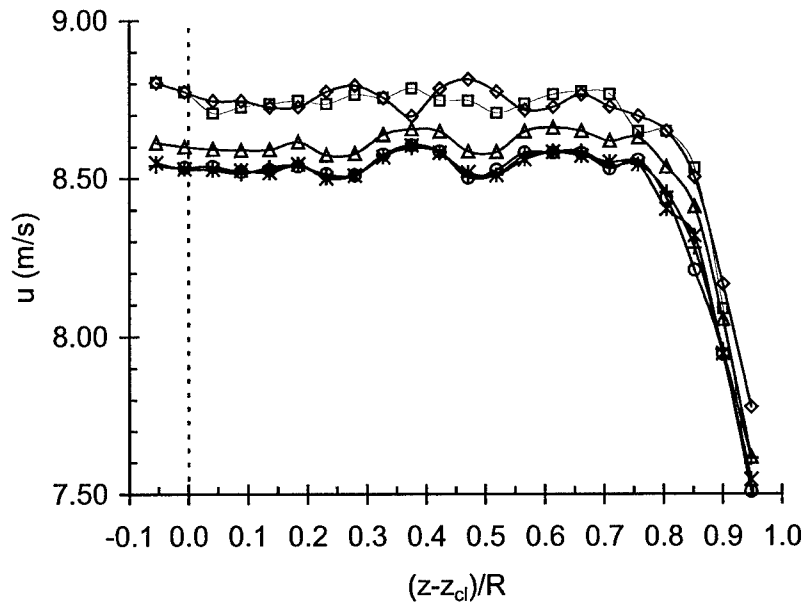


Figure 4.5: Velocity profiles taken at  $x/L = 0.492$ , 500 rpm, showing typical velocity shift and non-uniform profile.

During the initial testing of the LDV system on the water tunnel, numerous measurements were taken at a fixed point within the test section to determine the optimal LDV system configuration settings. During this time the motor was set to a constant speed. It was observed that the mean velocity would occasionally shift up or down by approximately 0.5 m/s. After several occurrences of this phenomenon, it was noted that the shifts seemed to occur suddenly after an approximate 20-minute period. No motor speed fluctuations were noted in the motor controller feedback. Several long period tests were performed to try to capture the exact period of the velocity shift, but these proved inconclusive. Besides being a physical phenomenon of the tunnel, the velocity shift could have been caused by a faulty LDV Bragg cell that was only working intermittently.

The kinks in the velocity profiles that were repeatable from data set to data set, even when the velocity shift occurs, were most likely caused by the local differences in the optical properties of the test section wall. As the measurement volume was moved across the test section, the actual area of the wall that the beams passed through changed. The repeatability of these kinks at the same  $r/R$  positions indicates that the local optical properties of the test section were affecting the crossing angle or the location of the beam intersection that formed the measurement volume. The standard deviation from the local mean velocities was found to be no more than 0.06 m/s at any point in the test section, which amounted to a systematic uncertainty estimate of  $\pm 0.12$  m/s in velocity measurement due to the optical properties of the test section.

Figures 4.6, 4.7, and 4.8 show the local turbulence intensity factor  $u_{rms}/u$  at  $x/L = 0.492$  and motor input speeds of 500, 550, and 600 rpm. The typical value for the freestream turbulence intensity is 1.5 %, which is slightly higher than is desirable. Figures 4.9, 4.10, and 4.11 illustrate the typical uncertainty associated with the velocity profile measurements. Figure 4.12 plots the same data as Figure 4.11, but the velocity axis has been expanded to full scale to give a better sense of the relative magnitudes of the error. The error in the velocity measurements includes the fossilized systematic error from the calibration, the systematic uncertainty estimate due to the test section optics, and the random uncertainty of each of the point measurements. The radial position errors are due to uncertainties in the traverse calibration, the finite length of the measurement volume, and the uncertainty in the test section radius  $R$ .

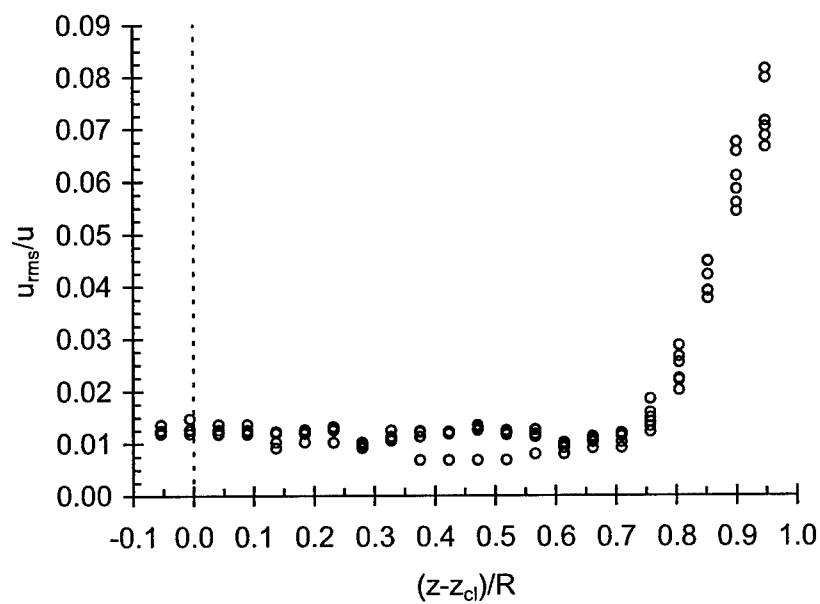


Figure 4.6: Local turbulence intensity factors at  $x/L = 0.492$ , 500 rpm.

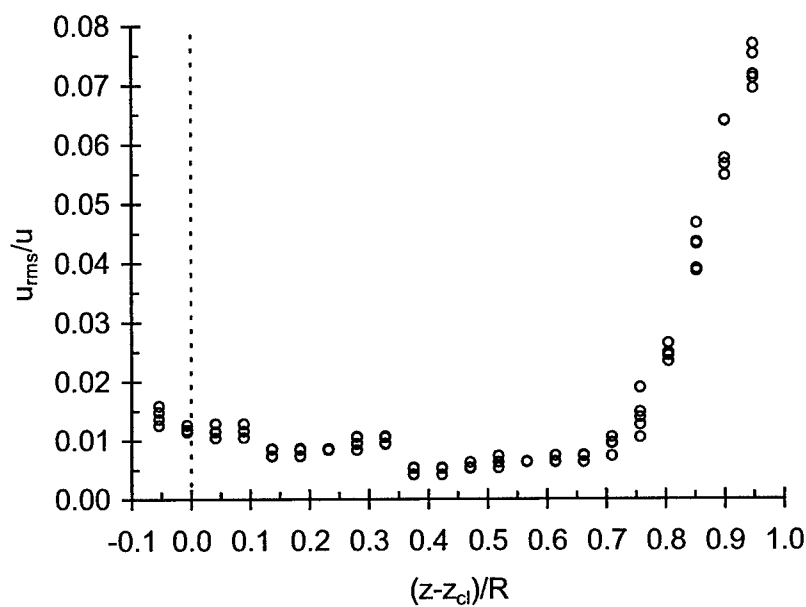


Figure 4.7: Local turbulence intensity factors at  $x/L = 0.492$ , 550 rpm.

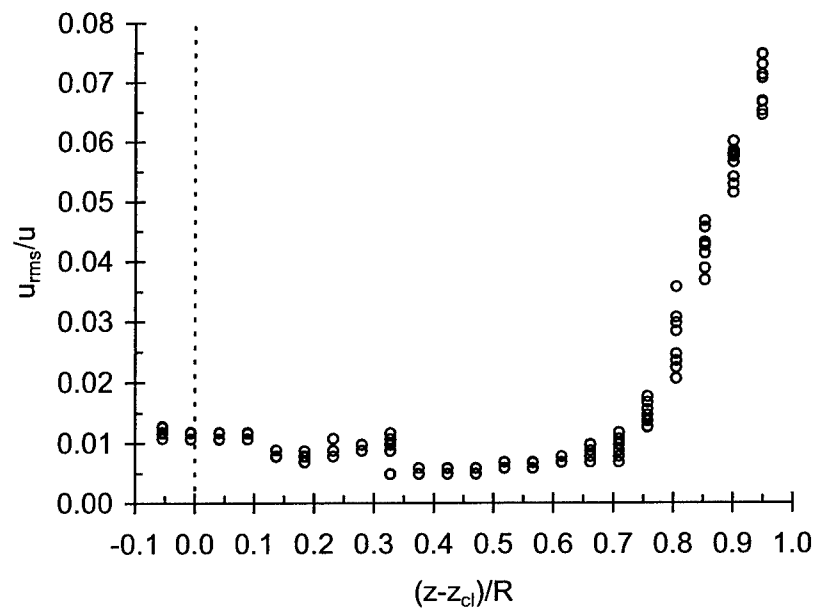


Figure 4.8: Local turbulence intensity factors at  $x/L = 0.492$ , 600 rpm.

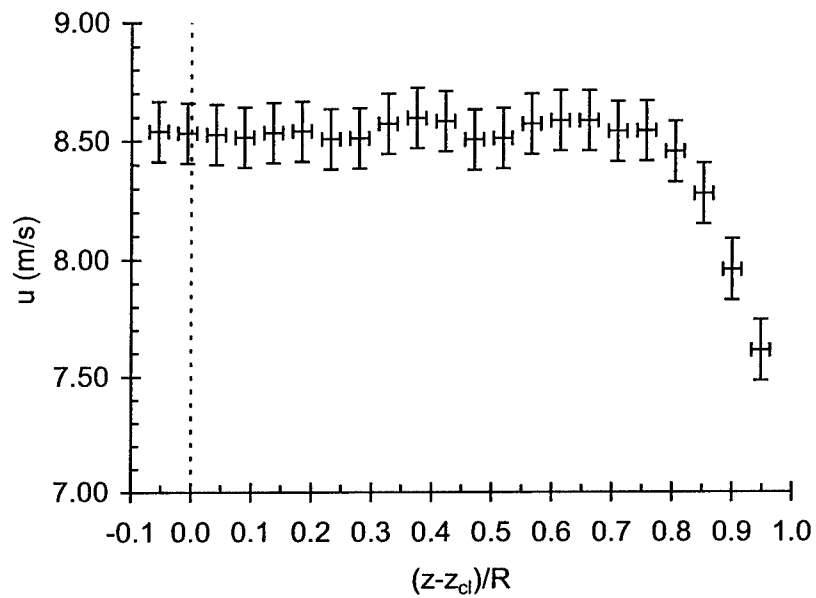


Figure 4.9: Typical velocity profile with error bars,  $x/L = 0.492$ , 500 rpm.

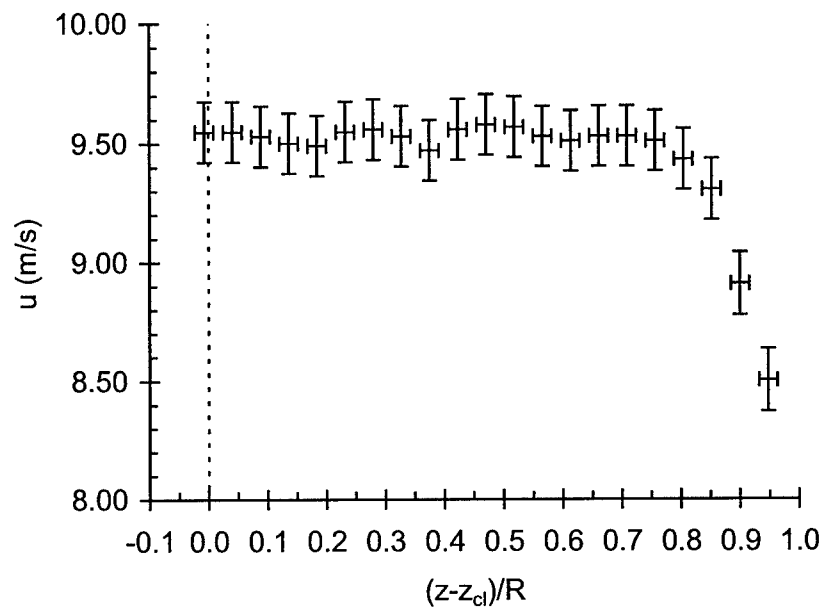


Figure 4.10: Typical velocity profile with error bars,  $x/L = 0.492$ , 550 rpm.

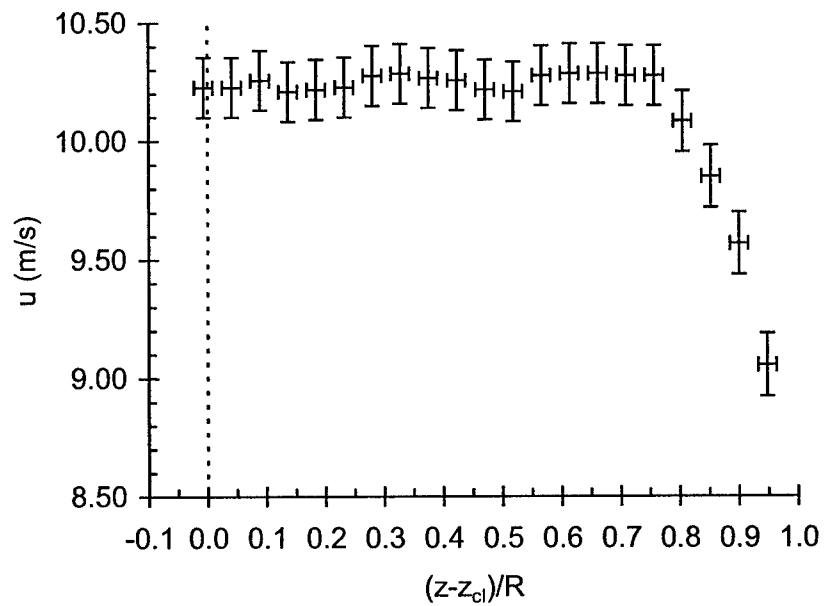


Figure 4.11: Typical velocity profile with error bars,  $x/L = 0.492$ , 600 rpm.



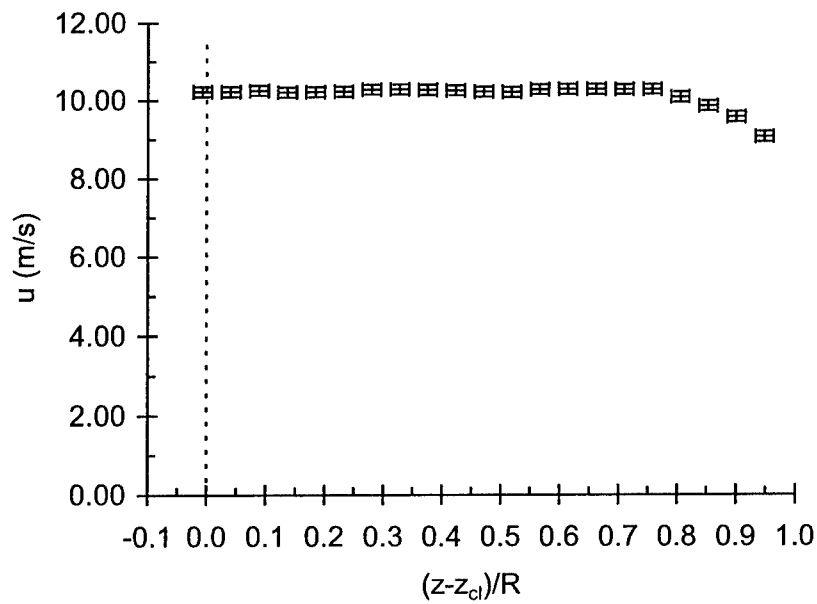


Figure 4.12: Typical velocity profile with error bars,  $x/L = 0.492$ , 600 rpm, repeated with full velocity scale to show relative magnitude of errors.

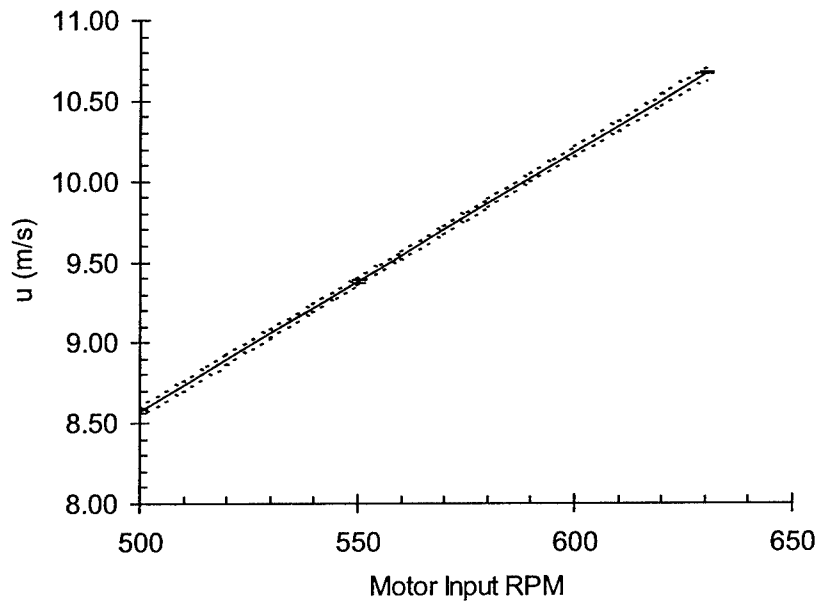


Figure 4.13: Mean test section velocity at  $x/L = 0.125$  versus motor input speed. Error bars are shown on the data points, and uncertainty bands are shown around the curve fit.

Figure 4.13 demonstrates the linear relationship between motor input speed and test section velocity as measured at  $x/L = 0.125$ . The error bars are shown on the three data points at 500, 550, and 630 rpm. The uncertainty bands that are shown apply to the curve fit, and are derived from the “classical approach” to regression uncertainty as described in Coleman and Steele <sup>7</sup>. A least squares linear regression to this data is given by the equation:

$$U_{\infty} = 0.0161 \Omega + 0.5241, \quad (4.1)$$

where  $\Omega$  is the motor input speed in revolutions per minute and  $U_{\infty}$  denotes the test section velocity at  $x/L = 0.125$ . The uncertainty associated with the regression is given by the equation:

$$U_{U_{\infty}-regress} = 0.040878 \left[ \frac{1}{3} + \frac{(\Omega - 560)^2}{8600} \right]^{1/2}. \quad (4.2)$$

The uncertainty of  $U_{\infty}$  from the curve fit could be reduced by a factor of six by taking velocity profiles at nine different motor speeds rather than just using three motor speeds.

### 4.3 Submarine Model Wake Experiments

For the submarine wake measurements, the tunnel motor speed was set to 500 rpm. Velocity profiles were taken at several  $x/d$  stations behind the model, where  $x/d = 0$  is the end of the model. Velocity profiles were measured at  $x/d = 10, 13, 16, 19, 22, 25$ , and 28. The time required to complete one complete set of profiles was approximately 5 hours. Most of that time was spent measuring the wake velocity deficits, which had accompanying low data rates. Optimum LDV settings for the wake profile measurements

were found through trial and error. The laser current setting for the tests was 16 Amps. The PMT high voltage setting was 1050, with no seeding in the tunnel. A drape was used over the test section and traverse to block light noise from the overhead lights. A dark drape was also hung vertically behind the test section to reduce glare off of the wall.

The wake velocity profiles and the turbulence intensity factors from the five days of testing are shown in Figure 4.14 through Figure 4.23. The point spacing for the 5/16/02 through 5/22/02 data was 3.33 mm, which corresponded to a traverse movement of 2.5 mm. For the remaining days, the point spacing was reduced to 2 mm (corresponding to a traverse movement of 1.5 mm) and the measurement of the velocity profile at  $x/d = 28$  was discontinued. The point spacing was reduced to increase the number of points in the wake. The effect of measurement volume overlap was ignored. The measurements at  $x/d = 28$  were discontinued for an operational time savings of nearly half an hour.

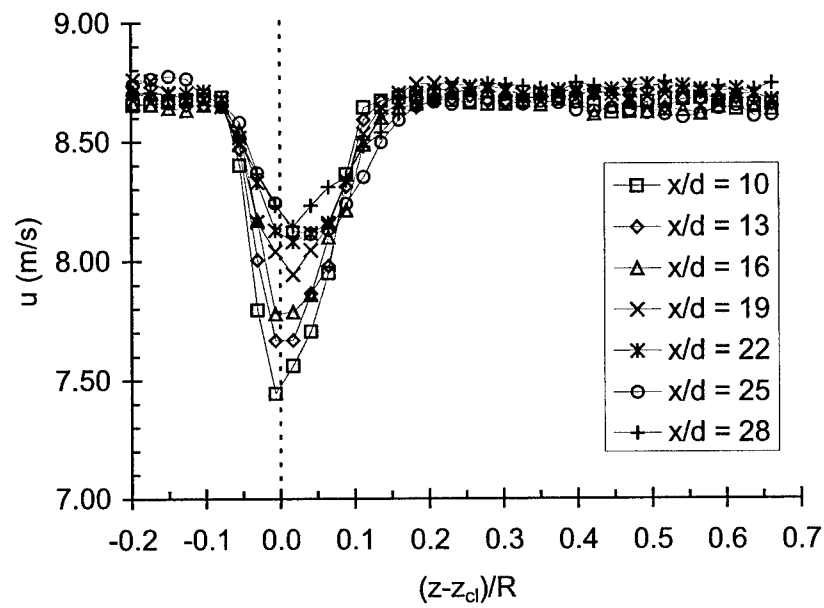


Figure 4.14: Mean velocity profiles from 5/16/02.

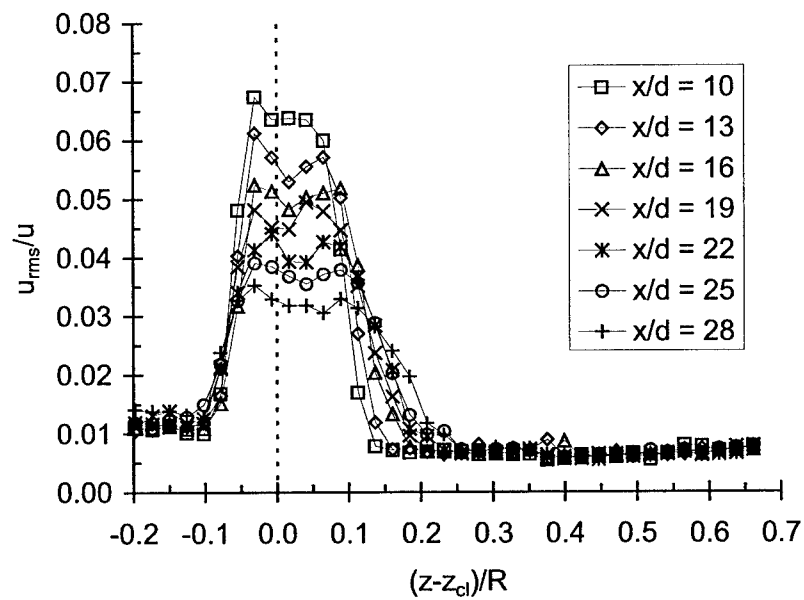


Figure 4.15: Turbulence intensity from 5/16/02.

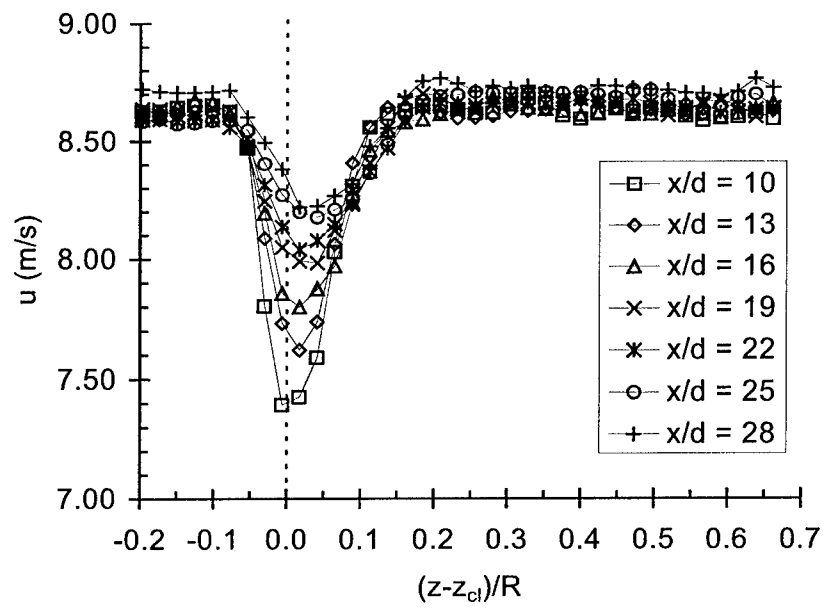


Figure 4.16: Mean velocity profiles from 5/17/02.

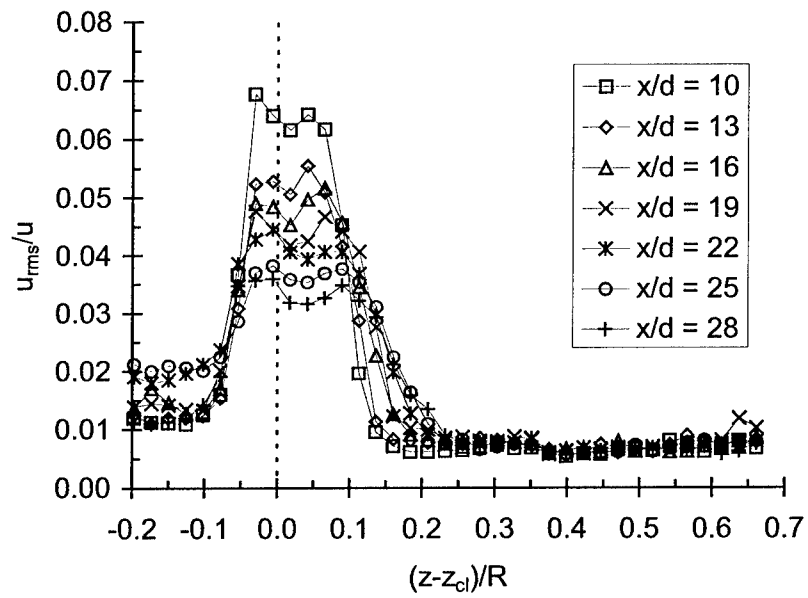


Figure 4.17: Turbulence intensity from 5/17/02.

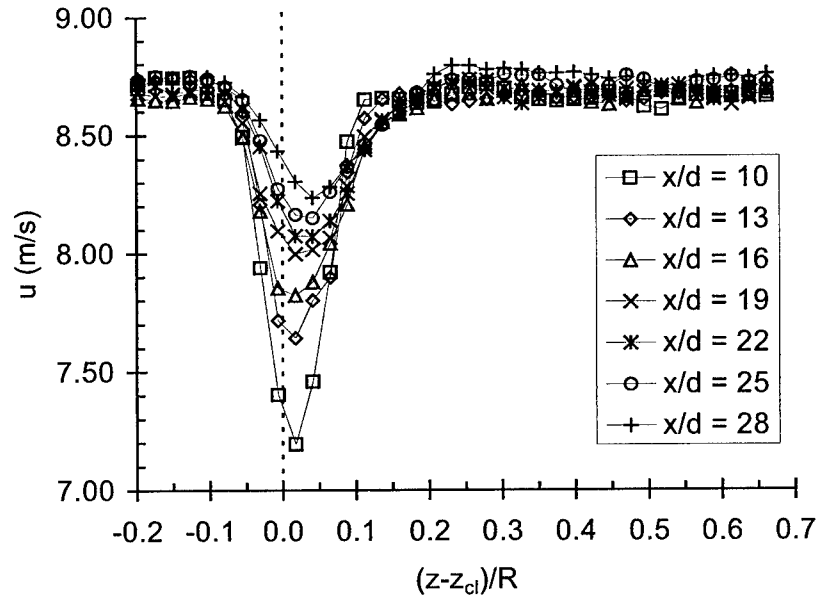


Figure 4.18: Mean velocity profiles from 5/22/02.

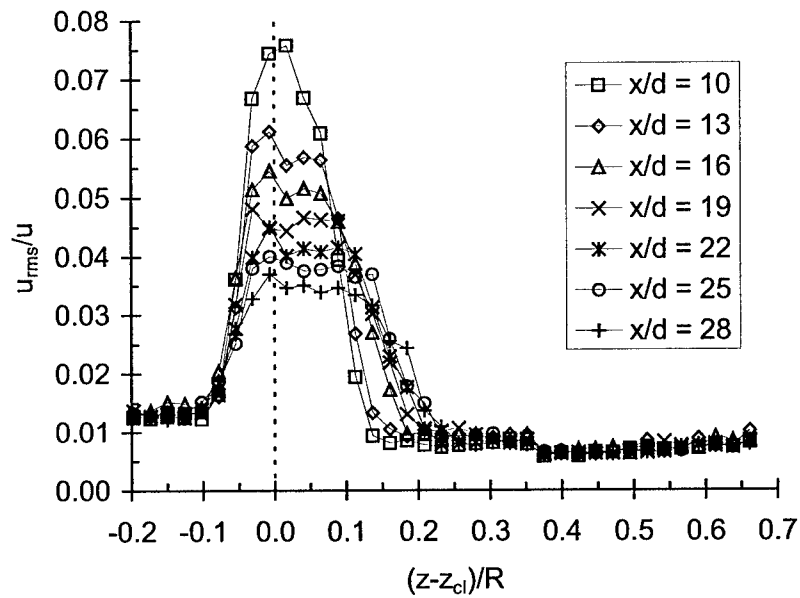


Figure 4.19: Turbulence intensity from 5/22/02.

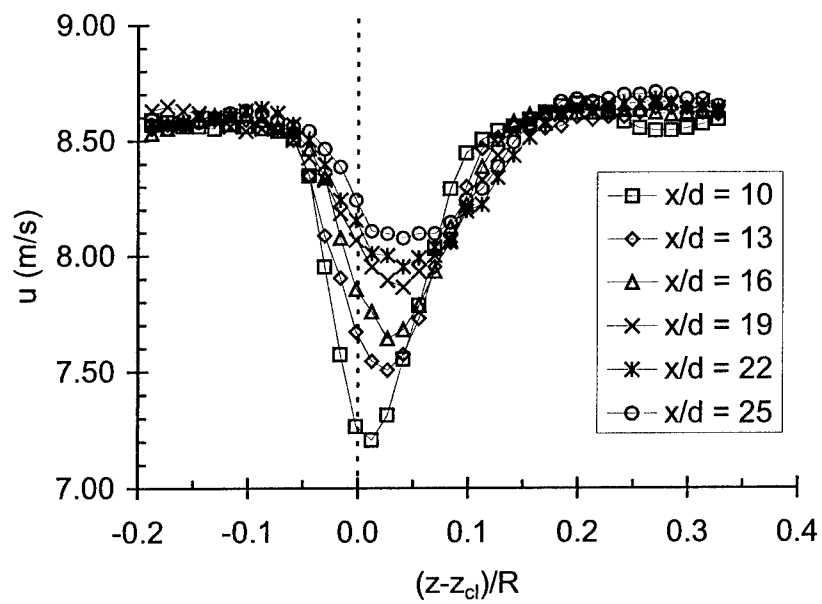


Figure 4.20: Mean velocity profiles from 5/30/02.

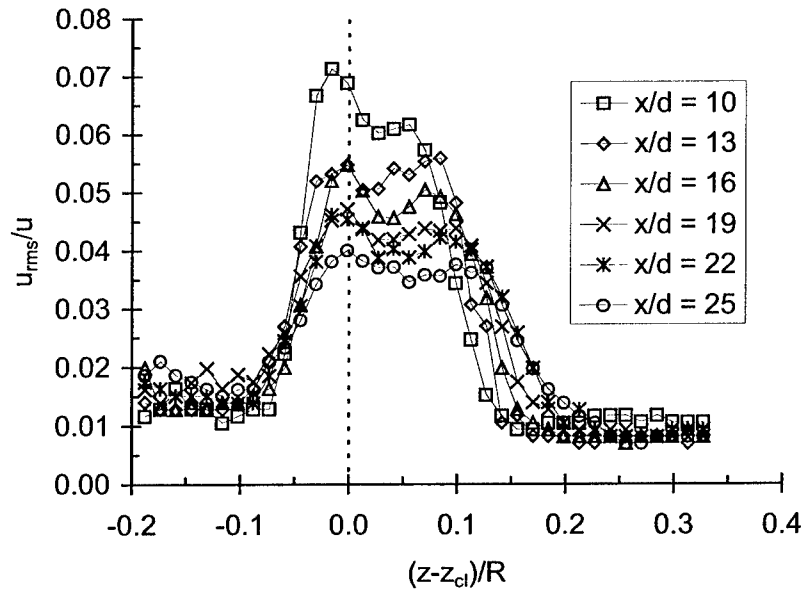


Figure 4.21: Turbulence intensity from 5/30/02.

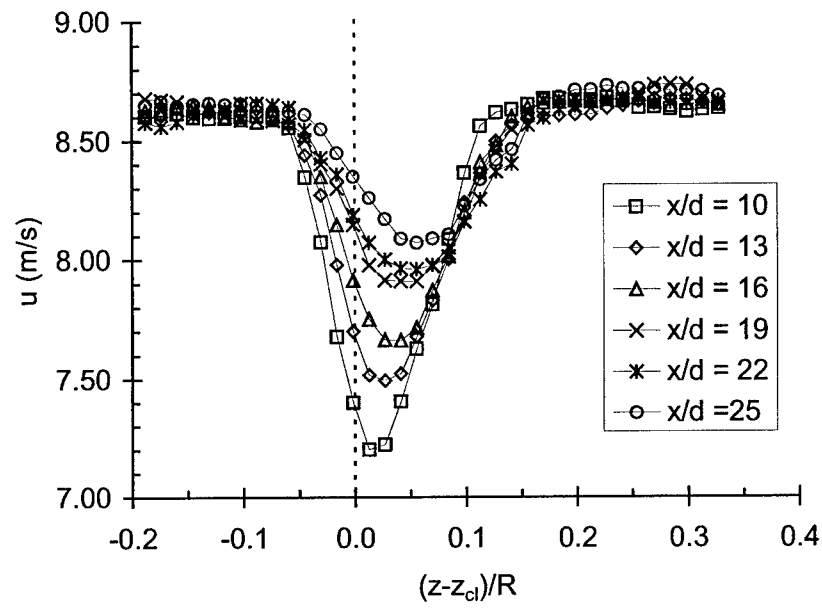


Figure 4.22: Mean velocity profiles from 6/4/02.

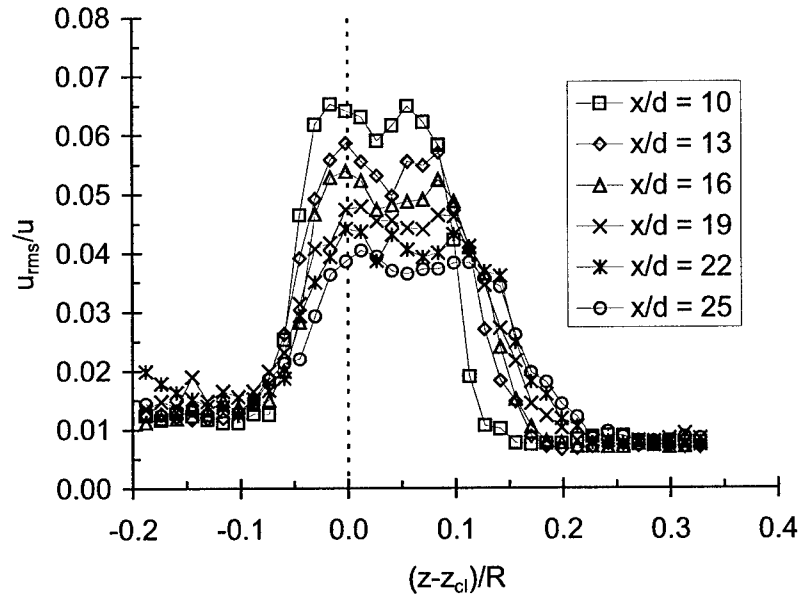


Figure 4.23: Turbulence intensity from 6/4/02.



The mean velocity profiles are asymmetric and are generally not centered along the measured centerline of the test section. The measurements of the wake beyond the centerline were characterized by higher turbulence intensity and lower data rates. The peculiar behavior of the velocity profiles suggests that the model was not aligned properly with the flow. After the model was mounted, the accuracy of alignment was checked and found to be within  $0.5^\circ$ . However, previous studies had discovered that the test section becomes distorted when pressurized. According to measurements by Lindsey <sup>6</sup>, the test section bulged 0.009 in (0.23 mm) when pressurized to 50 psi. It is possible that the deflection of the test section while under pressure caused a misalignment of the model with the mean flow. Also, it was observed during operation that the strut would occasionally deflect from side to side. These strut deflections may have contributed to the asymmetry of the wake profiles.

The wake centerline drift seen in the plots represents an offset of approximately  $0.5^\circ$ . During later measurements of the test section wall surface irregularities, it was discovered that the traverse x-axis was misaligned by  $0.7^\circ$  in the same direction as the centerline shift. This misalignment did not affect the final drag calculations as the wake centerline was corrected in the curve fitting process. The uncertainty that the angular misalignment imposed on the LDV velocity measurements was approximately  $\pm 0.007$  m/s.

Figures 4.24, 4.25, and 4.26 illustrate the typical uncertainty associated with the velocity measurements. The data is taken from the series of measurements from 5/22/02,

and at  $x/d = 10, 16, 25$ . The velocity and position error sources are taken to be the same as those used in the test section characteristic profiles.

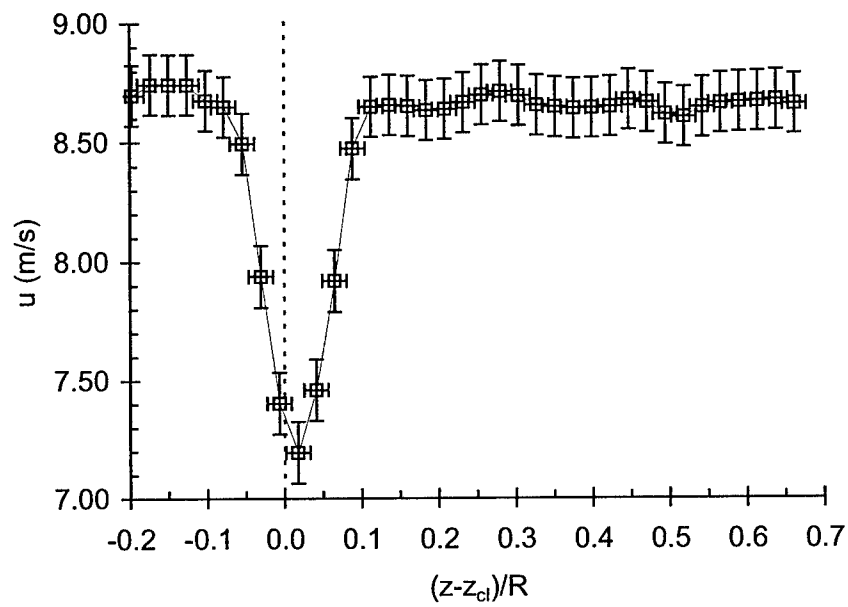


Figure 4.24: Velocity profile with typical uncertainties, 5/22/02,  $x/d = 10$ .

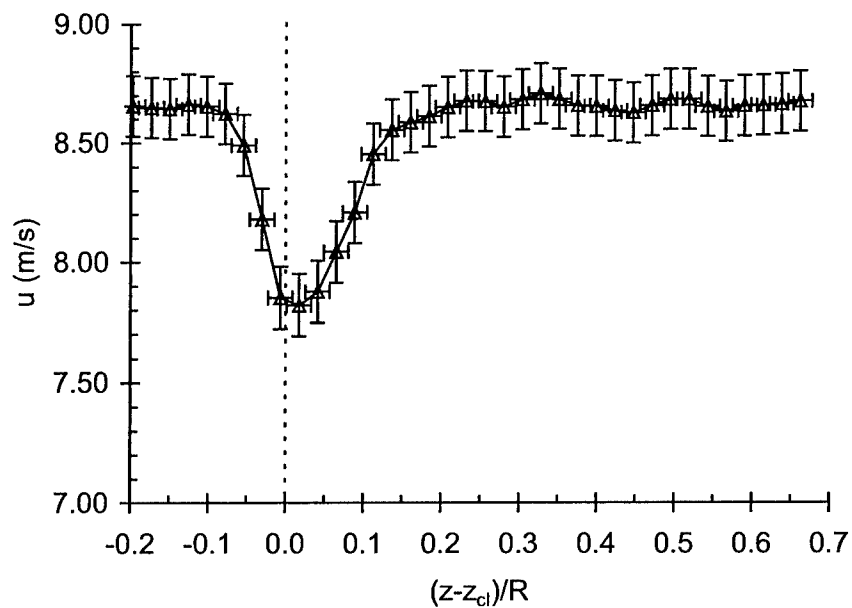


Figure 4.25: Velocity profile with typical uncertainties, 5/22/02,  $x/d = 16$ .

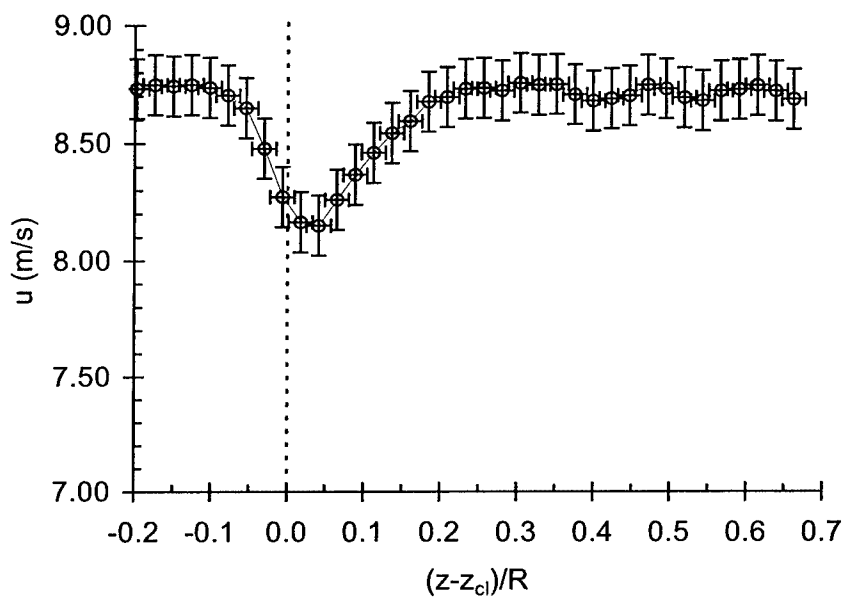


Figure 4.26: Velocity profile with typical uncertainties, 5/22/02,  $x/d = 25$ .

#### 4.3.2 Curve Fits to Wake Profile Data

The wake profile data was fit using the numerical form of equation (2.59) so that the drag coefficient of the hull form could be calculated. The curve fits were done in MathCAD using the “genfit” function. The genfit function finds the least squares fit of an arbitrary function to a given data set. First, the wake velocity profile data  $z$  and  $u$  were read from a file and the Gaussian curve fit function was applied in the form:

$$u(z) = U_0 - u_0 e^{\frac{-(z-z_0)^2}{b^2}} \quad (4.3)$$

where  $U_0$ ,  $u_0$ ,  $z_0$ , and  $b$  were generated from the curve fit.  $z_0$  is the wake centerline location,  $b$  is the wake width parameter,  $u_0$  is the velocity scale factor, and  $U_0$  is the mean velocity outside of the wake. Since the curve fit process did not include the  $(\ln 2)$  factor, the wake width parameter was corrected after the curve fit by dividing by  $\sqrt{(\ln 2)}$ . This curve fitting process was repeated for each  $x/d$  location.

After the wake curve fit was completed, the fits of length scale and velocity scale were performed to obtain the coefficients  $c_u$  and  $c_l$  that were introduced in equations (2.61) and (2.62). The set of data  $x/d$ ,  $u_0$ , and  $b$  were again used with the genfit function to fit the velocity defect function:

$$\frac{u_0(x)}{d} = c_u \left( \frac{x-x_0}{d} \right)^{-2/3} \quad (4.4)$$

The curve fit yielded  $c_u$  and  $x_0/d$ . The  $x_0/d$  value was then used in the function fit for the wake width parameter to find  $c_l$  :

$$\frac{b(x)}{d} = c_l \left( \frac{x - x_0}{d} \right)^{1/3}. \quad (4.5)$$

In order to use these power law fits, the measurements had to be made in a region of the wake where the velocity deficit and width parameters follow this behavior. In experiments conducted by Chevray <sup>8</sup>, the wake of a 6:1 prolate spheroid achieved similarity at  $x/d \approx 10$ . All measurements in the current experiments were made at an  $x/d \geq 10$ , and since the submarine model had a larger fineness ratio than that of Chevray's spheroid, the wake of the submarine model should have been self-similar at all the measured positions. The self-similarity of the submarine wake profiles is illustrated in Figure 4.27 and Figure 4.28. The wake velocity profiles are clearly self-similar and fit the Gaussian function, although the region outside the wake is noisy in the 5/22/02 data.

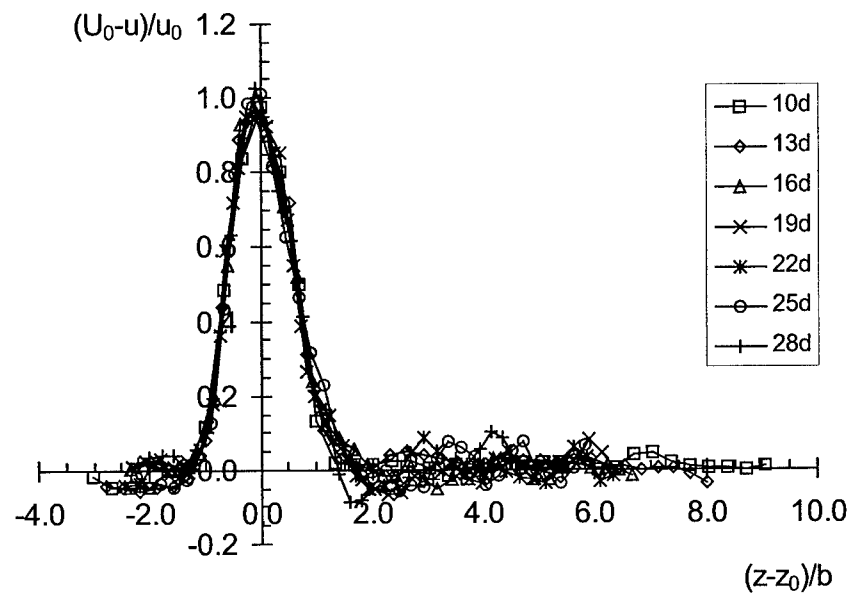


Figure 4.27: Similarity profiles for 5/22/02 data.

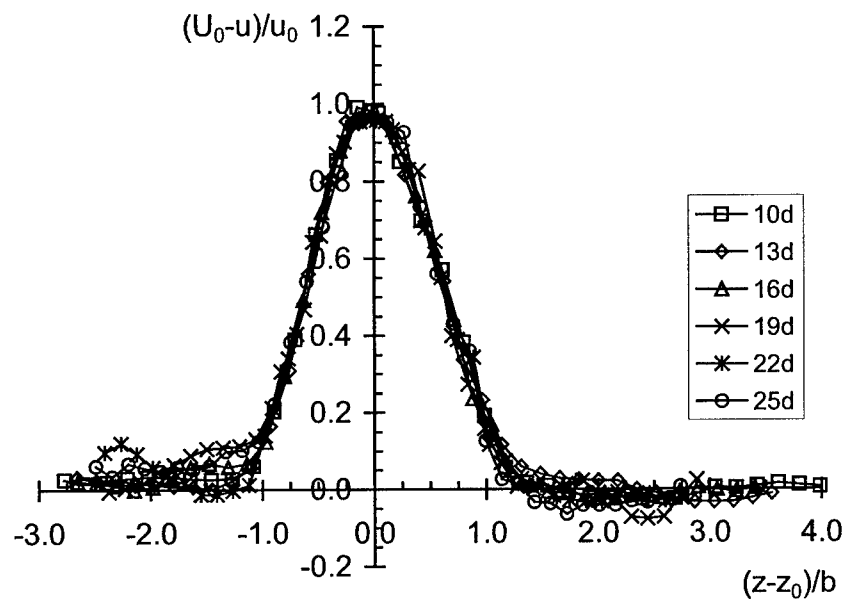


Figure 4.28: Similarity profiles for 6/4/02 data.

Figure 4.29 illustrates the variation of the freestream velocity  $U_0$  outside the wake as  $x/d$  changes. The general trend is that  $U_0$  increases as  $x/d$  increases; however, there are local variations in this trend that were not repeatable. Figure 4.30 plots the changes in nondimensionalized velocity deficit  $u_0/U_0$  with  $x/d$ . The results are similar, if not consistent. Figure 4.31 plots the changes in the wake width parameter  $b/d$  over  $x/d$ . The fits are not very repeatable.

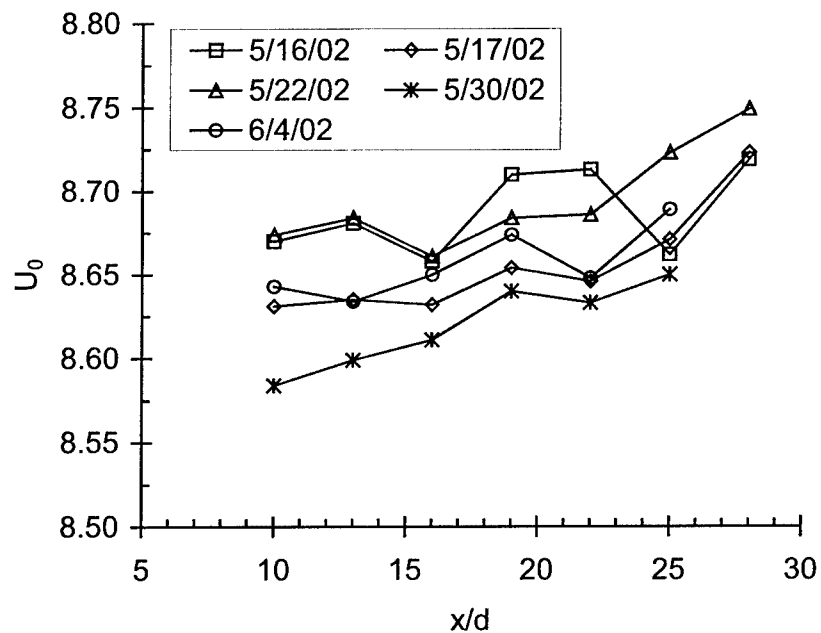


Figure 4.29: Freestream velocity  $U_0$  outside of wake.

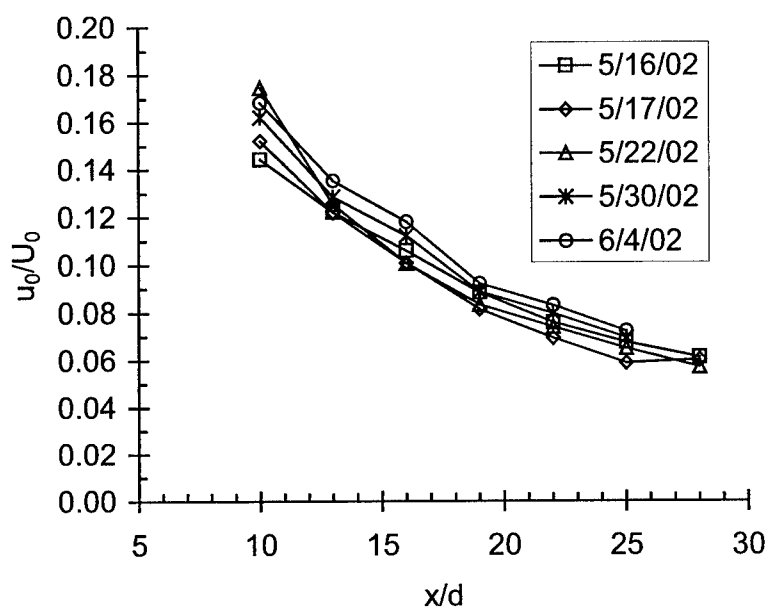


Figure 4.30: Velocity deficit  $u_0/U_0$ .

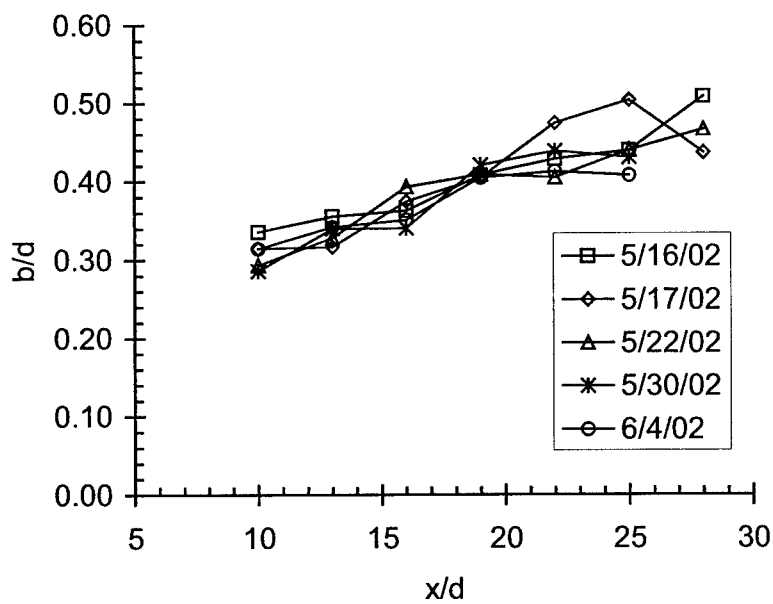


Figure 4.31: Wake width parameter  $b/d$ .



### 4.3.3 Drag Coefficient of Model

The drag coefficient may be calculated from each day's data through the use of equation (2.65). The drag coefficient can then be corrected for the pressure gradient that exists in the test section. This pressure gradient was measured by Lindsey <sup>6</sup> for various tunnel speeds. For a tunnel speed setting of 500 rpm, the pressure gradient is  $-0.0058$  psi/in, with an uncertainty of  $\pm 0.0009$  psi/in. The drag coefficient due to the pressure gradient is given by:

$$C_{D,p} = \frac{8F_p}{\rho \pi d^2 U_\infty^2}, \quad (4.6)$$

where  $F_p$  is the reaction force on the body due to the pressure gradient, and  $U_\infty$  is the freestream velocity as given by equation (4.1). The pressure reaction force  $F_p$  is found by multiplying the pressure gradient with the volume of the body:

$$F_p = \frac{dp}{dx} V_{body}. \quad (4.7)$$

This is the standard form for the so-called "buoyancy drag" as reported in AGARDograph 109 <sup>9</sup>. The resulting pressure force in any case is approximately 0.04 lbf, and the resulting contribution to the drag coefficient is  $\Delta C_{D,p} \approx 0.010$ , where the reference velocity is  $U_\infty = 8.575$  m/s.

The results of the fits are reported in Table 4.1. As can be seen, the results were varied and unrepeatable. The range of drag coefficients were from 0.122 to 0.351. The uncertainty in the drag coefficient due to the uncertainty in the pressure gradient is  $\pm 0.002$ . The drag coefficient was expected to be approximately 0.2. This expectation

was based on previous experiments with the same model at the LCC and on computational studies by Cash <sup>10</sup>. The result that most nearly approaches the expected value is from the 5/16/02 data set; yet it is still 15.5% higher than the expected value.

Table 4.2: Curve fit results for each day's experiment.

Experiment Date	$x_0/d$	$c_u$	$c_l$	$C_D$ (neglecting pressure gradient)	$C_D$
5/16/02	2.501	0.566	0.192	0.241	0.231
5/17/02	4.377	0.49	0.253	0.361	0.351
5/22/02	5.55	0.475	0.169	0.157	0.147
5/30/02	3.595	0.565	0.208	0.283	0.283
6/4/02	3.511	0.594	0.139	0.132	0.122

The test conditions varied from day to day, which may account for some of the scatter in the results. The data from 5/16/02 and 5/17/02 were some of the first measurements to be taken of the wake profiles. During these tests, the tunnel fill valve was not left open. The tunnel was pressurized to 50 psi, and then the fill valve was turned off. Normally, the tunnel would remain at constant pressure. However, it had been noticed that the water tunnel leakage had increased during the first tests. After the tests were completed on 5/22/02, it was noticed that the static pressure in the tunnel had dropped to 25 psi. This had not been observed before. It was decided to keep the fill line on for all the tests thereafter to keep the tunnel pressurized at 50 psi. The velocity profiles measured on 5/30/02 and 6/4/02 were taken under a constant pressure of 50 psi,

and demonstrated distinct differences from the profiles of the three previous days, although the input speed of the motor was the same for all tests. This difference in behavior is illustrated in Figure 4.32.

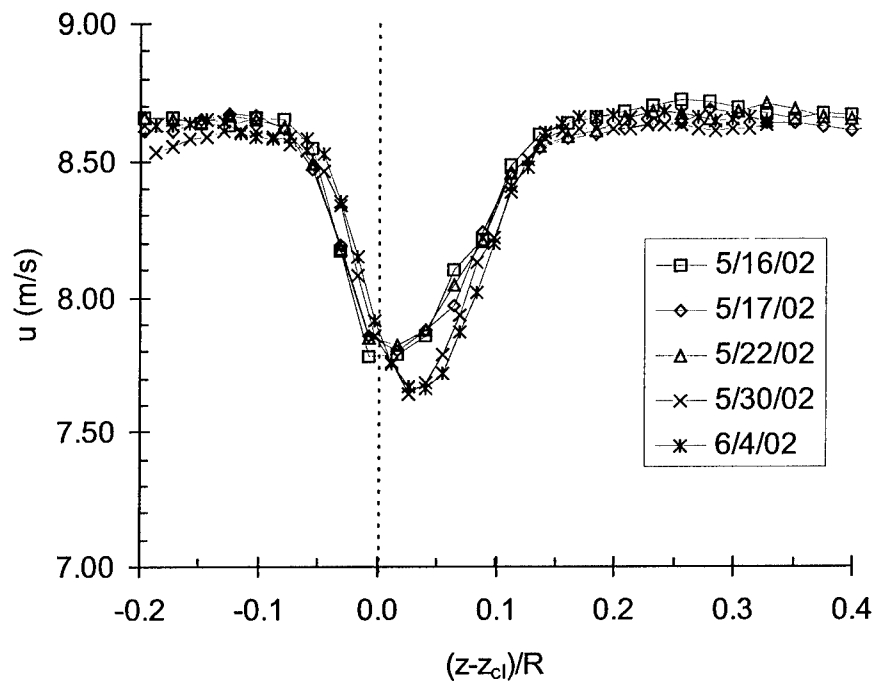


Figure 4.32: Comparison of wakes profiles at  $x/d = 16$  for all five data sets.

After the wake measurements on 6/4/02, a study was performed to test the effect of decreasing pressure on the flow velocity within the test section. The LDV measurement volume was placed in the freestream and velocity measurements were taken continuously while the tunnel static pressure was allowed to bleed off from 50 psi to 25 psi. A plot of the time histories for the velocity and pressure readings is shown in Figure 4.33. The results were unexpected—the velocity fluctuated wildly with no

apparent relation to the pressure drop. A similar test was performed with the tunnel fill valve left open, so that the tunnel remained at a constant static pressure of 46 psi. The results are shown in Figure 4.34. Except for a sudden drop in velocity observed near the beginning of the test, the velocity was fairly constant for nearly an hour. This test came to an abrupt end when the third corner of the water tunnel catastrophically failed under pressure. The failure prevented further study into the effects of decreased tunnel pressure and the velocity shifts that were noted earlier.

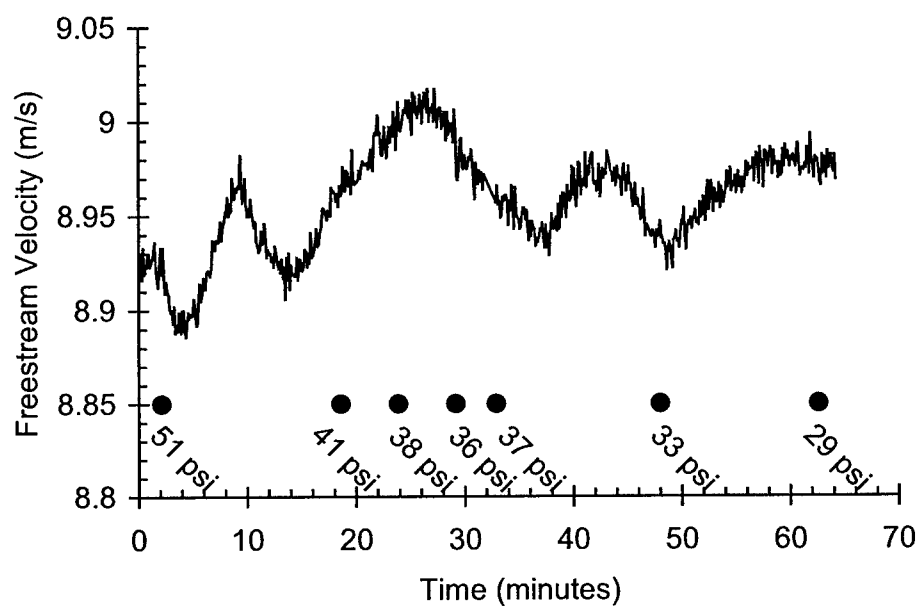


Figure 4.33: Test section freestream velocity behavior over a period of decreasing static pressure.

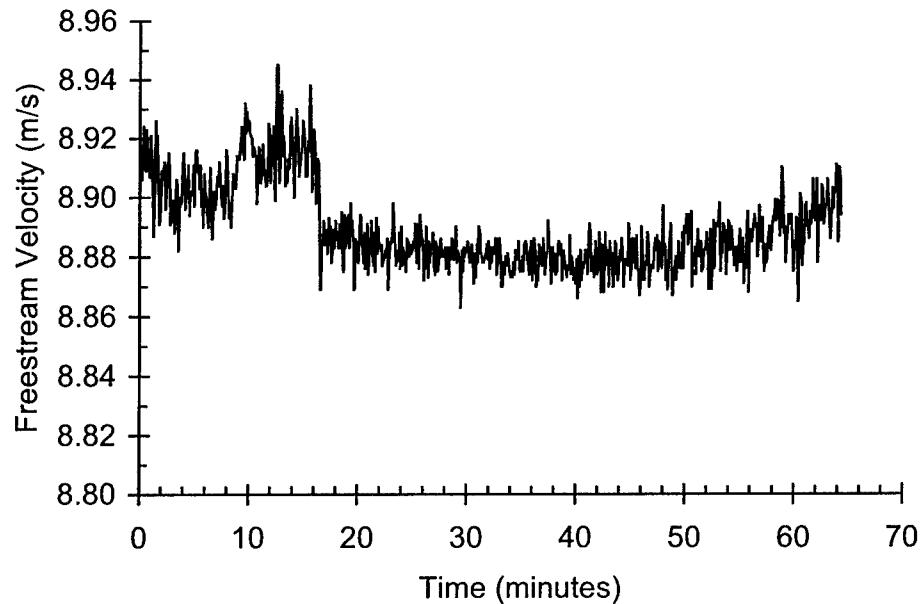


Figure 4.34: Test section freestream velocity behavior over a period of constant static pressure of 46 psi.

The profiles of 5/16/02 and 5/17/02 were taken under similar conditions. The tunnel water was seeded with 5-micron silicon carbide, which was found during the test section studies to improve data rates. However, with the presence of the model and its wake, the seeding was found to be detrimental. The water was drained after the tests on 5/17/02, and clean water was used on 5/22/02 and every day thereafter, with much better readings within the wake. The data taken on 5/16/02 and 5/17/02 were not originally intended to be analyzed and reported, but they were analyzed after the failure of the tunnel prevented any further testing to see if any other clues to the inconsistent measurements could be found. The tunnel pressure was not observed during the tests on

5/16/02 or 5/17/02. Another difference in operating conditions was the absence of shading from the overhead lighting, which was present from 5/22/02 and afterwards.

After 5/22/02, the fill line was left on during the tests to maintain the static pressure in the tunnel. The tests of 5/30/02 and 6/4/02 were run with constant static pressure of approximately 50 psi, consistent ambient lighting, and clean water. It was expected that these later tests would yield the most acceptable data. The drag coefficients from these later tests were 0.283 and 0.122, which are approximately 40% higher and lower than the expected drag coefficient of approximately 0.2.

To further explore the effect of the different operating conditions, the data was divided into two groups. The first three days' data represented the low pressure operating condition, and the last two days' data represented the high pressure operating condition. The velocity profile similarity parameters of the individual days' data were averaged to form composite velocity profiles representing the low pressure and the high pressure operating conditions. The power law fits were then applied to these two sets of data, as shown in Figure 4.35 through Figure 4.38.

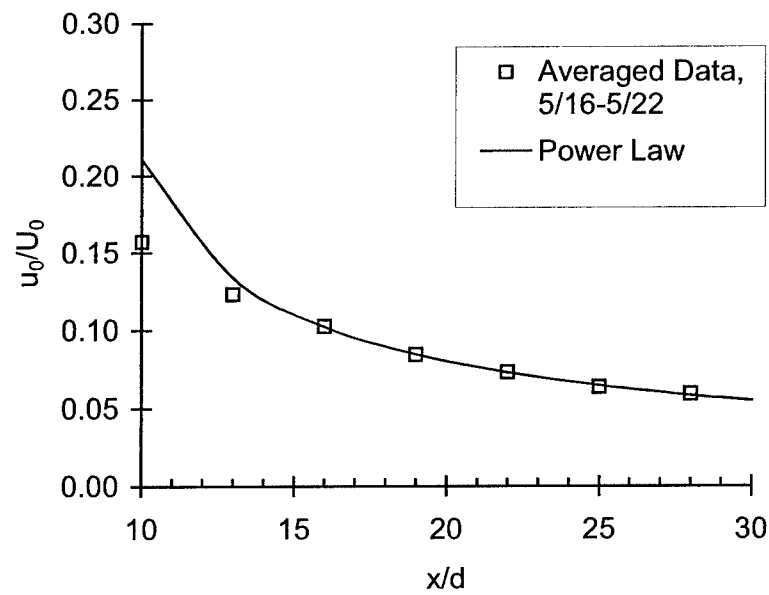


Figure 4.35: Comparison of averaged velocity deficit parameter from the first three days' experiments to the power law.

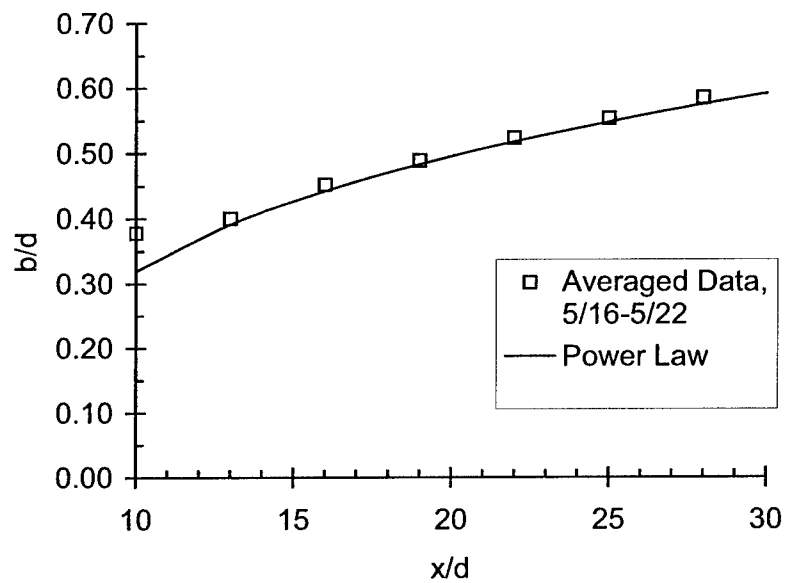


Figure 4.36: Comparison of averaged wake width parameter from the first three days' experiments to the power law.

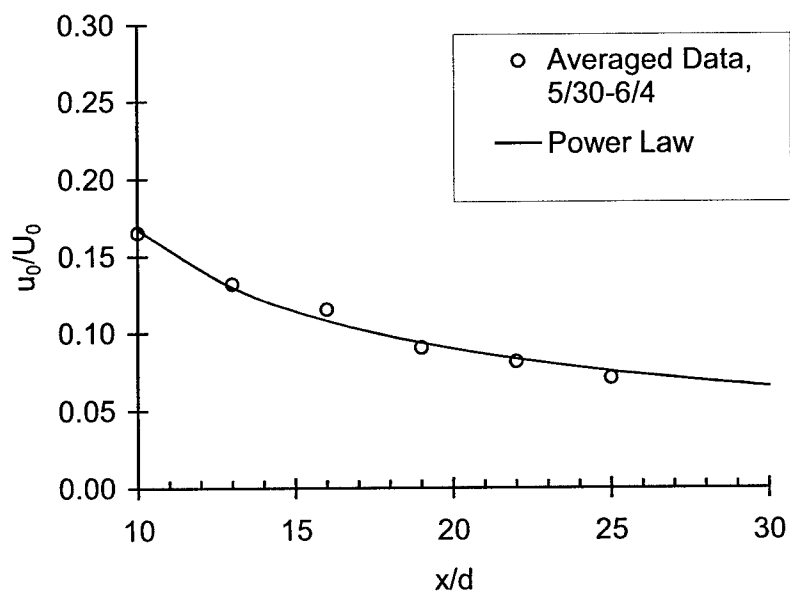


Figure 4.37: Comparison of averaged velocity deficit parameter from the last two days' experiments to the power law.

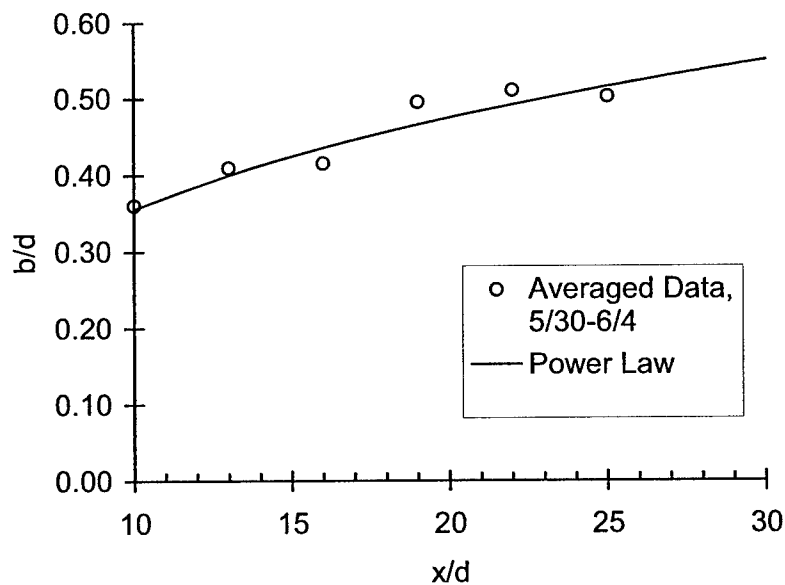


Figure 4.38: Comparison of averaged wake width parameter from the last two days' experiments to the power law.



The fits for  $u_0/U_0$  and  $b/d$  for the composite decreased pressure measurements are very close to the forms that should be expected. For the composite constant pressure measurements, the fit for  $u_0/U_0$  is fairly close to proper form, but the fit for  $b/d$  is erratic. The second fit parameters  $x_0/d$ ,  $c_u$ ,  $c_l$  and  $C_D$  are tabulated in Table 4.3. The drag coefficient results are very close to each other, and are in good agreement with the expected results from the LCC experiments and the computational results of Cash<sup>10</sup>. The computational results and the averaged experimental results for this hull shape are plotted in Figure 4.39. The individual and averaged experimental results are shown for two different temperatures, because the viscosity of water is very sensitive to the water temperature. The temperature of 20°C represents room temperature conditions. The temperature of 30°C is included because the water always seemed to be rather warm. No temperature of the water was taken, so the exact Reynolds number is unknown. Regardless, the averaged results are in good agreement with the trend of the computational results. This is again shown in Figure 4.40, which shows the averaged results along with Cash's computational results for three different submarine lengths.

Table 4.3: Curve fit results from composite data sets.

Experiment Date	$x_0/d$	$c_u$	$c_l$	$C_D$ (neglecting pressure gradient)	$C_D$
Composite 5/16, 5/17, 5/22	6.930	0.445	0.195	0.195	0.185
Composite 5/30, 6/4	3.552	0.580	0.174	0.201	0.191

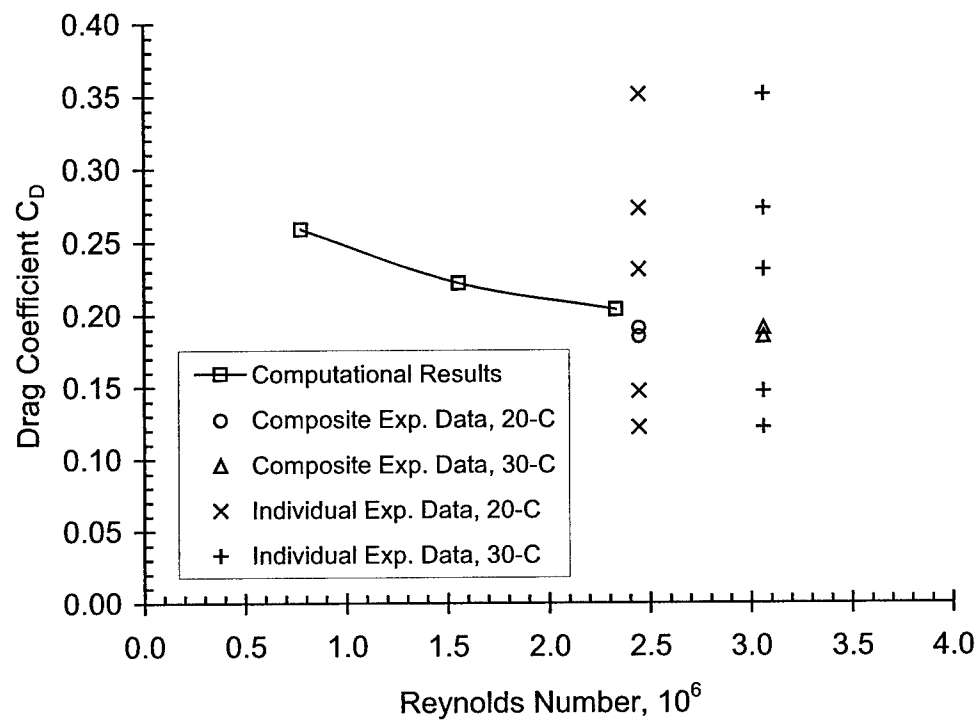


Figure 4.39: Comparison of experimental results with computational results of Cash.

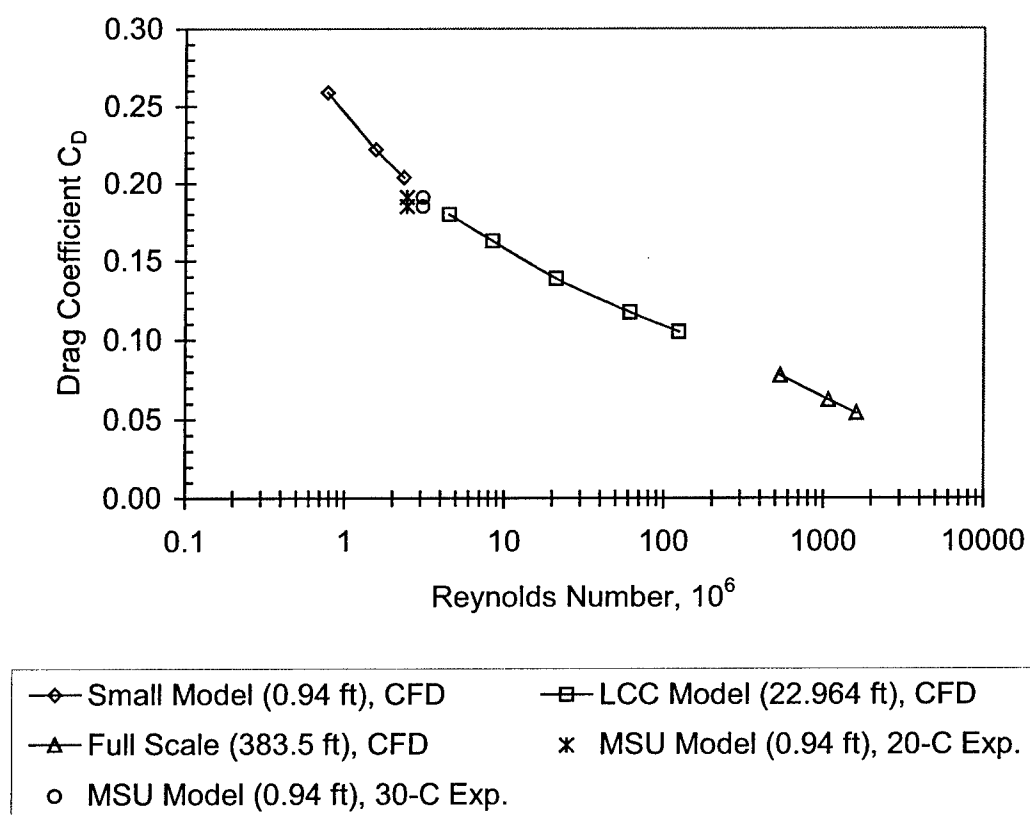


Figure 4.40: Averaged experimental results for MSU model and computational results of Cash for three different submarine lengths.

## CHAPTER V

### CONCLUSIONS AND RECOMMENDATIONS

#### 5.1 Conclusions

The water tunnel was repaired after numerous problems developed after its last operational period. The corners of the water tunnel and the drive section were repainted with several coats of protective paint. The drive system of the tunnel was modified to solve a longstanding problem of bearing burn-out. After these renovations were completed, the water tunnel was run nearly daily for a period of two months.

A calibration device was constructed for the Aerospace Engineering Department's new LDV system. An uncertainty analysis of the calibration process was completed. Once calibrated, the LDV system was found to be accurate to within 0.75% for the velocity range of 5-10 m/s.

The water tunnel test section velocity profiles were measured with high accuracy using the LDV system. These velocity profiles are the first detailed measurements of the tunnel flow quality. Generally, the turbulence intensity of the freestream is 1.5%. A highly accurate tunnel speed curve was developed so that for a given motor input speed, the freestream velocity at  $x/L = 0.125$  is accurately known. Also, it was discovered that the velocity profiles of the undisturbed freestream had repeatable kinks at a given  $x/L$ . These kinks are believed to have been caused by local optical properties in the Plexiglas® test section. During repeated measurements, it was noticed that the

freestream velocity shifted occasionally by almost 0.5 m/s. The cause or possible period of this shift was not determined. It is possible that static pressure drop due to leakage was a cause, or that the LDV system had a faulty Bragg cell. The effects of tunnel pressure on velocity measurements were studied later after the measurements of the submarine wake had been completed. It was during these studies that the water tunnel ruptured under pressure.

An 11.278-inch long submarine model was mounted along the tunnel centerline. The wake velocity profiles were measured at 10, 13, 16, 19, 22, 25, and 28 body diameters downstream of the stern of the model on five different days. The velocity profiles exhibited asymmetry and a centerline shift. The velocity profiles were fit to a Gaussian function, and self-similarity parameters were obtained. The wake velocity profiles were found to be self-similar beyond  $x/d = 10$ . Power law fits were applied, and the drag coefficient of the submarine model was calculated. The individual data sets were very inconsistent, with  $C_D$  ranging from 0.122 to 0.351. However, when the data sets were combined into two sets, one representing measurements under decreasing tunnel pressure and one representing measurements under a high constant tunnel pressure, the drag coefficients were 0.185 and 0.191, respectively. Although no firm conclusions can be made about the drag coefficient results, it is believed that the distortion of the tunnel test section under high pressure may have caused the submarine model to become misaligned with the flow. This could have caused premature boundary layer separation and a higher drag coefficient as compared to the low-pressure results.

## **5.2 Recommendations**

The third corner of the water tunnel must be repaired or replaced before the tunnel is operated again. There is a 2-ft long rupture in the fiberglass, as well as several bubbles in the inner coating. It is likely that water penetrated into the fiberglass, causing the layers to debond and thus weaken the structural integrity of the section. Since the bubbles are located throughout the damaged section, it is likely that water penetrated everywhere and the existing corner must be scrapped. Discussion with Raspet Flight Research Laboratory personnel who performed the repainting work revealed that the base coats did not adhere well to the tunnel parts. In light of this, all the corners and the drive section should be inspected for water damage.

Besides repair work, the one improvement that would greatly expand the research capability of the water tunnel would be to construct a rectangular test section so that the LDV is not restricted to velocity measurements on the horizontal plane of the centerline. This effect can be achieved by building a transparent box around the existing cylindrical test section, and filling it with water. A ray-tracing program may be needed if this is done, to account for four changes of media instead of only two.

A number of smaller modifications can be made to the water tunnel to expand its capability. A thermometer to measure the temperature of the water inside the tunnel would be useful for accurately determining Reynolds number for experiments. It is also recommended that the tunnel drive system be improved for smoother operation. It was

found that the water tunnel vibrated excessively at operating speeds higher than 550 rpm. This limits the test section velocity to about 9.7 m/s (31.8 ft/s).

A more rigid and adjustable platform for the LDV traverse would also expand the measurement capability of the system. The current traverse can only cover half the length of the test section at one time. If the traverse were mounted on a platform that could be easily rolled while maintaining alignment with the tunnel test section, measurements could be made anywhere in the test section during a single period of testing. A rail-mounted platform is envisioned for this purpose, with the angular alignment of the rails being adjustable to remain parallel with the tunnel test section wall.

Finally, the LDV system needs to be examined to determine that it is in good working order. The sudden velocity shifts observed during the experiment may be due to the intermittent operation of the LDV Bragg cell. Successive measurements of a constant LDV calibration disk speed over a long period of time may show whether the velocity shifts in the data were caused by an anomaly in the LDV system or in the water tunnel.

## BIBLIOGRAPHY

- <sup>1</sup> Goldstein, S., ed., *Modern Developments in Fluid Dynamics: An Account of Theory and Experiment Relating to Boundary Layers, Turbulent Motion and Wakes*, Vol. 1, Dover Publications, New York, 1965.
- <sup>2</sup> Dimotakis, Paul E., "Laser Doppler velocimetry momentum defect measurements of cable drag at low to moderate Reynolds numbers," Naval Construction Battalion Center, Contract No. N62583/77-M-R541, August 1977.
- <sup>3</sup> Townsend, A.A., *The Structure of Turbulent Shear Flow*, Cambridge University Press, Cambridge, Great Britain, 1976.
- <sup>4</sup> White, Frank M., *Viscous Fluid Flow*, McGraw-Hill Book Co., New York, 1974.
- <sup>5</sup> Wells, Wm. Graham, "Design Principles for a High Speed Fiberglass Water Tunnel," Research Report No. 51, Aerophysics Department, Mississippi State University, April, 1964.
- <sup>6</sup> Lindsey, Michael Lamar, "Renovation and Initial Operation of a High-Speed Water Tunnel," M.S. Thesis, Department of Aerospace Engineering, Mississippi State University, December 1998.
- <sup>7</sup> Coleman, Hugh W. and W. Glenn Steele, Jr., *Experimentation and Uncertainty Analysis for Engineers*, John Wiley & Sons, Inc., New York, 1999.
- <sup>8</sup> Chevray, R., "The Turbulent Wake of a Body of Revolution," *Journal of Basic Engineering*, June 1968, pp. 275-284.
- <sup>9</sup> Garner, H. C., Rogers, E. W. E., Acum, W. E. A., and Maskell, B. C., "Subsonic Wind Tunnel Wall Corrections," AGARDograph 109, October 1966, pp.319-321.
- <sup>10</sup> Cash, Allison Nicole, "Computational Studies of Fully Submerged Bodies, Propulsors, and Body/Propulsor Interactions," M.S. Thesis, Department of Aerospace Engineering, Mississippi State University, December 2001.



REPORT DOCUMENTATION PAGE				Form Approved OMB No. 0704-0188	
<p>The public reporting burden for this collection of information is estimated to average 1 hour per response, including the time for reviewing instructions, searching existing data sources, gathering and maintaining the data needed, and completing and reviewing the collection of information. Send comments regarding this burden estimate or any other aspect of this collection of information, including suggestions for reducing the burden, to Department of Defense, Washington Headquarters Services, Directorate for Information Operations and Reports (0704-0188), 1215 Jefferson Davis Highway, Suite 1204, Arlington, VA 22202-4302. Respondents should be aware that notwithstanding any other provision of law, no person shall be subject to any penalty for failing to comply with a collection of information if it does not display a currently valid OMB control number.</p> <p><b>PLEASE DO NOT RETURN YOUR FORM TO THE ABOVE ADDRESS.</b></p>					
1. REPORT DATE (DD-MM-YYYY) 01-08-2004		2. REPORT TYPE Final		3. DATES COVERED (From - To) 05-04-1999 -- 15-12-2002	
4. TITLE AND SUBTITLE Investigations of Scaling Effects on Submarine Propeller and Stern Boundary Layer Flows				5a. CONTRACT NUMBER	
				5b. GRANT NUMBER N00014-99-0534	
				5c. PROGRAM ELEMENT NUMBER	
6. AUTHOR(S) Bridges, David H. Cash, Allison C. Freudenthal, John L.				5d. PROJECT NUMBER	
				5e. TASK NUMBER	
				5f. WORK UNIT NUMBER	
7. PERFORMING ORGANIZATION NAME(S) AND ADDRESS(ES) Department of Aerospace Engineering, Mississippi State University P.O. Drawer A Mississippi State, MS 39762				8. PERFORMING ORGANIZATION REPORT NUMBER MSSU-ASE-04-02	
9. SPONSORING/MONITORING AGENCY NAME(S) AND ADDRESS(ES) Office of Naval Research ONR 333 Ballston Centre Tower One 800 North Quincy Street Arlington, VA 22217-5660				10. SPONSOR/MONITOR'S ACRONYM(S) ONR	
				11. SPONSOR/MONITOR'S REPORT NUMBER(S)	
12. DISTRIBUTION/AVAILABILITY STATEMENT APPROVED FOR PUBLIC RELEASE					
13. SUPPLEMENTARY NOTES					
14. ABSTRACT <p>A common problem in submarine design is the inability to build and test models at conditions that match the Reynolds number of prototype submarines, leaving computational simulations as the only method for testing new designs. A study was performed in which experimental and computational estimates of drag and propeller performance were obtained using models which differed in length by an order of magnitude. The purpose was to see how well the computational results would track the experimental results over the large jump in length, so that insight might be obtained into how well the computational results would predict the full-scale flows at lengths an order of magnitude larger than the large model used. The computations predicted the propeller performance well over the range of parameters simulated. The computational simulations under-predicted the drag of the bare submarine hull at the largest Reynolds number tested for the large model. This difference was attributed to limitations in the grid and/or turbulence model, and showed that significant care would need to be exercised in extending the computations to very large Reynolds number.</p>					
15. SUBJECT TERMS submarine, Reynolds number effects, propeller, scaling, thrust, drag					
16. SECURITY CLASSIFICATION OF:			17. LIMITATION OF ABSTRACT  UU	18. NUMBER OF PAGES  252	19a. NAME OF RESPONSIBLE PERSON David H. Bridges
a. REPORT U	b. ABSTRACT U	c. THIS PAGE U			19b. TELEPHONE NUMBER (Include area code) 662-325-8298